DISSERTATION

HORIZONTAL VORTICITY REDISTRIBUTION AND VORTEX ALIGNMENT IN DEVELOPING AND MATURE TROPICAL CYCLONES

Submitted by

PAUL D. REASOR

Department of Atmospheric Science

In partial fulfillment of the requirements

for the degree of DOCTOR OF PHILOSOPHY

Colorado State University

Fort Collins, Colorado

Summer, 2000

COLORADO STATE UNIVERSITY

June 5, 2000

WE HEREBY RECOMMEND THAT THE DISSERTATION PREPARED UNDER OUR SUPERVISION BY PAUL D. REASOR ENTITLED HORIZONTAL VORTICITY REDISTRIBUTION AND VORTEX ALIGNMENT IN DEVELOPING AND MATURE TROPICAL CYCLONES BE ACCEPTED AS FULFILLING IN PART REQUIREMENTS FOR THE DEGREE OF DOCTOR OF PHILOSOPHY.

Committee on Graduate Work

Adviser

Department Head

ABSTRACT OF DISSERTATION

HORIZONTAL VORTICITY REDISTRIBUTION AND VORTEX ALIGNMENT IN DEVELOPING AND MATURE TROPICAL CYCLONES

The three-dimensional redistribution of vorticity within a vortex is examined here in the context of tropical cyclone (TC) structure and intensity change. Aspects of the horizontal vorticity mixing dynamics are first presented in a novel analysis of high temporal resolution wind fields derived from airborne dual-Doppler observations of Hurricane Olivia (1994). Seven consecutive composites of Olivia's wind field with 30-min time resolution depict a weakening storm undergoing substantial structural changes.

The problem of vortex alignment (and the attendant three-dimensional redistribution of vorticity) is then re-examined in an effort to further understand the underlying dynamics of TC-like vortices tilted by vertical shear. The study is motivated in part by the analysis of Hurricane Olivia. Olivia's asymmetric evolution in the presence of increasing environmental vertical shear is consistent with that predicted by existing "vortex in shear" theories. These theories, however, are based on a nonlinear interpretation of unforced vortex alignment originally developed to explain the emergence of vertically-coherent vortex structures in geostrophic turbulence. For small to moderate vortex tilts, a simpler and more insightful linear model for unforced vortex alignment is presented. This model provides the basis for a deeper understanding of the dynamics of rapidly-rotating, vertically-sheared vortices.

The linear model is formally valid as long as the tilted vortex can be meaningfully represented through a wave, mean-flow decomposition. This is typically true if the vortex cores at upper and lower levels overlap. The validity of the linear model is tested for

a range of vortex tilts using a quasi-geostrophic model in both its complete and linear, equivalent-barotropic forms.

The vertical alignment dynamics in the aforementioned small to moderate tilt regime is accurately captured by linear vortex Rossby wave processes. For internal Rossby deformation radii larger than the horizontal scale of the tilted vortex, an azimuthal wavenumber one near-discrete vortex Rossby wave, or quasi-mode, exists. The quasi-mode is characterized by its steady cyclonic propagation, long lifetime, and resistance to differential rotation, behaving much like a discrete vortex Rossby wave. The quasi-mode traps disturbance energy causing the vortex to precess and thus prevents alignment. For internal deformation radii smaller than the horizontal vortex scale, the quasi-mode disappears into the continuous spectrum of vortex Rossby waves which promote complete alignment by irreversibly (but linearly) redistributing potential vorticity (PV).

The linear alignment theory is extended to stronger vortices in the Asymmetric Balance system with results similar to those for geostrophic vortices. In addition to providing new insight into the asymptotic dynamics of vortex merger in three dimensions, these results also are believed to have relevance to the problem of tropical cyclogenesis. Cyclogenesis initiated through the merger of low-level convectively-generated positive PV within a weak incipient vortex is captured by quasi-linear dynamics. A potential dynamical barrier to TC development in which the quasi-mode frustrates vertical alignment can be identified using the linear alignment theory in this case.

PAUL D. REASOR
Department of Atmospheric Science
Colorado State University
Fort Collins, Colorado 80523
Summer, 2000

ACKNOWLEDGEMENTS

I first wish to thank my advisor, Prof. Michael Montgomery, for quality mentoring over the years. His dedication of time and intellectual effort to his students is a model for advising. His exuberance and genuine interest in my work has made my time at CSU a truly enjoyable one. I also wish to thank my committee members, Prof. Wayne Schubert, Prof. Steve Rutledge, Prof. Michael Kirby, and Dr. Frank Marks for their valuable insight and contributions to this work.

Much of the observational work presented here would not have been possible without the support of the Hurricane Research Division (HRD) in Miami. I would like to thank Dr. Hugh Willoughby for supporting visits to the lab over past summers and encouraging the partnership between students and the lab that I have greatly benefited from. Dr. Frank Marks has been my "mentor away from home" during my visits to Miami and has taught me much about airborne Doppler radar in hurricanes. His many contributions to this work are greatly appreciated. Dr. John Gamache provided the three-dimensional wind analyses used in this study. I have benefited from many discussions with John regarding the details of dual-Doppler analysis. Everyone at HRD went out of their way to help me. I thank them all for their time and expertise. Finally, I want to thank the lab for allowing me to take part in the annual hurricane field program. Quite an experience!

I would like to thank the Montgomery group for providing a stimulating environment for research: Mr. John Persing, Mr. Tom Cram, Mr. John Fulton, and Dr. David Nolan. Mr. Persing has been especially helpful in the IDL graphics department. I would also like to thank former Montgomery group members, Ms. Holly Snell and Dr. Janice Enagonio for their contributions to this work. Ms. Snell's boundary layer expertise and Dr. Enagonio's many beneficial discussions over the years and help with the QG routines are appreciated.

I especially wish to thank Drs. Lloyd Shapiro and Dominique Möller for welcomed criticisms and suggestions regarding the observational portion of this work. It was greatly improved as a result. I also wish to thank Prof. William Frank, Dr. Sarah Jones, and Dr. Wen-Chau Lee for insightful discussions. I thank Mr. Matthew Eastin for providing the flight-level data used here and Dr. James Kossin for many helpful discussions regarding vorticity mixing in hurricanes and the observationally elusive tripole.

CONTENTS

LIST OF FIGURES

Chapter 1

INTRODUCTION

Despite decades of research on the dynamics and thermodynamics of tropical cyclones (TCs), prediction of intensity remains an operational challenge (DeMaria and Kaplan 1997). Although previous studies have identified the primary mechanisms for TC intensity change, including atmosphere-ocean interaction (Ooyama 1969; Rotunno and Emanuel 1987; Emanuel 1999), forcing by the large-scale atmospheric flow (Molinari et al. 1995; Montgomery and Farrell 1993), and the internal vortex dynamics (Montgomery and Kallenbach 1997; Montgomery and Enagonio 1998; Schubert et al. 1999; Möller and Montgomery 1999, 2000), no one influence is generally regarded as *the* determining factor in most situations. A case in point is the rapid intensification of Hurricane Opal (1995) as it approached the Florida panhandle on 4 October 1995. During a 12-hr period prior to the eye making landfall, Opal's maximum tangential winds increased by roughly 20–25 ms^{-1} (NHC Best Track). The dramatic strengthening of Opal has been attributed to both the presence of a warm-core oceanic eddy (Shay et al. 2000) and the favorable interaction of the storm with a nearby upper-tropospheric trough (Bosart et al. 2000). Thus, in some situations intensity change may result from a combination of mechanisms.

It is well known that the import of latent heat energy into the cyclone core is necessary for sustaining convection and strengthening a TC (Ooyama 1969). But can the fluctuations in intensity, which are sometimes dramatic, be explained simply through axisymmetric, thermodynamic arguments? Emanuel (1999) suggested that intensity change in most cases (including Opal) is controlled to zeroth order by the response of the axisymmetric TC to variations in the thermodynamic structure of the ocean. In many of the cases he presented where environmental vertical shear was not a factor, the long-time trends

in intensity were captured by his axisymmetric atmosphere-ocean model. The results do not confirm, however, that axisymmetric thermodynamics is solely responsible for the more rapid changes in intensity (i.e., fluctuations > 20 ms^{-1} per day) observed over open ocean, suggesting that environmental and internal asymmetric mechanisms are also likely contributing.

The uncertainty in intensity change prediction applies not only to mature storms, but also to incipient tropical disturbances. The large-scale environment is an important factor in TC genesis, as has been documented in climatological studies (e.g., Gray 1968; Zehr 1998). But why do so few storms form even under the best synoptic and oceanic conditions? On average 100 tropical disturbances are observed in the Atlantic basin during hurricane season, yet only about 10-15 develop into tropical storms (Frank 1975).

Bister and Emanuel (1997) proposed an axisymmetric model for TC genesis based on observations of TC Guillermo (1991) and supporting axisymmetric numerical simulations. A re-analysis of the Guillermo Doppler wind data by Bracken (1999), however, suggests a more prominent role played by asymmetries during the initial stages of genesis. Montgomery and Enagonio (1998, hereafter ME98) demonstrated that TC genesis can occur asymmetrically through the merger of convectively-generated low-level positive potential vorticity (PV) within an incipient vortex. Might the presence of convective blow-ups near the incipient vortex core be an additional condition for genesis? Once again, the role of internal (asymmetric) vortex dynamics in intensity change must be evaluated.

In the absence of in-situ and radar measurements within and in the vicinity of a TC, just quantifying intensity is a challenge. Determining the relative importance of various phenomena in producing intensity change is therefore a difficult task. Remote measurements from satellite are relied upon in such a situation. Satellite remote sensing can provide some information on the sea-surface temperatures (SSTs) (which may not necessarily be representative of the thermodynamic makeup of the ocean immediately below the surface) and the large-scale thermodynamic structure of the TC (Velden and Brueske 1999). Additionally, it can provide valuable information on the synoptic flow in which the TC is embedded.

Presently, satellite remote sensing is incapable of providing detailed mappings of the three-dimensional flow structure of a TC, which are needed to quantify the dynamical role of asymmetric external forcings and internal vortex dynamics. Airborne techniques for sampling a TC wind field have improved since the early days of aircraft measurements along the flight track, where composites over many storms had to be performed just to resolve the symmetric structure. Airborne Doppler radar was first used in the early 1980's (Marks and Houze 1984) and now permits the three-dimensional, low-azimuthal wavenumber TC core structure to be resolved for a single storm over an extended period of time. Despite the limited spatial coverage of the aircraft data, the flight-level winds still can be quite useful when used in conjunction with a sound dynamical theory, as exemplified in a recent study of vorticity mixing in the hurricane core by Kossin and Eastin (2000). The aircraft data also provide an important means of validating the Doppler-derived wind fields. But whereas the aircraft measurements can only suggest vortex-scale phenomena, the Doppler-derived wind fields can provide a complete picture of the low-wavenumber vortex core evolution, allowing the symmetric and (aliased) asymmetric structure to be clearly defined and distinguished (except in the hurricane eye). Consequently, asymmetric aspects of TC dynamics can now be studied observationally in conjunction with theory, as was done for decades in the study of axisymmetric mechanisms, thus bringing a greater balance to the study of intensity change.

In the work described below the role of internal asymmetric vortex dynamics in intensity change is examined from the perspective of newly-developed theoretical insights and a novel analysis of the evolving three-dimensional wind field of an observed TC. The role of horizontal vorticity redistribution in effecting structure and intensity change in the TC core, as discussed in recent numerical and theoretical studies (e.g., Montgomery and Kallenbach 1997, hereafter MK; ME98; Schubert et al. 1999, hereafter S99; Möller and Montgomery 1999, 2000; Kossin et al. 2000), is first addressed utilizing dual-Doppler radar observations of Hurricane Olivia (1994). The vorticity redistribution ideas are also applied to the problem of vortex vertical alignment. A new linear conceptual model for quasi-geostrophic (QG) vortex alignment is developed for vortices exhibiting small initial

tilts, with application to the problem of TC genesis. The QG results are then extended to higher Rossby number vortex flows as a first step in understanding the basic dynamics of arbitrarily strong vortices embedded in vertical shear. An observational strategy for exploring the dynamics of a TC in vertical shear is presented, again using wind data from Hurricane Olivia.

1.1 TC Vorticity Dynamics

A vorticity asymmetry placed on a continuous vortex monopole will tend to be sheared to finer radial scales by the differential rotation of the (azimuthal) mean tangential flow. This process was illustrated by Melander et al. (1987) in a nonlinear 2D nondivergent model initialized with an elliptical patch of vorticity. Filaments of vorticity were thrown outwards as the core of the vortex became circular. The reduction of the aspect ratio of the vortex patch in this way is referred to as 'axisymmetrization'. Guinn and Schubert (1993) related the formation of spiral bands in hurricanes to the filamentation of PV often observed in vortex axisymmetrization experiments. The spiral bands were shown to project minimally onto the fast inertia-gravity wave component and were argued to form as a result of PV wave breaking. Using a two-dimensional nondivergent model and shallow water Asymmetric Balance (AB) model (Shapiro and Montgomery 1993), MK, building upon the spiral band work of Guinn and Schubert, showed that when the aspect ratio of the vorticity ellipse is close to unity, the axisymmetrization of vorticity can be explained using linear dynamics. MK further demonstrated that the outward moving filaments of vorticity are actually radially propagating vortex Rossby waves which owe their existence to the radial gradient of azimuthal-mean vortex vorticity. A local vortex Rossby wave mechanics developed by MK provides standard wave quantities like phase and group velocity as well as the stagnation radii for these radially and azimuthally propagating waves.

The fact that the vortex Rossby waves are confined to the vortex and therefore must interact with it as they are sheared to finer radial scales was utilized by MK in an application to hurricanes. They proposed a mechanism by which vorticity perturbations (e.g., convectively or environmentally induced) to the symmetric hurricane vortex disperse as

vortex Rossby waves, propagate radially outward, and then interact with the mean vortex. The radially-inward momentum flux associated with the sheared vortex Rossby waves leads to an acceleration of the mean tangential flow inside the stagnation radius and a deceleration radially outside this radius. A vortex can undergo substantial structure and intensity changes through this mechanism.

ME98 validated the predictions of MK for small, but finite-amplitude vorticity disturbances in a barotropic nondivergent model and then applied the theory to the problem of tropical cyclogenesis at order one wave amplitudes in a three-dimensional QG model. They demonstrated how three-dimensional axisymmetrization of convectively-generated PV anomalies near a weak mid-level parent vortex can lead to the spin-up of a surface cyclonic circulation beneath the pre-existing mid-level vortex. The development of a warm-core vortex was found to be a natural by-product of axisymmetrization.

A subsequent study by Möller and Montgomery (1999) extended ME98 to larger Rossby numbers through an investigation of the axisymmetrization of small, but finite amplitude and large amplitude disturbances in the nonlinear AB shallow water model. The spin-up of the mean tangential winds agreed with the quasi-linear predictions of MK as well as the predictions of a primitive equation model. Möller and Montgomery (2000) next examined vortex axisymmetrization in the context of a three-dimensional AB model. To avoid changes in the vortex center that result from a "single-cluster" PV perturbation (e.g., from a single, mesoscale blow-up of convection) Möller and Montgomery (2000) focused primarily on double-cluster perturbations to the mean vortex. Through successive double-cluster pulses, a vortex of tropical storm strength was intensified to hurricane strength. This asymmetric mode of intensification, which occurred largely through wave-mean interactions for the perturbation amplitudes considered, is an alternative to the conventional symmetric mode of intensification (Ooyama 1969).

As Fig. 1.1 shows for Hurricane Olivia (1994), the symmetric component of wind magnitude in the inner-core region in the lower to middle troposphere can be an order of magnitude greater than the higher wavenumber contributions (see also Fig. 1 of Shapiro and Montgomery 1993). Thus, in the absence of strong flow instability, linear theory and

its wave-mean predictions should give useful qualitative insight into the vorticity dynamics of the near-core region and internally-generated intensity change.

The nonlinear vorticity dynamics of the hurricane core region has also received attention in the work of S99. They proposed that during periods in which convective forcing is weakened or suppressed altogether the breakdown of the PV ring encircling the hurricane eye via barotropic instability will promote vorticity mixing in the eye region, thereby influencing the eye dynamics and thermodynamics. As part of the breakdown process, eyewall mesovortices were observed to form before the ultimate reconsolidation into a vortex monopole. In real hurricanes these secondary vortices may have local wind speeds which exceed that of the symmetric circulation, increasing locally the destructive potential of the hurricane (Black and Marks 1991; Hasler et al. 1997).

1.2 Airborne Doppler Radar Observation of TCs

While the vorticity dynamics of the hurricane's near-core region has been the subject of recent numerical and theoretical studies, it has yet to be explored in great observational detail. The lack of observational focus on the vorticity dynamics may be, in part, a consequence of the complications that convection provides to the idealized dynamical theories described above, but is also likely a result of inadequate observations of the hurricane near-core evolution. Aside from the chance encounter of a landfalling hurricane with a ground-based radar, the only way to get a three-dimensional look at the wind field (both vortex scale and mesoscale) of the hurricane core is to fly through the storm with a radar-equipped plane.

The use of airborne Doppler radar to study air motions in convective storms was first proposed by Lhermitte (1971). In pushing for the implementation of airborne radar, Lhermitte emphasized the freedom that an airborne platform affords by allowing the scientist to go to the phenomenon of interest. One of the first questions that had to be addressed was what kind of radar to use. Balancing concerns over attenuation, radar size, and beam width, the 3.2 cm wavelength X-band radar was chosen. Lhermitte envisioned the airborne radar pointing vertically up or down in a non-scanning mode (i.e., vertical

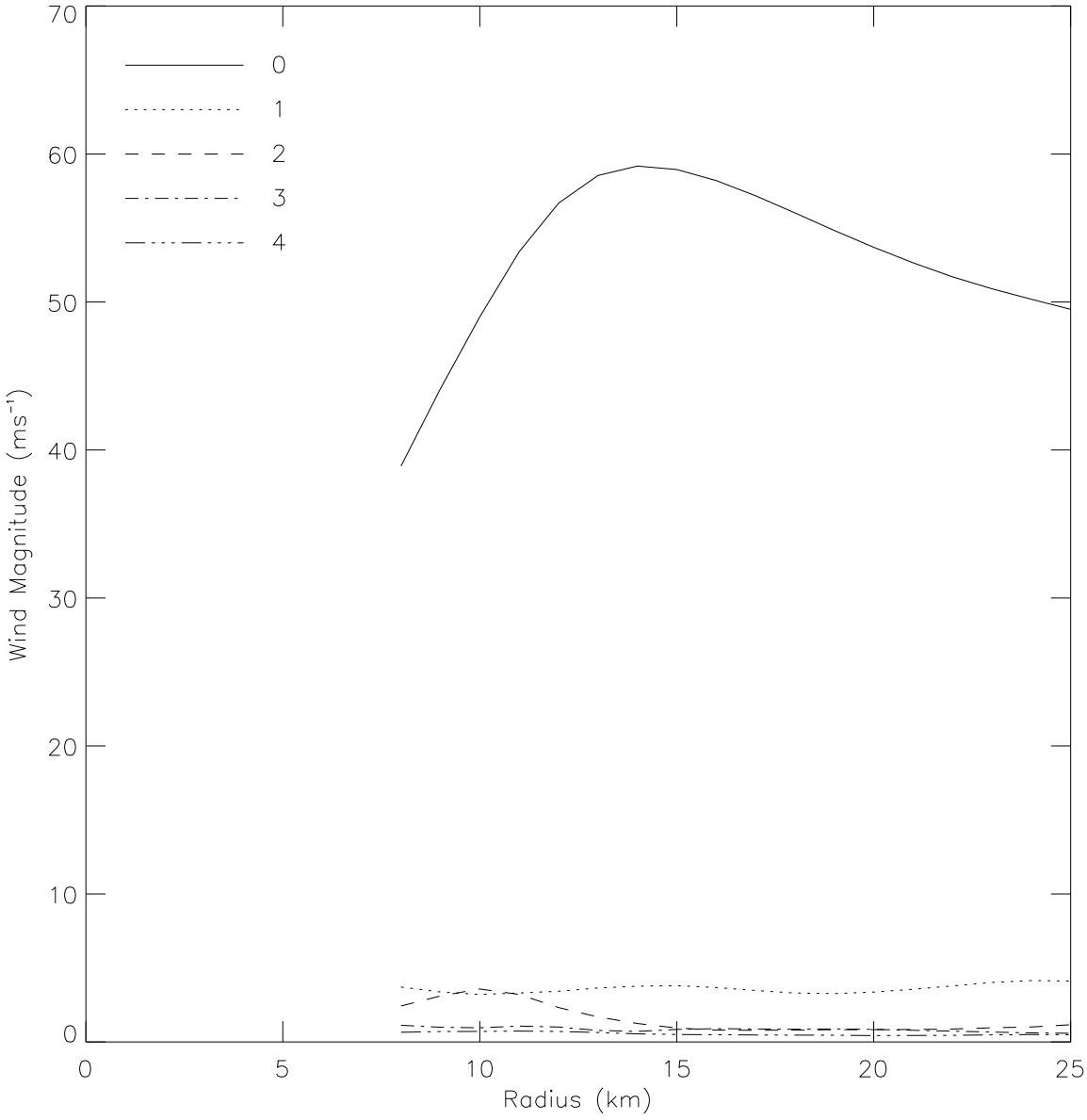

Figure 1.1: Olivia dual-Doppler derived wind magnitude (m s^{-1}) at 1.5 km height averaged over the observation period. Shown are the symmetric, wavenumber one, wavenumber two, wavenumber three, and wavenumber four components. The "no-scatter" region of the eye (i.e., within approximately 8 km radius) is blocked out here and in subsequent plots.

incidence) as the plane traversed the convective storm. Vertical cross-sections through the storm could then be obtained over a timescale short enough to consider the measurements stationary.

In 1976 the National Oceanographic and Atmospheric Administration (NOAA) equipped two WP-3D aircraft with tail X-band radars. Doppler measurements were made possible once the Doppler receivers were installed during the period 1980–1981. The radars not only could make vertical incidence measurements, but could also scan in the vertical plane perpendicular to the flight track, thus providing the possibility of horizontal wind measurements. The first successful test of the Doppler system was made by Jorgensen et al. (1983) in a comparison of airborne and ground-based Doppler winds. The accuracy of the airborne Doppler radial winds was found to be ~ 1 ms^{-1}, confirming Lhermitte's (1971) predictions.

The first airborne Doppler radar study of TC wind structure was reported by Marks and Houze (1984) for Hurricane Debby (1982). A pseudo dual-Doppler approach was employed in which a single plane flies near-orthogonal legs through the storm and stationarity of the flow is assumed. From the two radar views a horizontal wind vector can be constructed, most accurately in the horizontal plane of the radar. The wind fields suggested the presence of small-scale eddies embedded in the primary circulation, as well as an apparent mesocyclone and its attendant low-level vorticity. They speculated that advection of the mesocyclone vorticity into the storm core by the radial inflow might influence storm development. Marks and Houze (1987) extended this work to a more fully developed storm, Hurricane Alicia (1983). The first observational confirmation of the radial outflow layer at upper levels was made. Additionally, they included an analysis of the vertical winds along the flight track. This was the first study to capture the inner-core secondary circulation in a single storm.

A more complete three-dimensional mapping of the hurricane wind field, including the vertical wind, was performed by Marks et al. (1992, hereafter MHG) for Hurricane Norbert (1984). Only a single wind composite spanning roughly 2 h was made, so information on the time evolution of the three-dimensional wind field was unavailable. Nevertheless,

with an average time separation of about 7.5 min between measurement of orthogonal components of the horizontal wind, details of the mesoscale structure of the eyewall could be provided in each individual quadrant of the storm. At 3 km height and above they observed a cyclonic and anticyclonic vortex couplet in the flow field with maximum amplitude at the radius of maximum tangential wind (RMW). Individual changes in and the interaction between the mean horizontal flow and this vortex couplet were discussed as possible mechanisms for intensity change.

1.3 Descriptive Outline of Dissertation

The subject of this dissertation is the asymmetric vorticity dynamics of the tropical cyclone from genesis to lysis. We begin by addressing the problem of horizontal vorticity redistribution in the TC core. According to the theoretical arguments and numerical simulations discussed above, symmetrizing bands of vorticity and discrete vorticity features in the eyewall should be present as part of this ongoing redistribution of vorticity. We therefore ask:

- **Can asymmetric vorticity redistribution be demonstrated observationally using wind fields derived from airborne dual-Doppler radar measurements within the TC core?**

A review of radar meteorology in the TC setting is provided in Chapter 2 for those unfamiliar with the basic ideas behind radar remote sensing. This includes a brief discussion of TC microphysics and standard airborne dual-Doppler techniques. Also discussed are the data used and the wind analysis methodology. The evolution of symmetric and asymmetric components of storm vorticity are presented in Chapter 3 in the context of the dynamical theories discussed in Section 1.1. This is the first study to analyze Doppler-derived asymmetric vorticity within the hurricane core with these ideas in mind. Complimenting the observational analyses are barotropic numerical simulations which suggest that the observed vorticity evolution is intimately related to the barotropic stability of the mean vortex.

With regards TC genesis, both the horizontal redistribution of vorticity and vertical alignment of vorticity are necessary for development. Previous work has viewed the vertical alignment of a geostrophic vortex as a fundamentally nonlinear process. In light of recent work on vortex merger summarized in Section 1.1 we hypothesize:

• **The evolution of a vortex exhibiting small initial tilt can be understood using linear vortex Rossby wave theory.**

Chapter 4 presents the numerical models used to test this hypothesis. In Chapter 5 we demonstrate that the co-rotation of upper- and lower-level PV anomalies associated with an initially-tilted vortex is explained by the presence of a near-discrete vortex Rossby wave, or more precisely a long-lived quasi-mode of the geostrophic vortex. Complete alignment occurs through the irreversible redistribution of PV by sheared linear vortex Rossby waves. In Chapter 6 we extend the QG results to include finite Rossby number effects and demonstrate how external shear can be included in the linear problem to more accurately represent tropical conditions. An analysis of dual-Doppler observations of a hurricane interacting with increasing vertical shear shows consistency with recent dynamical arguments regarding the transverse circulation of a vortex in shear. The asymmetric PV generation excited by the coupling of this transverse circulation with the boundary layer may impact the alignment dynamics. We propose that:

• **The dual-Doppler wind analysis procedure outlined here, in conjunction with the new insights into vortex alignment, can be used towards the goal of understanding and predicting tropical cyclogenesis.**

In Chapter 7 the major conclusions of this dissertation are summarized.

Chapter 2

AIRBORNE RADAR OBSERVATIONS: HURRICANE OLIVIA (1994)

2.1 TC Radar Meteorology

2.1.1 Radar Basics

The basic idea behind radar remote sensing is as follows: A pulse of electromagnetic (EM) energy is emitted from the radar antenna and propagates through the atmosphere until a scattering object, or target, is encountered. Part of the initial pulse energy is backscattered in the direction of the radar receiver, which measures the power of the returned signal and notes the time it took for the pulse to reach the target and return. The power scattered by the target will depend on its shape, size, and intrinsic properties (e.g., phase in the case of water targets) as well as the wavelength of the incident radiation. Since EM waves travel at the speed of light, c, the travel time is easily converted into a range, r, from the radar. Assuming isotropic scatterers, the power, P_r, returned from a single target is given by

$$P_r = P_t \cdot \frac{A_e}{4\pi r^2}, \tag{2.1}$$

where P_t is the power intercepted by the target and A_e is the effective cross-sectional area of the radar. Since the EM energy is initially focused into a beam by a parabolic dish, the transmitted power is given by the original value P_{out} multiplied by the radar antenna gain, G. Meteorological targets do not in general radiate isotropically. An effective target area can be defined, however, which backscatters energy as an isotropic source, but returns the same backscattered power at the radar as the actual target. This effective area is called

the back-scattering cross-section, σ_i. The power backscattered by the target is then given by

$$P_t = P_{out} G \cdot \frac{\sigma_i}{4\pi r^2}. \tag{2.2}$$

The effective cross-sectional area of the antenna is (Battan 1973)

$$A_e = \frac{G\lambda^2}{4\pi}, \tag{2.3}$$

where λ is the wavelength of the emitted EM radiation. From a practical standpoint this is a very important relation. To minimize attenuation, longer wavelength radars are desired. But the effective area of the antenna goes like the square of the wavelength. Therefore, for airborne platforms, where bulk must be minimized, only wavelengths around 3–5 cm can be used. The unfortunate consequence is that in heavily precipitating regions the radar range may only be 30–40 km. This turns out to be a real restriction in TC flights where one would like to obtain the vortex structure over as large a domain as possible.

Combining equations (2.1)–(2.3) and considering the power returned by a pulse volume (which will contain a number of targets),

$$V = \pi \left(\frac{r\theta}{2}\right)^2 \frac{c\tau}{2} \qquad \text{(for a circular beam)}, \tag{2.4}$$

where θ is the beamwidth and τ is the pulse duration (typically ~ 1 μs), yields the so-called radar equation,

$$\overline{P}_r = A P_{out} G^2 \lambda^2 \theta^2 \tau \cdot \frac{\eta}{r^2}, \tag{2.5}$$

where $A = c/512\pi^2$ and η is the back-scattering cross-section per unit volume, commonly referred to as the radar reflectivity ($\mathrm{cm^2 m^{-3}}$). The returned power has been averaged over several samples of the pulse volume.

For Rayleigh scattering conditions (i.e., when the radar wavelength is much greater than the target diameter) the backscattering cross-section is known. Given a homogeneous distribution of spherical targets, the radar reflectivity is expressed as

$$\eta = \frac{\pi^5}{\lambda^4} |K|^2 \sum_{vol} D_i^6, \tag{2.6}$$

where $|K|$ is a dielectric factor and D_i is the diameter of the ith target in the unit volume (denoted by *vol*). The reflectivity factor, Z ($\mathrm{mm^6 m^{-3}}$), is defined as

$$Z = \sum_{vol} D_i^6. \tag{2.7}$$

Note that the reflectivity factor involves an inherent ambiguity since it depends on both target size and the distribution of targets. Many small targets can give the same reflectivity as a few big targets. This is especially important to keep in mind when trying to relate particle fall speed or rain rate to the reflectivity factor.

For a 3-cm wavelength radar the Rayleigh approximation is valid for particle diameters less than approximately 2 mm. For larger drop sizes, scattering from higher order electric and magnetic dipoles must be included in the expression for the backscattering cross-section. A more general expression for the backscattering cross-section which includes these effects is given by Mie theory (see Battan 1973 for discussion). In tropical cyclones the particle concentration tends to peak near 1 mm, so Eq. (2.6) is only marginally valid (although it will give qualitatively correct results). To account for the departures from Rayleigh scattering conditions, Z is replaced by an effective reflectivity factor, Z_e.

Rewriting the radar equation (2.5) in terms of the effective reflectivity factor yields

$$\overline{P}_r = A' P_{out} G^2 \theta^2 \tau \cdot \frac{|K|^2 Z_e}{\lambda^2 r^2}. \tag{2.8}$$

where A' is a constant proportional to A which also takes into account the fact that the power is not uniform across the beam width. Given the power, range, radar parameters, and target properties, one can solve for Z_e. Typically Z_e is converted into dBZ,

$$dBZ = 10 \log_{10} Z_e. \tag{2.9}$$

This quantity will henceforth be referred to as the reflectivity.

In the above discussion we have alluded to certain choices that must be made in deciding which type of radar to use and how to use it. In designing a field experiment several factors, in fact, must be weighed. We briefly discuss a few of the more important ones in the context of TCs.

Given radar size limitations, the 3-cm X-Band radar is typically used on airborne platforms (e.g., NOAA WP-3D tail radars, NCAR Electra ELDORA radar). The physical dimensions of the radar antenna (i.e., dish diameter, D) and the wavelength determine the beamwidth. For a *circular* paraboloidal antenna, the beamwidth is given by (e.g., see Fowles (1989) for a discussion of the diffraction pattern of a circular aperture)

$$\theta = \frac{1.27\lambda}{D}. \tag{2.10}$$

In the case of the WP-3D tail radars (which usually scan perpendicular to the flight track) the horizontal and vertical beamwidths are 1.35° and 1.9°, respectively. Because uncorrelated samples are desired at each (radar) azimuthal viewing angle, the beamwidth sets a maximum azimuthal resolution. Large beamwidths can lead to insufficient filling of the pulse volume at large range. For example, at 50 km range a vertical beamwidth of 2° results in a 1.5–2 km pulse volume depth, a fraction of which may contain targets (especially near echo top).

The need for good resolution along the flight track necessitates a rapid scan rate in the azimuth. But this must be weighed against the need for many independent looks at the same pulse volume for the best sampling statistics. The resolution along the beam (i.e., range gate spacing) is set by the pulse length and is typically about 150 m for a 1 μs pulse.

The pulse repetition frequency (PRF) sets the maximum unambiguous range

$$r_{max} = \frac{c}{2 \cdot PRF} \tag{2.11}$$

which is how far a pulse can go out in range and get back to the radar in time for the next pulse to be sent out. More importantly for TC applications, the PRF also sets the maximum unambiguous velocity

$$v_{max} = \frac{\lambda \cdot PRF}{4} \tag{2.12}$$

which is the maximum velocity that can be sampled along a radial without aliasing. It is based on the maximum frequency that the radar can detect, i.e., the Nyquist frequency

$$f_{max} = \frac{PRF}{2}. \tag{2.13}$$

Combining (2.13) with the Doppler shift frequency, $f = 2v/\lambda$, yields (2.12). Velocities measured beyond v_{max} are "folded". As an example, the PRF of the WP-3D tail radar is 1600 Hz, resulting in $v_{max} \approx 13$ ms^{-1}. A measured velocity of 20 ms^{-1} will be recorded as -6 ms^{-1}. Unfolding the velocity can be a time consuming process, especially in cases where multiple folds occur and in regions of strong shear. The unfolding process is facilitated in the case of airborne Doppler radar since in-situ aircraft measurements at the radar can be used as a first guess in the unfolding of the data. An automated routine based on the method of Bargen and Brown (1980) is generally able to unfold much of the wind data.

2.1.2 TC Microphysics

The hurricane is comprised of a generally precipitation-free eye surrounded by a convective eyewall, outside of which are found stratiform rainbands (with embedded convective cells) spiraling around the storm (see Fig. 2.1). Using reflectivity data from the tail radar of the NOAA WP-3D aircraft when it was pointing vertically, Jorgensen (1984) documented the radius-height structure of hurricane precipitation in each of these regions for multiple storms. His results are summarized below.

Within the eyewall of a mature storm reflectivity is typically greater than 40 dBZ with local maxima of 50–55 dBZ. Because of sloping updrafts in the eyewall (Shapiro and Willoughby 1982; Jorgensen 1984; Marks and Houze 1987) hydrometeors fall out at radii outside of the convective updraft at low levels, leading to a mismatch between the location of maximum low-level vertical velocity and reflectivity. Black et al. (2000) have recently documented the azimuthal structure and evolution of convection in the eyewall. They observed convective cells initiated at low levels in the eyewall grow as they are advected by the tangential flow of the vortex. The reflectivity maxima occur downwind of the region of cell initiation as hydrometeors fall out of the mature convective cells. As the cells move above the 0°C isotherm, falling precipitation induces low-level downdrafts. Above 6 km height ice particles are swept around the storm and radially outward in the upper-level outflow layer.

The rainbands are characterized by reflectivities of about 30–35 dBZ and isolated cells of 40 dBZ. They lie within a larger region of stratiform precipitation with reflectivity

less than 30 dBZ. The stratiform regions show a clear bright band in reflectivity below the 0°C isotherm ($\sim$ 5 km height). The bright band results from the coating of ice particles with water as they fall below the melting level. The radar basically sees large liquid hydrometeors. Since $Z \propto D^6$, elevated reflectivity (the bright band) is observed. As the ice lattice collapses and the drops become less concentrated in space, the reflectivity decreases below the bright band. Although the heaviest rain rates are in the convective eyewall, the stratiform precipitation region covers a much greater area. According to Marks (1985), 50 to 60 percent of inner-core rainfall can be accounted for by the stratiform precipitation.

For purpose of estimating particle fall speeds (V_T) and rain rates (R) using reflectivity data, it is important to understand how particle size and concentration contribute to Z in the TC setting. Equation (2.7) can be written in terms of the particle concentration,

$$Z = \sum_i N(D_i) D_i^6, \tag{2.14}$$

where N has units of number of particles per m^3. The rain rate (mm h^{-1}) is given by

$$R = \frac{\pi}{6} \sum_i N(D_i) D_i^3 V_T(D_i). \tag{2.15}$$

Using a PMS Optical Array Spectrometer Probe mounted on the WP-3D aircraft, Jorgensen and Willis (1982) obtained particle size and distribution measurements in a hurricane. From these measurements, and estimates of V_T, both Z and R were computed using Eqs. (2.14) and (2.15), respectively.

Typical drop-size distributions in a hurricane, which is comprised of both convective and stratiform regions, compare well with measurements made in general tropical convective systems. Drop-size distributions in tropical cloud cores compiled by Cunning and Sax (1977) during the GATE experiment show that the particle concentration peaks for $D_i < 1$ mm. Drop sizes greater than 4 mm are rare except near cloud base in the convective regions. The Z-R relationship derived by Jorgensen and Willis (1982), applicable to both the convective and stratiform regions of a hurricane below the 0°C isotherm, is

$$Z = 300 R^{1.35}. \tag{2.16}$$

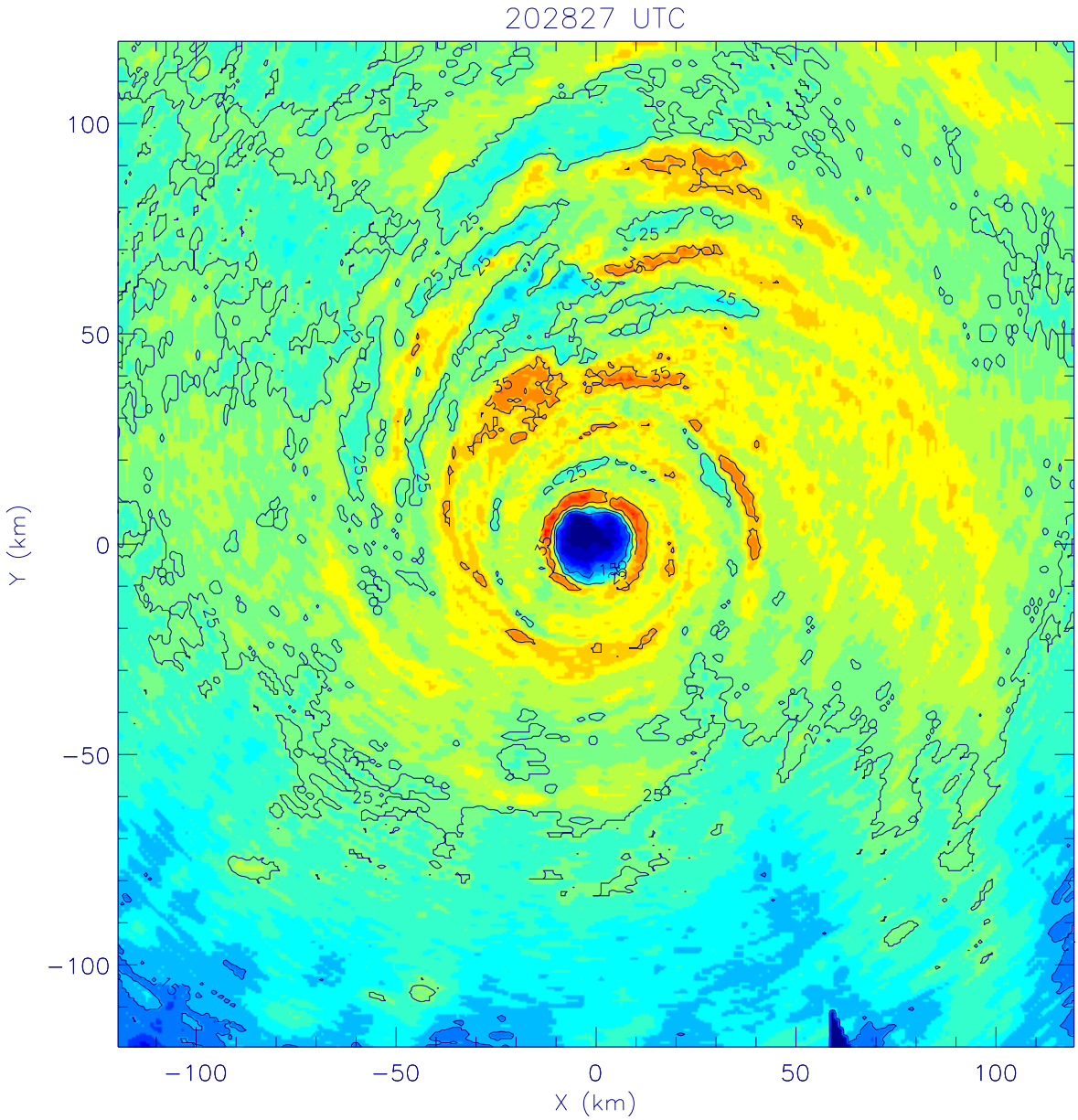

Figure 2.1: Composite of lower fuselage reflectivity from Hurricane Olivia at 2028 UTC, 25 September 1994. Contour interval is 10 dBZ. (1) The precipitation-free eye. (2) The convective eyewall. (3) The stratiform spiral rainband region.

2.1.3 TC Dual-Doppler Methods

Velocity is measured using Doppler radar by computing the phase shift between the emitted and returned EM pulses

$$\Delta\phi = \frac{4\pi r}{\lambda}. \tag{2.17}$$

The Doppler velocity is then obtained from the time rate of change of the phase, i.e.,

$$v = \frac{\lambda}{4\pi}\frac{d\phi}{dt}. \tag{2.18}$$

Since it is actually a pulse volume that is measured, a distribution of velocities is returned from which a mean radial velocity can be computed. The distribution can actually be quite broad in turbulent situations or regions with large shear. Such regions are identified by large spectral width.

Constructing a three-dimensional wind field from raw airborne Doppler data is in large part a scientific endeavor, but also admittedly involves a fair amount of artistry. Unlike ground-based dual-Doppler observations, the geometry of the airborne platforms is constantly changing. Aircraft translation, drift, pitch, and roll must all be taken into account in converting from radar-relative to earth-relative winds (Lee et al. 1994). Navigation errors resulting from uncertainties in the inertial navigation system have, for the most part, been eliminated with the advent of GPS tracking.

For the purpose of this discussion, we will focus on dual-Doppler observing methods based on track-normal scanning of the tail radar (i.e., the tail radar scans in a plane perpendicular to the aircraft flight track). The FAST scanning method in which the tail radar alternately scans fore and aft of the normal to the flight track is discussed by Gamache et al. (1995) in the hurricane context and will not be discussed here. In a single plane mission through a hurricane, pseudo dual-Doppler observations are obtained by flying consecutive near-orthogonal legs into and out of the storm core. In this way two independent views of the horizontal winds are made in an individual quadrant. Of course, for azimuthal elevation angles of the radar near zero this is an accurate statement. When the beam is pointing so as to project onto the vertical, the wind vector that one constructs no longer lies in the horizontal plane, and in fact is no longer simply a measurement of

air motion. The hydrometeor fall speeds must be removed. To remove the fall speeds one needs to know how large the particles are. Reflectivity is a strong measure of particle size, but it also depends on concentration. Nevertheless, standard empirically-based Z-V_T relations are used above and below the 0°C isotherm (Marks and Houze 1987):

$$V_T = \begin{cases} 2.6Z^{0.107}, & \text{altitudes} < 5.1 \text{ km} \\ 0.817Z^{0.063}, & \text{altitudes} > 7.5 \text{ km}. \end{cases} \tag{2.19}$$

The larger exponent for the fall velocity below 5 km reflects observations of rain at those levels. Above 5-6 km ice is commonly observed which has a much smaller fall velocity, as reflected in the reduced exponent. Both of these relations, which are based on surface observations, are applied at higher vertical levels by multiplying by a density correction, $[\rho_0/\rho(z)]^{0.45}$, where ρ_0 is the surface density.

There are numerous ways of deriving a three-dimensional wind field using iterative (Marks et al. 1992) or variational techniques (Gamache 1998) with different vertical boundary conditions. In the iterative method the two Doppler measurements of velocity at a point ($v_r^{(1)}$ and $v_r^{(2)}$) are expressed in terms of the Cartesian velocity components (Jorgensen et al. 1983),

$$v_r^{(1)} = u \sin\beta^{(1)} \sin\theta^{(1)} + v \cos\beta^{(1)} \sin\theta^{(1)} + (w + V_T) \cos\theta^{(1)} \tag{2.20}$$

$$v_r^{(2)} = u \sin\beta^{(2)} \sin\theta^{(2)} + v \cos\beta^{(2)} \sin\theta^{(2)} + (w + V_T) \cos\theta^{(2)},$$

where $\beta^{(i)}$ are the antenna pointing angles for each radar relative to north and $\theta^{(i)}$ are the elevation angles from the vertical. In order to solve this system of equations, an initial guess for $W = w + V_T$ must be made. One typically uses $W = 0$ as a first guess, but can use $W = V_T$ given by Eq. (2.19) as a more accurate estimate. After solving for u and v, an estimate of w can be attempted by vertically integrating the mass continuity equation. The new estimate of w is then substituted back into (2.20) and new u and v are computed. This procedure is repeated until some convergence criterion is met. If the two Doppler velocity measurements were made far apart in time such that horizontal derivatives of the composited wind field cannot be trusted, it makes little sense to try and converge on a solution. The first guess for the horizontal wind field is probably the best one can hope

for. Only if the wind field is approximately stationary during the compositing period should the iterative scheme be employed. Beams at elevation angles greater than 45° (and therefore minimal projection onto the horizontal winds) should not be included in the analysis since they tend to make the iterative scheme unstable.

Obtaining w is not a trivial matter. Boundary conditions on w must be assumed for each vertical column. Since airborne radar is generally unable to resolve the boundary layer when flying at 3–4 km height due to sea clutter, setting w equal to zero at the lowest *resolved* level is bound to result in large errors in the upward integration, especially in a hurricane where boundary layer convergence is known to be large. Furthermore the density weighting of the convergence will only accentuate low-level errors. Thus, downward integration of the continuity equation using $w = 0$ at echo top is the preferred method. Errors will still arise even if the reflectivity top can be defined, since w does not necessarily have to be zero there.

The wind fields used in this study were created through a refinement to the above technique. A variational method outlined by Gamache (1998), and in the spirit of the MUSCAT technique of Bousquet and Chong (1998), was employed in which the dual-Doppler equations and continuity equation are solved simultaneously. According to Gamache (1998) this solution method should be more stable than the iterative method for Doppler radials with high incidence angle (i.e., large elevation angles from the horizontal). As opposed to the iterative method which accumulates errors in the downward integration of the continuity equation, the variational scheme attempts to distribute the errors in a more natural way by effectively integrating the continuity equation along the path perpendicular to the planes containing the two Doppler velocity vectors (i.e., the characteristic).

Following Gamache (1998), the cost function is given by

$$f = \mu^{(1)} j^{(1)} + \mu^{(2)} j^{(2)} + \mu^{(3)} j^{(3)} + \mu^{(4)} j^{(4)}, \tag{2.21}$$

where

$$j^{(1)} = \sum_{ijkl} (v_{r,l}^{(1)} - u_{ijk} \sin\beta_l^{(1)} \sin\theta_l^{(1)} - v_{ijk} \cos\beta_l^{(1)} \sin\theta_l^{(1)} - (w_{ijk} + V_{T,l}^{(1)}) \cos\theta_l^{(1)})^2, \quad (2.22)$$

$$j^{(2)} = \sum_{ijkl} (v_{r,l}^{(2)} - u_{ijk} \sin\beta_l^{(2)} \sin\theta_l^{(2)} - v_{ijk} \cos\beta_l^{(2)} \sin\theta_l^{(2)} - (w_{ijk} + V_{T,l}^{(2)}) \cos\theta_l^{(2)})^2, \quad (2.23)$$

$$j^{(3)} = \sum_{ijk} [\nabla \cdot (\rho_k \mathbf{V}_{ijk})]^2, \quad (2.24)$$

and

$$j^{(4)} = \sum_{ijk} [(\nabla^2 u_{ijk})^2 + (\nabla^2 v_{ijk})^2 + (\nabla^2 w_{ijk})^2]. \quad (2.25)$$

The i, j, and k indices denote x, y, and z locations, respectively, and the l index accounts for multiple views from the same radar at a given location. The μ factors are the weights for each of the cost functionals. The first two functionals are the Doppler radar equations, the third is the continuity equation, and the fourth is the Laplacian filtering. The cost function is minimized with respect to u, v, and w, ultimately yielding the three-dimensional wind field.

2.2 Data

2.2.1 Hurricane Olivia on 25 September 1994

Eastern Pacific storm Olivia strengthened into a hurricane near 115°W and 15°N on 24 September 1994. According to Pasch and Mayfield (1996), Olivia continued to strengthen on 24 September, reaching a minimum surface pressure of 949 mb by the end of the day. SSTs were approximately 28°C (Gamache et al. 1997). Peak intensity was observed around 1200 UTC on 25 September with sustained tangential wind speeds of approximately 67 m s^{-1}. Following this time Olivia fell under the influence of a mid- to upper-tropospheric cyclone west of southern California, resulting in a 4-5 m s^{-1} northward storm motion. Late on 25 September two NOAA Aircraft Operations Center (AOC) WP-3D research aircraft flew through Hurricane Olivia. The eyewall reflectivity was found to be axisymmetric at the beginning of the observation period, and to evolve into a highly asymmetric distribution over the following 4 h (Fig. 2.2). As Olivia continued to move north-northeast under increasing southwesterly vertical shear and somewhat cooler SSTs ($\sim$ 27°C), the winds gradually weakened to tropical storm strength late on 26 September.

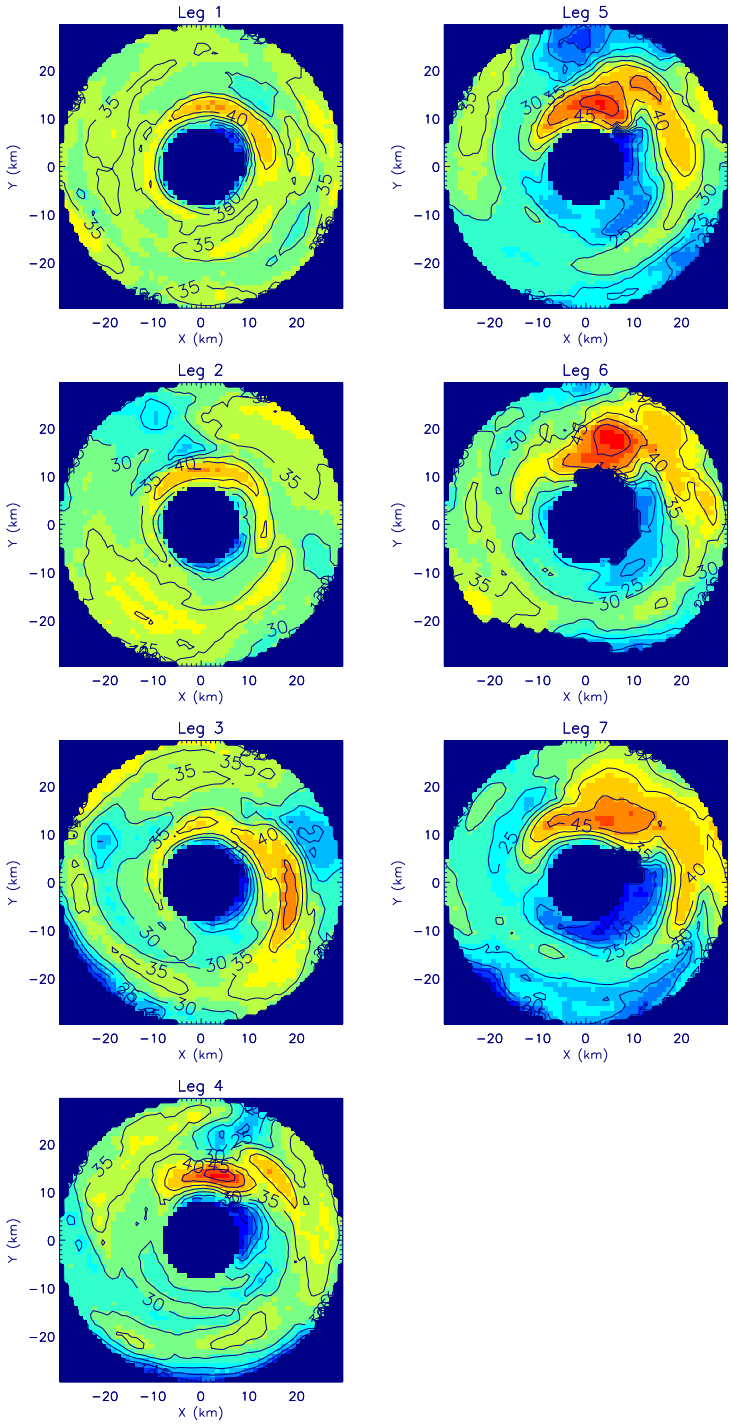

Figure 2.2: Composites of Olivia's inner-core reflectivity near 5 km height derived from the TA radars for each flight leg. See Table 2.1 for the compositing times associated with each leg. Contour interval is 5 dBZ. In this and all subsequent horizontal contour plots, geographical north is located at the top of the plot. Note regions of attenuation radially outside the reflectivity maximum in the northern quadrant of the storm.

Leg	Composite time (UTC)	N42RF (3 km) flight track	N43RF (4 km) flight track
1	2027-2039	N to S	ENE to W
2	2100-2113	SE to NW	SSW to NNE
3	2132-2143	W to E	N to S
4	2204-2217	NE to SW	SSE to NW
5	2244-2253	S to N	WSW to ENE
6	2310-2330	NW to SE	NNE to SSW
7	2343-2355	E to W	S to N

Table 2.1: Dual-Doppler composite times for the seven flight legs through Hurricane Olivia on 25 September 1994, and the NOAA WP-3D aircraft (N42RF at 3-km altitude, N43RF at 4-km altitude) flight tracks through the inner core.

2.2.2 Radar Observation of Hurricane Olivia

The two WP–3D aircraft equipped with Doppler radar flew simultaneous, near-orthogonal flight tracks through the inner core of Hurricane Olivia on 25 September 1994. Seven consecutive flight legs through the eye were made during the period 2027–2355 UTC (see Table 2.1 for details). Dual-Doppler coverage was available out to a radius of 60–70 km from the storm center.

Horizontal scans of radar reflectivity obtained from the lower fuselage (LF) C-band (5.5 cm wavelength) radar antenna of the lower aircraft are used in Chapter 3 to look at the fine-timescale evolution of Olivia's inner core. Throughout the rest of this dissertation three-dimensional composites of reflectivity from the tail (TA) X-band (3.2 cm wavelength) radar antenna, which scans perpendicular to the aircraft ground track, are used to show the reflectivity evolution over the 3.5 h observation period. Further details of the TA and LF radars are provided by Jorgensen (1984). The method of TA radar reflectivity compositing is discussed by Marks and Houze (1984).

The use of two TA radar platforms allows for a true dual-Doppler sampling technique to be employed. The upper and lower aircraft fly orthogonal legs through the hurricane inner core, providing near-simultaneous measurements of orthogonal components of the horizontal wind over a period of 10–15 min. In the two quadrants of the storm where the TA radar beams intersect, the average time separation between measurement of the

horizontal wind components is 2.7 min. In the other two quadrants of the storm an average time separation of 6 min exists. The time between three-dimensional samplings of the inner-core wind field is roughly 20 min. Seven consecutive wind composites were constructed for the 3.5 h observation period.

The domain of the TA wind and reflectivity composites extends 30 km from the storm center in the horizontal and from 0.75 km to 6 km in the vertical. Data above 6 km height are available, but not used (except in the calculation of area-averaged horizontal wind discussed in Chapter 6). The filtering of the dual-Doppler data used in this study is not uniform in space. This is in large part a consequence of the difference in tangential and radial velocity found in a hurricane. Between Doppler wind measurements at a point in space, features in the wind field are advected much greater distances in the azimuth than in the radial. During the average time separation between measurements in the eyewall ($\sim$ 3 min) parcels are advected 5–10 km in the azimuth (20–40° at 15 km radius) and 1–2 km in radius. Thus, we will focus on wavenumbers 0, 1, and 2 in the azimuth and scales $\geq$ 4 km in radius.

2.2.3 Data Quality

The winds derived from the true dual-Doppler sampling of Olivia are compared to the in-situ aircraft wind measurements made along the flight tracks at 3 km height. Flight-level wind measurements were smoothed with a 2-km Bartlett filter to match the Doppler analysis resolution (courtesy of Matthew Eastin, personal communication). Figure 2.3 shows the flight-level estimate of the wind at a point along the flight track versus the Doppler-derived estimate nearest that point in space. All flight-level points within the dual-Doppler domain are considered, and all seven flight legs are utilized. Good agreement exists for the horizontal components of the wind (Figs. 2.3a and 2.3b). The slopes of the linear best fits to the U and V winds are 0.98 and 1.01, respectively. The correlation coefficient for the U-fit is 0.98, while for the V-fit is 0.99. These findings are consistent with those found by MHG for pseudo dual-Doppler measurements in Hurricane Norbert (1984).

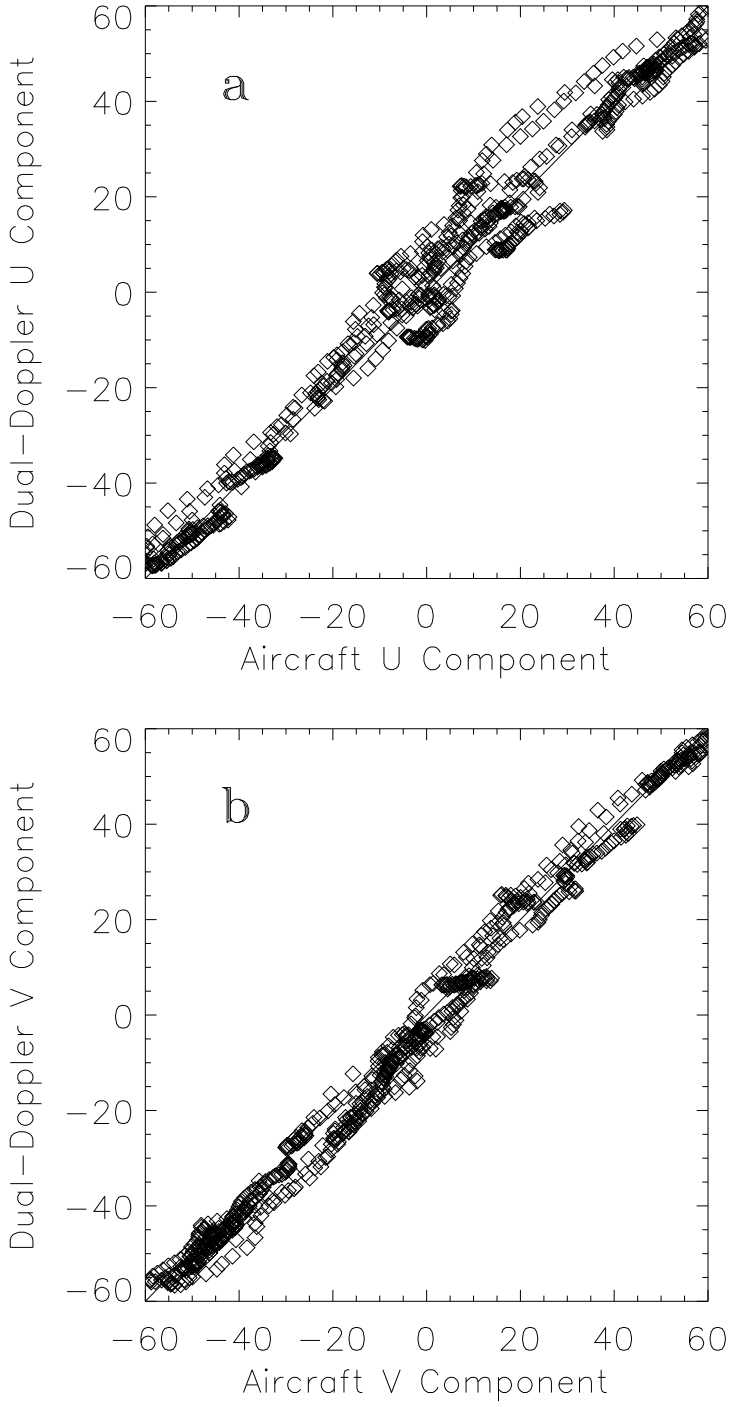

Figure 2.3: Point-by-point comparison between aircraft wind measurements at 3 km height during the period 2027–2355 UTC and the Doppler-derived wind estimates nearest in space. The (a) zonal and (b) meridional components of the wind (m s^{-1}) are shown separately. Interpolated data within Olivia's eye are included in the comparison.

The agreement between aircraft and Doppler-derived vertical velocities is not expected to be as good as found for the horizontal winds. As noted by MHG, the inherent spatial averaging involved in the computation of Doppler-derived vertical velocity from horizontal wind divergence alters the magnitude and location of the vertical velocity maxima. MHG did find however that the *distributions* of vertical velocity for the Doppler and in-situ observations in Hurricane Norbert were quantitatively similar.

2.3 Wind Decomposition

Based on the results of Fig. 1.1 and other observations of the hurricane near core (e.g., MHG; Franklin et al. 1993) we may regard the hurricane inner-core horizontal winds as a superposition of an axisymmetric tangential flow plus weaker azimuthal perturbations, with weak radial flow above the inflow layer and below the upper–tropospheric outflow layer. In order to focus on the symmetric and asymmetric components of the vortex winds separately, and to obtain insight into the dynamics governing the evolution of these components of the total flow, an azimuthal Fourier decomposition of the wind field is performed. The storm–relative winds ($\mathbf{V}_r$) are first obtained by subtracting the storm motion from the total (earth-relative) winds ($\mathbf{V}_{total}$):

$$\mathbf{V}_r = \mathbf{V}_{total} - \mathbf{V}_s, \tag{2.26}$$

where $\mathbf{V}_s$ is the time-dependent, spatially-constant storm motion vector (see Willoughby and Chelmow 1982). The initial wind analysis at each level is centered on the flight-level vortex center at roughly 3 km height. Following MHG, we instead choose to center the vortex at each height at the origin of a common cylindrical coordinate system, thus minimizing the asymmetry due to vortex center mislocation. In studying vortex alignment one would not necessarily want to make this transformation. A coordinate system based on the vortex centroid would be more useful. But because of the general lack of scatterers within the eye, the Doppler-derived wind field within roughly 8 km from the storm center cannot be obtained. By centering the vortex at each level we reduce the chance of incorporating interpolated wind data within the eye into our Fourier decomposition of

the wind. A simplex algorithm is used to find the center that maximizes the symmetric component of the tangential winds within an annulus centered on the RMW (Neldar and Mead 1965). Using the newly defined center at each level, $\mathbf{V}_r$ is decomposed into azimuthal mean and perturbation wind components. The perturbation wind field is then Fourier decomposed in azimuth in order to focus on the structure and evolution of the low-wavenumber components.

The asymmetric component of $\mathbf{V}_r$ will contain, in addition to internally-generated vortex asymmetries, the environmental flow and asymmetries resulting from the interaction of the hurricane with its environment (e.g., upper-level PV anomalies, beta-gyres, etc.). Consequently, it is not a straightforward task to simply separate $\mathbf{V}_r$ into environmental and hurricane components. Nevertheless, it proves useful and convenient to define an *estimate* of the environmental vertical shear:

$$\frac{\partial \mathbf{V}_e}{\partial z}(z) = \frac{1}{\pi r_{max}^2} \int_0^{2\pi} \int_0^{r_{max}} \frac{\partial \mathbf{V}_{total}}{\partial z}(r, \lambda, z) r dr d\lambda, \tag{2.27}$$

where $r_{max} = 28$ km. This quantity will henceforth be referred to as the local vertical shear. The wind vector $\mathbf{V}_e$ is the area-averaged total wind at each level, which should contain information on the environmental flow as discussed by MHG for Hurricane Norbert (1984).

Chapter 3

OBSERVATIONS OF VORTICITY MIXING IN THE TC CORE

3.1 Symmetric Vortex Evolution

3.1.1 Tangential Wind Budget

Figure 3.1 shows the symmetric structure of Hurricane Olivia's primary circulation at the beginning (Fig. 3.1a) and end (Fig. 3.1b) of the observation period. In the vicinity of the RMW ($\sim$ 12 to 16 km) the tangential winds decrease by 5-10 m s^{-1} just above the boundary layer and by a more substantial 10-20 m s^{-1} around 6 km height. A near-linear decrease in tangential winds with time is observed near the RMW. The f-plane contributions to the observed tendency in symmetric tangential wind in the inner core are:

$$\frac{\partial \overline{v}}{\partial t} = -\left(f + \overline{\zeta}\right)\overline{u} - \overline{w}\frac{\partial \overline{v}}{\partial z} - \left(\overline{u'\zeta'} + \overline{w'\frac{\partial v'}{\partial z}}\right) + \overline{F}, \tag{3.1}$$

where u is the radial velocity, v the tangential velocity, w the vertical velocity, f the Coriolis parameter, and ζ the vertical vorticity. The bar denotes an azimuthal average and the prime a departure therefrom. The first two terms are the radial flux of mean vorticity by the mean radial wind and the vertical advection of mean tangential momentum by the mean vertical wind, respectively. The next two terms are the eddy counterparts of the first two terms, and the last term represents frictional and unresolved effects. The symmetric transverse circulation involved in the first two terms is shown in Fig. 3.2. Over the observation period the symmetric transverse flow is highly variable. Although some of the structure may be accounted for by errors in the three-dimensional variational scheme (recall the discussion in Chapter 2 regarding the difficulty in computing vertical velocity), one cannot rule out the possibility that the features are physical. Mechanisms

likely involved in the evolution of the secondary circulation include frictional and diabatic forcing, precipitation loading, inertia-gravity wave propagation, and asymmetric vorticity dynamics. It should be noted that the period of pure inertial oscillations in the inner core ranges from 10 to 40 minutes, which is less than or equal to the time resolution of the data. Thus, the presence of inertia-gravity waves may preclude quantitative, and perhaps qualitative, comparison between observed and budget tendencies from one wind composite to the next.

The role of vorticity asymmetry in producing mean flow change is considered in Section 3.2. Here, we focus on purely symmetric phenomena. A comparison of the left-hand side of (3.1) and the sum of the first two terms on the right-hand side is shown in Fig. 3.3 for the flow evolution from leg 1 to 7. Although the observed tangential wind tendency is an order of magnitude less than the budget tendency, qualitative agreement between the two is found. Both depict a negative tendency in the vicinity of the RMW and a positive tendency outside this radius.

Insight into the observed weakening trend in the primary circulation may be obtained using axisymmetric vortex spin-down ideas. For an axisymmetric hurricane in approximate gradient and hydrostatic balance the theoretical predictions of Eliassen and Lystad (1977, hereafter EL) are appropriate. EL predicted the decrease in tangential winds with time for a vortex with differential rotation under the influence of a quadratic drag law for the surface stress in a neutrally-stratified atmosphere. Figure 1.1 shows the wind asymmetry to be an order of magnitude smaller than the symmetric wind in the case of Olivia, but measurements of the stratification are unavailable. Neutral buoyancy in the near core-region (excluding the eye) is supported by Emanuel (1986). As long as these assumptions hold approximately true, EL's theory appears to be useful as a zeroth-order description of hurricane spin-down.

The basic dynamics of vortex spin-down are relatively simple. The departure of the flow from exact cyclostrophic balance in the vortex boundary layer due to the presence of frictional drag drives a radial inflow. This radial inflow transports angular momentum into the inner core, compensating for the frictional losses of angular momentum into

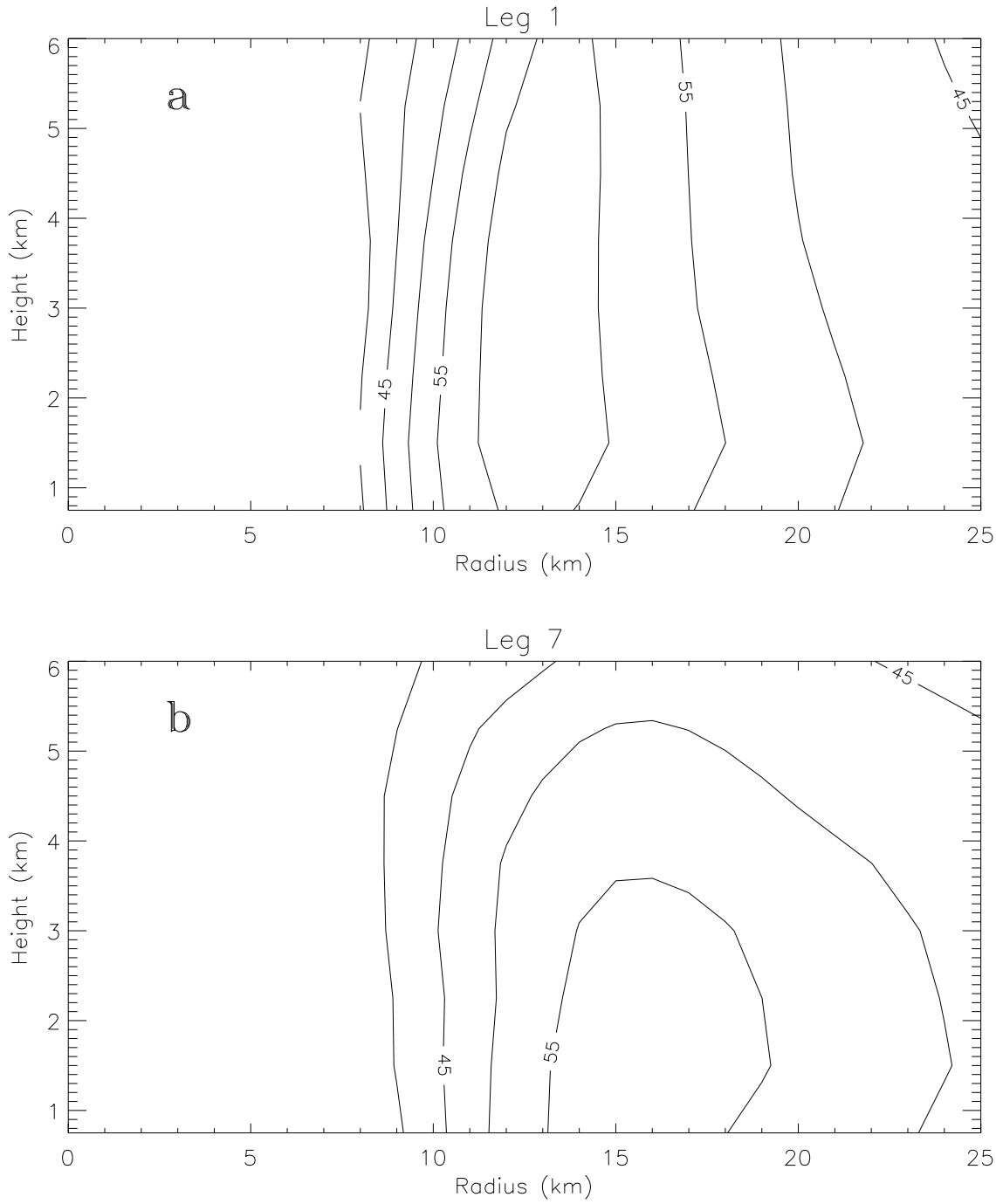

Figure 3.1: Radius-height structure of the symmetric tangential winds during (a) leg 1 and (b) leg 7. Contour interval is 5 m s^{-1}.

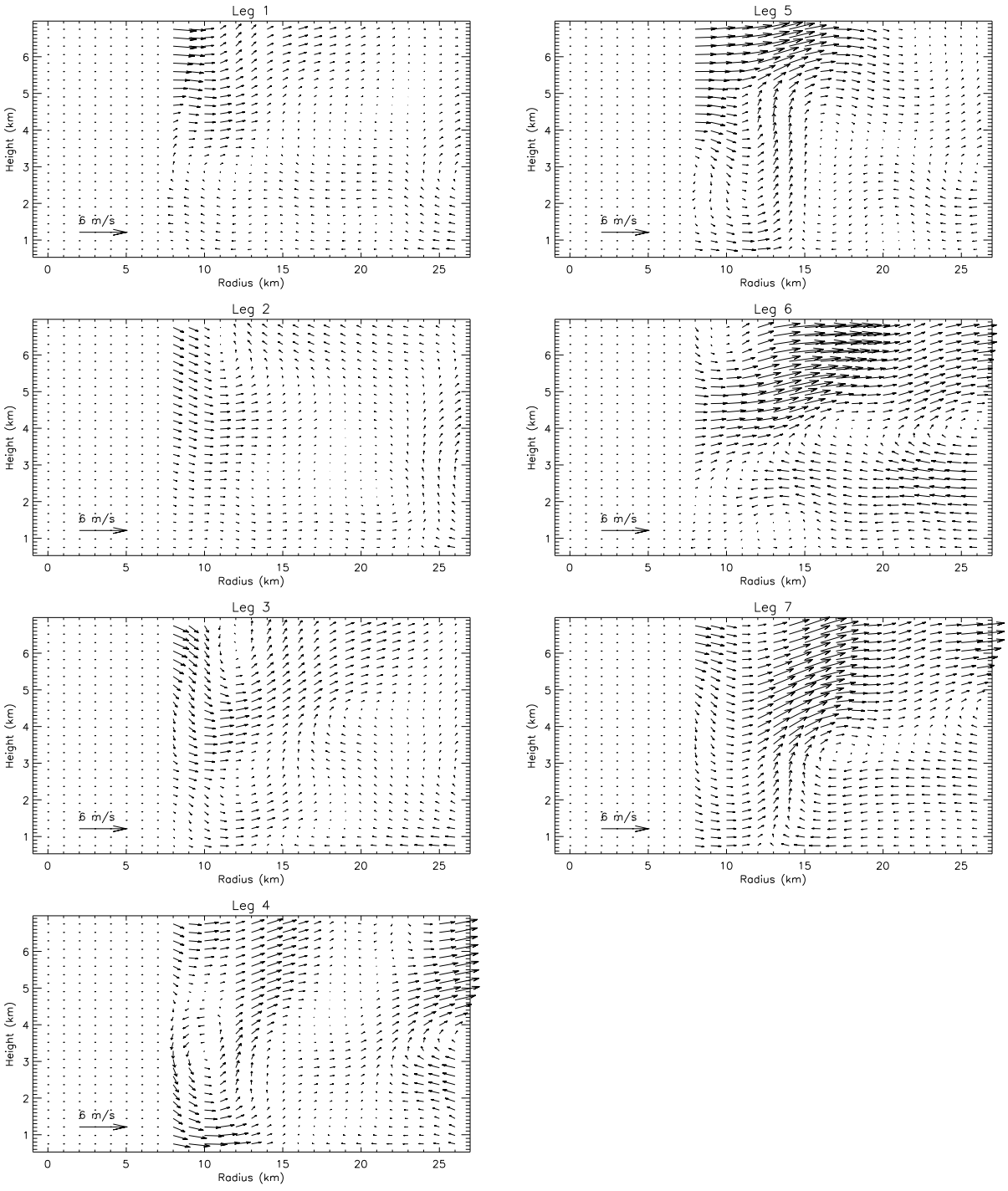

Figure 3.2: Radius-height structure of the symmetric transverse flow (u,w) for each flight leg. Wind vectors of the same length, pointing horizontally or vertically, represent the same speed. Maximum wind vector is 6 m s^{-1}.

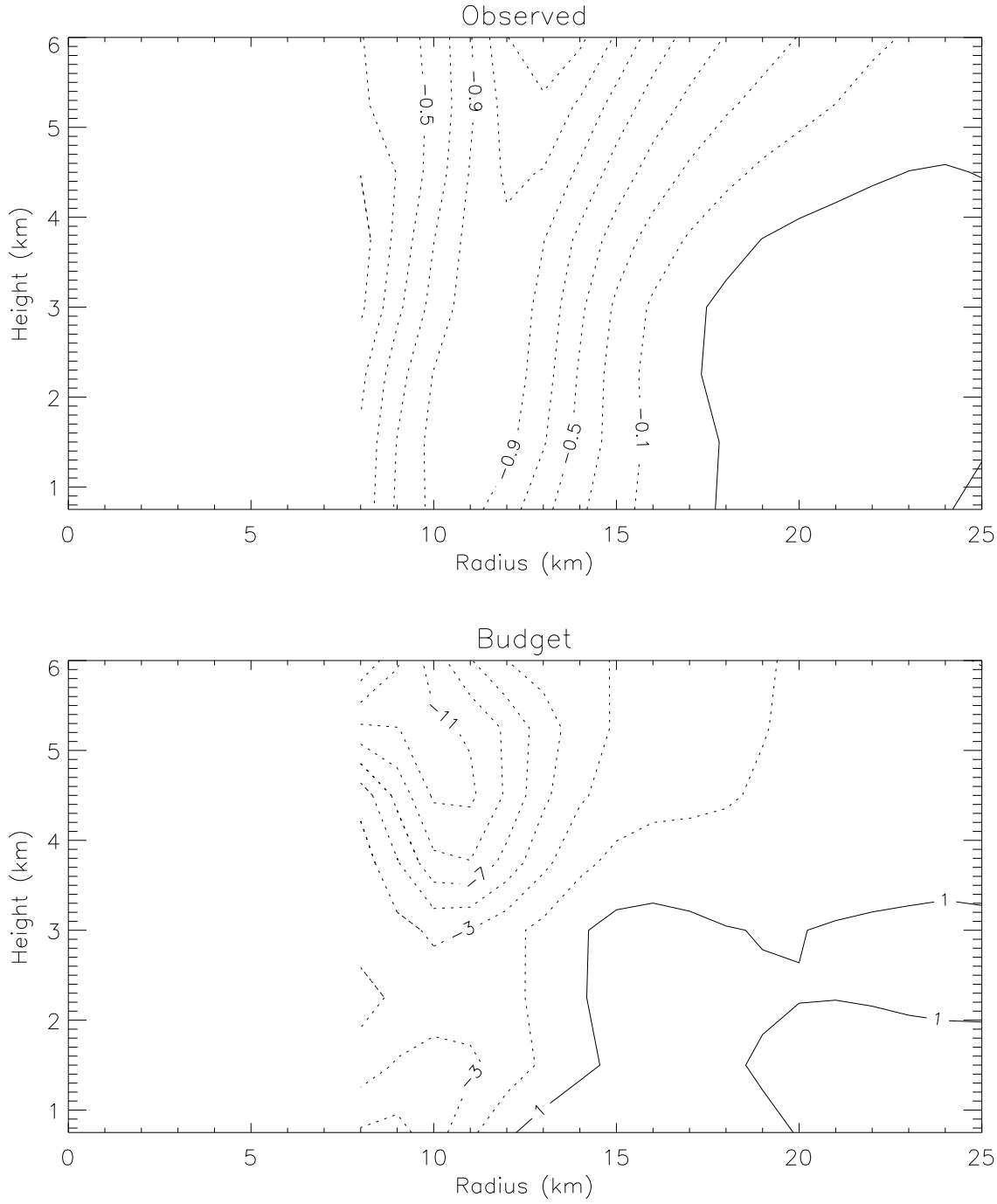

Figure 3.3: A comparison between the observed and budget tendencies of symmetric tangential wind for the transition from leg 1 to 7. Only the symmetric radial vorticity flux and vertical advection terms of Equation 3.1 are used in the budget tendency calculation. The average of the leg 1 and leg 7 wind fields are used in the budget calculation. Contour intervals for the observed and budget tendencies are 0.2×10^{-3} m s^{-2} and 2×10^{-3} m s^{-2}, respectively. Negative values are depicted by the dashed curves.

the ocean. In the absence of diabatic forcing and the attendant radial inflow above the boundary layer, the free atmosphere radial flow will be outward at all levels (Willoughby 1979). By conservation of angular momentum the tangential winds above the boundary layer must decrease, and the vortex spins down.

The time average of Olivia's symmetric transverse flow over the 3.5 h observation period is shown in Fig. 3.4. Although inflow is still observed up to 3.5 km height, the flow above this level is outward at all radii. This prevalence of radial outflow was also observed by MHG for weakening Hurricane Norbert.

The rate at which the spin-down occurs was determined heuristically by EL for weak vortices (maximum tangential winds ~ 10 m s^{-1}). They used a first-order K theory to parametrize the eddy stresses in the mixed layer and a quadratic drag law for the surface stress. A state of near-cyclostrophic balance was assumed to exist throughout the fluid in an absolute coordinate system. The free-atmosphere tangential wind, $v(r,t)$ is given by

$$\frac{1}{|v|} = \frac{1}{|v_0|} + \frac{C_D \chi^2 t}{H-h}, \tag{3.2}$$

where $|v_0(r)|$ is the initial tangential wind, C_D the assumed constant drag coefficient, χ the ratio of the boundary layer to free atmosphere tangential wind, i.e., the reduction factor, H the total depth of the fluid, and h the boundary layer depth. Snell and Montgomery (1999) and Montgomery et al. (2000) investigated the validity of (3.2) for hurricane-strength vortices (maximum tangential winds ≥ 33 m s^{-1}) using an axisymmetric Navier-Stokes model which includes the non-cyclostrophic terms neglected by EL. They found that the model-derived half-life times of the stronger vortices showed good agreement with the predictions of EL. We therefore use (3.2) to predict the time-evolution of Olivia's tangential winds above the boundary layer (~ 3 km height) at 12 km radius from the vortex center and compare with the observations. Using the drag coefficient of Deacon (Roll 1965) for 49 m s^{-1} winds in the boundary layer ($C_D \sim 3 \times 10^{-3}$), $H = 15$ km, $h = 1$ km, $\chi = 0.8$, and $|v_0| = 61$ m s^{-1}, we estimate a tangential wind of 58 m s^{-1} during leg 4 and 55 m s^{-1} during leg 7. The observed tangential winds during legs 4 and 7 are approximately 54 m s^{-1} and 51 m s^{-1}, respectively. Thus, in spite of the simplifications

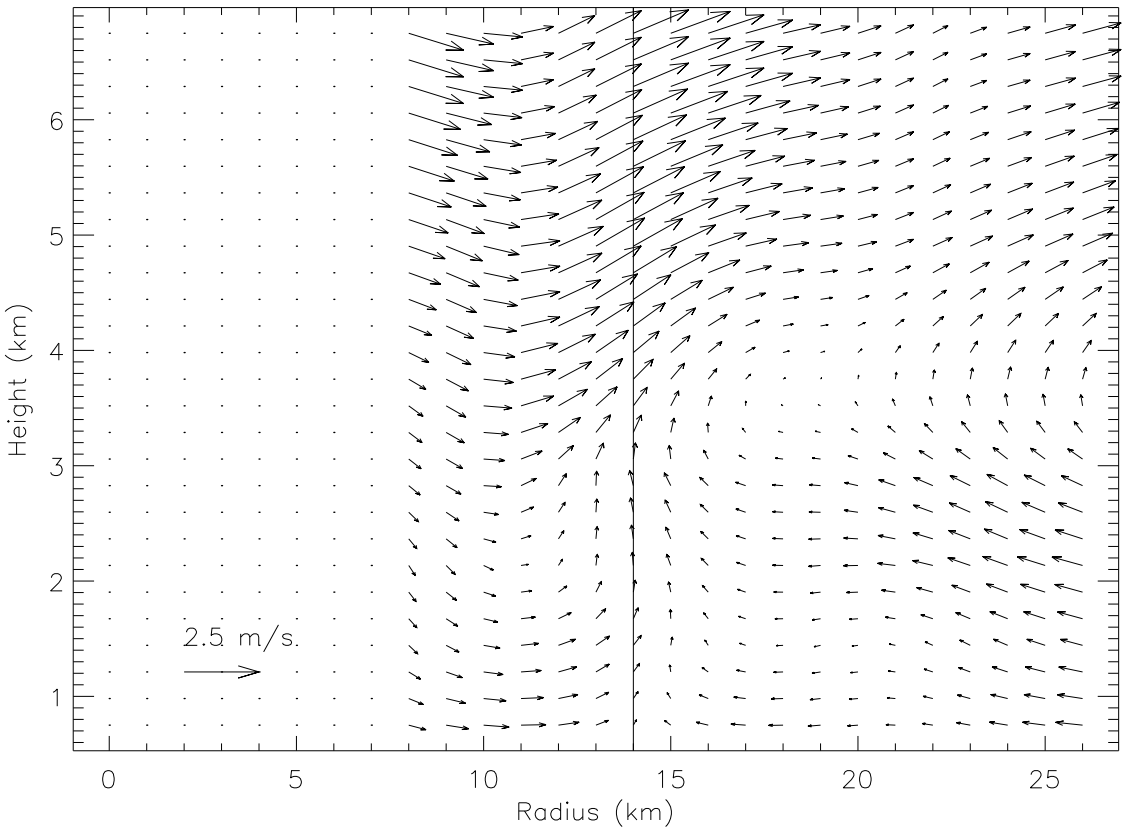

Figure 3.4: As in Fig. 3.2, but averaged over the period 2027–2355 UTC. Maximum wind vector is 2.5 m s^{-1}. The solid line denotes the time-average location of the RMW as a function of height.

made in deriving (3.2) and the greater complexity of Olivia's environment (e.g., vertical shear), the magnitude of the observed spin-down of the tangential winds is consistent with the axisymmetric predictions of EL.

3.1.2 Symmetric Vorticity Evolution

The evolution of Olivia's symmetric vorticity derived from the dual-Doppler winds at 3 km height is shown in Fig. 3.5a. Consistent with the vortex weakening discussed in the previous section is a decrease in the radial vorticity gradient near the RMW, most pronounced between legs 3 and 5. One explanation for this gradient reduction is the symmetric divergence(convergence) of absolute vorticity inside(outside) ~ 12 km radius. Such changes to the symmetric vorticity profile can also occur through asymmetric mechanisms. The vortex spin-down ideas may only be a partial explanation for the observed symmetric evolution. For example, the interaction of convectively-forced vortex Rossby waves with the mean flow will lead to changes in the mean vorticity profile (MK; ME98; Möller and Montgomery 1999, 2000). Nonlinear mixing of vorticity through the barotropic instability mechanism discussed by S99 will also erode sharp radial gradients of symmetric vorticity.

The details of the internal asymmetric mechanisms are dependent upon the symmetric structure of the vortex. Consider a vortex with monotonically decreasing vorticity with radius. This flow satisfies Rayleigh's sufficient condition for exponential stability, prohibiting the mixing mechanism of S99. Vorticity redistribution through vortex Rossby waves can still occur. The Rossby wave phase and group velocities, and the location of wave-mean interaction for such a stable vortex will depend on both the symmetric shear and vorticity profiles. In the case where a reversal in the sign of the vorticity gradient is present and exponential instability is possible, the mean vorticity structure will determine which azimuthal wavenumbers are unstable and their growth rates. Thus, in considering the asymmetric dynamics of Olivia's inner core, it proves useful to first examine the symmetric vorticity structure.

The lack of scatterers within the eye prohibits us from obtaining the complete symmetric vorticity profile in Olivia's inner core using dual-Doppler data alone. If the aircraft wind measurements at 3 km height are averaged over a sufficient number of flight legs

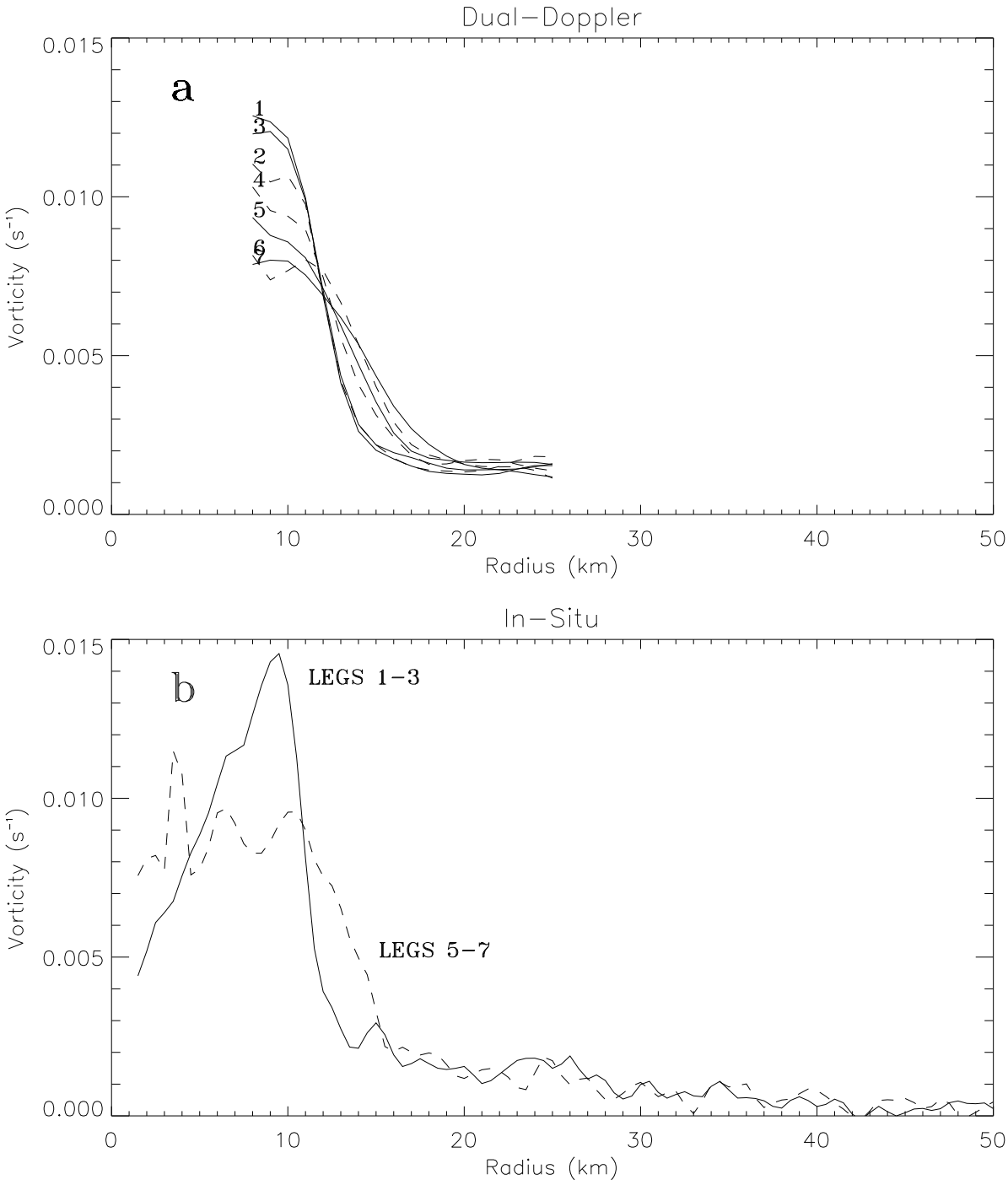

Figure 3.5: Symmetric vorticity (s^{-1}) profiles at 3 km height (a) derived from the dual-Doppler analysis (legs 1-7) and (b) computed from aircraft wind measurements averaged over the first three legs (1-3) and last three legs (5-7). For the latter profile, only leg 7 data is used inside 6 km, resulting in a somewhat noisier vorticity distribution.

through the storm, a proxy for the azimuthal-mean vorticity within the eye can be computed (Fig. 3.5b). Averaging the six radials through Olivia during legs 1 through 3, we find that the radial profile of vorticity takes the form of a ring, with maximum values around 9.5 km radius. A similar analysis for legs 5 through 7 shows a weaker vorticity gradient near the RMW as depicted in Fig. 3.5a. Also observed is a broader region of maximum vorticity inside 10 km with values reduced from earlier legs. The lack of flight-level data inside 6 km radius during legs 5 and 6 precludes an accurate extension of the "symmetric" profile to the vortex center. The vorticity profile derived solely from leg 7 data does show a small depression of the vorticity down to about 8×10^{-3} s^{-1}. This evolution of the symmetric vorticity resembles that presented in S99 for a hurricane-like vorticity ring perturbed by a broad-band vorticity asymmetry. They predicted that some of the high vorticity of the ring is ultimately mixed into the center of the hurricane vortex, forming a monotonic symmetric vorticity profile. High vorticity is also ejected outward, qualitatively in accordance with what is expected from simple vortex Rossby wave theory. We will revisit these observations and ideas in Section 3.2 when considering the source of Olivia's vorticity asymmetry.

Kossin and Eastin (2000) have performed a more comprehensive study of the evolution of symmetric vorticity derived from flight-level data for a number of different storms. They confirmed that during hurricane intensification the vorticity profile tends to be ring-like. For most cases when the storm is steady or weakening the vorticity profile becomes more monotonic, consistent with the barotropic instability mechanism of S99 and the observations presented here.

3.2 Asymmetric Vorticity Structure and Evolution

Figure 3.6 shows the azimuthal variance of vorticity averaged over the 3.5 h observation period. Above 3 km height most of the variance is explained by wavenumber 1. We should note that the magnitude and, to some extent, the structure of wavenumber 1 in vorticity is sensitive to the vortex center definition at each level. Wavenumber 2, which accounts for most of the variance below 3 km height, is fairly robust under changes to the

vortex center identification. Higher wavenumbers show a smaller contribution to the total variance, but this may be *in part* a consequence of the aliasing that occurs during the sampling of the inner core. Ideally, one would like actual snapshots of the wind field at each level. The TA radar, however, scans perpendicular to the flight track, requiring planes to fly through the inner core in order to obtain a horizontal wind composite. Parcels of air moving with the tangential winds at the RMW will go through about 90 degrees during the time it takes to composite the inner 15 km of the storm. Therefore, some of the energy contained in the higher wavenumbers will be projected onto lower wavenumbers. While wavenumbers 1 and 2 will be modified by aliasing, simple dynamical ideas to be discussed below do support their observed dominance.

Examination of the perturbation vorticity, ζ', at 3 km height in Fig. 3.7 shows spiral bands of vorticity with radial wavelengths on the order of 5-10 km located radially outside the regions of high vorticity associated with the above-mentioned wavenumber 2 asymmetry. They are *persistently* located near 20 km radius during the first three legs and then slightly outside this radius during the final legs. The maximum vorticity of the bands ranges from 0.5-1$\times 10^{-3}$ s^{-1}. The bands may be symmetrizing vortex Rossby waves, predicted by MK to occur in the hurricane near-core region. If so, this is the first observational evidence of such features in the hurricane wind field. One source for the bands may be the symmetrization of the large wavenumber 2 vorticity perturbation near 12 km radius.

We also note the persistent bands of elevated reflectivity in the vicinity of the vorticity bands (see Fig. 2.2). Enhanced convection could be triggered by the asymmetric transverse circulation generated in response to momentum flux convergences associated with the vorticity bands. Inner-core spiral bands of reflectivity over open ocean have also been observed by Gall et al. (1998) using ground-based radar. They speculated that the features were similar to boundary layer rolls (Fung 1978), but had insufficient data to make definitive statements about their origin. As discussed in Chapter 1, understanding the role of vortex Rossby waves in tropical cyclone structure and intensity change is an important motivation for this work. The possibility that this data may lend itself to the resolution of fine-scale spiral vortex Rossby waves is encouraging.

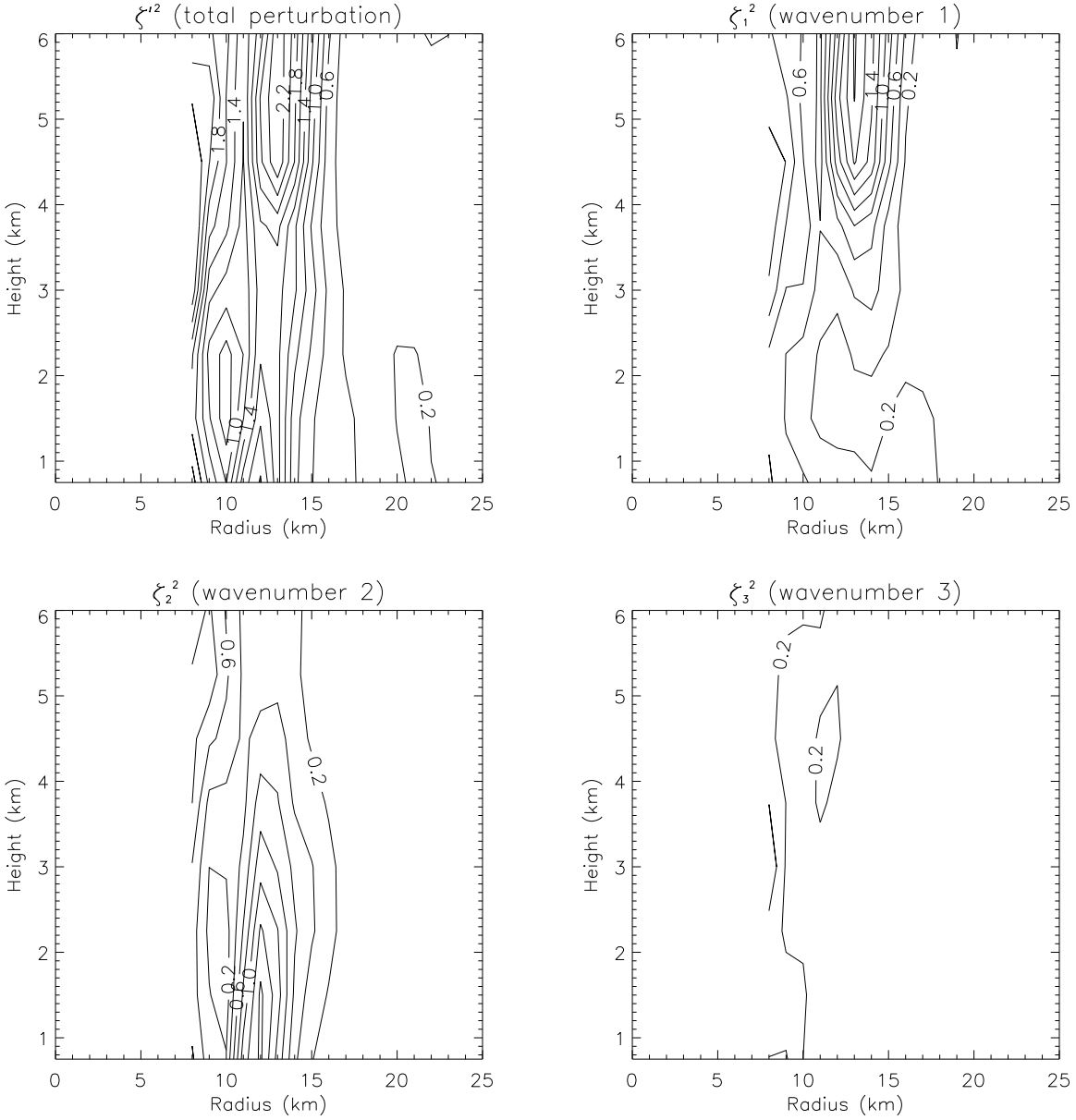

Figure 3.6: Radius-height structure of the azimuthal variance of vorticity averaged over the period 2027–2355 UTC. Also shown are individual wavenumber contributions to the azimuthal variance (i.e., wavenumber components of vorticity squared and azimuthally averaged). Contour interval is 0.2×10^{-6} s^{-2}.

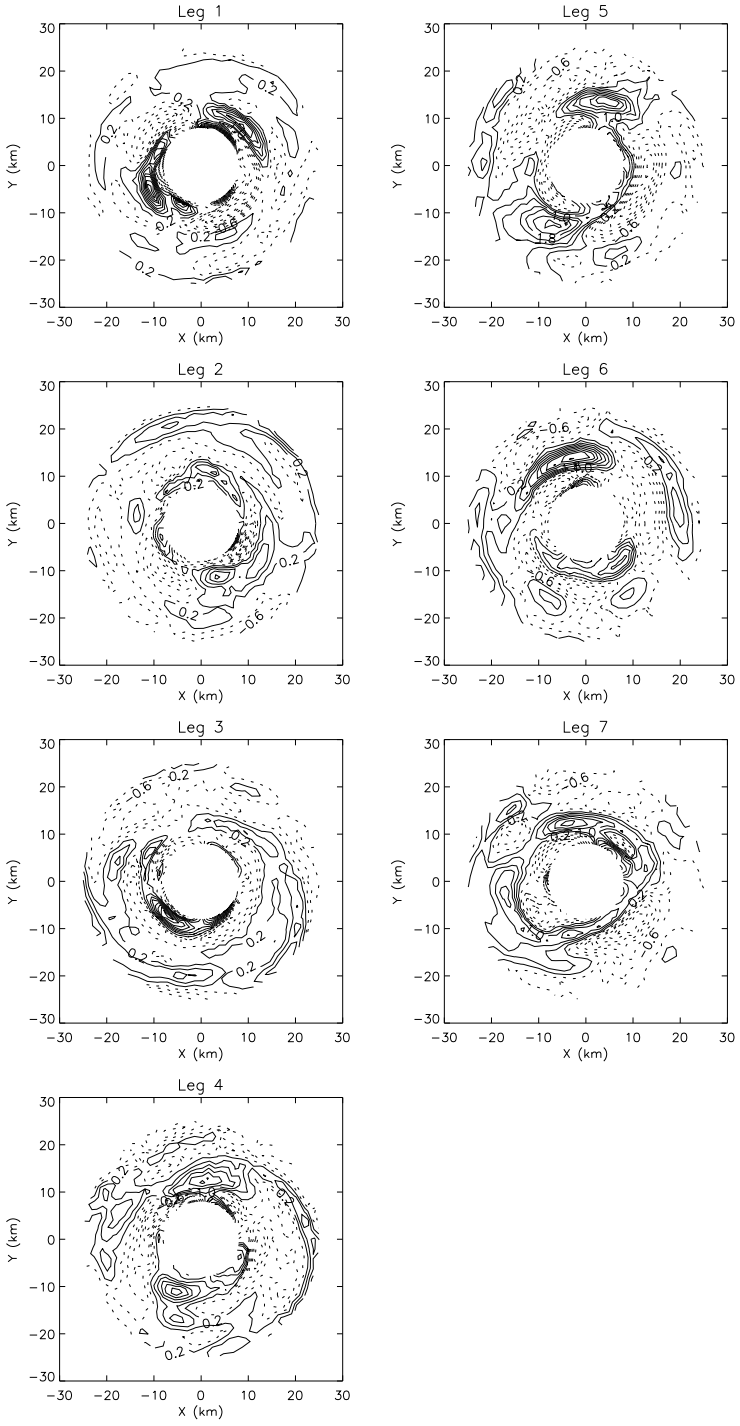

Figure 3.7: Perturbation vorticity, ζ', at 3 km height for each flight leg. Contour interval is 0.4×10^{-3} s^{-1}. Negative values are depicted by the dashed curves.

The azimuthal structure of perturbation vorticity at 12 km radius is shown in Fig. 3.8. Maximum values of positive vorticity are approximately 3-4$\times 10^{-3}$ s^{-1}. During legs 1 and 2, when the symmetric vortex from low to mid levels is nearly barotropic, the vorticity asymmetry tilts little in the azimuth with height. A clear azimuthal wavenumber 2 pattern exists at all heights within the domain during leg 1 and only below 3 km during leg 2. As the vertical shear, vortex tilt, and baroclinicity of the symmetric vortex increase, the azimuthal tilt becomes more pronounced. It is also observed following leg 2 that the vorticity in the northern quadrant above 3 km height is persistently large and appears to join with an equally large perturbation just above, and extending down into, the boundary layer of Olivia. During legs 4 through 7 a second positive vorticity asymmetry is observed in the southern quadrant of the storm, although it appears to extend up from low levels and does not reach much above 4 km height. This accounts for the dominance of wavenumber 2 at low levels and the transition to wavenumber 1 at middle levels observed in Fig. 3.6.

The evolution of the wavenumber 2 component of vorticity at low levels is shown in Fig. 3.9. Since the phase and radial location of the wavenumber 2 asymmetry are nearly constant with height below 3 km, we have vertically averaged the vorticity at low levels to provide a bulk estimate of the amplitude. Approximately 20 min separates the end of one composite and the beginning of the next. A parcel of air being advected by the tangential winds at the RMW will make almost an entire orbit around the storm during this time period. The wavenumber 2 vorticity asymmetry may not move with the advective speed, making time continuity difficult to discern simply by looking at consecutive composites.

Following Kuo et al. (1999) we use high temporal resolution radar reflectivity composites to provide an indication of the "instantaneous" tangential speed of this wavenumber 2 feature. In their study of Typhoon Herb (1996) using reflectivity from a WSR-88D Doppler radar, Kuo et al. found an approximately elliptical eye rotating cyclonically with a period of 144 min. They hypothesized that the eye rotation observed in the reflectivity might be the manifestation of a propagating wavenumber 2 vortex-Rossby edge wave. According to the linear wave theory of Kelvin (Lamb 1932), the azimuthal phase speed of a vortex-Rossby edge wave propagating on the vorticity discontinuity of a Rankine vortex

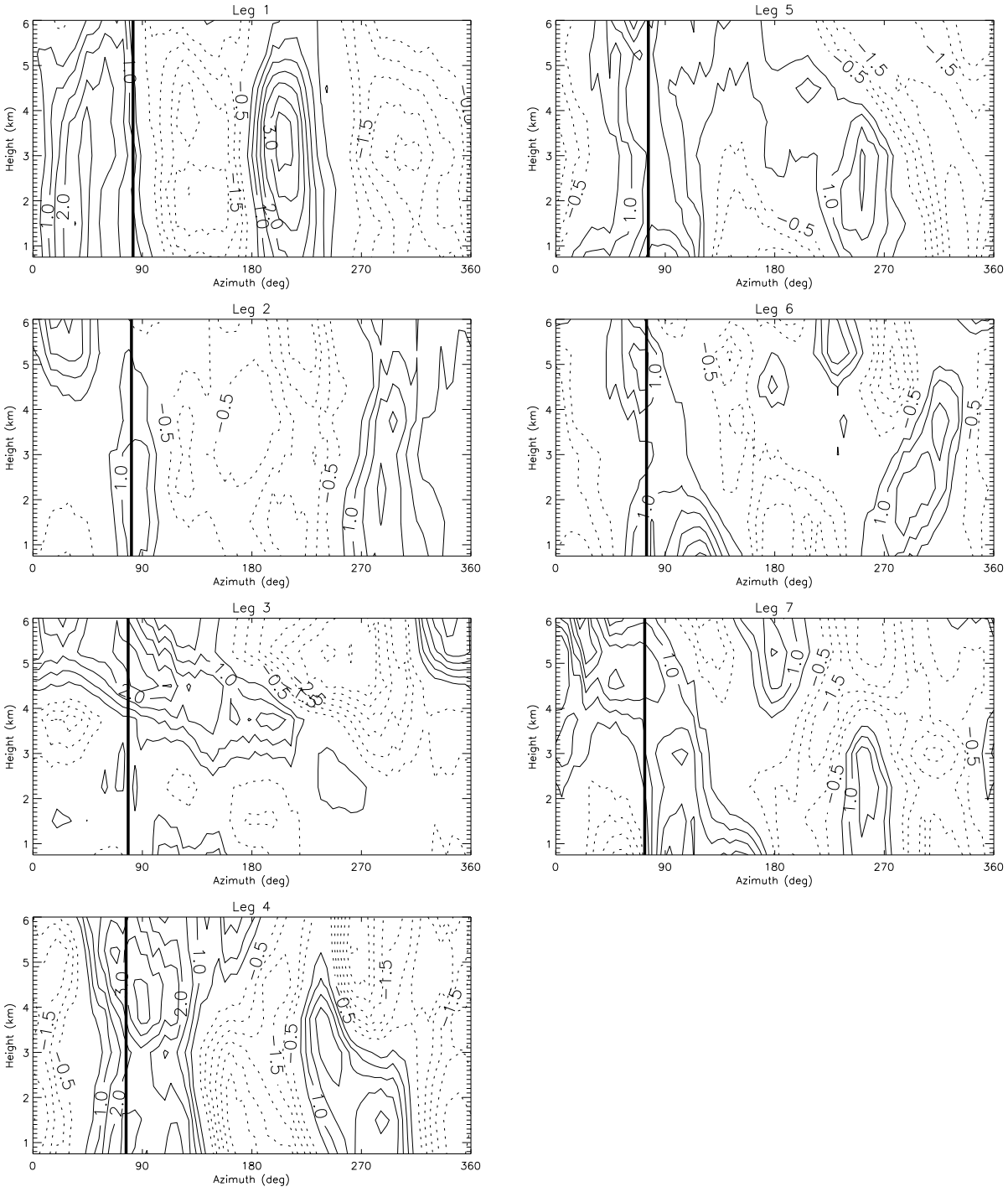

Figure 3.8: Azimuth-height cross-section of perturbation vorticity at 12 km radius from the storm center for each flight leg. North is located at 90° and west is located at 180°. Contour interval is 0.5×10^{-3} s^{-1}. Negative values are depicted by the dashed curves. The heavy, solid vertical line denotes the direction of storm motion.

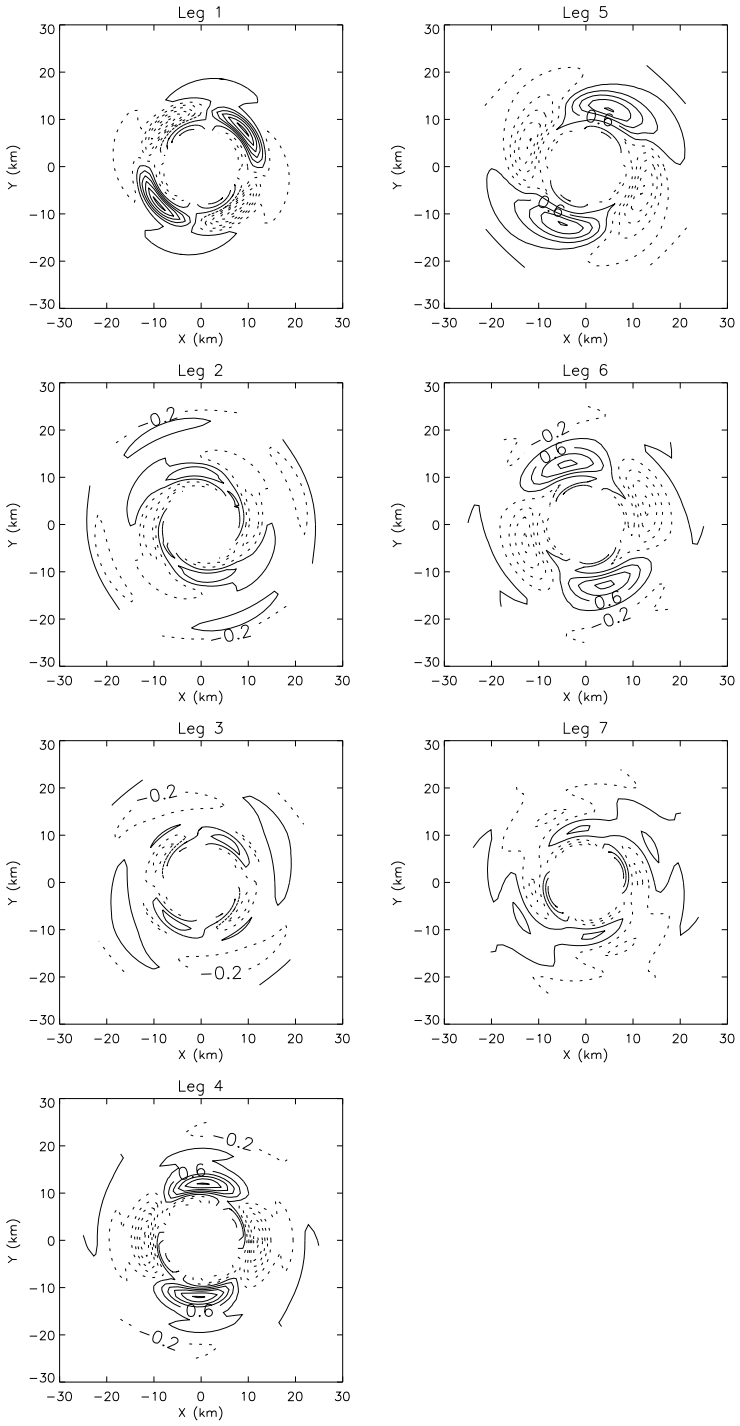

Figure 3.9: Azimuthal wavenumber 2 component of vorticity vertically averaged over the lowest 3 km for each flight leg. Contour interval is 0.4×10^{-3} s^{-1}. Negative values are depicted by the dashed curves.

is given by

$$c_p = v_{max}(1 - \frac{1}{n}), \tag{3.3}$$

where v_{max} is the maximum tangential wind speed and n the azimuthal wavenumber. Thus, for wavenumber 2 the propagation speed is one half v_{max}. Relating the observed elliptical eye rotation period in the reflectivity field to the propagation period for a vortex Rossby edge wave, Kuo et al. found that (3.3) was approximately valid. It should also be noted that the nonlinear Kirchhoff solution for elliptical eye rotation (Lamb, 1932) agrees well with the above linear solution as long as the ratio of minor to major axis is close to unity. Figure 3.10 shows the LF reflectivity evolution of Hurricane Olivia's inner core at 3 km height during the period spanned by leg 5. As in the case of Typhoon Herb, the eye appears elliptical and rotates cyclonically in time. The ratio of minor to major axis is approximately 0.7. Over the 7 minute period the eye rotates through about 50 degrees. The eye rotation period is then estimated to be 50 minutes. From the wind analysis during this time the RMW and maximum tangential wind speed at 3 km height are 14 km and 57 m s^{-1}, respectively. The circulation period for a parcel being advected around the vortex at the RMW is then 25 minutes, or one half the eye rotation period, as predicted by (3.3).

Supplementing the reflectivity with the wind field data allows this hypothesis linking the rotation of the reflectivity ellipse to the rotation of the associated vorticity asymmetry to be examined further. The orientation of the reflectivity ellipse observed in Fig. 3.10 is consistent with the phase of the wavenumber 2 component of vorticity shown in Fig. 3.9 for leg 5, i.e., the positive vorticity asymmetry lies along the major axis. An attempt to extend this interpretation to other times by comparing the observed phase evolution to that predicted by (3.3) was met with limited success. Only between legs 5 and 6 did the phase of wavenumber 2 evolve in a manner consistent with a vortex-Rossby edge wave. In addition to aliasing issues, discrepancies between observations and the linear theory described by (3.3) may be attributed to physical complications heretofore neglected.

The basic state vorticity shown in Fig. 3.5 is not Rankine. Although the radial gradient of mean vorticity outside the RMW is quite steep, discrepancies between Kelvin's edge wave solution and the wave solution on a continuous vorticity profile are expected. In the

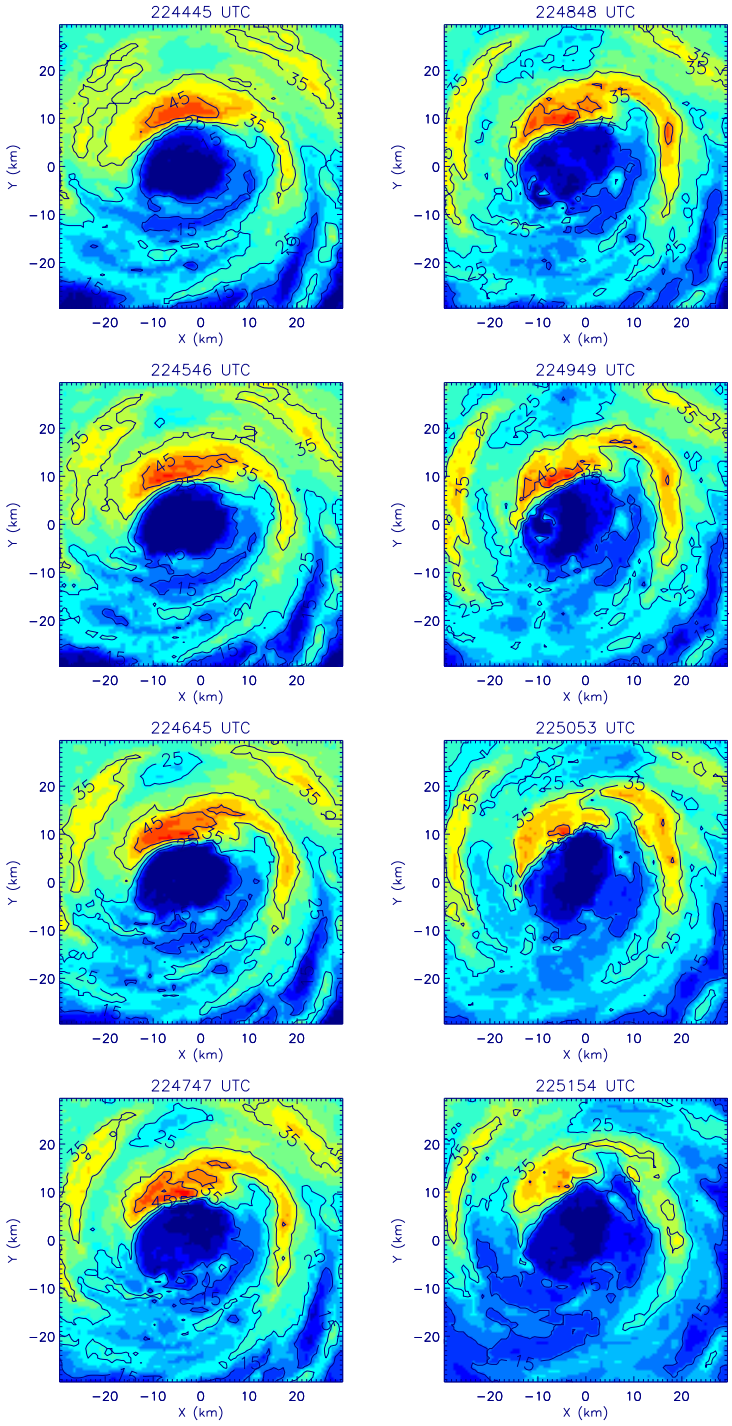

Figure 3.10: Olivia inner-core LF reflectivity composites at 3 km height. Period spanned is 2244-2251 UTC at 1 min time intervals. Contour interval is 10 dBZ.

inviscid limit the vorticity waves described by (3.3) propagate indefinitely around the vortex as discrete normal modes which never axisymmetrize. When the gradient of vorticity is no longer confined to a single radius (but the profile remains monotonic), axisymmetrization of the initial vorticity asymmetry is expected for all azimuthal wavenumbers in the *linear* problem (Sutyrin 1989; Carr and Williams 1989; Smith and Montgomery 1995; MK). The axisymmetrization mechanism also effects the phase propagation such that as the central radial wavenumber increases due to the shearing by the basic state flow, the azimuthal phase speed of the Rossby waves approaches the local tangential wind speed (MK).

The influence of cumulus convection on the Rossby wave propagation must inevitably be considered. The extension of the two-dimensional barotropic *local* dispersion relation for vortex Rossby waves derived by MK to a stably stratified barotropic circular vortex in gradient balance is given by (Möller and Montgomery 2000)

$$\omega = n\bar{\Omega}_0 + \frac{n}{R}\frac{\bar{\xi}_0}{\bar{q}_0}\frac{\bar{q}_0'(r)}{[k^2 + n^2/R^2 + (\bar{\eta}_0\bar{\xi}_0 m^2)/N^2]}, \tag{3.4}$$

where n, k, and m are the azimuthal, radial, and vertical wavenumbers, respectively, R the reference radius (see MK), $\bar{q}_0'$ the radial derivative of the barotropic basic state PV, $\bar{\eta}_0$ the absolute vorticity, $\bar{\xi}_0$ the inertia parameter, and $\bar{\Omega}_0$ the angular velocity. In regions of convection the static stability, and thus N^2, will be reduced from that in the non-convective regions, so the phase propagation of the waves will be modified. According to (3.4), the decrease in Rossby deformation radius in the convective regions will reduce the retrograde propagation of vortex Rossby waves. The precise dependence of vortex Rossby wave propagation on static stability could be explored with a high spatio-temporal resolution data set generated by a full-physics numerical model.

We conclude that over the time interval defined by leg 5 (and perhaps leg 6) the wavenumber 2 asymmetry in vorticity propagates in a manner consistent with a vortex Rossby wave packet of near-discrete structure. Although symmetrization and convection will modify its propagation speed, the greatest obstacle to extending this interpretation to other observation times is the 30-min time resolution of the dual-Doppler wind data.

The hypothesized propagation period of the vorticity asymmetry is approximately 50 min. Thus, to shed further light on the propagation characteristics, snapshots of the wind field would be required about every 10 min. Insight into the *source* of the wavenumber 2 vorticity asymmetry may still be obtained by examining the observations in the context of recent numerical and theoretical studies of vortex dynamics.

3.3 Sources of Vorticity Asymmetry

3.3.1 Convective and Environmental Sources

Asymmetric convection in the eyewall is expected to produce asymmetries in PV. The gradient of the diabatic heating rate associated with convection projected onto the absolute vorticity vector tends to be positive at low levels and negative at high levels. Thus, according to the PV equation, a positive(negative) anomaly will tend to be produced at low(high) levels (Haynes and McIntyre 1987). Convection in the eyewall will project onto a number of azimuthal wavenumbers, but it is not apparent from observations of Olivia's vertical velocity and reflectivity structures that wavenumber 2 is being preferred. Nevertheless, convective asymmetries will play an important role in the internal vorticity dynamics to be discussed below by providing broad-band vorticity perturbations to the symmetric vortex.

The interaction of Hurricane Olivia with the large-scale deformation field could have excited the near-core wavenumber 2 asymmetry in vorticity (e.g., Glatz and Smith 1996). Another facet of the vortex-environment interaction is the vertical shearing of the hurricane. The downward projection of the upper-level PV of the tilted vortex on the low-level vortex PV results in vorticity asymmetry at low levels. Wavenumber 1 will dominate the asymmetry in the case of unidirectional shear. Higher wavenumbers may become increasingly important if the direction of vortex tilt varies with height. As will be discussed in Chapter 6, this vertical shear mechanism could be activated following leg 3, when the local vertical shear increases, but seems an unlikely candidate for the production of the wavenumber 2 asymmetry observed during leg 1. At that time the vortex shows little tilt with height.

The enhanced convection on the east side of Olivia argued in Chapter 6 to be triggered by increased vertical shear following leg 2 is generally flanked radially inward by strong downdrafts. Gamache et al. (1997) suggested that perturbation vorticity may be produced in such regions via the tilting of radial vorticity filaments by the radially-sheared vertical winds (e.g., in the front right quadrant of Fig. 3.7 during leg 5). The positive vorticity in the front quadrant of Olivia following leg 2 near 12 km radius *could* have resulted from such a mechanism, leading to the persistent wavenumber 1 in vorticity above 3 km height. One could alternatively make the argument that pre-existing vertical vorticity associated with the vorticity asymmetry in the southern quadrant during leg 2 was vertically and azimuthally advected. Stretching of this vorticity in the region of strong updrafts in the eastern quadrant could have then resulted in the mid-level vorticity asymmetry observed during leg 3. Both mechanisms, while plausible, mainly shed light on the origin of the wavenumber 1 vorticity asymmetry observed above 3 km height.

3.3.2 Internal Dynamics: An Analogue Model

We now consider the possibility that the production of the dominant wavenumber 2 asymmetry in vorticity at low levels is directly tied to the inner-core symmetric vortex profile of Olivia. To elucidate the dynamical mechanisms we utilize the nondivergent barotropic vorticity equation,

$$\frac{\partial \zeta}{\partial t} + u\frac{\partial \zeta}{\partial r} + \frac{v}{r}\frac{\partial \zeta}{\partial \lambda} = 0, \tag{3.5}$$

in a series of four numerical experiments. A semispectral model was used to perform the simulations. A discussion of the pertinent model details is provided in Chapter 4 in the more general equivalent barotropic context. The nondivergent model is recovered by setting the baroclinic terms to zero. The radial grid spacing used here is 0.5 km and the number of radial points is 200. The azimuthal truncation is 16 modes.

Figure 3.11 shows the initial vorticity profiles used in each of the four cases. The profiles are based on Olivia's observed symmetric vorticity shown in Fig. 3.5 with some modifications. Although the aircraft measurements suggest a ring profile of vorticity, we first consider the case where the vorticity inside the eye is well-mixed as in a modified

Rankine vortex (Cases A and B). We then examine the asymmetric dynamics of an elevated vorticity ring (Cases C and D) as discussed in S99. In Cases A-C the profile of dual-Doppler derived tangential wind outside 18 km radius was replaced by an $r^{-0.4}$ fit to the flight-level observations. In Case D we consider the effect of the "bump" in symmetric vorticity observed near 25 km radius during legs 1 and 2 on the asymmetric evolution of the flow. All of the above vortices were perturbed with an initial pulse of cyclonic vorticity centered at 12 km radius and radially aligned:

$$\zeta' = \zeta'_{max} e^{-(r'/r_d)^2}, \tag{3.6}$$

where $\zeta'_{max} = 0.1\bar{\zeta}_{RMW}$, $r_d = 5$ km, and r' is the radius from the asymmetry center.

Cases A and B demonstrate the dependence of the asymmetric vorticity evolution on the slope of the mean vorticity gradient in the vicinity of the RMW. Solid-body rotation is assumed inside the RMW in both cases, but the larger radial vorticity gradient of Case A reflects the observations of leg 1 and the weaker gradient of Case B the observations of leg 4. In cases A and B the vortex is exponentially stable for all azimuthal wavenumbers (Gent and McWilliams 1986). The linear dynamics is then governed exclusively by the continuous spectrum of sheared vortex-Rossby wave disturbances (Smith and Montgomery 1995; MK). The linear evolution of the vorticity perturbation (3.6) appears similar in both cases, taking the form of vortex-Rossby wave trailing spirals (not shown). This is in contrast to the observations in Fig. 3.7 which, for many of the flight legs, show a more modal (i.e., non-changing) structure to the vorticity asymmetry. When the profiles for Cases A and B are instead perturbed with a pure wavenumber 2 asymmetry, a noticeable distinction between the initial linear evolutions is evident. The steeper profile supports vortex Rossby waves which initially look modal in structure like the waves predicted by Kelvin's solution (Figure 3.12a). The estimated propagation period for the wave ($\sim$ 35 min) is consistent with (3.3). The profile with the radially broader transition region from high to low vorticity supports more tightly wound vortex Rossby waves (Figure 3.12b). Although the anticyclonic horizontal shear is less in this case, the Rossby elasticity is also less. The net result is a greater tendency for sheared, trailing spiral disturbances. In

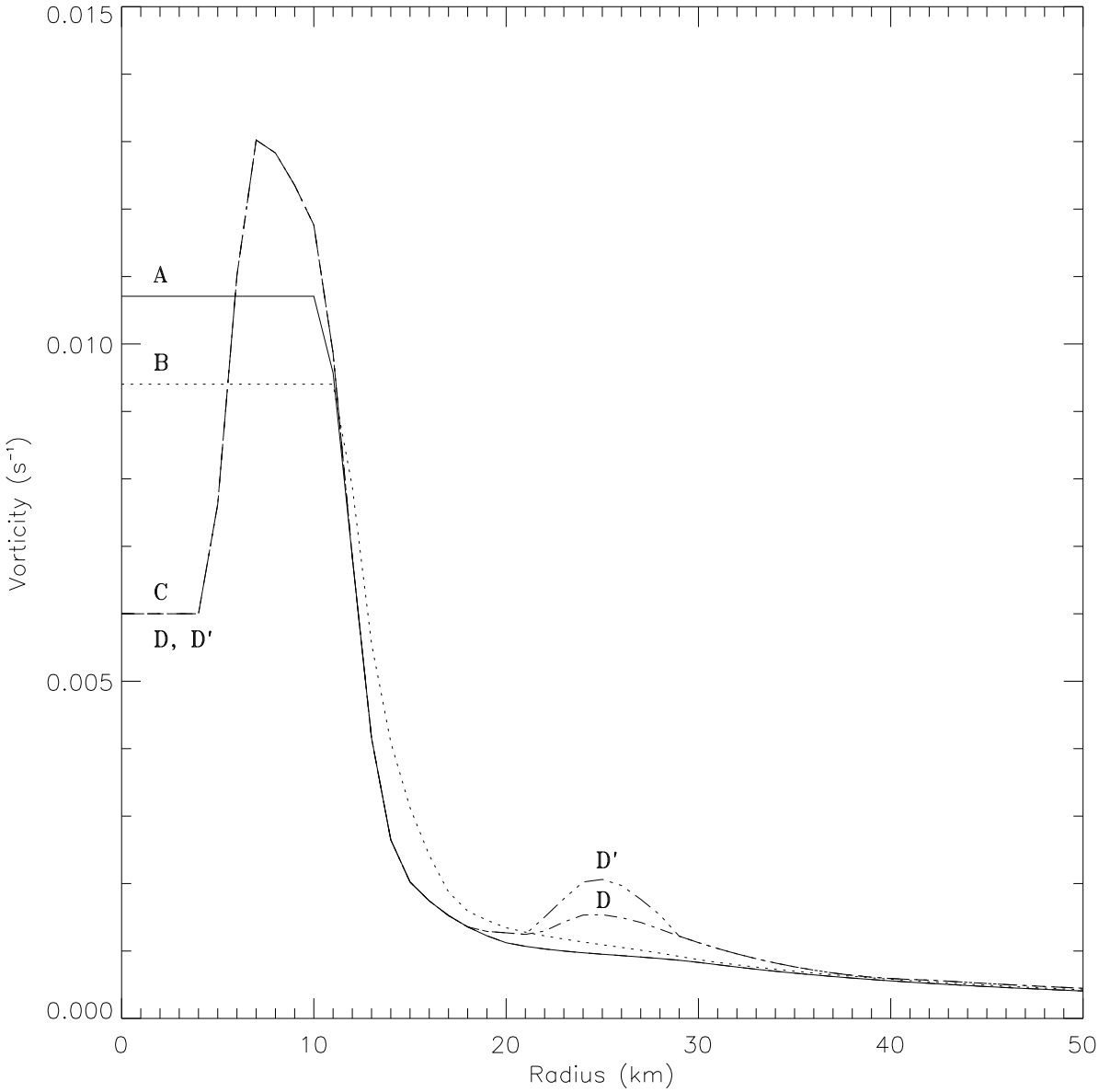

Figure 3.11: Initial profiles of symmetric vorticity (s^{-1}) used in the nondivergent, barotropic numerical simulations. Shown are Case A (solid), Case B (short dash), Case C (long dash), Case D (dash dot), and Case D′ (dash dot dot dot).

both cases the wavenumber 2 vorticity asymmetry ultimately decays as axisymmetrization proceeds. This distinction in wave structures for Cases A and B is not readily apparent in the observations shown in Fig. 3.9. We also note that these profiles, while they may allow azimuthal propagation of wavenumber 2, do not prefer the emergence of wavenumber 2 over other wavenumbers.

The next two profiles (C and D) highlight the potential importance of barotropic instability in the generation of asymmetric vorticity in the near-core region, and more specifically a mechanism preferring the emergence of wavenumber 2. (Algebraic instabilities associated with wavenumber 1 may also be playing a role in the asymmetric evolution of Olivia (Smith and Rosenbluth 1990; Nolan and Montgomery 2000)). Both profiles C and D satisfy Rayleigh's necessary condition for barotropic instability (Gent and McWilliams 1986). To determine whether the profiles indeed support linearly unstable modes, we performed an inviscid, nondivergent eigenanalysis of the continuous problem (see Appendix C). Nonlinear simulations in which the mean profiles were perturbed by (3.6) have been carried out and are summarized in order to convey the effects of nonlinearities on the asymmetric vorticity evolution.

The ring profile of Case C is exponentially unstable for wavenumbers 2 through 4, with wavenumber 2 being the most unstable. All other wavenumbers are exponentially stable. The e-folding time for the unstable wavenumber 2 eigenmode is 45 min. Changes in the width of the vorticity ring or the ratio of the maximum vorticity to the vorticity at the vortex center will alter the growth rate (S99). Keeping in mind that Olivia's actual vorticity profile may depart from the observations shown in Fig. 3.5, this value of the e-folding time is therefore considered a reasonable estimate of the actual growth rate.

The nonlinear simulation in which the Case C profile is perturbed by (3.6) shows the emergence of the unstable wavenumber 2 modal structure in the vicinity of the RMW after a few e-folding times (Figure 3.12c). Elevated vorticity from the ring mixes into the vortex center after 4-5 hours, resulting in a vortex profile with maximum symmetric vorticity at the center. The change in mean tangential wind over the first 4 hours of the simulation is shown in Fig. 3.14. As predicted by Stoke's theorem, the transport of vorticity into

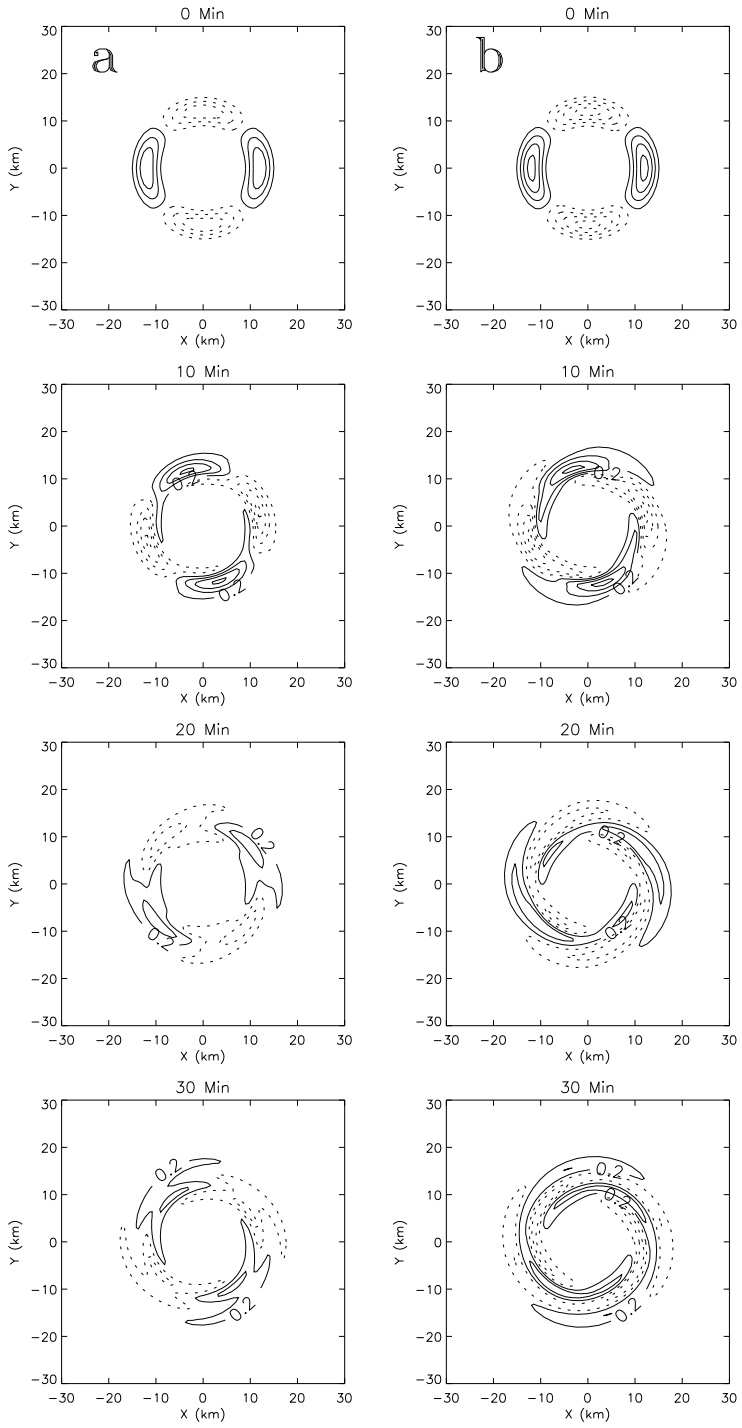

Figure 3.12: Numerical simulation of the wavenumber 2 component of vorticity for (a) Case A and (b) Case B. Contour interval is 0.4×10^{-3} s^{-1}. Initial condition is followed by snapshots of the evolution every 10 min. Negative values are depicted by the dashed curves. Also shown are numerical simulations of the total (mean plus perturbation) vorticity for (c) Case C and (d) Case D$'$. Contour interval is 2×10^{-3} s^{-1}. The initial condition derived from (3.6) is followed by snapshots of the evolution every 2 h, except for the last plot in the sequence which depicts the well-mixed state at 10 h.

the vortex center results in an increase in the mean tangential wind inside the RMW of approximately 7 ms^{-1} and a decrease at the RMW of roughly 3 ms^{-1}.

The transition of Olivia's symmetric vorticity from a well-defined ring to a near-monotonic profile, or at least a broader ring, resembles this simulated evolution. Figure 3.15 shows the change in mean tangential wind over the 3.5 hour observation period. Consistent with the Case C evolution, the mean tangential wind decreases in the vicinity of the RMW and increases inside the eye. It is plausible that the weakening of symmetric eyewall convection in Olivia inferred from Fig. 2.2 reduced the symmetric PV generation in the eyewall. In the absence of sufficient PV generation to maintain the ring, barotropic instability then set in to stabilize the vortex profile. The wavenumber 2 asymmetry at low levels of Olivia, according to Case C, could then be interpreted simply as a by-product of the vorticity mixing process. The magnitude of the spin-down ($\sim$ 10 ms^{-1}) and the presence of an acceleration outside the RMW are inconsistent with the barotropic instability mixing mechanism and are most likely the result of the axisymmetric spin-down mechanism discussed in Section 3.1.1.

The dual-Doppler observations in Fig. 3.5a indicate a possible secondary vorticity ring around 25 km radius during legs 1 and 2. This bump is incorporated into the profile of Case D. Before examining its effect on the inner-core dynamics, we consider first the question of why this bump in vorticity might exist where it does in the first place. The primary ring of vorticity is believed to form through frictional convergence and vortex-tube stretching in association with strong cumulus convection in the eyewall (e.g., Möller and Smith 1994). One explanation for the secondary bump in vorticity is that vortex Rossby waves excited in the eyewall prior to leg 1 propagated radially outward, stagnating outside the RMW. The nondivergent, barotropic simulations of MK suggest that the subsequent wave-mean interaction produces a decrease in mean relative vorticity in the vicinity of the stagnation radius and an increase in mean relative vorticity radially outward of the stagnation radius. The radial distance between the center of the initial wave packet and the stagnation radius, derived from (3.4), is given by

$$\delta r = \frac{\bar{\xi}_0 \bar{q}_0'}{\bar{q}_0 R \bar{\Omega}_0'} \frac{1}{[k_0^2 + n^2/R^2 + (\bar{\eta}_0 \bar{\xi}_0 m^2)/N^2]}, \tag{3.7}$$

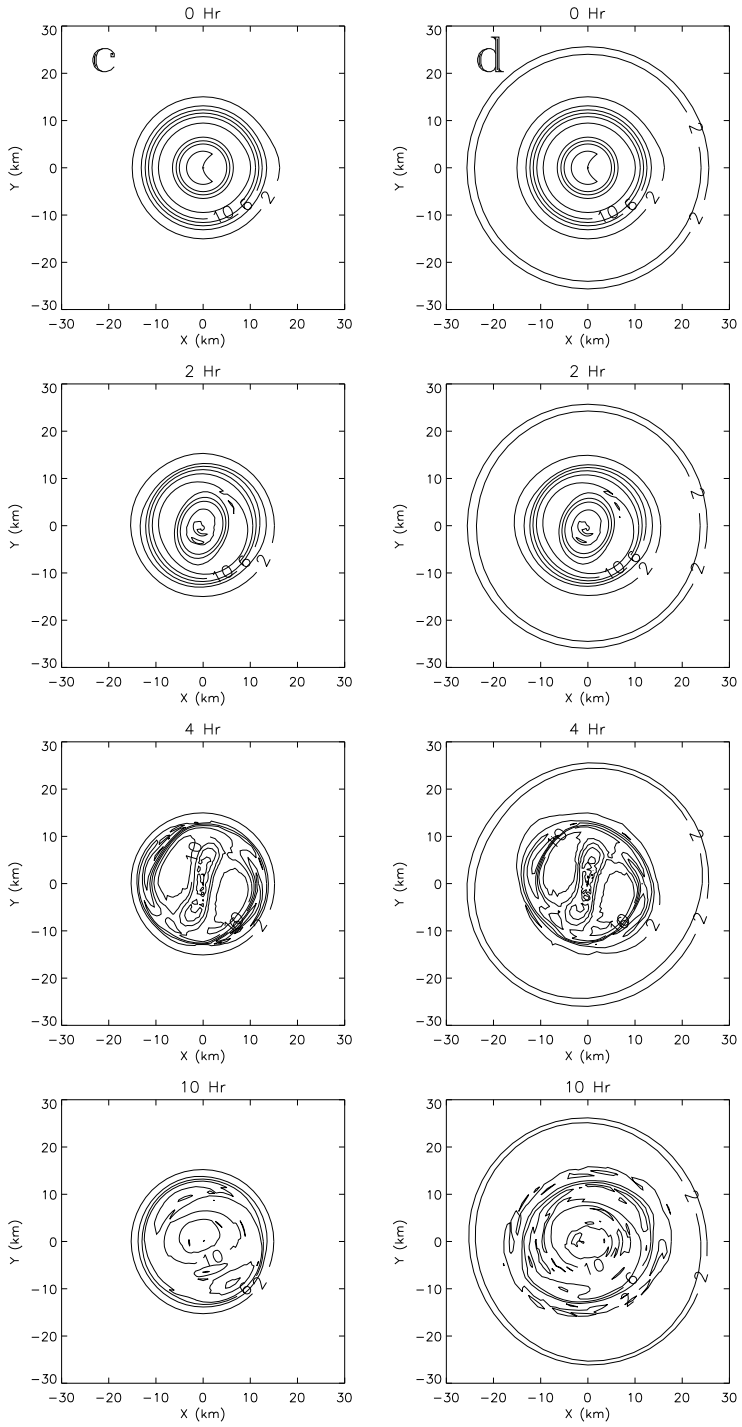

Figure 3.13: see Fig. 3.12

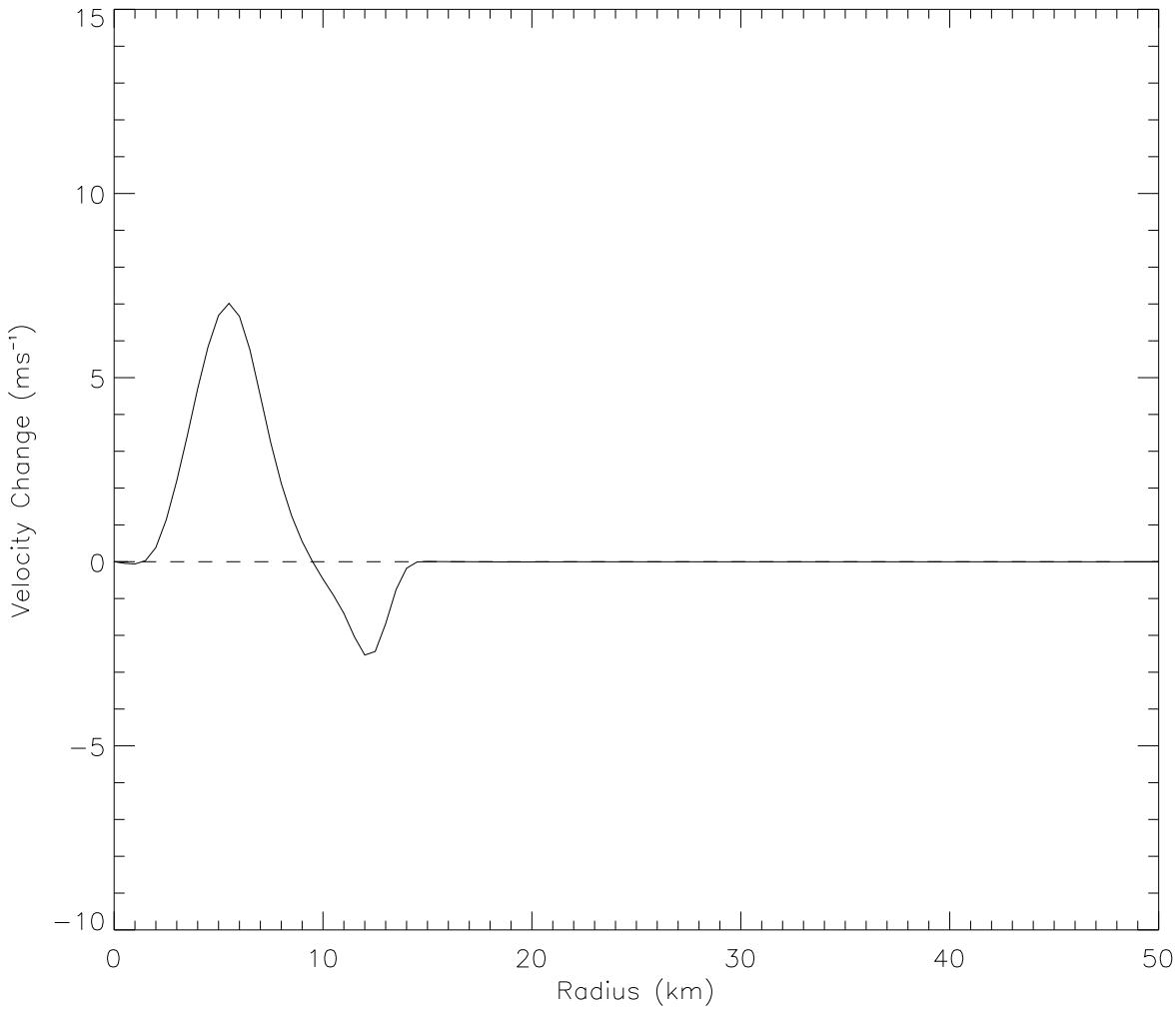

Figure 3.14: Symmetric tangential wind change (ms^{-1}) over the first four hours of the Case C simulation.

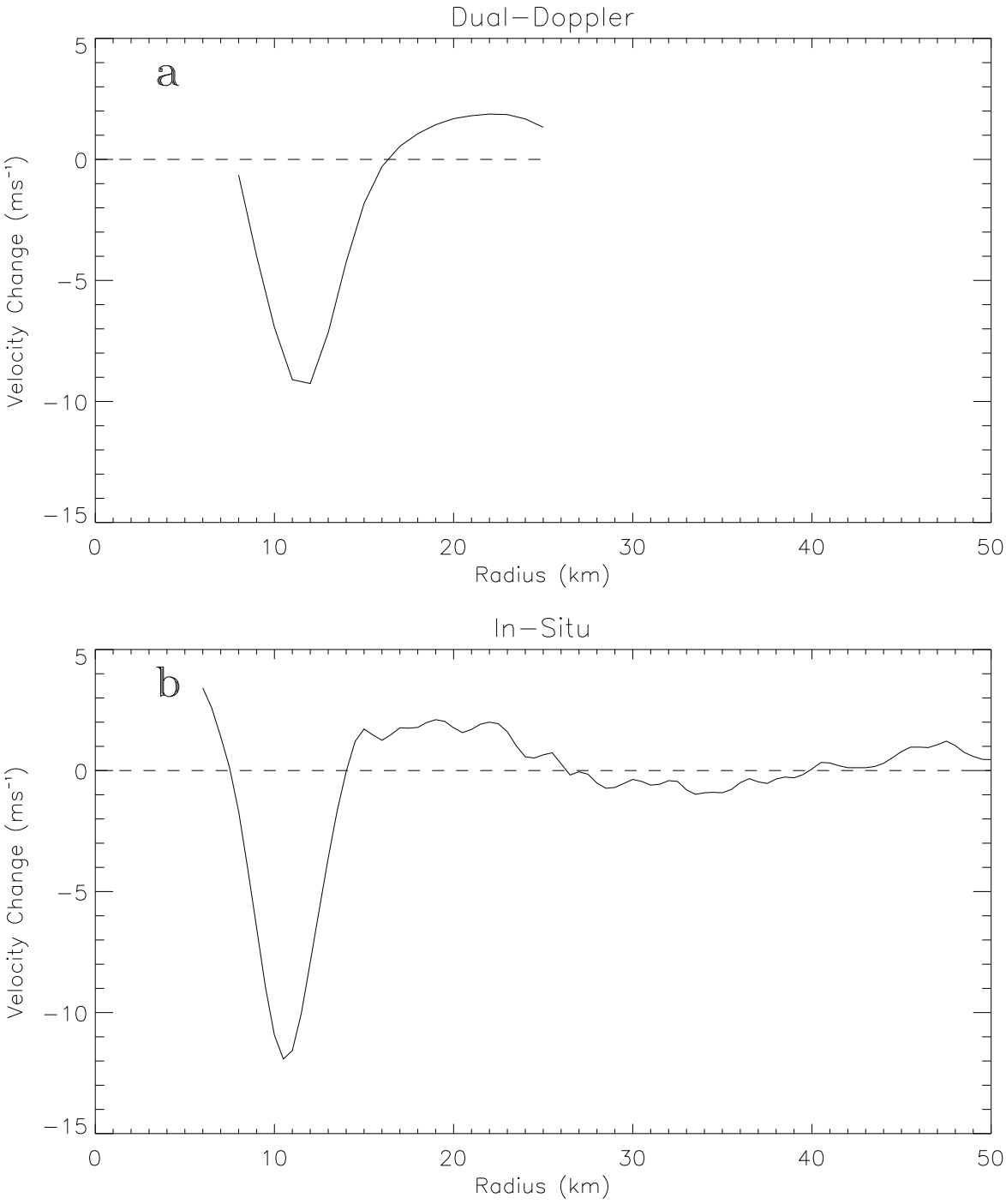

Figure 3.15: Symmetric tangential wind change (ms^{-1}) over the 3.5 h observation period at 3 km height (a) derived from the dual-Doppler analysis and (b) computed from aircraft wind measurements.

where k_0 is the initial radial wavenumber. Using Olivia's vortex profile at $R = 12$ km during leg 1, we estimate $\bar{\xi}_0 \approx 1 \times 10^{-2}$ s^{-1}, $\bar{\eta}_0 \approx 7 \times 10^{-3}$ s^{-1}, $\bar{q}_0 = N^2 \bar{\eta}_0 \approx 7 \times 10^{-7}$ s^{-3}, $R\bar{\Omega}'_0 \approx -3 \times 10^{-3}$ s^{-1}, and $\bar{q}'_0 \approx -3 \times 10^{-10}$ m^{-1}s^{-3}. Assuming an initial central radial wavenumber of 1/5 km^{-1} (inverse horizontal eyewall scale), a vertical wavenumber of 1/5 km^{-1} (approximate inverse depth of the vorticity bands), and $N^2 \approx 1 \times 10^{-4}$ s^{-2}, the stagnation radius for wavenumber 1 is found to be approximately 20 km from the RMW. In the convective regions the static stability N^2 will likely be less than the value used in the above calculation (Emanuel et al. 1987; Montgomery and Farrell 1992). Reduced static stability and the presence of symmetric radial inflow will reduce the value of δr. Thus, the estimated stagnation radius is consistent with the separation between eyewall and secondary bump, providing possible evidence for a vortex-Rossby wave induced change in the symmetric vortex.

The impact of the vorticity bump on the asymmetric vorticity evolution may be important, causing deviations from the evolution described for Case C. Laboratory experiments involving two-dimensional perturbations to two-dimensional vortices with monotonically increasing vorticity from the RMW to the vortex center and a bump in vorticity outside the RMW (i.e., an associated secondary tangential wind maximum) have been found to produce tripolar vortex structures dominated by wavenumber 2, with a central elliptical region of high vorticity and satellite regions of anticyclonic vorticity along the minor axis of the ellipse (e.g., Legras et al. 1988; Polvani and Carton 1990; Kloosterziel and van Heijst 1991). If the vorticity profile satisfies Rayleigh's necessary condition for barotropic instability, one often finds that such stable tripolar vortex structures emerge. Montgomery and Enagonio (1998) were evidently the first to reveal a tripolar vortex in three-dimensional vortex flow in the published literature. When a two-cluster convective anomaly was used to perturb an initially barotropic vortex, a tripole-like structure emerged at the upper levels of their QG model. In the context of 2D nondivergent dynamics Kossin et al. (2000) demonstrated that tripolar vortices can also emerge from hurricane-like vortex profiles with a symmetric secondary vorticity maximum radially outside the maximum at the vortex center.

Experiments using the modified Rankine profile of Case A with the secondary bump of vorticity of Case D did not produce a stable tripolar vortex. A barotropic stability analysis of a piecewise-uniform approximation to this profile showed that wavenumber 2 is in fact marginally stable (James Kossin, personal communication). A stable tripolar vortex was observed to emerge, however, upon increasing the vorticity of the bump by 35 percent. The question then arises of whether a stable tripolar vortex can emerge when the vorticity is depressed in the central region of the vortex, as might be expected in the lower- to mid-tropospheric portion of a hurricane (see Fig. 3.5b).

The vorticity profile for Case D$'$ is similar to that of case D, but with the secondary bump in vorticity elevated by 35 percent. A continuous nondivergent eigenanalysis of this profile found, in addition to the mode described in case C, a second unstable mode for wavenumber 2. Upon examining the vorticity map plot of this eigenmode, the mode is identified with the phase-locking of vortex Rossby waves propagating on the outer edge of the primary ring and the inner edge of the outer bump (not shown). Its e-folding time is 85 min, or approximately twice that of the mode associated with the primary vorticity ring. According to linear dynamics, then, the unstable mode observed in Case C should emerge first and tend to dominate the solution. Whether this remains true once wave-wave interactions become significant has important implications for the excitation of tripolar vortex structures in the lower-tropospheric region of hurricanes that are weakly forced.

The nonlinear simulation in which the Case D$'$ profile is perturbed by (3.6) shows essentially the same evolution of total vorticity as was observed in Case C (Fig. 3.12d). A tripolar vortex structure is not observed to emerge at long times. As long as the growth rate of the unstable mode associated with the primary ring is significantly larger than that of the bump, we find that tripolar structures do not materialize. Thus, based on the simple nonlinear initial-value experiments presented here, the most plausible (barotropic) internal mechanism for producing Olivia's wavenumber 2 asymmetry in vorticity at low levels during the observation period is the barotropic instability of the primary ring of vorticity.

The role of vorticity redistribution in TC development is next considered in the three-dimensional context. Redistribution of vorticity by vortex Rossby waves is found to play

a key role in the vertical alignment (or non-alignment) of vortices exhibiting small initial tilts and in the merger of convectively-generated PV within an incipient vortex. The latter is believed to be especially relevant to the problem of tropical cyclogenesis as first demonstrated by ME98. We further show that a dynamical barrier to TC development can be elucidated using linear vortex Rossby wave thinking.

Chapter 4

NUMERICAL MODEL DESCRIPTIONS

4.1 Three-Dimensional QG Model

Motivated by the geostrophic nature of large-scale flows in the middle-latitude atmosphere and ocean, the QG system has been used extensively in the study of vortex merger and alignment (McWilliams 1989; Polvani 1991; Viera 1995; Dritschel and Juarez 1996; Sutyrin et al. 1998). Its utility as a benchmark model for testing basic dynamical theories also has been exploited in recent studies of TCs (ME98; Smith et al. 2000). The PV conservation equation, invertibility relation, and thermodynamic equation in Boussinesq form on an f-plane are, respectively,

$$\frac{\partial q}{\partial t} + J\left(\psi, q\right) = 0, \tag{4.1}$$

$$q = f_0 + \nabla_h^2 \psi + \frac{1}{\rho_0}\frac{\partial}{\partial z}\left(\frac{\rho_0 f_0^2}{N^2}\frac{\partial \psi}{\partial z}\right), \tag{4.2}$$

$$\frac{\partial}{\partial t}\frac{\partial \psi}{\partial z} + J\left(\psi, \frac{\partial \psi}{\partial z}\right) + N^2 w = 0, \tag{4.3}$$

where q is the PV, ψ the flow streamfunction (which equals the geopotential, ϕ, divided by f_0), ρ_0 the density, f_0 the constant Coriolis parameter, N^2 the constant static stability, and w the vertical velocity. In Cartesian coordinates the Jacobian, $J(\psi, q) = \partial\psi/\partial x \cdot \partial q/\partial y - \partial\psi/\partial y \cdot \partial q/\partial x$. The details of the three-dimensional numerical model used to solve Eqs. (4.1)–(4.3), henceforth referred to as QG3D, are described by ME98. One difference from ME98 is that in the non-dimensional numerical simulation of (4.1)–(4.3) we will not require the horizontal scale, L, equal the Rossby deformation radius, $L_R = NH/f$, where H is the model depth. The thermal vorticity in the nondimensional invertibility relation (ME98, Eq. 5) is then multiplied by the vortex Burger number, $(L_R/L)^2$. Unless otherwise stated, no explicit diffusion is included in the model.

4.2 Equivalent Barotropic QG Model

A tilted PV column vertically bound by rigid lids can be decomposed into a barotropic mode and internal baroclinic modes. In general the interior flow results from both interior PV and potential temperature anomalies on the vertical boundaries (Hoskins et al. 1985). Hurricane observations show that the potential temperature gradients on the boundaries are weak (e.g., Hawkins and Rubsam 1968). Consistent with these observations and recent numerical studies of TCs (e.g., Möller and Montgomery 2000), we make the simplifying assumption of isothermal vertical boundaries at $z = 0$ and H. The streamfunction and PV can then be expressed as the sum of the vertical modes:

$$\psi(r,\lambda,z,t) = \sum_{m=0}^{\infty} \hat{\psi}_m(r,\lambda,t)\cos\left(\frac{m\pi z}{H}\right) \tag{4.4}$$

$$q(r,\lambda,z,t) = \sum_{m=0}^{\infty} \hat{q}_m(r,\lambda,t)\cos\left(\frac{m\pi z}{H}\right),$$

where m is the vertical wavenumber. Substitution of (4.4) into Eqs. (4.1)–(4.3) yields an equivalent barotropic (EQB) system of nonlinear equations for the real-valued, time-dependent amplitudes, $\hat{\psi}_m$ and $\hat{q}_m$. The nonlinear equations truncated at $m = 1$ are shown below. Because of the natural circular geometry of the problem, the equations are evaluated in cylindrical coordinates. The semi-spectral model described by ME98 (see also Montgomery et al. 2000 for more detail), modified to allow finite L_R, is used to perform the numerical computations (see below). A 2000 km radius domain with radial grid spacing $\Delta r = 5$ km and 8 mode azimuthal truncation was used. All nonlinear simulations were run with a diffusion coefficient ν varying from 100 to 200 $\mathrm{m^2 s^{-1}}$ to keep the integration stable at long times.

4.2.1 Nonlinear Initial-Value Model

For the tilted vortex (Section 5.1) and $m = 1$ isolated PV anomaly (Section 5.2) experiments, it is sufficient to simulate the vortex evolution using only the barotopic mode ($m = 0$) and first internal baroclinic mode ($m = 1$). Truncating (4.4) at $m = 1$ and

then substituting into the PV equation (4.1) yields the following nonlinear PV tendency equations for $m = 0$ and 1, respectively,

$$\left(\frac{\partial}{\partial t} + \frac{1}{r}\frac{\partial \hat{\psi}_0}{\partial r}\frac{\partial}{\partial \lambda} - \frac{1}{r}\frac{\partial \hat{\psi}_0}{\partial \lambda}\frac{\partial}{\partial r}\right)\hat{q}_0(r,\lambda,t) + \frac{1}{2}\left(\frac{1}{r}\frac{\partial \hat{\psi}_1}{\partial r}\frac{\partial}{\partial \lambda} - \frac{1}{r}\frac{\partial \hat{\psi}_1}{\partial \lambda}\frac{\partial}{\partial r}\right)\hat{q}_1(r,\lambda,t) = 0, \quad (4.5)$$

and

$$\left(\frac{\partial}{\partial t} + \frac{1}{r}\frac{\partial \hat{\psi}_0}{\partial r}\frac{\partial}{\partial \lambda} - \frac{1}{r}\frac{\partial \hat{\psi}_0}{\partial \lambda}\frac{\partial}{\partial r}\right)\hat{q}_1(r,\lambda,t) + \left(\frac{1}{r}\frac{\partial \hat{\psi}_1}{\partial r}\frac{\partial}{\partial \lambda} - \frac{1}{r}\frac{\partial \hat{\psi}_1}{\partial \lambda}\frac{\partial}{\partial r}\right)\hat{q}_0(r,\lambda,t) = 0. \quad (4.6)$$

This system of equations will tend to underestimate the magnitude of the azimuthal mean flow change since the $m = 2$ tendency associated with the self interaction of $(m, n) = (1, n)$ is excluded.

In Section 5.1, where the wave-mean interaction is not critical to understanding the vortex evolution, the above truncated system is solved. The $\hat{(\,)}_m$ are first expanded in a truncated azimuthal Fourier series following Appendix B of ME98:

$$\hat{\psi}_m(r,\lambda,t) = \sum_{n=-N}^{N} \tilde{\psi}_{mn}(r,t)e^{in\lambda} \quad (4.7)$$

and

$$\hat{q}_m(r,\lambda,t) = \sum_{n=-N}^{N} \tilde{q}_{mn}(r,t)e^{in\lambda}, \quad (4.8)$$

where n is the azimuthal wavenumber, N is the azimuthal mode truncation, and $\tilde{(\,)}_{mn}$ are the complex Fourier coefficients. This semi-spectral formulation is advantageous for swirling flows where the mean flow dominates the asymmetric component of the flow. Since the radial and azimuthal resolutions are independent, one can reduce the number of degrees of freedom by choosing a minimum allowable azimuthal resolution. For simple experiments involving axisymmetrization on stable vortex monopoles, one may only need to retain a few azimuthal wavenumbers to accurately capture the flow evolution. This dimensionality reduction will reduce computational time (Montgomery et al., 2000). Substitution of (4.7) and (4.8) into the flux form of equations (4.5) and (4.6) yields, respectively,

$$\frac{\partial \tilde{\psi}_{0n}}{\partial t} = \nabla_{0n}^{-2}\tilde{F}_{0n}(r,t) \quad (4.9)$$

and

$$\frac{\partial \tilde{\psi}_{1n}}{\partial t} = \nabla_{1n}^{-2}\tilde{F}_{1n}(r,t), \quad (4.10)$$

where

$$\begin{aligned}\tilde{F}_{0n}(r,t) &= \frac{1}{r}\{\sum_{\substack{|k|\le N\\ |n-k|\le N}}[ik\frac{\partial}{\partial r}(\tilde{\psi}_{0,k}\tilde{q}_{0,n-k}) - in\tilde{q}_{0,n-k}\frac{\partial\tilde{\psi}_{0,k}}{\partial r} + \\ &\quad \frac{1}{2}(ik\frac{\partial}{\partial r}(\tilde{\psi}_{1,k}\tilde{q}_{1,n-k}) - in\tilde{q}_{1,n-k}\frac{\partial\tilde{\psi}_{1,k}}{\partial r})] + \\ &\quad in\frac{d\bar{\zeta}}{dr}\tilde{\psi}_{0,n} - in\frac{d\bar{\psi}}{dr}\tilde{q}_{0,n}\} + \nu\nabla^2_{0n}\tilde{q}_{0,n}, \qquad (4.11)\end{aligned}$$

$$\begin{aligned}\tilde{F}_{1n}(r,t) &= \frac{1}{r}\{\sum_{\substack{|k|\le N\\ |n-k|\le N}}[ik\frac{\partial}{\partial r}(\tilde{\psi}_{0,k}\tilde{q}_{1,n-k}) - in\tilde{q}_{1,n-k}\frac{\partial\tilde{\psi}_{0,k}}{\partial r} + \\ &\quad (ik\frac{\partial}{\partial r}(\tilde{\psi}_{1,k}\tilde{q}_{0,n-k}) - in\tilde{q}_{0,n-k}\frac{\partial\tilde{\psi}_{1,k}}{\partial r})] + \\ &\quad in\frac{d\bar{\zeta}}{dr}\tilde{\psi}_{1,n} - in\frac{d\bar{\psi}}{dr}\tilde{q}_{1,n}\} + \nu\nabla^2_{0n}\tilde{q}_{1,n}, \qquad (4.12)\end{aligned}$$

and $\nabla^2_{mn} = (1/r)\partial/\partial r + \partial^2/\partial r^2 - n^2/r^2 - \gamma_m^2$, where $\gamma_m = m\pi/L_R$ is the inverse Rossby deformation radius for internal mode m. $\overline{\zeta}$ is the azimuthal-mean geostrophic relative vorticity and $\overline{\psi}$ is the azimuthal-mean streamfunction. The last term in both equations is the explicit diffusion. Note that the linear terms involve *only* the barotropic component of the azimuthal mean vortex, i.e., $\bar{\psi}(r,t) = \tilde{\psi}_{00}(r,t)$ and $\bar{q}(r,t) = \tilde{q}_{00}(r,t)$. The tendency in the azimuthal mean quantities is transferred to the mean vortex after each time step, and then set to zero before the next time step. Consistent with the barotropic mean vortex constraint, we impose $\tilde{F}_{10} = 0$. In other words, we neglect the small nonlinear interactions between the $m = 1$ asymmetries and the $m = 0$ asymmetries that project onto the azimuthal mean vortex.

In Section 5.2 where the mean flow change predicted by the QG3D and EQB models is compared, we wish to include the full effect of the self-interaction of $(m,n) = (1,n)$, i.e., both the $(0,0)$ and $(2,0)$ contributions. The wave-mean terms which contribute to the tendency in $(0,0)$ are in fact the same terms that contribute to the tendency in $(2,0)$. Thus, to account for the $m = 2$ tendency we simply double the wave-mean terms in the $(0,0)$ equation. This approximation is equivalent to assuming $m = 0$ in the inversion of potential vorticity for streamfunction, and will tend to overestimate the magnitude of the mean-flow change. The inclusion of $m = 2$ in this way is consistent with the quasi-linear approximation presented in Section 5.2.

4.2.2 Linear Initial-Value Model

An advantage of the above semi-spectral formulation is that it allows easy implementation of the linearized system of equations governing the evolution of perturbations to a circular vortex flow. Retaining only the linear terms in Eqs. (4.11) and (4.12) yields the following inviscid linear equations for the Fourier coefficients:

$$\left(\frac{\partial}{\partial t} + in\overline{\Omega}\right)\tilde{q}_{mn}(r,t) - \frac{in}{r}\frac{\mathrm{d}\overline{\zeta}}{\mathrm{dr}}\tilde{\psi}_{mn}(r,t) = 0, \tag{4.13}$$

$$\frac{1}{r}\frac{\partial}{\partial r}\left(r\frac{\partial\tilde{\psi}_{mn}}{\partial r}\right) - \left(\frac{n^2}{r^2} + \gamma_m^2\right)\tilde{\psi}_{mn} = \tilde{q}_{mn}, \qquad n \geq 1, \tag{4.14}$$

$$\frac{1}{r}\frac{d}{dr}\left(r\frac{\mathrm{d}\overline{\psi}}{\mathrm{dr}}\right) = \overline{\zeta}. \tag{4.15}$$

The vortex evolution simulated by the linear EQB model will be compared to that simulated by the nonlinear models in Chapter 5 to gain insight into the nature of the alignment dynamics.

For disturbances that are sheared by the differential rotation of the basic state flow, finer and finer radial scales will be produced placing a limit on how long the inviscid linear simulations can be integrated. This time limit was shown by Smith and Montgomery (1995) to be

$$t_{max} \leq \left|\frac{\pi}{n\Delta r d\overline{\Omega}/dr}\right|, \tag{4.16}$$

where n is the azimuthal wavenumber, Δr is the radial grid spacing, and $\overline{\Omega}$ is the azimuthal-mean angular velocity. For $n = 1$, $\Delta r = 5$ km, and the mean vortex to be described in Section 5.1, $t_{max} \approx 54$ days. All inviscid integrations shown here are restricted to time intervals less than 54 days.

Before the first timestep, the QG3D model subtracts the mass-weighted average of PV from the total field to ensure conservation of domain-integrated PV. This small correction to the total PV adds a constant anticyclonic rotation to the domain. For comparison with the EQB simulations the QG3D map plots are rotated cyclonically by the azimuthal angle consistent with this constant rotation.

4.3 Equivalent Barotropic Asymmetric Balance (AB) Model

Finite Rossby number effects are not contained within the QG system. To consider more rapidly rotating vortices we could use Eliassen's (1951) balance formulation which views a vortex as proceeding from one (quasi) gradient balanced state to the next. Eliassen's formulation, however, is valid only for symmetric vortices. A more generalized balance theory is required to capture the non-axisymmetric processes of vortex merger and alignment. The Asymmetric Balance (AB) theory for rapidly rotating vortices (Shapiro and Montgomery 1993) has proven useful in the context of asymmetric TC dynamics (MK; Möller and Jones 1998; Möller and Montgomery 1999, 2000). AB theory is accurate for order unity Rossby numbers and order unity asymmetric divergence, remains qualitatively useful at even higher Rossby numbers (Möller and Montgomery 1999; Montgomery et al. 1999), and has the desirable property of filtering gravity and inertia waves (as in the QG formulation). As the Rossby number approaches zero, the AB system reduces to the QG system.

The linear equivalent barotropic AB model is derived following the three-dimensional derivation of Shapiro and Montgomery (1993). The radial and tangential momentum, thermodynamic, and continuity equations in hydrostatic, Boussinesq form on an f-plane, linearized about a barotropic mean vortex are, respectively,

$$\frac{D_v u'}{Dt} - \overline{\xi} v' = -\frac{\partial \phi'}{\partial r}, \tag{4.17}$$

$$\frac{D_v v'}{Dt} + \overline{\eta} u' = -\frac{1}{r}\frac{\partial \phi'}{\partial \lambda}, \tag{4.18}$$

$$\frac{D_v}{Dt}\left(\frac{\partial \phi'}{\partial z}\right) + N^2 w' = 0, \tag{4.19}$$

$$\frac{1}{r}\frac{\partial}{\partial r}(r u') + \frac{1}{r}\frac{\partial v'}{\partial \lambda} + \frac{\partial w'}{\partial z} = 0 \tag{4.20}$$

where

$$\frac{D_v}{Dt} = \frac{\partial}{\partial t} + \frac{\overline{v}}{r}\frac{\partial}{\partial \lambda} \tag{4.21}$$

is the material derivative operator following the mean tangential wind, ϕ' is the perturbation geopotential, $\overline{\xi} = f + 2\overline{v}/r$ is the modified Coriolis parameter, and $\overline{\eta} = f + \overline{\zeta}$ is the

absolute vertical vorticity. The mean tangential wind is assumed in gradient balance with the mean geopotential field, i.e.,

$$f\overline{v} + \frac{\overline{v}^2}{r} = \frac{\partial \overline{\phi}}{\partial r}. \tag{4.22}$$

Differentiating (4.17) and (4.18) with respect to $\frac{D_v}{Dt}$ and then cross-substituting (4.17) and (4.18) into these expressions to eliminate the first derivatives of u' and v' yields

$$\frac{D_v^2 u'}{Dt^2} + \overline{\eta}\overline{\xi}u' + \frac{D_v}{Dt}\left(\frac{\partial \phi'}{\partial r}\right) = -\frac{\overline{\xi}}{r}\frac{\partial \phi'}{\partial \lambda} \tag{4.23}$$

$$\frac{D_v^2 v'}{Dt^2} + \overline{\eta}\overline{\xi}v' + \frac{1}{r}\frac{D_v}{Dt}\left(\frac{\partial \phi'}{\partial \lambda}\right) = \overline{\eta}\frac{\partial \phi'}{\partial r}. \tag{4.24}$$

A naive scaling of the orbital "acceleration" D_v^2/Dt^2 yields (Shapiro and Montgomery 1993)

$$\frac{D_v^2}{Dt^2} \sim n^2 \frac{\overline{v}^2}{r^2}. \tag{4.25}$$

A local Rossby number squared defined as the square of the ratio of the orbital acceleration to the inertial frequency is given by

$$R_n^2 = \frac{n^2 \overline{v}^2 / r^2}{\overline{\eta}\overline{\xi}}. \tag{4.26}$$

For local Rossby number squared much less than unity the first term in Eqs. (4.23) and (4.24) can be neglected compared to the second term. Shapiro and Montgomery (1993) verified this approximation using observations from Hurricane Gloria (1985). They observed R_1^2 less than unity everywhere within the storm except just outside the RMW and within an isolated region at three times the RMW in the upper troposphere. Möller and Montgomery (1999) showed that the actual value of $D_v^2 u'/Dt^2$ can be much smaller than the naive estimate $n^2(\overline{v}^2/r^2)u'$ for hurricane-like vortices. Therefore, the actual local Rossby numbers within Gloria's core are likely much less than unity. For the weak vortices considered in this dissertation, the AB predictions will be accurate.

Solving for u', v', and w', and then substituting into the continuity equation results in a predictive equation for the geopotential perturbation:

$$\frac{1}{r}\frac{\partial}{\partial r}\left[-\frac{r}{\overline{\eta}\overline{\xi}}\frac{D_v}{Dt}\left(\frac{\partial \phi'}{\partial r}\right) - \frac{1}{\overline{\eta}}\frac{\partial \phi'}{\partial \lambda}\right] + \frac{1}{r}\frac{\partial}{\partial \lambda}\left[-\frac{1}{r\overline{\eta}\overline{\xi}}\frac{D_v}{Dt}\left(\frac{\partial \phi'}{\partial \lambda}\right) + \frac{1}{\overline{\xi}}\frac{\partial \phi'}{\partial r}\right] + \left(\frac{m\pi}{NH}\right)^2 \frac{D_v \phi'}{Dt} = 0, \tag{4.27}$$

where we have used the fact that $\partial^2\phi'/\partial z^2 = -m^2\pi^2\phi'/H^2$ for the equivalent barotropic system. Rearranging (4.27) yields

$$\frac{D_v}{Dt}\left[\frac{\overline{q}\overline{\xi}}{r}\frac{\partial}{\partial r}\left(\frac{r}{\overline{q}\overline{\xi}}\frac{\partial\phi'}{\partial r}\right) + \frac{1}{r^2}\frac{\partial^2\phi'}{\partial\lambda^2} - \gamma_m^2(r)\phi'\right] - \frac{\overline{\xi}}{\overline{q}}\frac{d\overline{q}}{dr}\frac{1}{r}\frac{\partial\phi'}{\partial\lambda} = 0, \tag{4.28}$$

where $\overline{q} = N^2\overline{\eta}$ and $\gamma_m^2(r) = (m\pi/NH)^2(\overline{\eta}\overline{\xi})$. Note that this predictive equation is virtually identical to (4.13) for the linear QG system, but with additional geometric factors in front of the radial derivatives and non-constant γ_m. Thus, the linear semi-spectral model used to time-integrate the QG EQB system is also used here with the appropriate modifications (i.e., redefine $\overline{q}$ and γ_m, and add the geometric factors).

The quantity in brackets in Eq. (4.28) is *not* the perturbation PV. The perturbation pseudo-PV is given by

$$q'_\xi = N^2\mathbf{k}\cdot\nabla\times\mathbf{u}'_\xi - \frac{N^2\gamma_m^2}{\overline{\xi}}\phi', \tag{4.29}$$

where $\mathbf{u}'_\xi$ is the generalization of the geostrophic wind and is written

$$\mathbf{u}'_\xi = \left(-\frac{1}{r\overline{\xi}}\frac{\partial\phi'}{\partial\lambda}, \frac{1}{\overline{\xi}}\frac{\partial\phi'}{\partial r}\right). \tag{4.30}$$

The perturbation pseudo-PV evolution equation can be obtained through a re-casting of (4.28) and is given by

$$\frac{D_v}{Dt}q'_\xi + u'_\xi\frac{d\overline{q}}{dr} = 0. \tag{4.31}$$

This equivalent barotropic AB system is used in Chapter 6 as a first step in the generalization of the QG vortex alignment findings presented in Chapter 5.

Chapter 5

QG VORTEX ALIGNMENT

A vertically-tilted vortex in the atmosphere either resists external forcings to align or succumbs to such influences by irreversibly shearing apart. The question of how and under what circumstances vertical alignment occurs has been addressed in previous studies with the large-scale atmospheric and oceanic circulations in mind (McWilliams 1989; Polvani 1991; Viera 1995; Dritschel and Juarez 1996; Sutyrin et al. 1998). The conceptual picture put forth for the evolution of an unforced tilted vortex is that PV at upper levels is advected by the vertically-penetrating flow associated with the PV at lower levels, and vice versa. Described in this way, the mutual advection is assumed to be a nonlinear process. Accordingly, the initial vertical tilt is a crucial parameter in determining the subsequent vortex evolution. Polvani (1991) showed that the evolution of a tilted vortex patch in a two-layer QG model can be predicted on the basis of its nearness to a geometric configuration known as a stable V-state in which the PV rotates without deformation of shape at a constant rate. Alignment tends to occur when the vortex is initially far from a V-state. The vortex in this case approaches a circular barotropic configuration through filamentation and axisymmetrization (e.g., Melander et al. 1987).

Here a new and complimentary approach to understanding the vertical alignment process for continuously-distributed vortices is developed utilizing the fact that for overlapping upper- and lower-level PV centers, the vortex is meaningfully decomposed into an azimuthal mean and departure therefrom (i.e., a wave, mean-flow partitioning). We explicitly simulate the linear interaction of perturbation and mean flow as well as the fully nonlinear vortex evolution to elucidate the alignment dynamics. Vortex Rossby waves are shown to play a key role in the vertical alignment process, just as they do in the

two-dimensional and quasi two-dimensional vortex axisymmetrization process described by MK and later confirmed by ME98, Möller and Montgomery (1999, 2000) and Enagonio and Montgomery (2000). A simple conceptual picture of vortex alignment emerges for small vertical tilts based solely on linear dynamics. Of course linear dynamics can only be expected to capture alignment for a certain range of vortex tilts, but it will be shown that this range can be surprisingly large. A physical explanation is provided for why linear thinking can be applied to vortices exhibiting large initial tilts in certain parameter regimes.

Recent dynamical studies of TCs have emphasized how such vortices resist the effects of vertical shear and other external strains during all lifecycle stages (Jones 1995; Smith et al. 2000). Jones (1995) considered the evolution of a hurricane-like vortex embedded in vertically-sheared flow. Her physical interpretation of the evolution from aligned to tilted vortex largely follows that of Polvani (1991) and other similar studies. Smith et al. (2000) reduced the TC vortex alignment problem in vertical shear to a two-layer nonlinear analogue model, solvable analytically. As an extension of Polvani (1991), they presented a portrait of upper- and lower-level vortex trajectories as a function of shear magnitude, vortex strength, and coupling between layers. The qualitative results of the model were verified using a two-layer QG model, but it should be noted that their analogue model becomes singular as the initial upper- and lower-level PV separation goes to zero. Our work compliments these studies by taking a step back and exploring the unforced problem for small to moderate initial tilts. According to our interpretation of the unforced vortex dynamics, the addition of vertical shear simply makes the problem a forced linear one as long as departures from vertical alignment are not too great. The extension of the present work to the forced problem is addressed in Chapter 6.

An axisymmetric view of TC genesis has been offered by Bister and Emanuel (1997) based on observations of TC Guillermo (1991) and supporting axisymmetric numerical simulations. A re-analysis of the Guillermo Doppler wind data by Bracken (1999), however, suggests a more prominent role played by asymmetries during the initial stages of genesis. ME98 presented an asymmetric model for genesis in which a pre-existing vortex (e.g.,

a mid-level mesoscale convective vortex (MCV) or closed circulation associated with an easterly wave) aligns with nearby convectively-generated positive PV at low levels.

An immediate application of the present work is towards further understanding the dynamics of the asymmetric TC genesis mechanism of ME98. This chapter is therefore organized as follows: The evolution of an initially-tilted vortex is examined in Section 5.1. In Section 5.2 we apply the linear alignment ideas to the problem of three-dimensional merger of an isolated anomaly with a pre-existing vortex. The simulations in the latter section are presented in the context of TC dynamics. During the initial stages of TC genesis convectively-generated positive PV at low levels moves into the core region of the pre-existing vortex. If the convection is initially close to the vortex core (i.e., within the RMW), the linear merger ideas will accurately describe this process. As the vortex becomes more vertically coherent, the tilted vortex ideas of Section 5.1 then become relevant.

5.1 Vortex alignment starting from a tilted vortex: Causes and conditions

5.1.1 Initial Conditions

In the experiments presented here the azimuthal-mean vortex will be assumed barotropic. The initial symmetric PV takes the form

$$\overline{q}(r) = \overline{q}_{max} e^{-(\sigma r)^2}, \tag{5.1}$$

where $\overline{q}_{max}$ is the maximum mean PV and σ is the inverse decay length of the PV profile. The mean vortex for $\overline{q}_{max} = 9.0 \times 10^{-5}$ s^{-1} and $\sigma^{-1} = 167$ km, used by ME98, is depicted in Fig. 5.1. The maximum wind speed is 5 ms^{-1} and the RMW is 200 km. As demonstrated in Section 5.1.4, the fundamental findings of this work are independent of the precise form of the monotonic profile of PV. We will therefore present most of our findings with this basic state vortex.

The initial PV asymmetry has the vertical structure of the first internal baroclinic mode ($m = 1$), unless otherwise stated, and is consistent with the assumption of isothermal

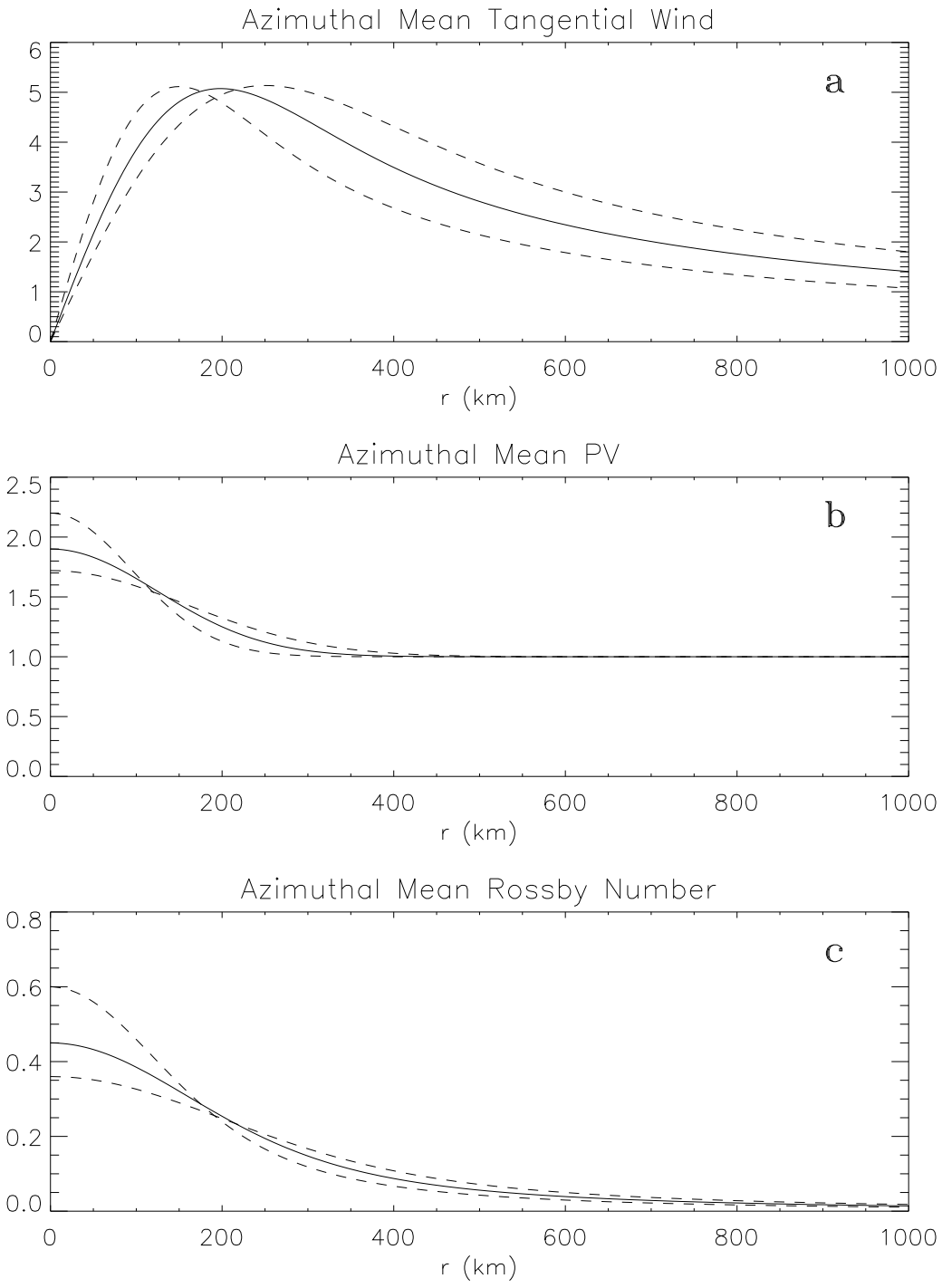

Figure 5.1: The azimuthal-mean vortex (solid) used in all simulations unless stated otherwise in the text. The vortices depicted by the dashed curves are described in Section 5.1.4. The (a) tangential wind is in units of ms^{-1} and the (b) PV is in units of 10^{-5} s^{-1}. The (c) Rossby number is defined as $\overline{\Omega}/f$, where $\overline{\Omega}$ is the azimuthal-mean angular velocity.

vertical boundary conditions discussed in Chapter 4. For simplicity, the mean vortex is perturbed with a single azimuthal Fourier mode:

$$q'(r,\lambda,z,t) = Re\left\{\tilde{q}_{1n}(r,t)\cos\left(\frac{\pi z}{H}\right)e^{in\lambda}\right\}, \tag{5.2}$$

where Re denotes the real part of the bracketed quantity. In the general case n can be any azimuthal wavenumber. Isolated anomalies composed of a superposition of azimuthal wavenumbers are considered in Section 5.2 in our investigation of the merger and alignment of convectively-generated PV within a pre-existing vortex. The horizontal structure of the PV perturbation is that of the azimuthal wavenumber one pseudo-mode (Michalke and Timme 1967; Weber and Smith 1993; Smith and Montgomery 1995; MK). The pseudo-mode in two-dimensional flows represents a vortex displacement and has the radial PV structure:

$$\tilde{q}_{11}(r) = \tilde{\alpha}\frac{\mathrm{d}\overline{\mathrm{q}}}{\mathrm{dr}}, \tag{5.3}$$

where $\tilde{\alpha}$ is a constant conversion factor. We define $\tilde{\alpha} = \alpha\overline{q}_{\max}/(\mathrm{d}\overline{\mathrm{q}}/\mathrm{dr})_{\max}$, where $(\mathrm{d}\overline{\mathrm{q}}/\mathrm{dr})_{\max}$ is the maximum mean PV gradient and α is a non-dimensional amplitude factor.

For a given mean vortex with horizontal scale L (roughly the RMW) and vertical scale H the only two adjustable parameters are α and γ_1. For $n = 1$, variation of α changes the angle of inclination of the PV column from the vertical. Equations (5.1)–(5.3) best represent a tilted vortex for values of α much less than unity. As α approaches unity, regions of negative PV arise and this initial condition is no longer suitable for studying the evolution of a tilted vortex. To better simulate large tilt in the EQB model higher azimuthal harmonics are included in expression (5.2) and a more accurate form for $\tilde{q}_{11}$ is used.

Before investigating the full α and γ_1 parameter space, we begin by defining a benchmark case and comparing the vortex evolution simulated by the QG3D and EQB models. The benchmark simulation using $\alpha = 0.3$ and $\gamma_1 = 3.14 \times 10^{-6}$ m^{-1} is shown in Fig. 5.2 in terms of PV. Mid-latitude values of $f = 10^{-4}$ s^{-1}, $H = 10$ km, and $N = 10^{-2}$ s^{-1} are used to define γ_1. To verify that (5.1)–(5.3) is a valid approximation to a tilted

vortex, the QG3D model is initialized with a linearly-tilted PV column having an angle of inclination from the vertical nearly identical to that of the EQB benchmark vortex. The vortex evolution simulated with the QG3D model (Fig. 5.2a) is replicated well by the nonlinear, truncated EQB model (Fig. 5.2b). The vortex wobbles about the stationary mid-level centroid with no obvious sign of alignment over the $4\tau_e$ period (where τ_e denotes a circulation period, which is approximately 2.9 days for this vortex). As evident from comparison of the two simulations, the interaction between vertical modes is not crucial to understanding the vortex evolution for the small tilts considered here. Therefore in our exploration of the alignment mechanism, the EQB model will be primarily used. All of the principle results to be shown, however, are still verified with the QG3D model.

The dependence of the alignment process on α is considered below. The initial horizontal distance between upper- and lower-level PV centroids (d_i) defined by

$$d_i = 2\left[\left(\frac{\int_A xqdA}{\int_A qdA}\right)^2 + \left(\frac{\int_A yqdA}{\int_A qdA}\right)^2\right]^{1/2}, \tag{5.4}$$

(where the integral over the domain area A can be evaluated at either the upper or lower level due to the mirror symmetry of the simulations about the middle level), and the tilt angle (θ) defined by

$$\tan\theta = d_i/H \tag{5.5}$$

are listed in Table 5.1 for each of the simulations. The mid-latitude value of $\gamma_1 = 3.14 \times 10^{-6}$ m^{-1} is used in all simulations, except in Section 5.1.3 where the γ-dependence of vortex alignment is explored.

5.1.2 Linear Vortex-Rossby Wave Dynamics

A useful diagnostic in the study of vortex merger and vortex axisymmetrization on a vortex with monotonically-decreasing basic state vorticity is the vortex beta Rossby number, R_β (Möller and Montgomery 2000; Enagonio and Montgomery 2000). Mathematically it is defined as the ratio of the nonlinear terms in the PV equation to the effective "beta" term involving the mean PV gradient of the basic state vortex. Whereas the vortex itself is the perturbation in the problem of vortex motion on a β-plane (McWilliams and Flierl

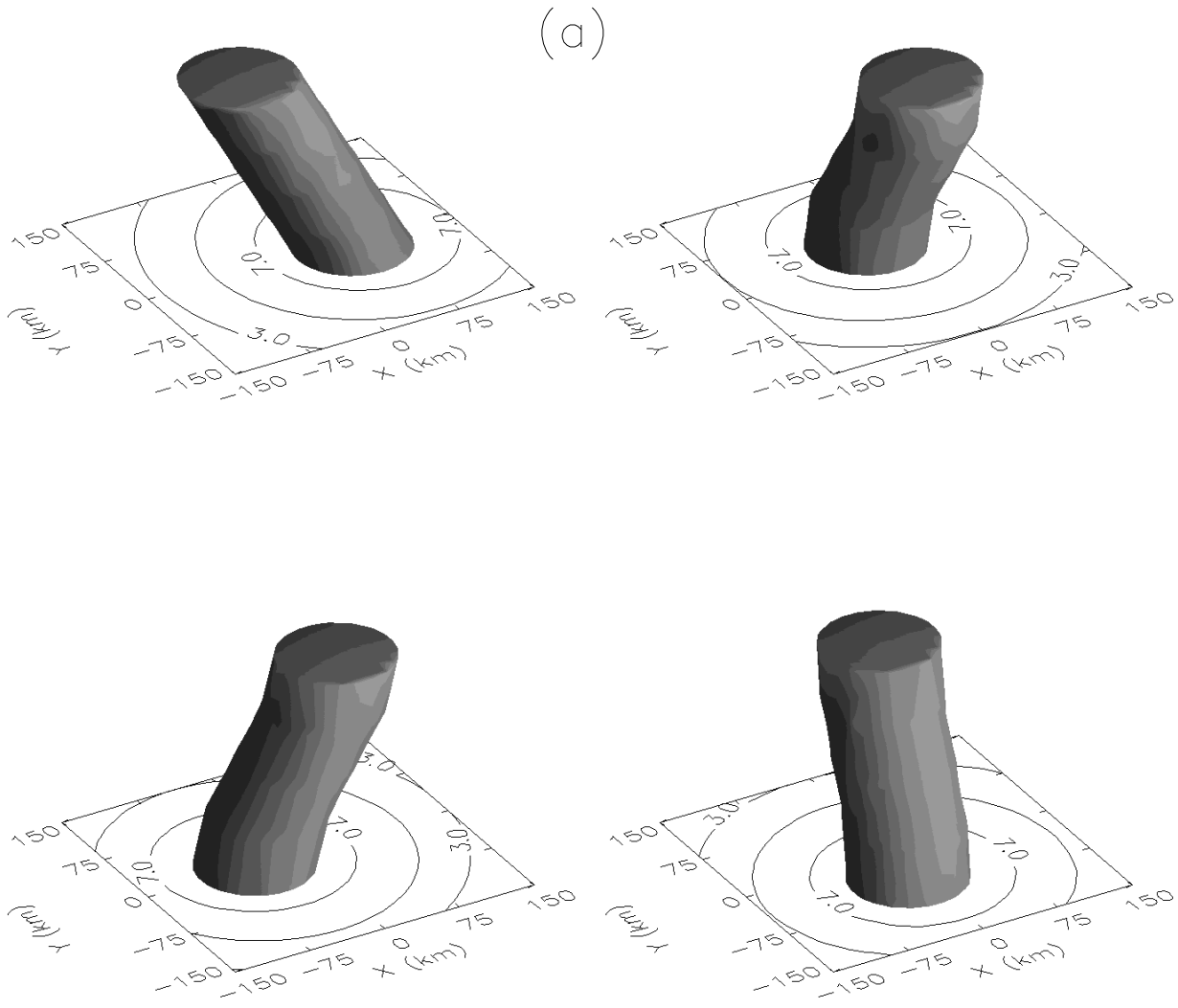

Figure 5.2: Evolution of vortex PV (from left to right) at t = 0, $1.5\tau_e$, $2.5\tau_e$, and $4\tau_e$ for the benchmark run with $\alpha = 0.3$ and $\gamma_1 = 3.14 \times 10^{-6}$ m^{-1}. Only the inner 300 km x 300 km is shown to emphasize the vortex tilt. The vertical depth is 10 km. Results from (a) the QG3D model with PV isosurface 8.0×10^{-5} s^{-1} and (b) the nonlinear EQB model with PV isosurface 8.5×10^{-5} s^{-1} are shown. The different initial conditions are described in the text. Contour interval is 2.0×10^{-5} s^{-1}.

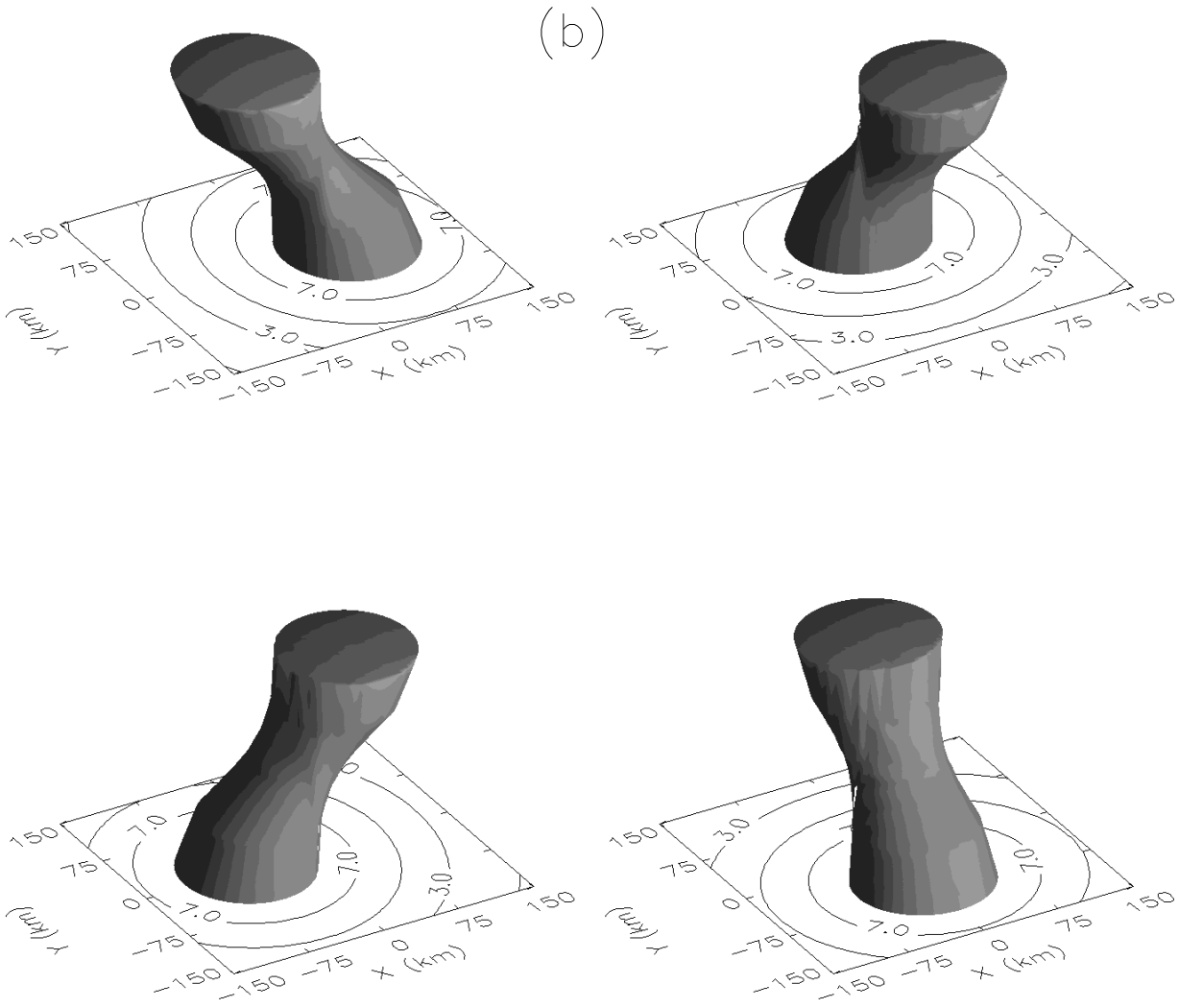

Figure 5.3: see Fig. 5.2.

γ_1 (x10^{-6} m^{-1})	α	θ (degrees)	d_i (km)	R_β
3.14	0.1	78	41	0.08
3.14	0.3	86	110	0.25
3.14	0.5	88	200	0.50
20.0	0.3	86	110	0.08

Table 5.1: Parameters used in the control simulations. For the benchmark basic state vortex the two parameters which define each simulation are the inverse internal Rossby deformation radius (γ_1) and tilt amplitude (α). Useful parameters derived from these two are the initial vortex angle of inclination from the vertical (θ), upper- and lower-level PV intercentroid separation distance (d_i), and vortex beta Rossby number (R_β). The latter is defined in Section 5.1.2.

1979; Montgomery et al. 1999), here the perturbation is the departure from vertical alignment. In studies of vortex motion the beta Rossby number is large compared to unity. The tilted vortices considered here are characterized by beta Rossby numbers less than unity. In the non-divergent limit the vortex beta Rossby number scales as

$$R_\beta \sim \frac{V'}{L'^2 \frac{\mathrm{d}\overline{\zeta}}{\mathrm{dr}}}, \tag{5.6}$$

where V' is the perturbation velocity amplitude, L' the perturbation horizontal scale, and $d\overline{\zeta}/dr$ the radial vorticity gradient of the basic state vortex. It provides a measure of how important nonlinear advection is compared to the vortex Rossby wave restoring mechanism. For R_β much less than unity perturbations on an everywhere monotonic mean vortex are expected to disperse as vortex Rossby waves. The wave-mean ideas of MK usefully and accurately characterize the dynamics in this parameter regime.

In previous work vortex alignment has been described in much the same way as vortex merger in two dimensions: The flow induced by the upper-level PV anomaly advects the lower-level anomaly, and vice versa. Implied in this conceptual picture is that the dynamics is fundamentally nonlinear, and therefore strongly dependent upon the initial horizontal separation of the PV anomalies (i.e., magnitude of the vertical tilt). We agree that this view is the correct one for upper- and lower-level anomalies initially separated by large distances, as one might observe in geostrophic turbulence simulations (McWilliams 1989; McWilliams et al. 1999; Dritschel et al. 1999). But is it true for upper and lower-level

anomalies separated by small distances, as one might observe in the case of an initially upright TC tilted by vertical shear? We propose that the asymptotic dynamics (i.e., when the vortices are close enough together) of vortex merger and alignment in three dimensions is more accurately viewed as linear. This is not to say that nonlinear advection is identically zero, but rather that its role in the evolution of vortices with small initial tilts is secondary to linear advection. The approach taken here is to begin with an aligned vortex and systematically increase the vertical tilt. With each progressive increase in the separation between upper- and lower-level anomalies we ask the question: To what extent is the subsequent vortex evolution described by linear dynamics?

A schematic illustration of what is meant by linear dynamics is shown in Fig. 5.4. The tilted PV column is decomposed into an azimuthal mean, $\overline{q}$, which for simplicity is assumed barotropic, and a departure from that mean, q'. In the linear approximation, $\overline{q}$ at upper(lower) levels is radially advected by the perturbation wind field associated with the upper(lower)-level PV anomaly and, depending upon the magnitude of the vertical penetration depth of the vortex flow, fL/N, the lower(upper)-level PV anomaly. It is this radial advection in conjunction with the azimuthal advection of q' by the mean tangential wind, $\overline{v}$, that governs the evolution of the tilted vortex in the linear approximation. Of course in the limit of large vertical tilt (and presumably large R_β), q' approaches the magnitude of $\overline{q}$, and linear theory will no longer be valid. Our intent is to provide physical insight into the vortex alignment process at small vertical tilts and to then illustrate the range of applicability of the linear ideas.

For the benchmark run with $\alpha = 0.3$, R_β, computed using the strict mathematical definition stated above, is found to be approximately 0.25 in the vicinity of the PV perturbation maximum. Figure 5.5 shows the total and wavenumber one PV at the surface ($z = 0$) from the linear and nonlinear EQB models. Although R_β is not infinitesimally small in this case, good agreement between the linear and nonlinear simulations is nevertheless observed. Both vortex simulations show radially-propagating, sheared vortex Rossby waves superposed on a quasi-discrete PV feature. The radial vortex Rossby wave propagation is illustrated in Fig. 5.6 for the linear simulation. Consistent with MK, the

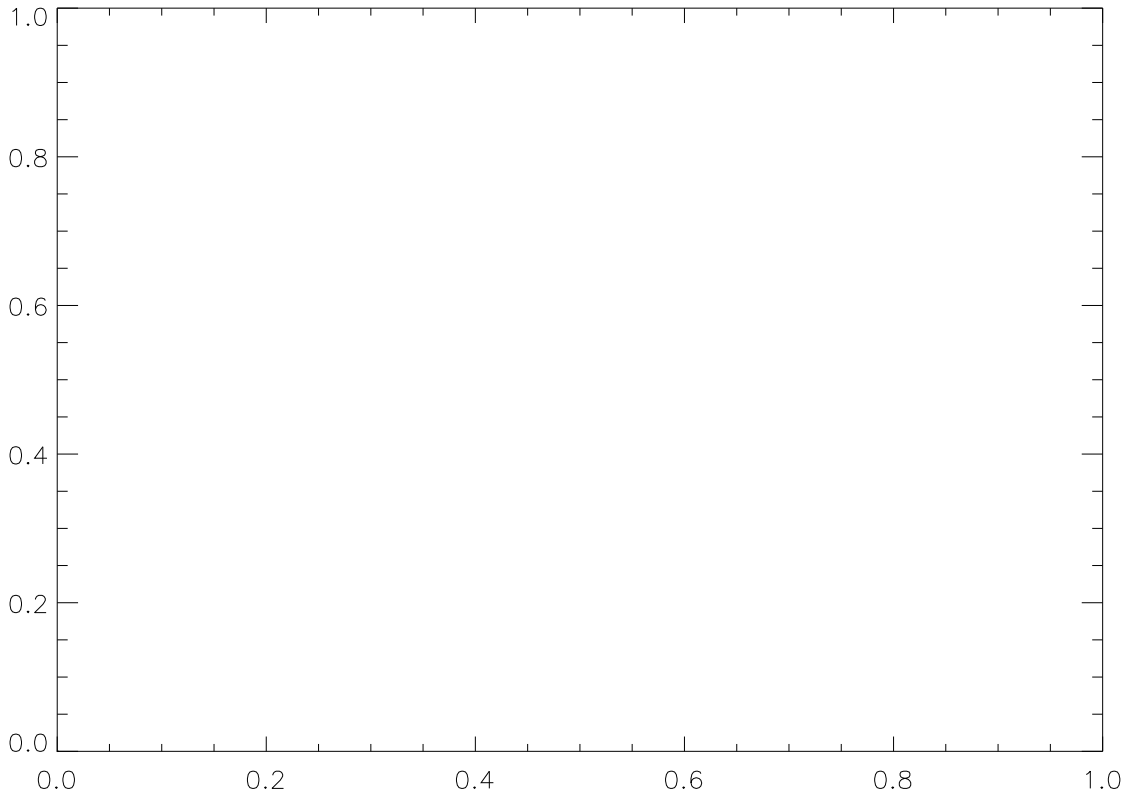

Figure 5.4: Schematic illustration of the linear vortex alignment mechanism. A PV column bound by rigid lids at $z = 0$ and H is tilted from west to east with height. For small tilts this configuration is decomposed into an azimuthal-mean barotropic vortex (with tangential wind and PV, $\overline{v}$ and $\overline{q}$, respectively) and an azimuthal wavenumber one asymmetry with vertical structure of the first internal baroclinic mode. The tendency in perturbation PV at upper(lower) levels is attributed to azimuthal advection of the perturbation PV by $\overline{v}$ and radial advection of $\overline{q}$ by the perturbation wind associated with the upper(lower)-level PV anomaly and, through vertical penetration (denoted by the coupling coefficient κ), the lower(upper)-level PV anomaly.

radial propagation speed of the wave packets decreases in time as the waves are sheared to finer and finer radial scales. The quasi-discrete wavenumber one PV asymmetry persists over the $5\tau_e$ period with only a 10-20% decrease in amplitude. Consistent with a quasi-discrete vortex Rossby wave it propagates cyclonically around the vortex at a speed less than the local mean tangential wind. Figure 5.5 also shows the PV evolution for the same initial vortex using the QG3D model. The azimuthal propagation and structure of the wavenumber one PV asymmetry are virtually identical in the two nonlinear simulations. Both nonlinear simulations also show less sheared vortex Rossby wave propagation than the linear simulation.

Figure 5.7 shows the domain-integrated perturbation energy (kinetic and available potential) contained in wavenumber one. The linear solution indicates only a 30% decrease in energy over the $5\tau_e$ period. Most of the initial asymmetry energy is trapped in the quasi-discrete vortex Rossby wave which slowly loses its energy through the outward propagating sheared vortex Rossby waves. Due to wave-wave interactions the nonlinear solution shows a more modest decrease in wavenumber one energy of 5-10%. The use of the pseudo-mode to represent the initial horizontal structure of wavenumber one PV is fortuitous since it projects strongly onto the quasi-discrete vortex Rossby wave. A general initial condition will tend to project more onto the sheared vortex Rossby waves, obscuring the quasi-discrete structure at early times. As demonstrated by Smith and Montgomery (1995, and references therein) and later extended by MK to account for the Rossby wave effects, the energy contained in the sheared Rossby waves will ultimately diminish with time. Thus, the quasi-discrete wave structure will eventually emerge. It is interesting to note that higher wavenumbers show a markedly different behavior than wavenumber one with the energy falling to near zero after only a 1-2τ_e period. We conclude that wavenumber one is unique within the parameter regime under consideration. The co-rotation resulting from the long-lived propagation of the wavenumber one asymmetry observed in the nonlinear simulations is reproducible using linear dynamics alone, validating the conceptual model illustrated in Fig. 5.4.

To determine the range of α for which linear vortex Rossby wave theory captures the essence of the alignment process we compare the intercentroid distance, d_i, between upper-

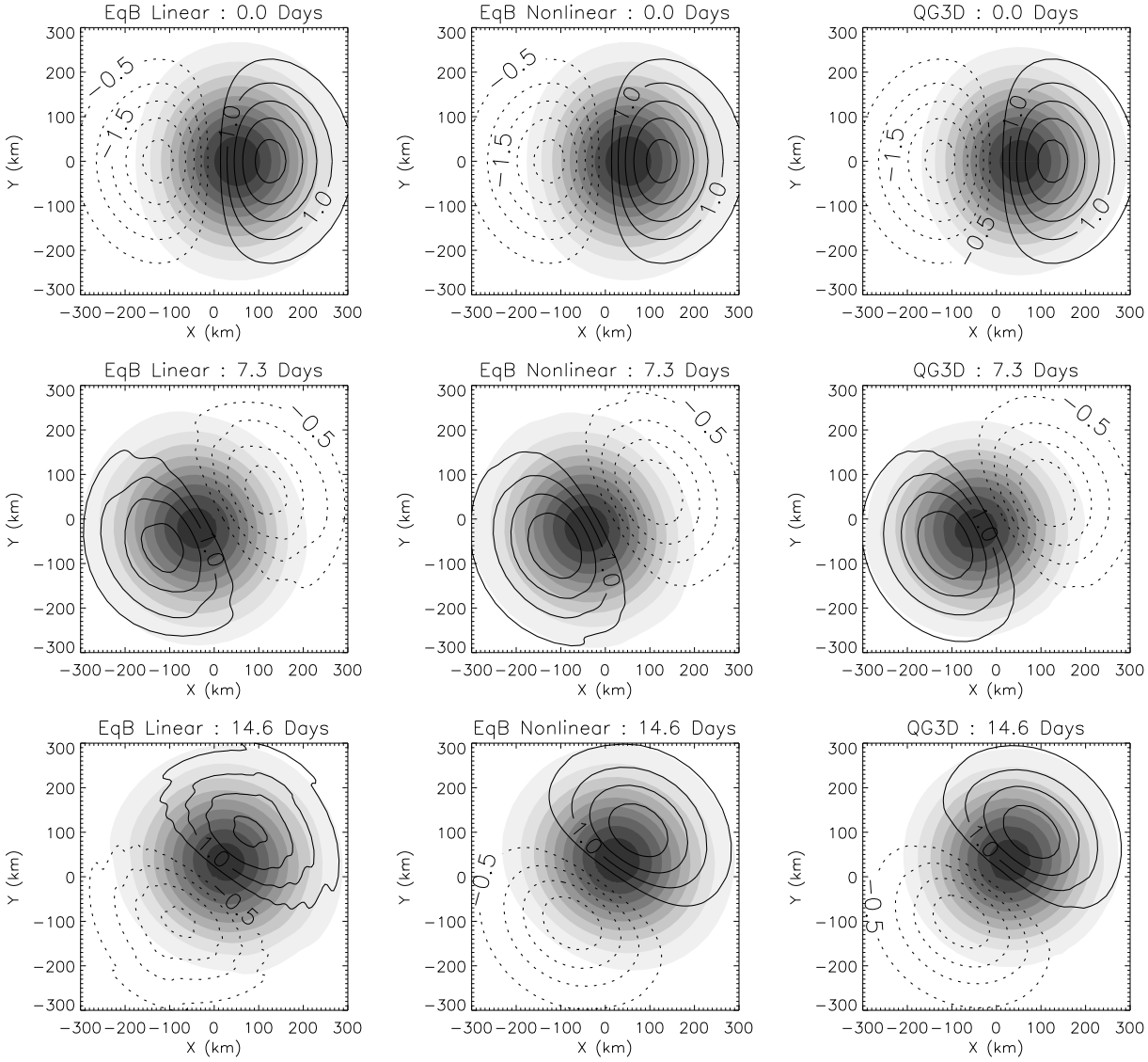

Figure 5.5: Evolution of total vortex PV (shaded) and wavenumber one component of PV (contour interval 0.5×10^{-5} s^{-1} with negative values dashed) at $z = 0$ over a $5\tau_e$ period for the benchmark run (see Fig. 5.2). From left to right are shown the results from the linear EQB, non-linear EQB, and QG3D models, respectively. Aside from the PV correction in the QG3D model, the initial conditions are identical.

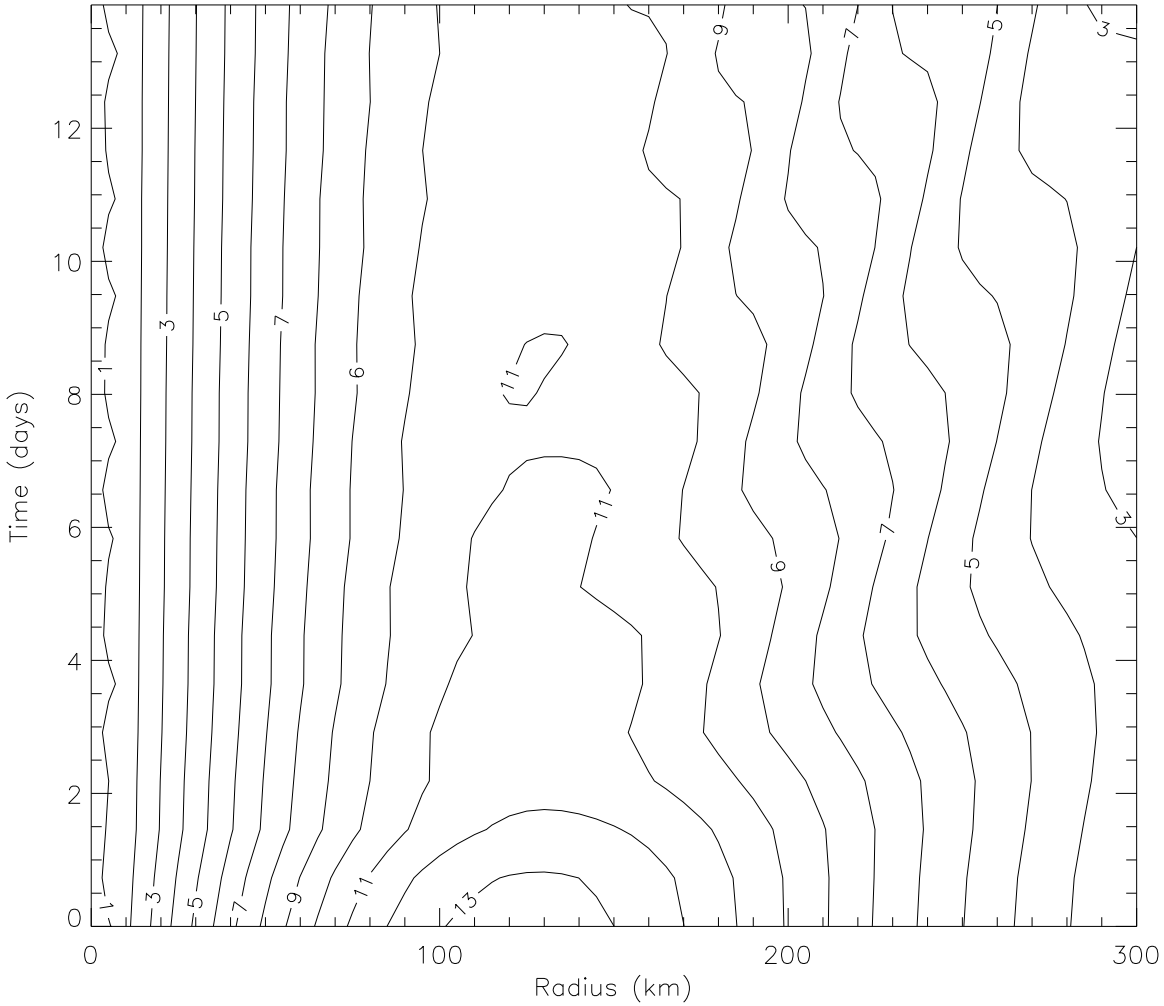

Figure 5.6: Radius-time plot of the wavenumber one PV amplitude at $z = 0$ over a $5\tau_e$ period for the benchmark run. The dashed lines denote the crest of the wave packets as they propagate radially outward in time. The quasi-discrete vortex Rossby wave persists near 130 km radius. Contour interval is 1.0×10^{-6} s^{-1}.

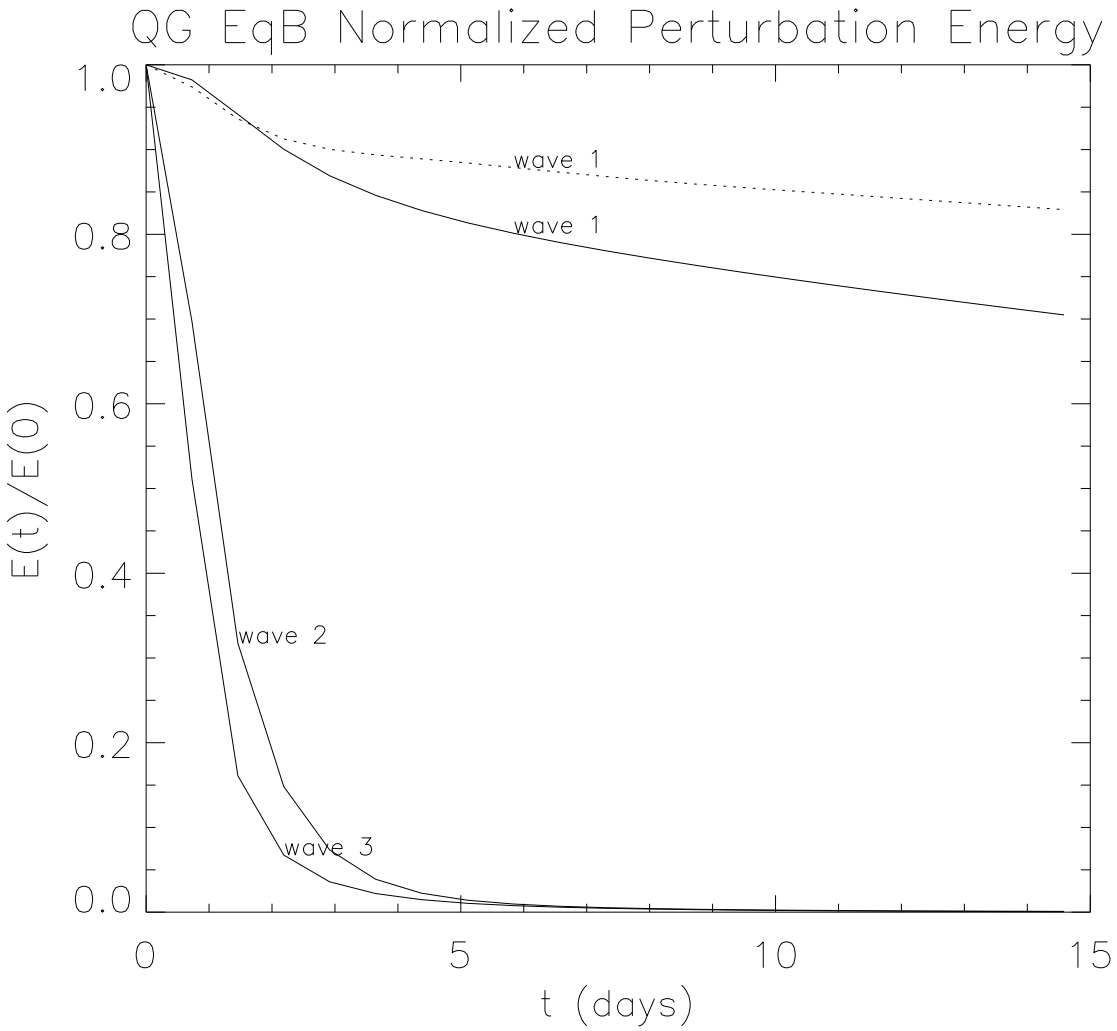

Figure 5.7: QG equivalent barotropic volume-integrated energy contained in wavenumber one from the nonlinear (dashed) and linear (solid) EQB benchmark runs as a function of time. Also shown is the linear energy evolution for initial conditions with the pseudo-mode radial structure, but azimuthal structure of wavenumbers two and three. The energy is normalized by its initial value in all cases.

and lower-level PV centroids predicted by the linear and nonlinear EQB models. Figure 5.8a shows the trajectories of the upper- and lower-level centroids for the benchmark case. In both simulations the centroid makes slightly more than one orbit at a radius of approximately 60 km during the $5\tau_e$ period. The discrepancy between the linear and nonlinear predictions of d_i increases to about 5 km during the period, as shown in Fig. 5.8b. The nonlinear prediction shows a reduced rate of alignment, although we would argue that the linear dynamics is still capturing the essence of the co-rotation and slow alignment of upper- and lower-level PV anomalies.

For an even smaller tilt amplitude of $\alpha = 0.1$, little discrepancy between linear and nonlinear simulations is found. In this case $R_\beta \approx 0.08$ which confirms the negligible role played by nonlinear advection. The quasi-discrete vortex Rossby wave has essentially the same structure and propagation speed in both simulations (see Fig. 5.9).

To simulate a vortex with more exaggerated tilt the EQB model is initialized with the mean vortex given by (5.1), but displaced 100 km to the east of the polar coordinate system origin at $z = 0$, and tilted linearly with height to the west. An azimuthal and vertical wavenumber decomposition of this initial condition shows that only four modes need be included in the EQB initialization: $(m, n) = (0, 0),\ (1, 1),\ (2, 0)$, and $(0, 2)$. In keeping with the assumption of a barotropic mean vortex, the $n = 0$ component of the vortex at $z = 0$ is used at all levels. For simplicity, the $n = 1$ and $n = 2$ components of the vortex at $z = 0$ are used to construct (1,1) and (0,2), respectively. For initial upper- and lower-level PV centers separated by 200 km, $\alpha \approx 0.5$ and $R_\beta \approx 0.5$.

Figure 5.10 shows the evolution of total and wavenumber one PV from the linear and nonlinear EQB models. Also shown is the PV at the lowest level of the QG3D model for a vortex tilted linearly with height (without the above approximations). The two nonlinear simulations basically agree, confirming the utility of the truncated equivalent barotropic approach even for relatively large vortex tilts. Even more remarkable is the similarity between linear and nonlinear simulations. Although there is considerably more radial vortex Rossby wave dispersion in the linear simulation (see Fig. 5.11), the rotation frequencies of the low-level vortex about the mid-level centroid are virtually the same (see

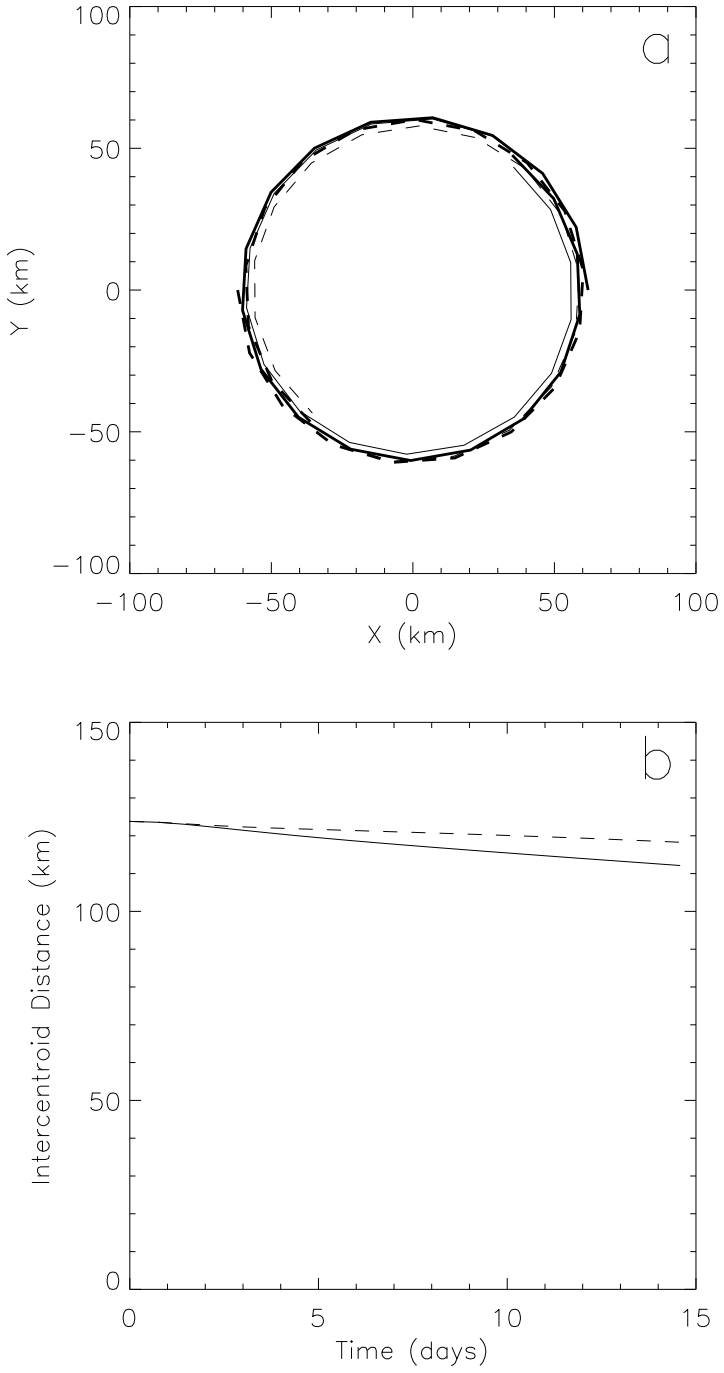

Figure 5.8: Evolution of the EQB PV intercentroid separation between $z = 0$ and H over $5\tau_e$ for the benchmark run. (a) Trajectory of the PV centroid at upper (solid) and lower (dashed) levels. The heavy lines show the nonlinear evolution, while the fine lines show the linear evolution. (b) Timeseries of intercentroid separation distance from the linear (solid) and nonlinear (dashed) models.

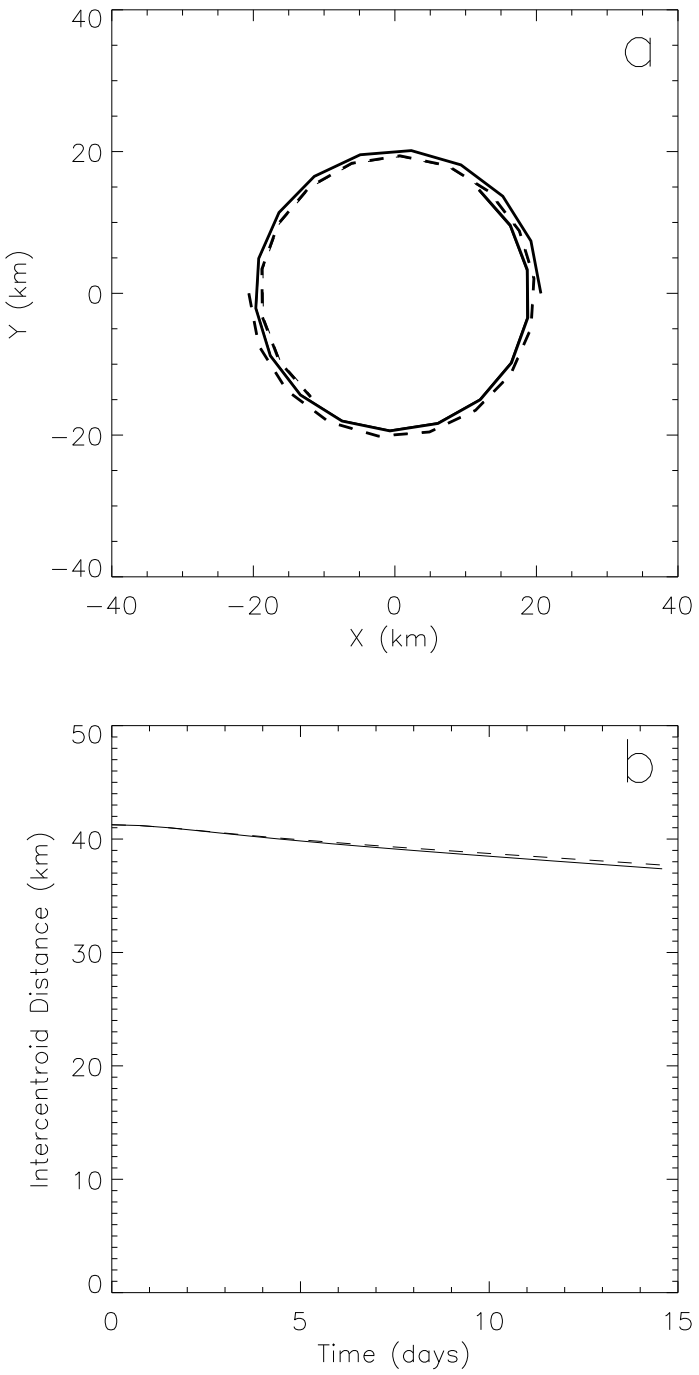

Figure 5.9: As in Fig. 5.8 but for $\alpha = 0.1$.

also Fig. 5.12). The details of the d_i evolution over $5\tau_e$ and departure from that shown in Figs. 5.8 and 5.9 can be attributed to the greater projection of the initial PV asymmetry onto sheared vortex Rossby waves. But overall the linear dynamics still captures the essence of the tilted vortex evolution. Thus, while nonlinear effects increase in importance with increasing R_β and modify the vortex structure (i.e., counteract the sheared vortex Rossby wave dispersion), the underlying quasi-discrete vortex Rossby wave persists in dominating the solution.

These results suggest a new interpretation for the co-rotation of vertically-separated, overlapping vortices for internal Rossby deformation radii greater than the horizontal scale of the vortex. Polvani (1991) explained the presence of co-rotation geometrically as a consequence of the initial vortex configuration being near a geostrophic PV equilibrium (i.e., a stable V-state). Here the co-rotation of *continuously-distributed* vortices is attributed to the cyclonic propagation of a quasi-discrete wavenumber one vortex Rossby wave. Analytical solutions to the linear QG equivalent barotropic problem are currently unavailable for continuous PV distributions, but may present themselves for carefully constructed initial conditions. Such a solution would allow one, for example, to predict the linear co-rotation frequency. For now we will continue to explore this linear interpretation of the alignment process, considering the effect of varying γ_1.

5.1.3 Dependence on Internal Deformation Radius

Varying γ_1 can be viewed in terms of changing the depth of the vortex, the static stability, or the planetary vorticity. The dependence of vortex alignment on vortex depth has been explored in recent studies motivated by observations from QG turbulence simulations (McWilliams 1989; Viera 1994; Dritschel and Juarez 1996). The tilted vorticity configurations in these studies attain equilibrium at certain vertical scales. Moist convection will increase γ_1 by reducing the static stability (Emanuel et al. 1987; Montgomery and Farrell 1992). As further discussed in Section 5.2, for more rapidly swirling flows, f in the expression for γ_1 is replaced by the geometrical mean of the modified Coriolis parameter and absolute vorticity associated with the basic state circular vortex (Shapiro

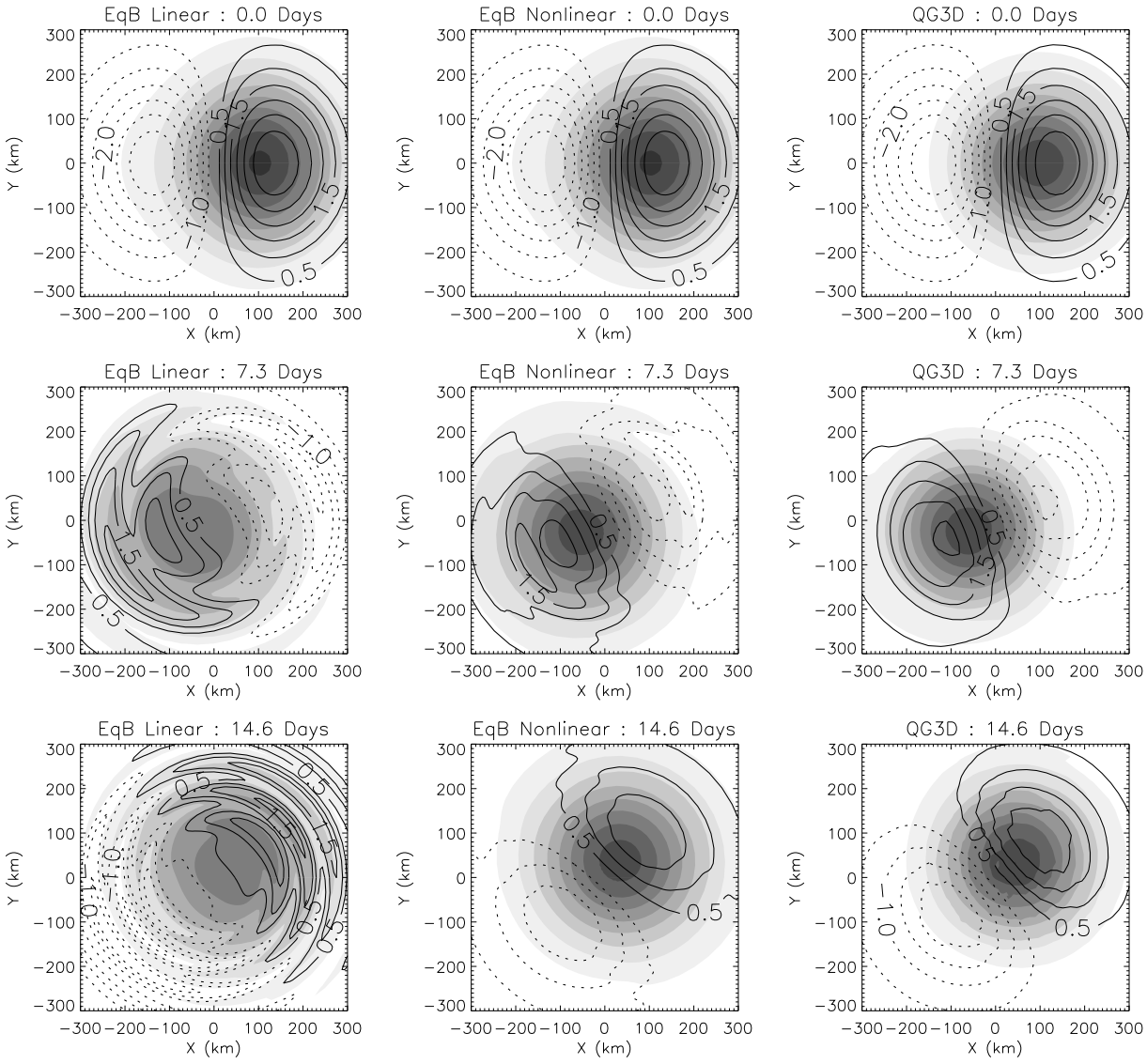

Figure 5.10: As in Fig. 5.5 but for $\alpha \approx 0.5$. See text for details on the initial conditions.

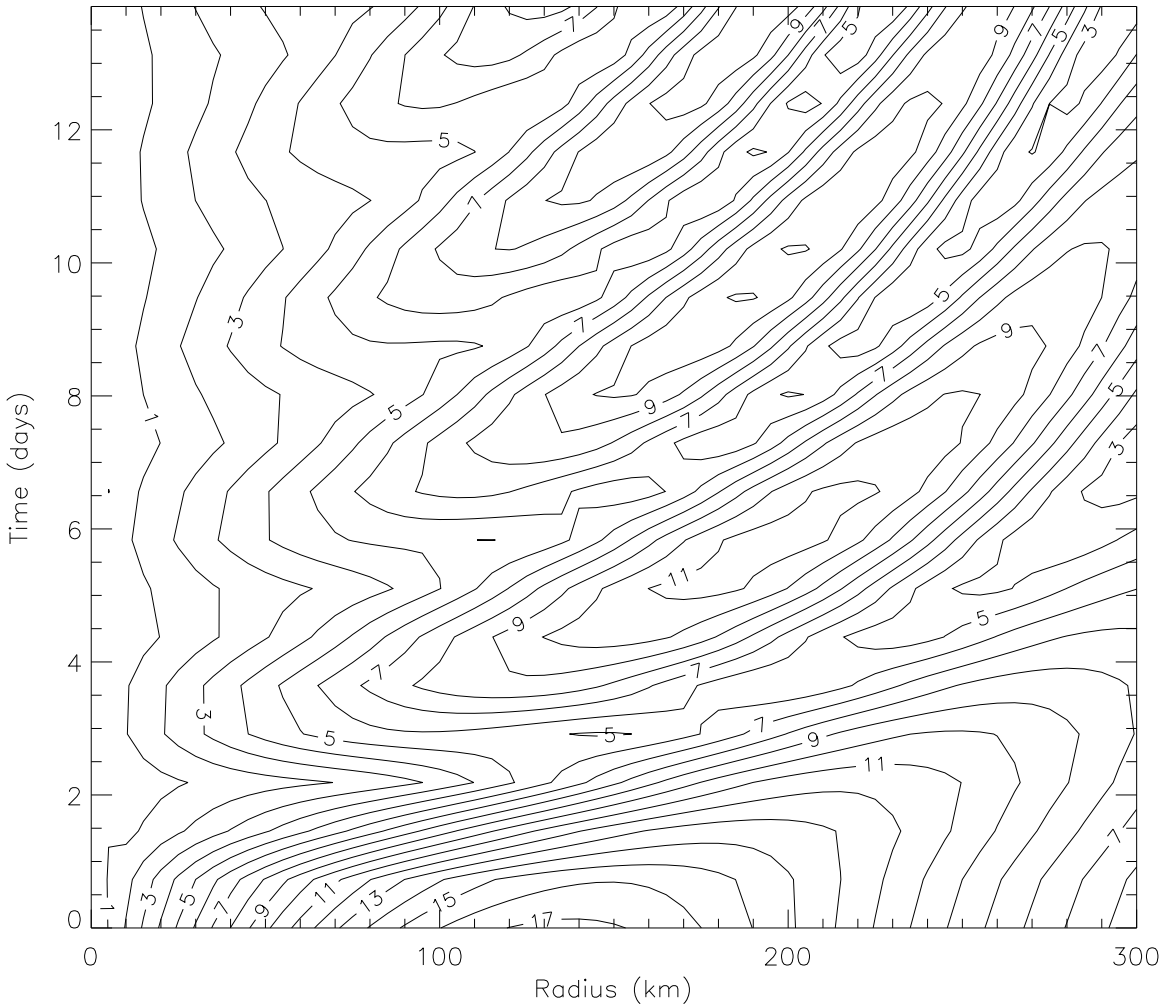

Figure 5.11: As in Fig. 5.6 but for $\alpha \approx 0.5$. The radially propagating sheared vortex Rossby waves mask the quasi-discrete wavenumber one structure at early times.

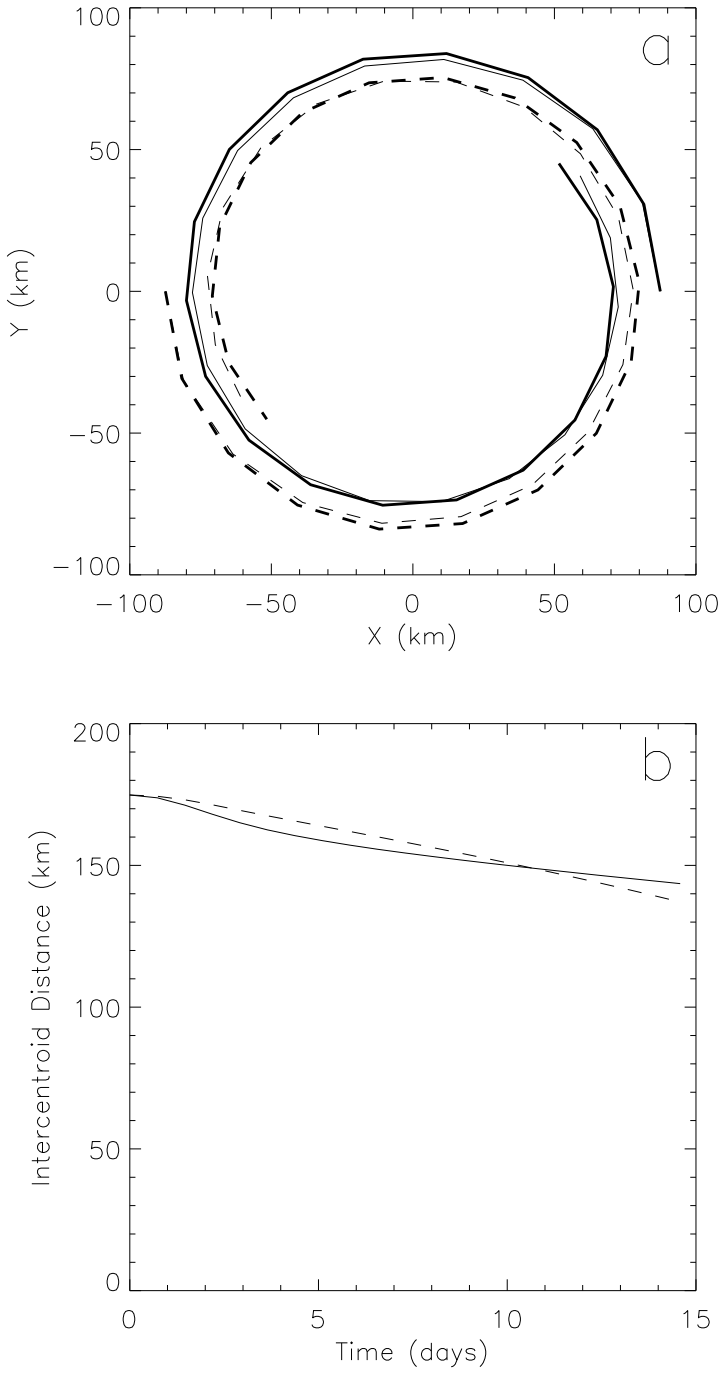

Figure 5.12: As in Fig. 5.8 but for $\alpha \approx 0.5$.

and Montgomery 1993). We may anticipate the vortex evolution for more rapidly swirling flows by increasing f in the QG formulation.

The dependence of vertical alignment on internal deformation radius and horizontal vortex scale is known from QG contour dynamics (CD) model simulations (Polvani 1991; Dritschel and Juarez 1996). For horizontal vortex scales greater than the internal deformation radius the vertically-tilted vortex tends towards alignment, while for smaller vortex scales alignment is inhibited and co-rotation is observed. The linear interpretation of the alignment mechanism can help explain why this is so.

In the benchmark simulation (see Fig. 5.2) we found that alignment was inhibited and the vortex precessed about its mid-level centroid with a small increase in the discrepancy between linear and nonlinear simulations with time out to several τ_e. Figure 5.13 shows the evolution of the same initial vortex, but for larger $\gamma_1 = 20.0 \times 10^{-6}$ m^{-1}. The QG3D (not shown) and nonlinear EQB models show nearly identical results, so we will focus on the vortex evolutions simulated by the EQB linear and nonlinear models. In both simulations alignment of the initial vortex and attendant filamentation of PV are observed, as found in previous studies (Polvani 1991; Viera 1995; Dritschel and Juarez 1996). The linear results confirm that the filamentation observed in the nonlinear simulation near the core of the stable vortex monopole is primarily a consequence of linear vortex Rossby wave dynamics and not 'wave breaking'. In both simulations the vortex undergoes a *complete* alignment within $5\tau_e$ at virtually identical rates (see Fig. 5.15).

The increased agreement between linear and nonlinear simulations for this larger value of γ_1 is understood by examining the γ-dependence of R_β. Figure 5.16 shows the initial R_β in the vicinity of the maximum perturbation PV for various α as a function of γ_1. In Section 5.1.2 it was shown that for a given value of the internal deformation radius, R_β decreases with decreased perturbation amplitude (recall $R_\beta \sim V'$) leading to increased agreement between linear and nonlinear simulations. The naive scaling (5.6) would not predict a dependence on γ_1, contrary to Fig. 5.16 which clearly shows R_β decreasing with increasing values. Farge and Sadourny (1989) explained the dependence of their QG shallow water turbulence simulations on deformation radius from the perspective of energy

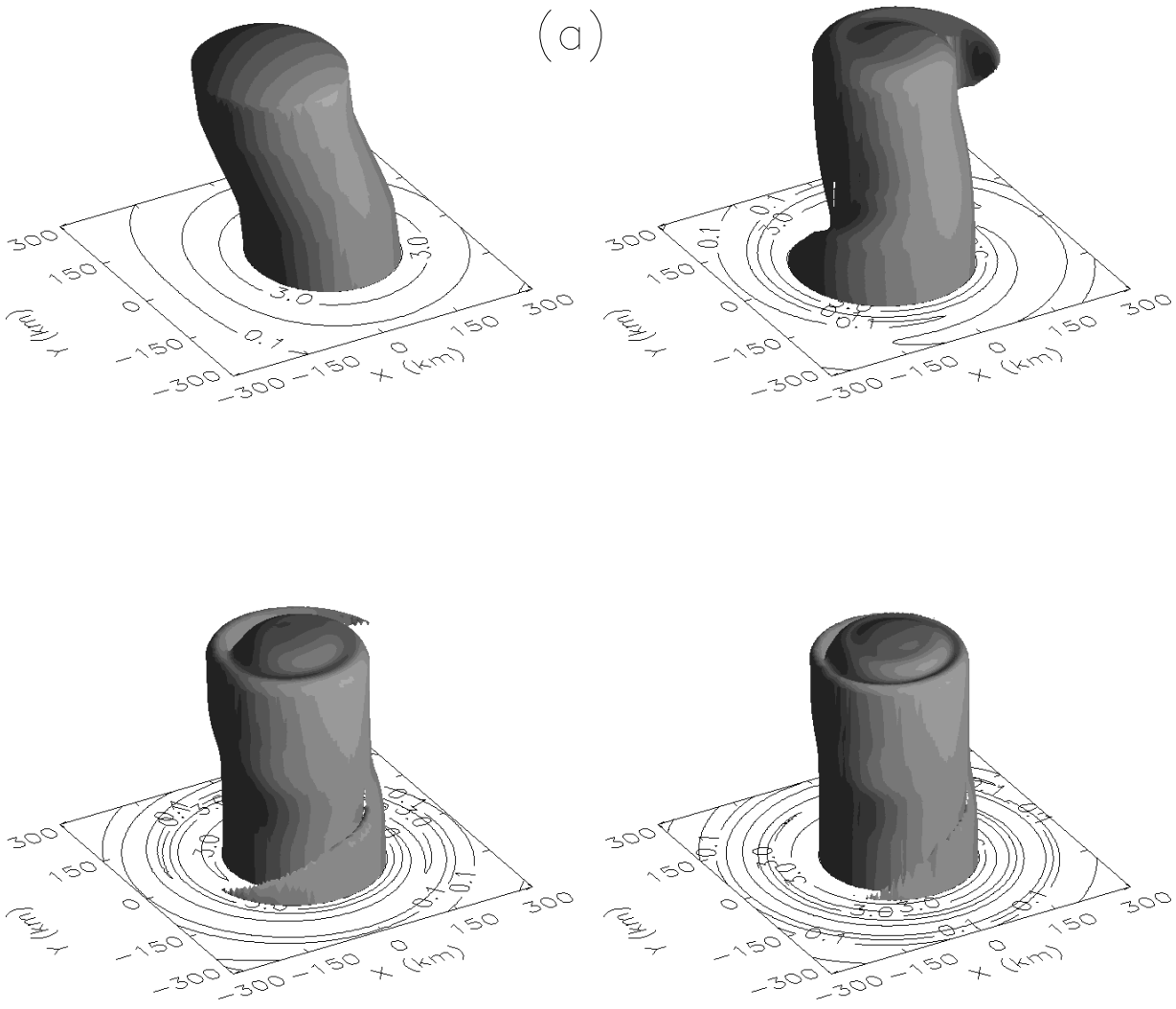

Figure 5.13: Evolution of vortex PV (from left to right) at t = 0, $1.5\tau_e$, $2.5\tau_e$, and $4\tau_e$ for $\alpha = 0.3$ and $\gamma_1 = 20.0 \times 10^{-6}$ m^{-1}. Only the inner 600 km x 600 km is shown to emphasize the vortex tilt. Results from (a) the nonlinear EQB model with PV isosurface 5.0×10^{-5} s^{-1} and (b) the linear EQB model with PV isosurface 5.0×10^{-5} s^{-1} are shown. The contours shown are $(0.1, 1, 3, 5) \times 10^{-5}$ s^{-1}.

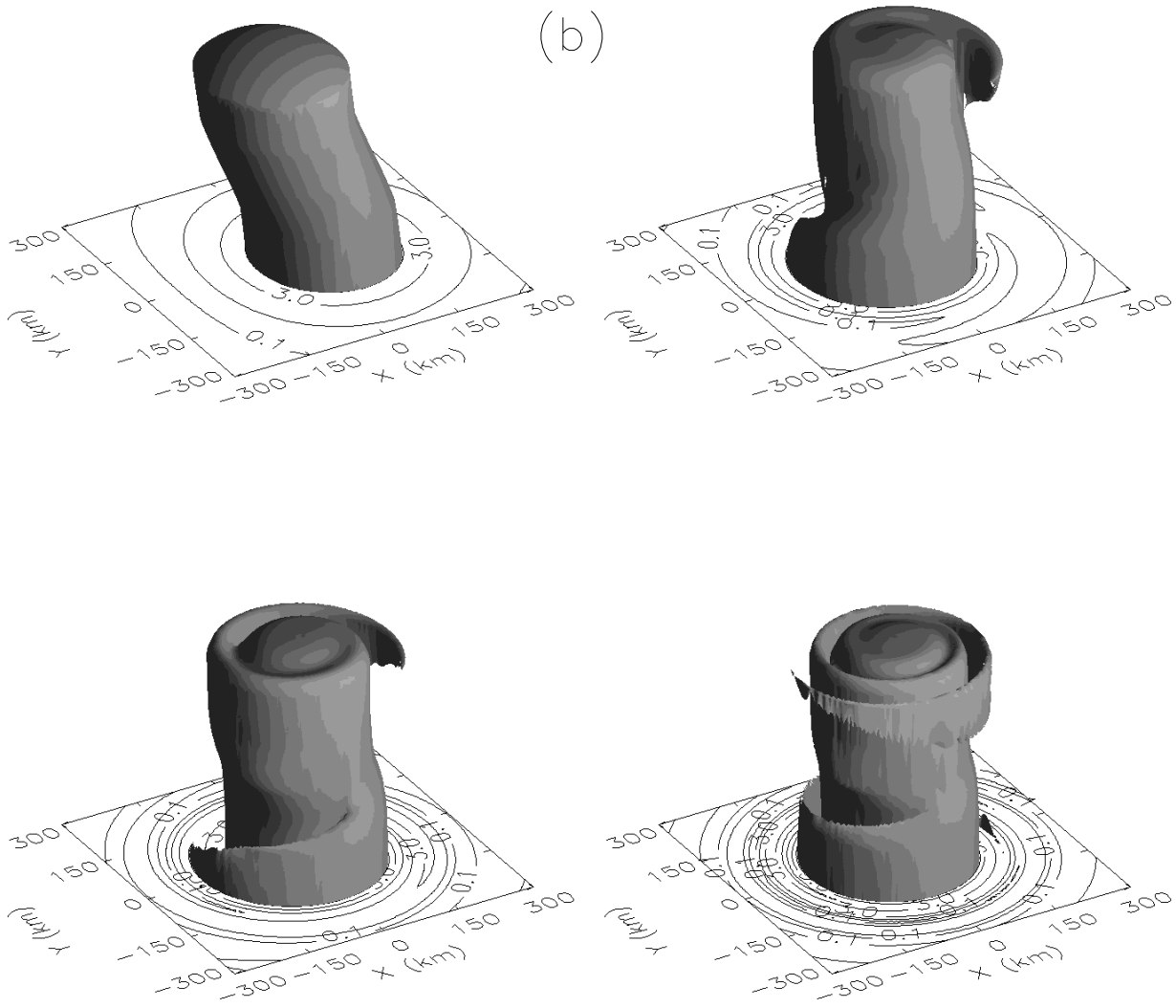

Figure 5.14: see Fig. 5.13.

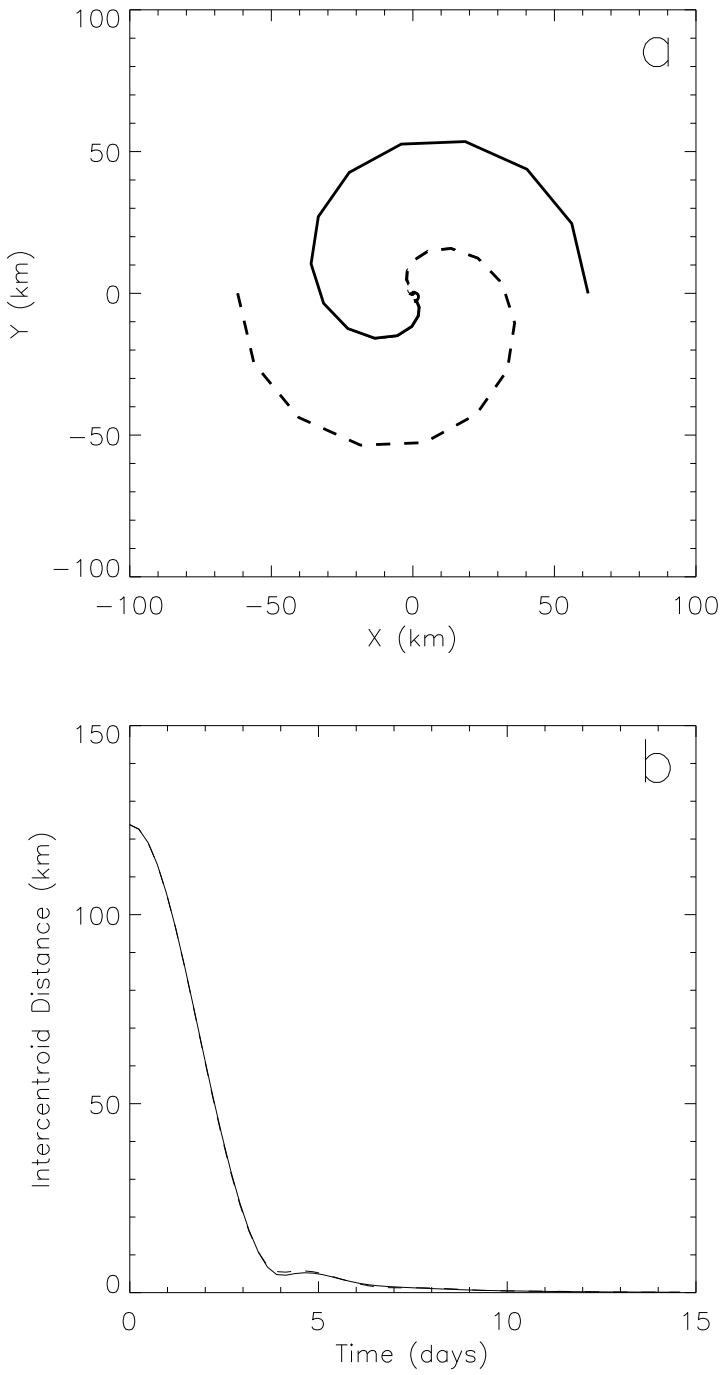

Figure 5.15: As in Fig. 5.5 but for $\gamma_1 = 20.0 \times 10^{-6}$ m^{-1}.

and enstrophy spectra. For large rotation rates (i.e., large γ) they demonstrated that the cascade of potential enstrophy to smaller scales is inhibited. This behavior can also be explained geometrically by examining the dependence of the QG (baroclinic) perturbation PV inversion on γ_1. For small γ_1, the Green's function decays slowly with radius and PV over a broad area is incorporated into the inversion for streamfunction at a point. In this case the streamfunction field is unable to replicate strong curvature of the PV field. For much larger γ_1, the Green's function decays rapidly with radius and the streamfunction field is better able to reproduce the curvature of the PV field over the entire domain, leading to near-parallel PV and streamline contours (see Fig. 5.17), i.e.,

$$J(\psi', q') \to 0 \text{ as } \gamma_1 \to \infty. \tag{5.7}$$

Thus for $\gamma_1 \to \infty$, R_β tends to zero and the linear and nonlinear simulations converge. An additional consequence of this dependence of R_β on γ_1 is that linear vortex Rossby wave dynamics will accurately capture the alignment process for a wider range of amplitudes the larger γ_1 is. Although our focus here is on small to moderate tilts from the vertical, even vortices for which $d_i/L \sim 2$ (i.e., the RMW's of the upper and lower vortices just overlap) the alignment process should still fall within the linear regime as long as γ_1 is large enough.

The complete picture of the dependence of vortex alignment on γ_1 for small initial tilts ($\alpha = 0.1$) is shown in Fig. 5.18. The intercentroid distance after $5\tau_e$ for both linear and nonlinear simulations is plotted as a function of γ_1. As expected, no discernible difference between the simulations is observed. After $10\tau_e$ the curve is essentially the same, except the transition region between small and large γ_1 is steeper (not shown). Three regions are clearly identifiable in the γ_1 phase space.

For $\gamma_1 \geq 10.0 \times 10^{-6}$ m^{-1} complete vertical alignment takes place. The corresponding threshold internal deformation radius is 100 km which is smaller than the scale of the current vortex. The presence of vertical alignment at small α (or equivalently small initial d_i) should be contrasted with the two-layer CD results of Polvani (1991). There, co-rotation was observed for all γ_1 in this range. As discussed in Appendix B, this is a

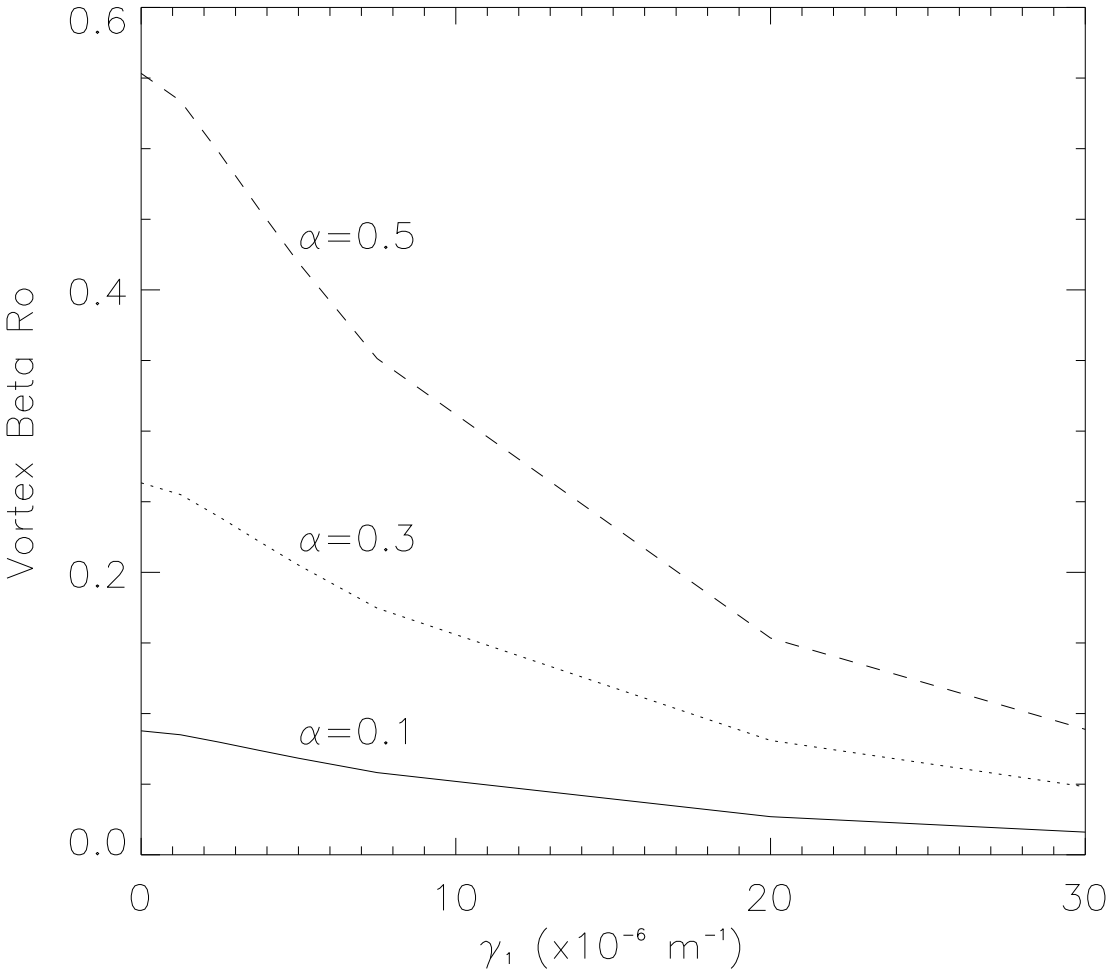

Figure 5.16: Dependence of vortex beta Rossby number at $z = 0$ on tilt (α) and γ_1. For consistency only $(m, n) = (1, 1)$ is used to define the perturbation. The simulation for $\alpha \approx 0.5$ does contain a small barotropic wavenumber two component which will elevate R_β slightly for all γ_1.

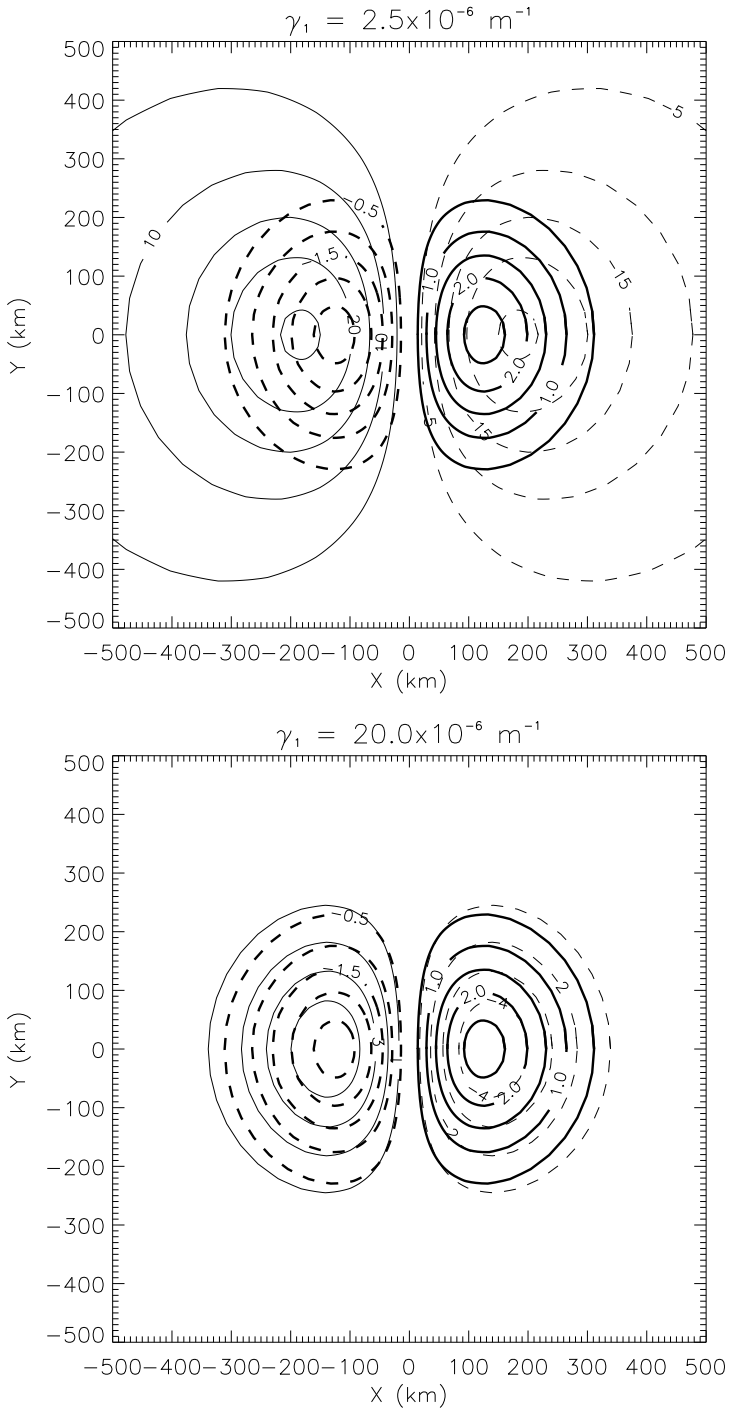

Figure 5.17: Comparison of the initial perturbation PV (heavy) and streamfunction (light) for the benchmark run. Negative values are dashed. (a) $\gamma_1 = 2.5 \times 10^{-6}$ m^{-1} (b) $\gamma_1 = 20.0 \times 10^{-6}$ m^{-1}. The perturbation PV and streamfunction isolines become more parallel with increasing γ_1. Note also that the perturbation streamfunction amplitude decreases with increasing γ_1. PV contour interval is 0.5×10^{-5} s^{-1}. Streamfunction contour interval is 5×10^4 m^{2}s^{-1} in (a) and 1×10^4 m^{2}s^{-1} in (b).

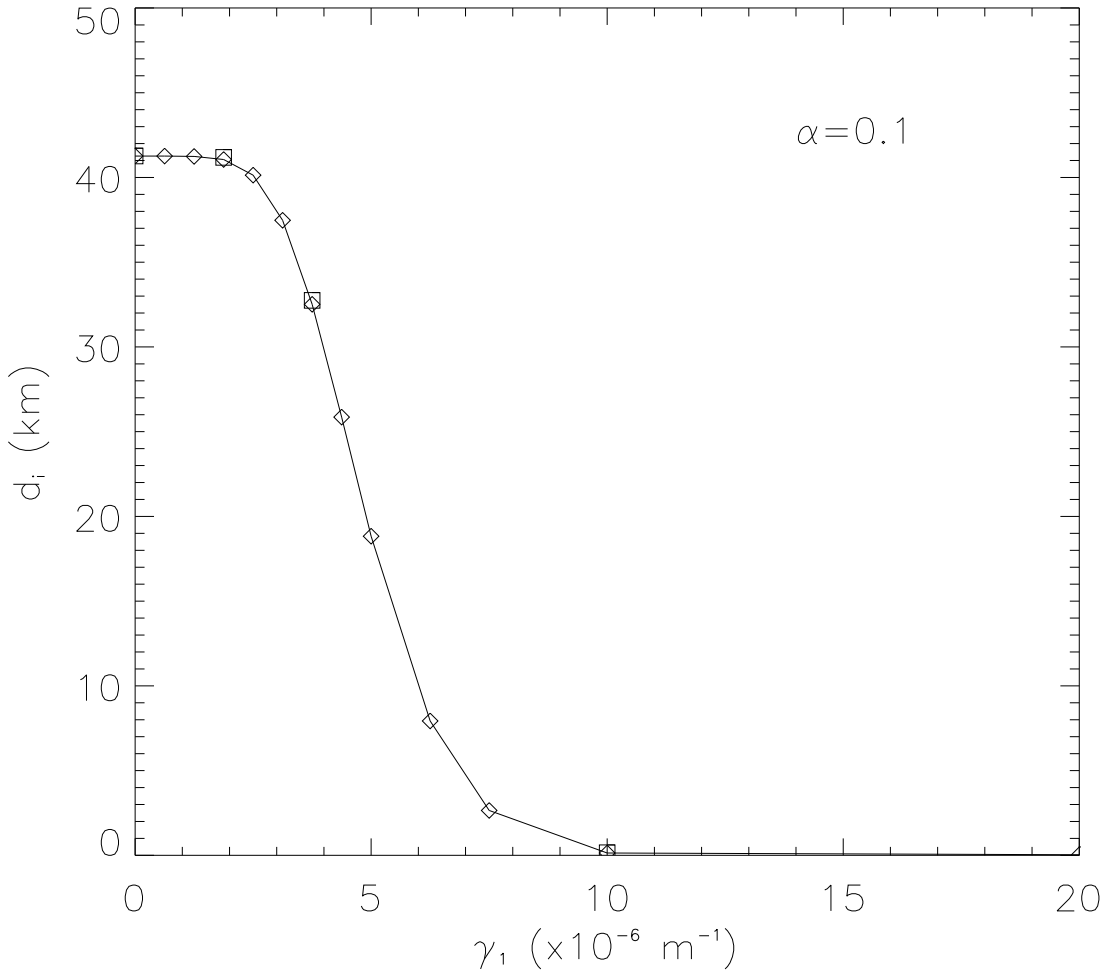

Figure 5.18: PV intercentroid separation between $z = 0$ and H after $5\tau_e$ as a function of γ_1 for $\alpha = 0.1$. The diamonds represent linear EQB simulations and the squares nonlinear EQB simulations.

consequence of using a single PV interface in the CD model. Utilizing the fact that the dynamics is fundamentally linear in this regime we can demonstrate why continuously-distributed vortex alignment *must* occur for all small initial d_i. The argument is essentially that when γ_1 is large, the effective "beta" term in the linearized PV equation can be neglected. The perturbation PV is then materially conserved following the local mean tangential winds, leading to simple spirals around the vortex and algebraic decay of the perturbation streamfunction in the limit of long times (see Appendix B for details). It is the sheared vortex Rossby waves which provide the irreversible deformation of the PV field needed for alignment.

The small-amplitude version of the benchmark run ($\gamma_1 = 3.14 \times 10^{-6}$ m^{-1}) falls within the transition zone in what we call the slowly aligning regime. The horizontal vortex scale lies close to the midpoint of this regime. It should be noted that the vortex does not actually align here according to our definition which requires $d_i = 0$. At longer times this transition region becomes narrower. Vortices at the large γ_1 end of the transition region enter into the alignment regime after a sufficiently long period of time, while little change in the structure of the curve at small γ_1 is ever observed during long-time integrations of the model.

The behavior of a tilted vortex for which $\gamma_1 \leq 2.5 \times 10^{-6}$ m^{-1} is unlike that found in the rest of the γ_1 phase space. Recall that the initial value of d_i is approximately 41 km. Thus, there is virtually no tendency for alignment (even after $10\tau_e$) in this regime. The vortex co-rotation is accounted for by the azimuthal propagation of the quasi-discrete vortex Rossby wave first noted in the benchmark simulation. In the limit of vanishing γ_1 the stationary pseudo-mode discussed by MK is recovered. As γ_1 is increased from the nondivergent limit, the long-time radial structure of azimuthal wavenumber one PV still closely resembles the pseudo-mode, but rotates at a non-zero frequency. If γ_1 becomes too large, the quasi-discrete feature ceases to exist, as discussed above. The origin and complete characteristics of this quasi-discrete vortex Rossby wave are discussed below.

Figure 5.19 shows a plot of the dependence of d_i on γ_1 as in Fig. 14, but for $\alpha = 0.3$. There is a more noticeable discrepancy between linear and nonlinear simulations for this

larger value of tilt, although the difference is small. The tilted vortex evolution is still captured by linear dynamics for all values of γ_1. While a decrease in discrepancy with increasing γ_1 in the alignment regime is expected based on vanishing R_β, the decrease in discrepancy with decreasing γ_1 in the strict non-alignment regime was not entirely anticipated. We believe that the continued good agreement between linear and nonlinear simulations in the latter regime is a consequence of the robustness of the quasi-discrete vortex Rossby wave.

5.1.4 Quasi-mode interpretation of three-dimensional vortex co-rotation

For an initially-tilted vortex satisfying $R_\beta < 1$ and small γ_1, the long-time inviscid solution is an azimuthal wavenumber one asymmetry with vertical structure of the first internal baroclinic mode propagating on the mean vortex. Although the rotation rate of the asymmetry is approximately constant (see Fig. 5.20) and the radial structure appears largely unaffected by differential rotation, the slow, almost imperceptible decay of the asymmetry for $\gamma_1 \leq 2.5 \times 10^{-6}$ m^{-1} suggests that it is not a neutral mode. In the nondivergent limit ($\gamma = 0$) wavenumber one does in fact become a smooth stationary mode, but it loses this modal characteristic once the Rossby deformation radius becomes finite. To understand this behavior of wavenumber one, consider stable solutions to Eq. (4.13) of the form

$$\tilde{\psi}_{mn}(r,t) = \tilde{\phi}_{mn}(r)e^{-i\omega_{mn}t}, \tag{5.8}$$

where ω_{mn} is a constant rotation frequency. Substitution into Eq. (4.13) yields

$$\frac{d^2\tilde{\phi}_{mn}}{dr^2} + \frac{1}{r}\frac{d\tilde{\phi}_{mn}}{dr} - \left(\frac{n^2}{r^2} + \gamma_m^2\right)\tilde{\phi}_{mn} - \frac{nd\overline{\zeta}/dr}{r(n\overline{\Omega} - \omega_{mn})}\tilde{\phi}_{mn} = 0. \tag{5.9}$$

This is an eigenvalue problem with eigenvectors, $\tilde{\phi}_{mn}$, and corresponding eigenfrequencies, ω_{mn}. In the nondivergent case an exact solution to (5.9) for $n = 1$ is $\tilde{\phi} = c\overline{v}$ with $\omega = 0$, where c is a constant (Michalke and Timme 1967). This is the aforementioned stationary pseudo-mode solution. For higher azimuthal wavenumber perturbations to a two-dimensional vortex with monotonically decreasing mean vorticity, there are no smooth modal solutions. Only singular continuous spectrum solutions exist, which decay to zero

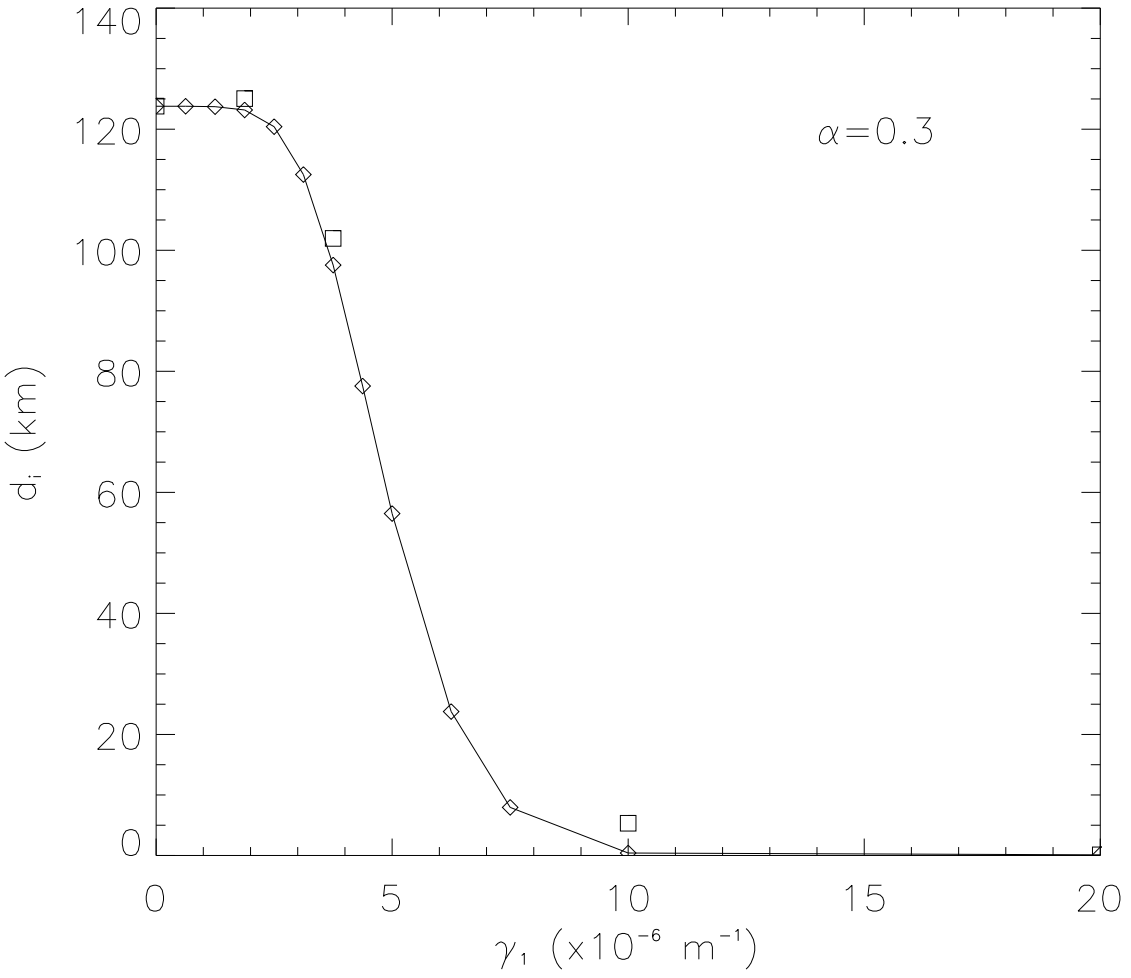

Figure 5.19: As in Fig. 5.18 but for $\alpha = 0.3$.

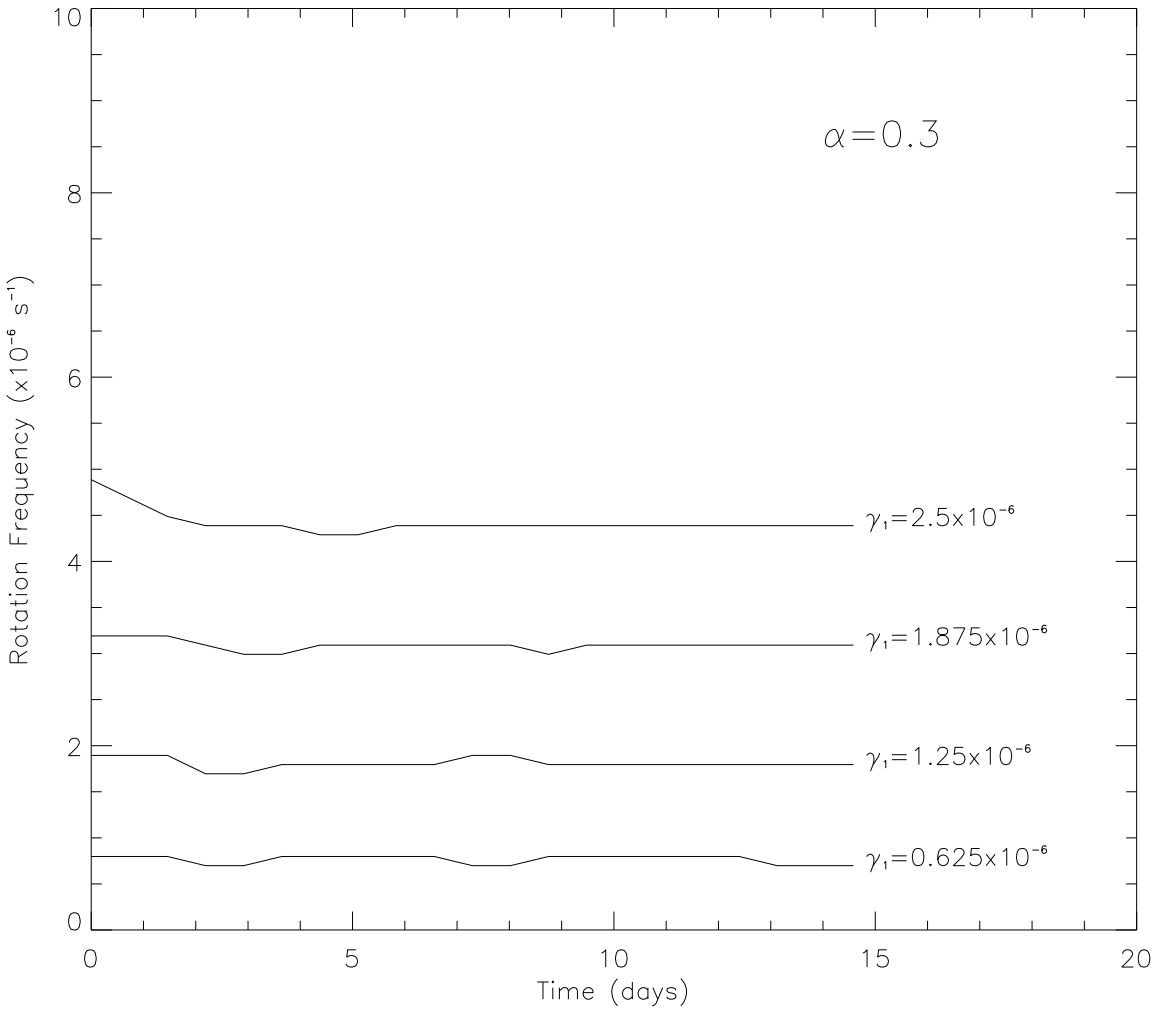

Figure 5.20: Instantaneous wavenumber one asymmetry rotation rate (ω) at $z = 0$ for small values of γ_1.

algebraically in the limit of long times (Sutyrin 1989; Carr and Williams 1989; Smith and Montgomery 1995; MK).

According to the QG numerical simulations at small γ_1, the rotation frequency of wavenumber one is small, but non-zero. The Doppler-shifted frequency, $\overline{\Omega} - \omega$, will therefore pass through zero at some large, but finite value of r. Since the simulated wavenumber one streamfunction is not observed to pass through zero and $d\overline{\zeta}/dr$ is non-zero for all r away from the origin and $r = \infty$, solutions must reside in the continuous spectrum of discrete singular modes. Why, then, do we observe a smooth, long-lasting wavenumber one asymmetry in the numerical simulations?

An answer is found through close examination of the $(m, n) = (1, 1)$ eigenmodes of (5.9) for the benchmark mean vortex (5.1) and $\gamma_1 = 1.25 \times 10^{-6}$ m^{-1}. The eigensolver following Gent and McWilliams (1986) and discussed in Appendix C is used, modified so as to permit finite deformation radius. Figure 5.21 shows the PV eigenvectors surrounding the eigenmode whose eigenfrequency is closest to the numerically-simulated wavenumber one rotation frequency. A grouping of eigenmodes with slightly different eigenfrequencies is found centered on the numerically observed rotation frequency with both a smooth structure and small-amplitude singular spike. The smooth structure is identical to that found in the numerical simulation at long times. The spikes occur at the radii where the Doppler-shifted frequency associated with each eigenmode equals zero and (5.9) becomes singular. There is in fact a continuum of these singular modes for frequencies between $\overline{\Omega}_{min}$ and $\overline{\Omega}_{max}$ (Case 1960).

If $d\overline{\zeta}/dr$ is zero outside some radius, r_a, there is a possibility of the vortex supporting a smooth, discrete mode since (5.9) is non-singular for $r > r_a$. Schecter et al. (1999) demonstrated this in the nondivergent context for two-dimensional vortex monopoles and $n = 2$ by taking a profile with $d\overline{\zeta}/dr$ everywhere nonzero and setting the gradient to zero outside some radius. A discrete mode was found in this case. Upon replacing the zero vorticity gradient region with a profile having small, but nonzero gradient, an eigenanalysis showed eigenstructures similar to the discrete mode for eigenfrequencies near the discrete mode value, but with small singular spikes, as in Fig. 5.21. The superposition

of these weakly singular continuum modes with nearly identical phase speeds is referred to as a quasi-mode because of the tendency for the singular modes to interact (linearly) and maintain a near-discrete structure in the presence of shear. Previous studies have investigated quasi-modes in the upper-tropospheric flow (Rivest and Farrell 1992) and in two-dimensional nondivergent vortex flows (Schecter et al. 1999). The singular modes that comprise the quasi-mode move with slightly different phase speeds, so the quasi-mode will slowly decay in time. Co-rotation of a geostrophic vortex with small initial tilt is therefore more accurately explained as the azimuthal propagation of a three-dimensional quasi-mode.

The longevity of the quasi-mode can be assessed by considering its spectral distribution. To illustrate this, an arbitrary linear PV perturbation is expanded in a weighted sum of the PV eigenmodes,

$$\tilde{q}(r,t) = \sum_k A_k e^{i\omega_k t} \tilde{\xi}_k(r), \tag{5.10}$$

where A_k is the expansion coefficient for the kth eigenmode, $\tilde{\xi}_k$, and ω_k is the corresponding eigenfrequency. The right-hand side of Eq. (5.10) is the discrete equivalent of a Fourier transform from the frequency domain to the time domain. For the PV perturbation given by Eq. (5.3), inversion of (5.10) at $t = 0$ yields the A_k. The expansion coefficients are plotted as a function of eigenfrequency in Fig. 5.22 for various values of γ_1. A discrete mode would be represented here as a δ-function in eigenfrequency space. The quasi-mode is clearly identified at small γ_1 as the narrow spike in the expansion coefficient spectrum. As γ_1 increases, the quasi-mode spectral peak broadens and takes on a more dipolar structure. The broader the peak, and therefore the broader the distribution of phase speeds of the individual modes that make up the quasi-mode, the faster a given initial wavenumber one asymmetry will find itself in the continuous spectrum of sheared vortex Rossby waves. In nondivergent analyses of two-dimensional vortex monopoles, Schecter et al. (1999) were able to relate the decay rate of the quasi-mode to the half-width of the spectral peak in the special case where only a single narrow peak exists. Since the quasi-mode closely approximates a discrete mode in this case, one can bring the eigenvector

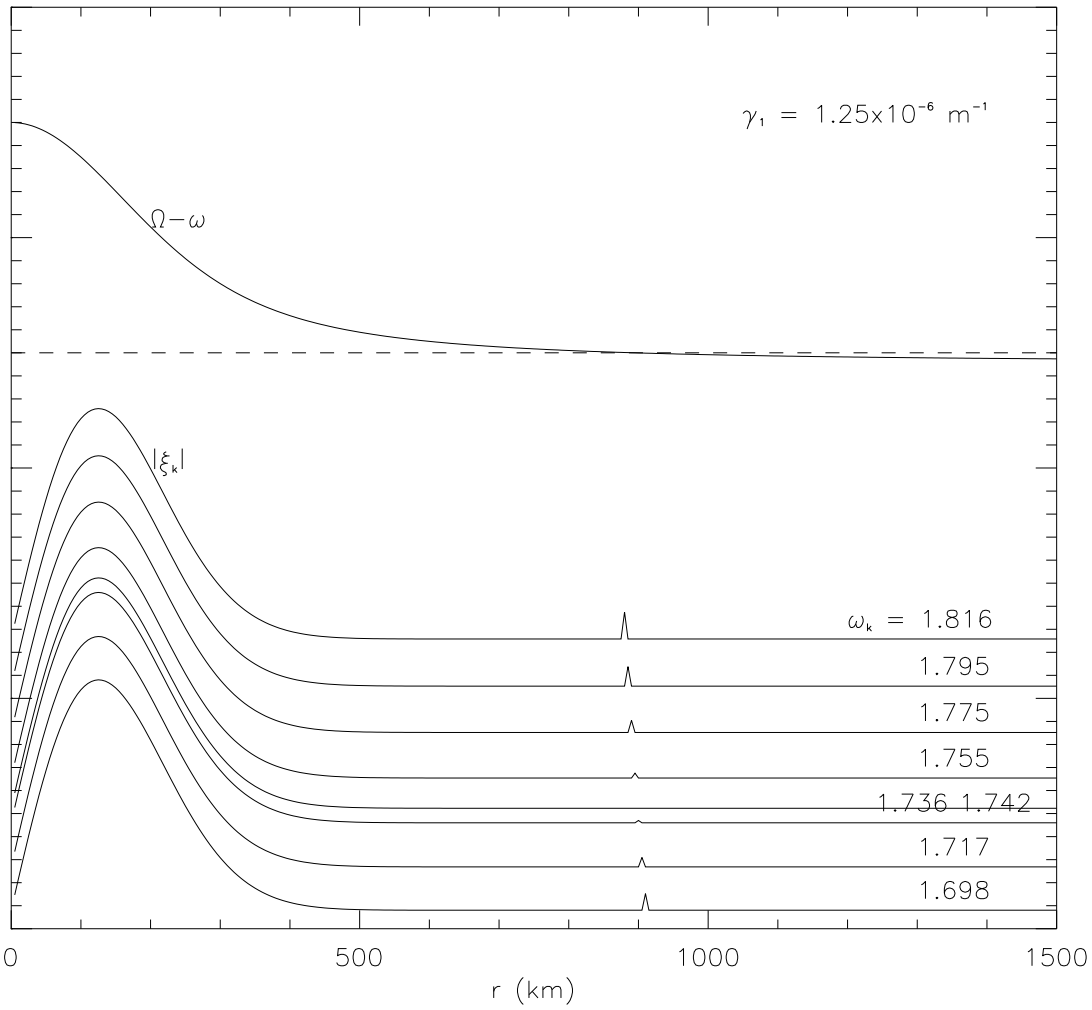

Figure 5.21: PV eigenvector solutions to Eq. 5.9 for the benchmark mean vortex and $(m, n) = (1, 1)$. Eigenfrequencies centered on the numerically-simulated rotation frequency are shown as well as $\overline{\Omega} - \omega$ for the central frequency. The units of ω are 10^{-6} s^{-1}.

outside the summation over frequency in Eq. (5.10). The time dependence of $\tilde{q}(r,t)$ is then obtained by computing the Fourier transform of $A(\omega)$. This was done by Schecter et al. (1999) assuming a Lorentzian form for $A(\omega)$ in the vicinity of the spectral speak. The presence of a dipole structure in the expansion coefficient spectrum found here prohibits an identification with a single decay rate.

Changing the width of the horizontal PV profile does not alter the basic results presented here. Figure 5.23 shows the PV intercentroid separation distance after $5\tau_e$ as a function of γ_1 for mean vortices smaller and larger than that used in our benchmark simulation (see Fig. 5.1). Recall that the vortex Burger number, $(L_R/L)^2$, is the parameter which appears in nondimensionalized invertibility relation and determines the partitioning between absolute and thermal PV. We observed in Section 5.1.3 that as the Burger number decreases from the nondivergent limit (i.e., γ_1 increases from zero) the vortex moves from the quasi-mode to alignment regime. For a value of γ_1 within the transition regime an increase(decrease) in L will decrease(increase) the vortex Burger number, bringing the vortex closer to(further from) the alignment regime. As Fig. 5.23 shows, the result is that the quasi-mode regime contracts with increasing vortex scale.

According to the arguments presented above, the existence and longevity of the quasi-mode depends on there being a region of near-zero mean vorticity gradient beyond some radius. As the scale of our Gaussian monopole increases, the radial region of small, but non-zero vorticity gradient decreases. Thus, there is a smaller range of frequencies for which Eq. (5.9) will support the weak singularity associated with the quasi-mode solutions. Precisely how this translates into the γ-dependence shown in Fig. 5.23 will depend on how vortex structure and γ_1 determine the quasi-mode frequency. This, we currently do not know, but hope to understand through ongoing work.

For a tilted vortex monopole with nonzero mean vorticity gradient at all radii (excluding the origin and $r = \infty$), alignment technically will *always* occur as $t \to \infty$, regardless of the nonzero value of γ_1. But for application to the atmosphere on physically-relevant timescales of a few τ_e, it is useful and insightful to make the distinction between the quasi-mode and the rest of the singular mode continuum, and therefore co-rotation and alignment.

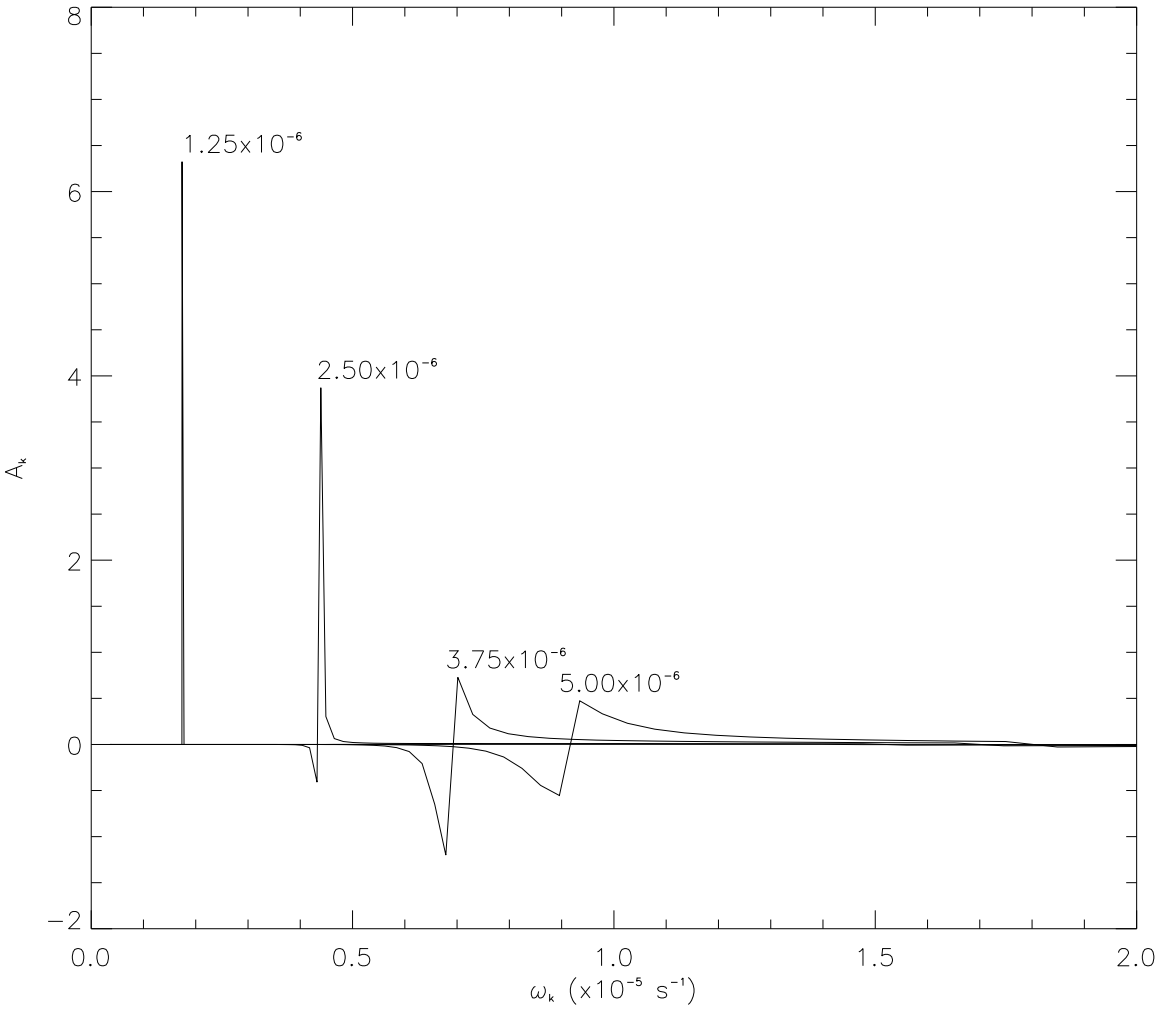

Figure 5.22: Expansion coefficient A_k as a function of eigenfrequency ω_k for values of γ_1 in the quasi-mode and transition regimes. The wave one asymmetry given by Eq. 5.3 and eigenvectors shown in Fig. 5.21 were used to obtain A_k.

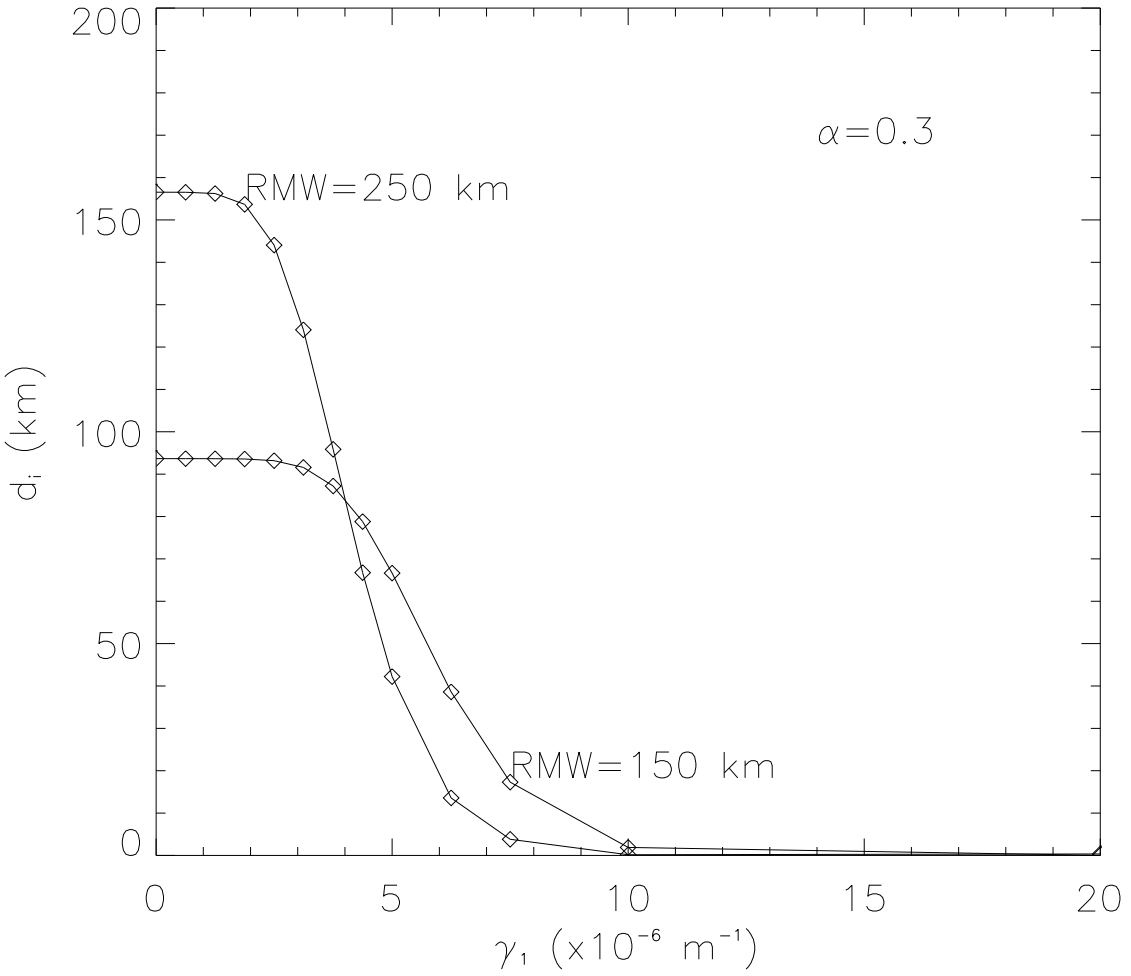

Figure 5.23: As in Fig. 5.19 but for mean vortices smaller and larger than the benchmark vortex.

5.2 Application to Tropical Cyclogenesis

5.2.1 Tilted Vortices

A small fraction of all tropical disturbances develop into TCs. For example, on average 100 tropical disturbances are observed in the Atlantic during hurricane season yet only about 10–15 achieve tropical storm status (Frank 1975). In addition to the existence of low- to mid-level cyclonic vorticity, environmental factors like weak vertical shear and warm sea-surface temperatures are generally regarded as necessary conditions for development. The role of vertical shear in inhibiting TC genesis and development has been explored both in observational studies (Gray 1968; Zehr 1992) and in numerical and theoretical works (Jones 1995; DeMaria 1996; Bender 1997; Frank and Ritchie 1999). According to Zehr (1992) the 200–850 mb vertical shear threshold above which development is severely inhibited is 12.5–15 ms^{-1}.

Before considering the more complicated problem of a weak vortex forced by vertical shear it is necessary to understand the unforced problem. One can interpret the tilted vortex of Section 5.1 as having resulted from some external forcing like environmental vertical shear or horizontal strain associated with nearby vortices. Depending upon the horizontal scale of the vortex and γ_1, the vortex will either return to a vertically-aligned state through the sheared vortex Rossby wave mechanism or precess about its mid-level centroid due to the wavenumber one quasi-mode propagation. For tropical conditions $f = 5 \times 10^{-5}$ s^{-1}, $H = 15$ km, and $N = 10^{-2}$ s^{-1}, resulting in $\gamma_1 = 1.0 \times 10^{-6}$ m^{-1}. For the mean vortex depicted in Fig. 5.1, $\gamma_1 < L^{-1}$, well within the non-alignment regime shown in Figs. 5.18 and 5.19. In the non-aligned state the vortex is especially vulnerable to further external forcing.

Recently Dritschel and Juarez (1996), using a multi-layer QG CD model, found that a vortex column subjected to two-dimensional strain will become unstable and reduce its vertical scale if the ratio of vortex height to width is greater than $3f/N$, or equivalently $\gamma_1 < \pi/6L$. Thus, for our vortex with $L = 200$ km, if $\gamma_1 < 2.5 \times 10^{-6}$ m^{-1}, vortex break down should occur. Recall that this range of γ_1 was identified using linear theory in

Section 5.1 as the non-alignment regime. Therefore, a hypothetical weak tropical vortex extending through the depth of the troposphere and supporting a quasi-mode will tend to reduce its vertical scale in the presence of external shear until the alignment regime is reached. As noted by Dritschel and Juarez (1996), the vortex height to width ratio of $3f/N$ is commonly observed for atmospheric vortices, including TCs. (Note that although TCs generally do not fall within the QG regime, by generalizing f to include vortex rotation effects, as discussed in Section 5.1.3 and demonstrated in Chapter 6, it is possible to extend the present results to vortices in approximate gradient balance.)

In the case of TCs, the asymmetric transverse circulation required to maintain thermal wind balance in the small-γ_1 tilted configuration may actually help development. If the persistent asymmetric low-level convergence and enhanced convection to the right of the tilt vector (Jones 1995; see also Chapter 6) is larger than would be produced through symmetric mechanisms alone, an enhanced strengthening of the vortex circulation through symmetrization of convectively-generated PV will occur (MK; ME98; Möller and Montgomery 1999, 2000). According to the QG vortex alignment mechanism, even though the vortex has strengthened, it would still continue to wobble about its mid-level centroid since γ_1 has not changed. If one naively extends the findings of Section 5.1 to include finite Rossby number effects by replacing f^2 in the expression for γ_1^2 with the product of the modified Coriolis parameter and absolute vorticity of the associated vortex flow, the increase in vortex strength will increase γ_1. The vortex could potentially leave the non-alignment regime and re-align itself without changing its vertical scale. In Chapter 6 preliminary experiments using the AB model (Shapiro and Montgomery 1993) in which the standard Rossby number approaches unity demonstrate that the qualitative findings of Section 5.1 still hold.

5.2.2 Merger of a Tropical Vortex and Convectively-Generated PV

We now extend the tilted vortex results of the previous section to the merger of a convectively-generated PV anomaly within an incipient vortex (e.g., easterly wave closed circulation, MCV, ITCZ-derived). The dynamics of this problem was explored by ME98 in the context of tropical cyclogenesis. They suggested the role of vortex Rossby waves in the

merger process by showing good agreement between nonlinear and quasi-linear predictions of mean flow change for a barotropic wavenumber two asymmetry on a barotropic mean vortex. Quasi-linear estimates of the mean flow change for a baroclinic two-cluster PV anomaly on a barotropic vortex also agreed with nonlinear simulations. Here we explicitly compare linear and nonlinear simulations of the merger of a single-cluster convectively-generated PV anomaly with a weak vortex to assess the nature of the dynamics.

The same barotropic mean vortex as ME98 is used (see Fig. 5.1). The single-cluster isolated anomaly with positive(negative) PV at lower(upper) levels is given by

$$q_{sc}(r,\lambda,z) = \kappa \overline{q}_0 e^{-(\beta\delta r)^2} \cos\left(\frac{\pi z}{H}\right), \tag{5.11}$$

where κ is an amplitude factor, β is the inverse decay length of the asymmetry, and $(\delta r)^2 = (x - x_c)^2 + (y - y_c)^2$. The parameters x_c and y_c denote the Cartesian location of the asymmetry center. In the experiment presented here $\kappa = 0.5$ and $\beta = 1.0 \times 10^{-5}$ m^{-1}. In order to initialize the EQB model with a barotropic mean vortex, as in the previous section, the azimuthal wavenumber zero component of the anomaly at $z = 0$ is added to the pre-existing mean vortex at all heights. In contrast to Section 5.1 we do allow the generation of azimuthal-mean vertical wavenumber two in the nonlinear EQB model through the wave-mean interaction of $(m, n) = (1, 1)$, but it is incorporated into the barotropic mean vortex (see Chapter 4). No modifications to (5.11) were made in the QG3D model, so the mean vortex contains a small baroclinic component. The grid spacing for this QG3D model simulation is 7.5 km and the domain is now 1500×1500 km. Horizontal "del-squared" diffusion of PV has also been included with $\nu = 100$ $\mathrm{m}^2\mathrm{s}^{-1}$.

The isolated anomaly is placed inside the RMW of the pre-existing vortex at $x_c = 125$ km and $y_c = 0$ km to simulate an outbreak of convection near the vortex core. Figures 5.24 and 5.26 show the PV evolution over $2.5\tau_e$ simulated by the EQB and QG3D models for $\gamma_1 = 3.14 \times 10^{-6}$ m^{-1}. Although we are now considering tropical conditions, a value of $f = 1.0 \times 10^{-4}$ s^{-1} was used as a crude way of including the vorticity of the vortex in the definition of γ_1 (see ME98). The linear and nonlinear simulations agree well, consistent with small R_β (~ 0.2) and the presence of the quasi-mode also observed in the tilted

vortex experiments at this value of γ_1. Because of the greater departure of the horizontal structure of the initial PV asymmetry from the barotropic pseudo-mode, more sheared vortex Rossby wave dispersion is evident. At longer times the sheared waves symmetrize, leaving just the quasi-mode. Discrepancies between the nonlinear simulations are likely accounted for by the different initial mean vortex structures used. The phase difference in the azimuthal wavenumber one PV fields after $2.5\tau_e$ is, however, only 30–40 degrees.

Complete merger of the low-level convectively-generated PV with the incipient vortex is not expected during the time period considered here due to the presence of the quasi-mode. But forward Lagrangian trajectories from the *linear* simulation do show that PV from the low-level positive anomaly is transported radially inward into the vortex core (see Fig. 5.27). Of course total PV is not materially conserved as the parcel moves towards the vortex center in the linear approximation, as evidenced by the reduction in peak PV in Fig. 5.26, but the linear vortex Rossby waves do irreversibly transport PV nonetheless. The radially-inward transport of cyclonic eddy vorticity and eddy PV implies a strengthening of the low-level mean tangential winds in the vortex core by Stokes' Theorem, and vice versa. This is illustrated in Fig. 5.28 for the above experiment. Over $2.5\tau_e$ the QG3D model shows an increase in low-level tangential winds of approximately 0.21 ms^{-1} radially inside the location of the initial PV asymmetry. The nonlinear EQB simulation produces a similar structure for the tangential wind change, $\delta\overline{v}$, but with a maximum value of 0.18 ms^{-1}.

It is not surprising that the QG3D and nonlinear EQB models should agree as well as they do given that the low-level PV evolution is largely captured by linear vortex Rossby wave dynamics. Since wave-wave interactions are small (recall $R_\beta \sim 0.2$), the bulk of the mean flow change is effected by the self-interaction of vertical wavenumber one (i.e., wave-mean interaction) as shown in Fig. 5.28. MK predicted, and it was later confirmed in a nondivergent model for small but finite-amplitude disturbances (ME98) and for near order one amplitude disturbances (Enagonio and Montgomery 2000), that in such a situation one can use the linear solution to estimate the mean flow change that would occur in a model where the wave-mean interaction was computed explicitly. The so-called quasi-linear approximation is an estimate because the mean flow is prohibited from changing

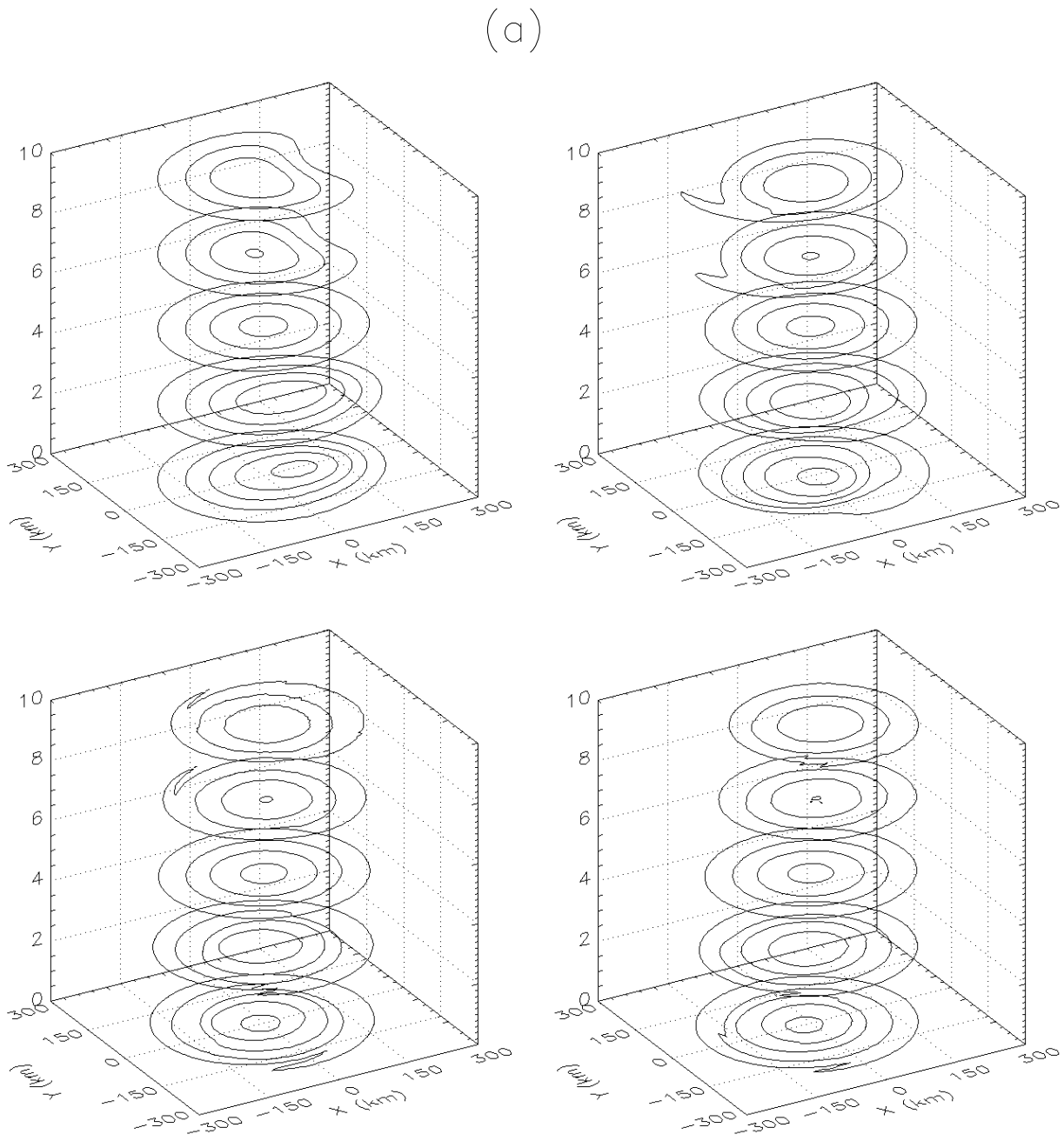

Figure 5.24: Evolution of vortex PV (from left to right) at t = 0, $0.5\tau_e$, $1.5\tau_e$, and $2.5\tau_e$ for the case of a barotropic mean vortex perturbed with an isolated baroclinic anomaly. Only the inner 600 km × 600 km is shown. The vertical depth is 10 km. The contour interval is 2.0×10^{-5} s^{-1}. (a) QG3D model (b) linear EQB model.

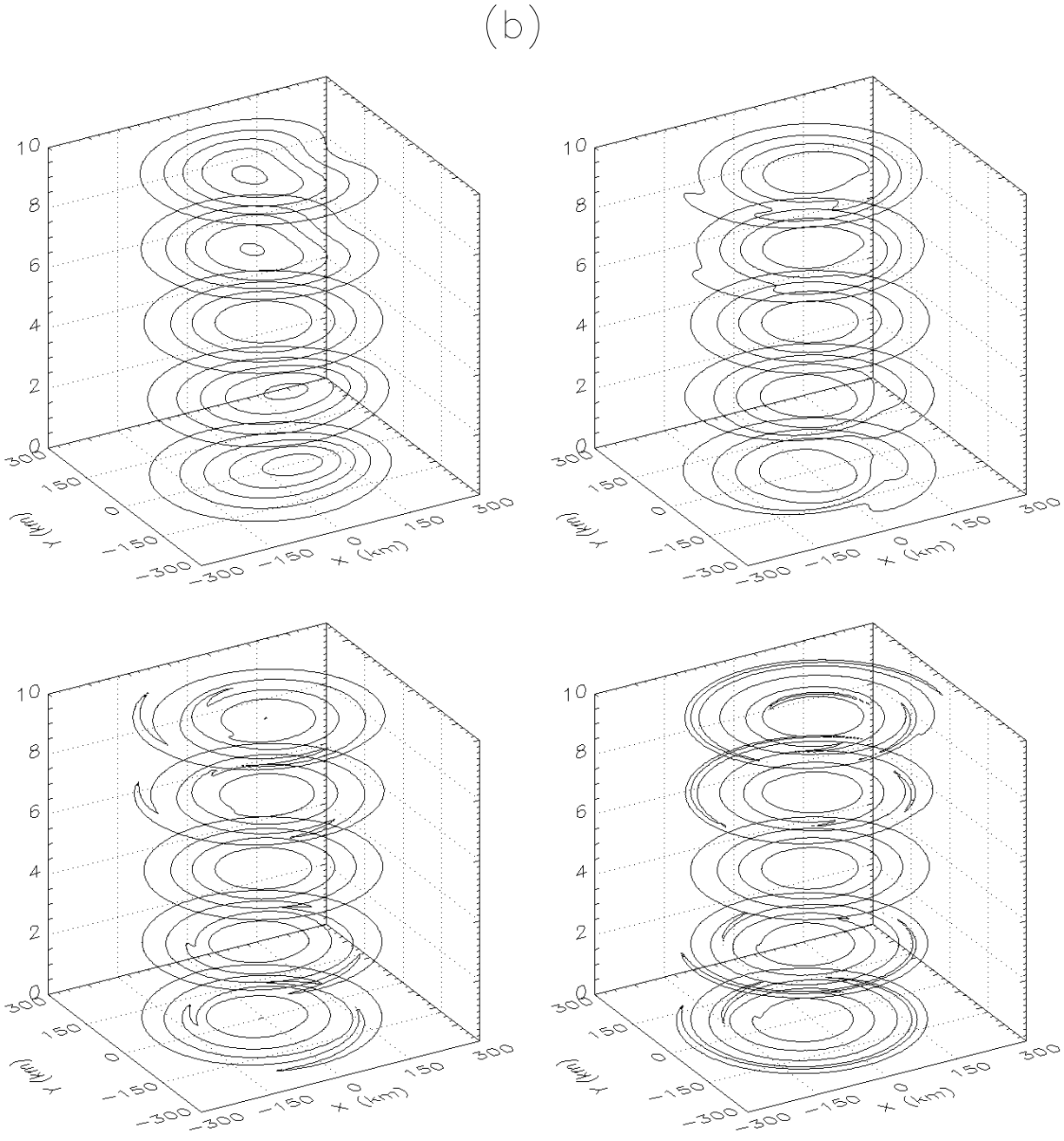

Figure 5.25: see Fig. 5.24.

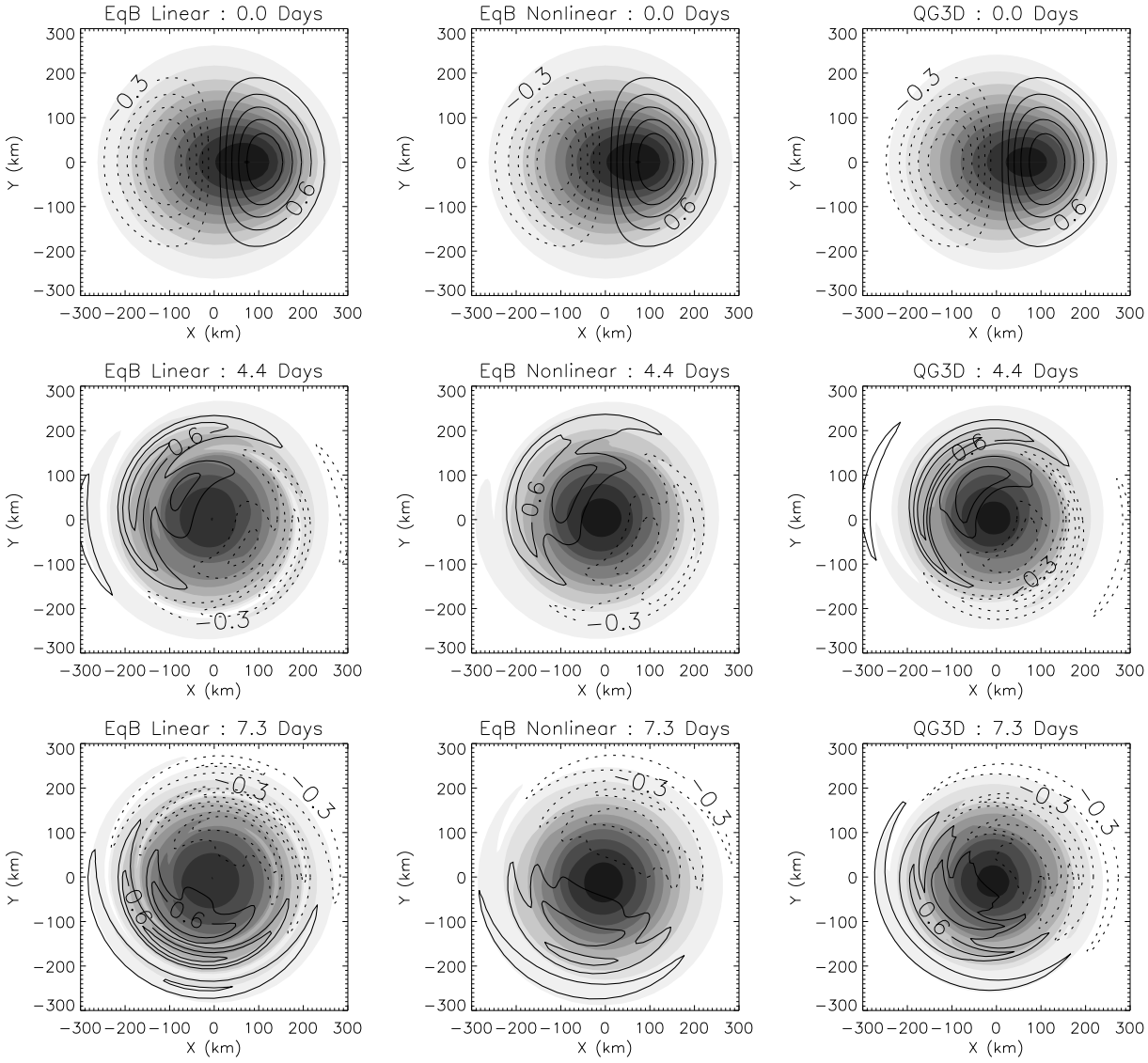

Figure 5.26: As in Fig. 5.5 but for the isolated anomaly experiment. See text for details on the initial conditions. Asymmetry contour interval is 0.3×10^{-5} s^{-1}.

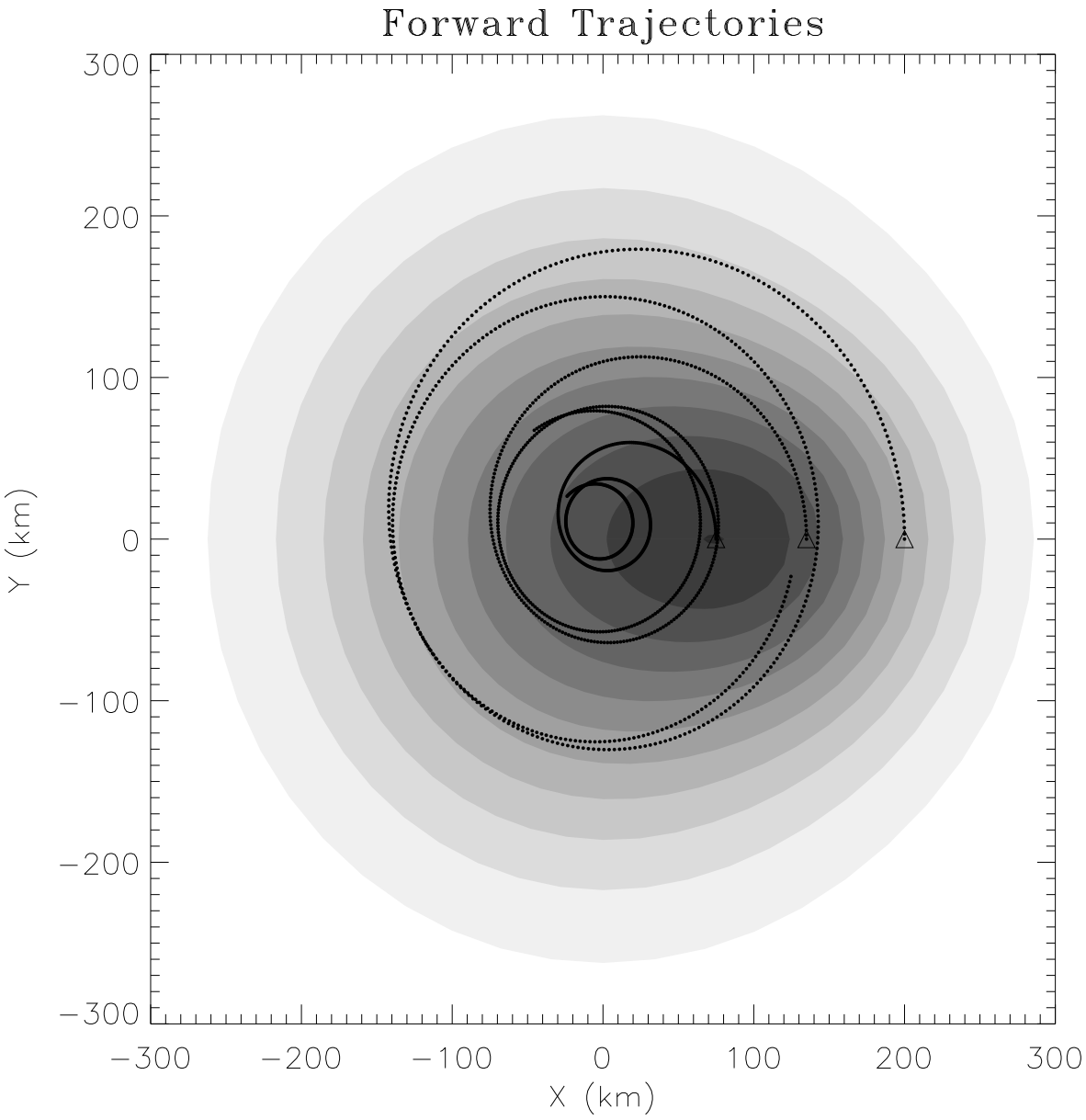

Figure 5.27: Forward Lagrangian trajectories of parcels originating within the isolated anomaly at $z = 0$ computed using winds simulated by the linear EQB model over $2.5\tau_e$. Note that high PV is transported in towards the vortex centroid.

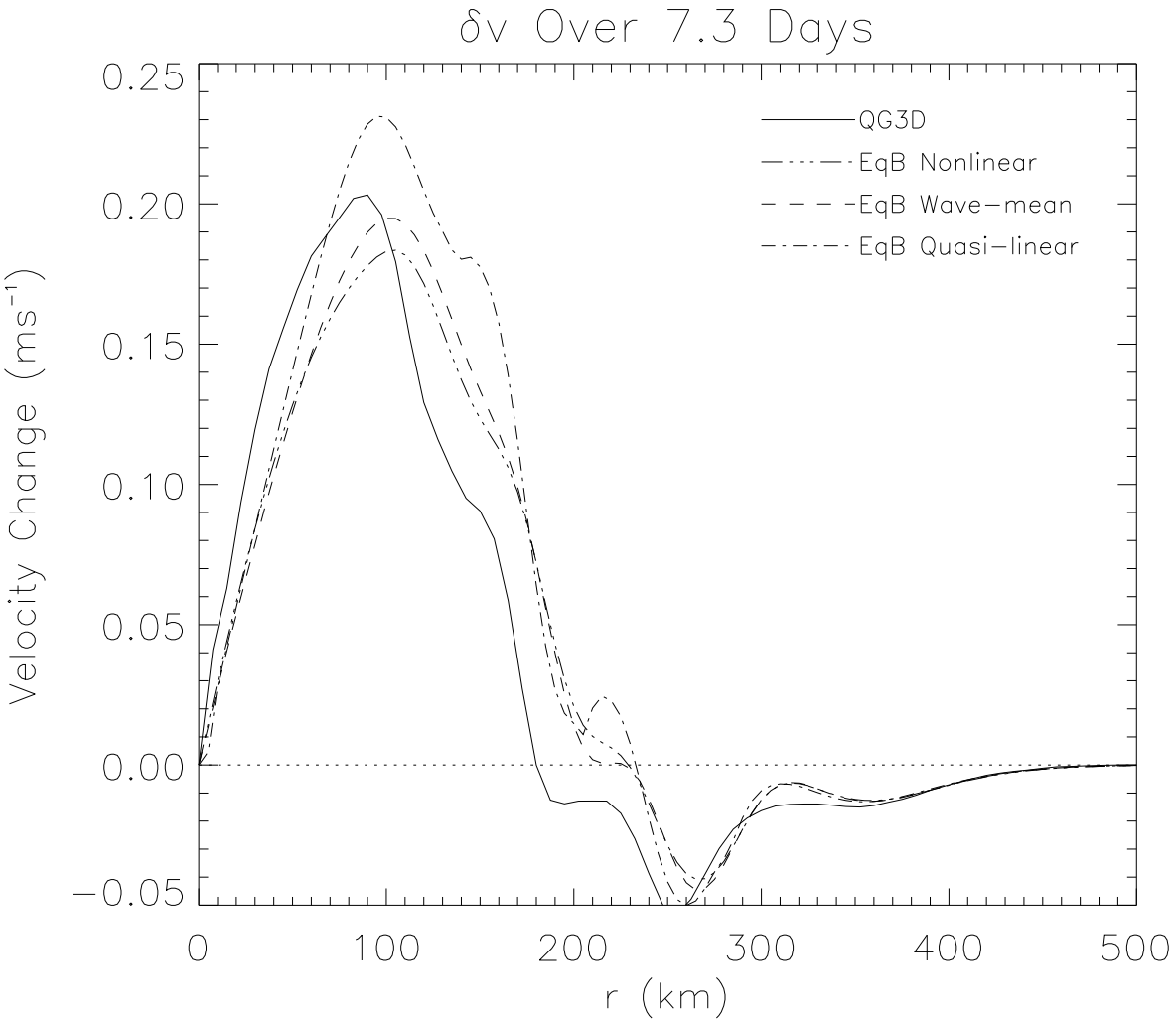

Figure 5.28: Change in azimuthal-mean tangential velocity at $z = 0$ over $2.5\tau_e$ as a function of radius for the isolated anomaly experiment. Shown are results from the QG3D and EQB models illustrating the quasi-linear nature of the low-level intensification of the mean flow by vortex Rossby waves.

in the linear model. The feedback on the wave dynamics is not captured as it is in the wave-mean model.

The quasi-linear formulation in the QG context is obtained following Held and Phillips (1987) and Holton (1992; Section 12.4). Starting with the mean PV equation,

$$\frac{\partial \overline{q}}{\partial t}(r,z,t) = -\frac{1}{r}\frac{\partial}{\partial r}(\overline{ru'q'}), \tag{5.12}$$

and using the fact that

$$\overline{ru'q'} = -\frac{\partial A}{\partial t}, \tag{5.13}$$

where $A(r,t) \equiv r\overline{q'^2}/(2d\overline{q}/dr)$ is the wave activity (or pseudo angular momentum), one obtains the following equation for the change in mean PV:

$$\delta\overline{q} = \frac{1}{r}\frac{\partial}{\partial r}(\delta A), \tag{5.14}$$

where δ denotes the difference between a mean quantity at $t \to \infty$ and $t = 0$.

Given the PV perturbation,

$$q' = \hat{q}_1(r,\lambda,t)\cos\left(\frac{\pi z}{H}\right), \tag{5.15}$$

where $\hat{q}_1$ is real-valued, the wave activity can be written as

$$A = \frac{\hat{A}}{2}\left[1 + \cos\left(\frac{2\pi z}{H}\right)\right], \tag{5.16}$$

where $\hat{A} = r\overline{\hat{q}_1^2}/(2d\overline{q}/dr)$. Therefore δA has both a barotropic and vertical wavenumber two component. The mean angular momentum change due to the barotropic component is obtained directly

$$\delta(r\overline{v}_0) = \frac{1}{2}\delta\hat{A}, \tag{5.17}$$

while the wavenumber two component is obtained by first solving the invertibility relation,

$$\frac{1}{r}\frac{\partial}{\partial r}\left(r\frac{\partial}{\partial r}(\delta\overline{\psi}_2)\right) - \gamma_2^2\delta\overline{\psi}_2 = \frac{1}{r}\frac{\partial}{\partial r}\left(\frac{\delta\hat{A}}{2}\right), \tag{5.18}$$

and then differentiating the incremental streamfunction

$$\delta(r\overline{v}_2) = r\frac{\partial}{\partial r}(\delta\overline{\psi}_2). \tag{5.19}$$

The total mean angular momentum change is the sum of these two contributions:

$$\delta(r\overline{v}) = \delta(r\overline{v}_0) + \delta(r\overline{v}_2)\cos\left(\frac{2\pi z}{H}\right). \tag{5.20}$$

Since γ_2 is relatively small in our case, we may assume $\delta\overline{v}_2 = \delta\overline{v}_0$ to provide an upper bound on $\delta\overline{v}$. The quasi-linear result derived from the linear EQB simulation is shown in Fig. 5.28. It not only replicates the general radial structure of the nonlinear $\delta\overline{v}$ predictions, but is also of the correct magnitude.

As a final note on the merger of an isolated anomaly with an incipient vortex, we comment on ME98's experiment involving the merger of an MCV-like vortex with convectively-generated PV. The initial pre-existing vortex has a large baroclinic component and the anomaly is given by (5.11). The anomaly in their experiment is placed well outside the RMW of the MCV vortex. For a convective blow-up inside the RMW, like that considered above, we would expect to be able to capture the subsequent alignment process using our linear model (linearized about a baroclinic mean vortex).

Chapter 6

VERTICAL ALIGNMENT OF STRONGER, SHEARED VORTICES

6.1 The Effects of Flow Curvature

For the benchmark mean vortex used in Chapter 5 with a 200-km RMW and maximum tangential wind of 5 ms^{-1}, the Rossby number is approximately 0.3 at the RMW. Although this value is less than unity, it is not entirely negligible either. To more accurately describe this vortex, we wish to utilize a balance theory appropriate for swirling flows. The AB model described in Chapter 4, based on a *local* Rossby number expansion, is used to validate the results of Chapter 5. Recall that the linear equivalent barotropic AB system looks very similar to the QG counterpart, except that the internal Rossby deformation radius is now a function of the mean vortex swirl and there are additional geometric factors. Therefore, to the extent that the local Rossby number is much less than unity and the AB formulation is formally valid, we expect at least qualitative agreement with the QG results, i.e., co-rotation at small values of γ_1 and alignment at large values of γ_1. Because of the dependence of γ_1 on radius we choose to characterize the simulations by the value at the RMW.

In the first experiment the benchmark vortex of Chapter 5 is used. The local Rossby number squared, standard Rossby number squared, and γ_1 are shown in Fig. 6.1. Because $R_1^2 \ll 1$, we expect the linear AB theory to be highly accurate for tilted vortices with Ro close to, but less than, unity. At large radius $\overline{\eta} \to f$ and $\overline{\xi} \to f$, so the value of $\gamma_1 = 3.14 \times 10^{-6}$ m^{-1} used in the QG simulation is recovered. Figure 6.2 shows the evolution of pseudo-PV at $z = 0$ over a $5\tau_e$ period. $\gamma_1 = 4.3 \times 10^{-6}$ m^{-1} in this case. The evolution of pseudo-PV is nearly identical to that shown in Fig. 5.5 simulated by the linear QG model. The radial vortex Rossby wave propagation is slightly more pronounced

in the AB simulation. We conclude that the inclusion of curvature effects in the case of a weak vortex does not substantially alter the quasi-mode found in the QG system.

Keeping the same tangential wind profile, but altering f and N should produce the same variability in vortex evolution presented in Chapter 5, obtained there by varying just γ_1. Figures 6.3 and 6.4 show the evolution of psuedo-PV upon increasing f and decreasing N by a factor of four, respectively. In the former case R_1^2 is decreased and $\gamma_1 = 13.7 \times 10^{-6}$ m^{-1}, and in the latter case R_1^2 remains the same as in 6.1 and $\gamma_1 = 17.2 \times 10^{-6}$ m^{-1}. Both simulations show axisymmetrization of perturbation pseudo-PV, i.e., vortex alignment, consistent with the QG evolution at $\gamma_1 = 20.0 \times 10^{-6}$ m^{-1} shown in Fig. 5.13. The complete picture of vortex alignment is therefore captured by QG theory for weak vortices.

The question remains as to whether the QG formulation still captures the essence of the alignment mechanism for rapidly rotating vortices. Figure 6.5 shows R_1^2, Ro^2, and γ_1 for the benchmark vortex (and benchmark environmental conditions), but with the maximum mean tangential wind increased to 10 ms^{-1}. The local Rossby number squared is still much less than unity in this case and therefore we still expect the AB theory to be accurate. Figure 6.6 shows the evolution of the stronger benchmark vortex. In this case we estimate $\gamma_1 = 5.4 \times 10^{-6}$ m^{-1}. The wavenumber one PV asymmetry rotates at a faster rate than in the benchmark case ($\sim$ twice as fast), but retains an underlying quasi-mode structure. The sheared vortex Rossby waves are much more prominent. Recall the discussion in Chapter 5 where it was noted that a general initial condition will tend to project more onto the sheared vortex Rossby waves at early times than when the vortex is perturbed with an asymmetry having the quasi-mode structure. Although the vortex in this simulation has been perturbed with an azimuthal wavenumber one asymmetry having radial PV structure of the pseudo-mode (which was identical to the quasi-mode structure in the QG simulations), the quasi-mode in the AB system at higher swirls may not take on this form. Therefore, sheared wave dispersion occurs as the vortex asymptotes to the quasi-mode solution. This hypothesis will be tested in future work by performing an AB eigenanalysis similar to that done for the QG system.

The above results are important in two regards. First, they suggest that the QG vortex alignment findings may be directly applied to the tropical cyclogenesis problem

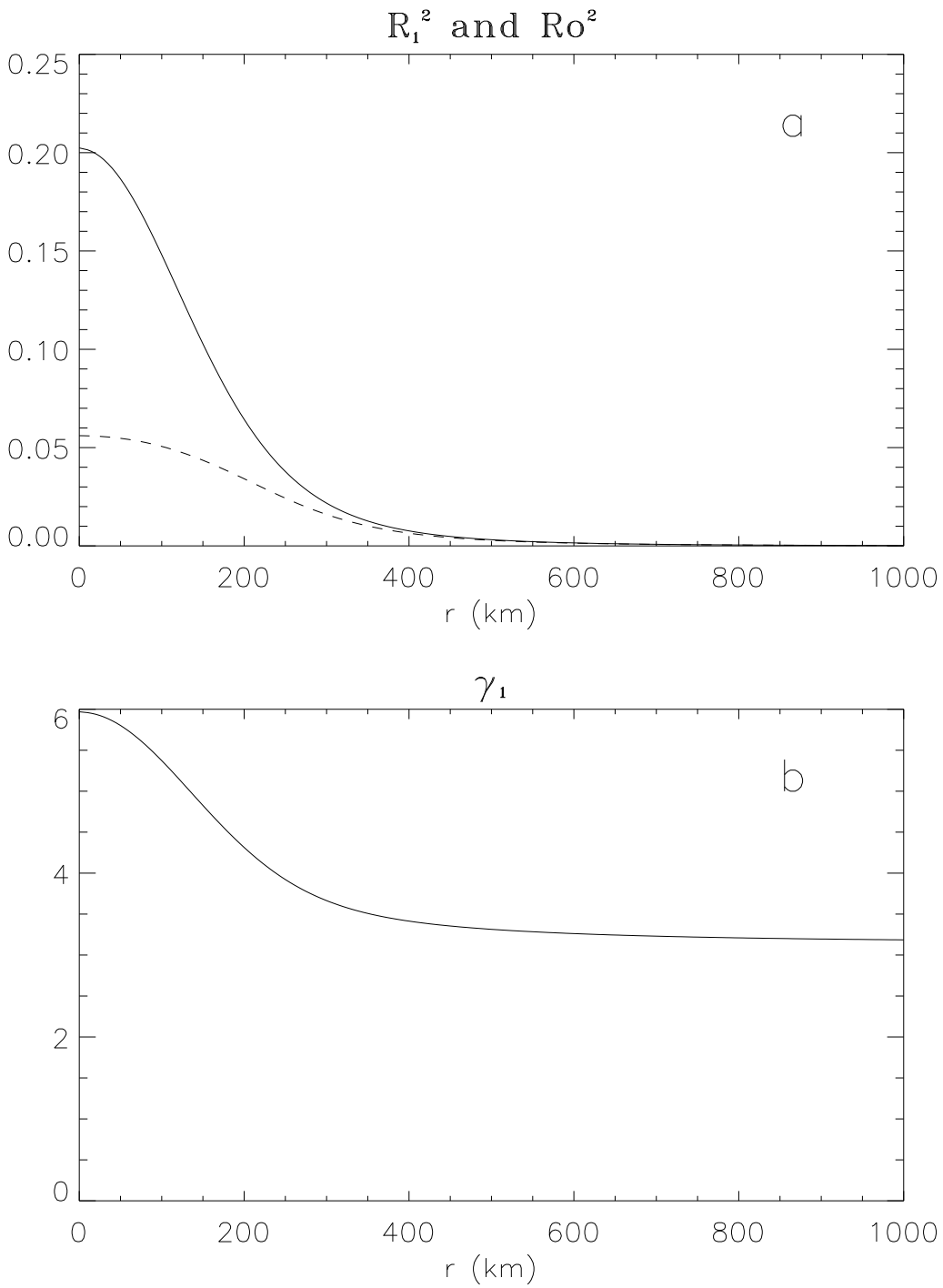

Figure 6.1: Benchmark vortex (a) Local Rossby number squared for azimuthal wavenumber one (dashed) and standard Rossby number squared (solid), and (b) inverse internal Rossby deformation radius for vertical wavenumber one (units 10^{-6} m^{-1}).

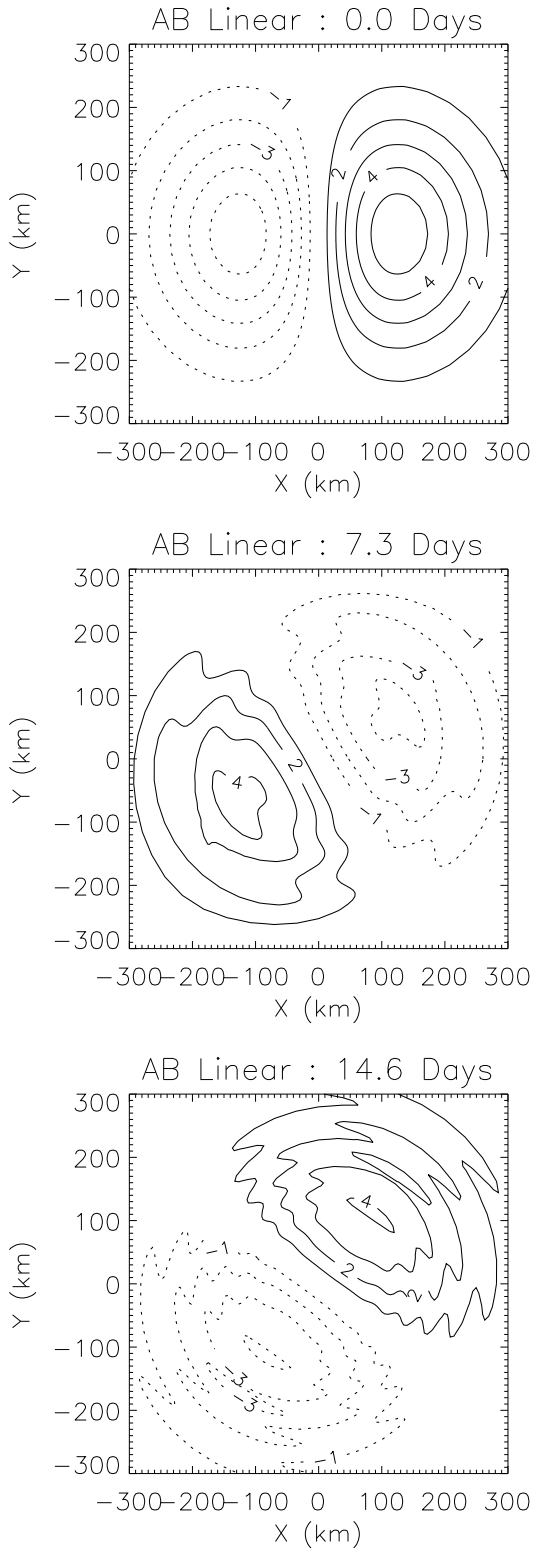

Figure 6.2: Linear equivalent barotropic AB simulation of the wavenumber one component of pseudo-PV (contour interval 1×10^{-9} s^{-3} with negative values dashed) at $z = 0$ over a $5\tau_e$ period for the benchmark run (compare with Fig. 5.5).

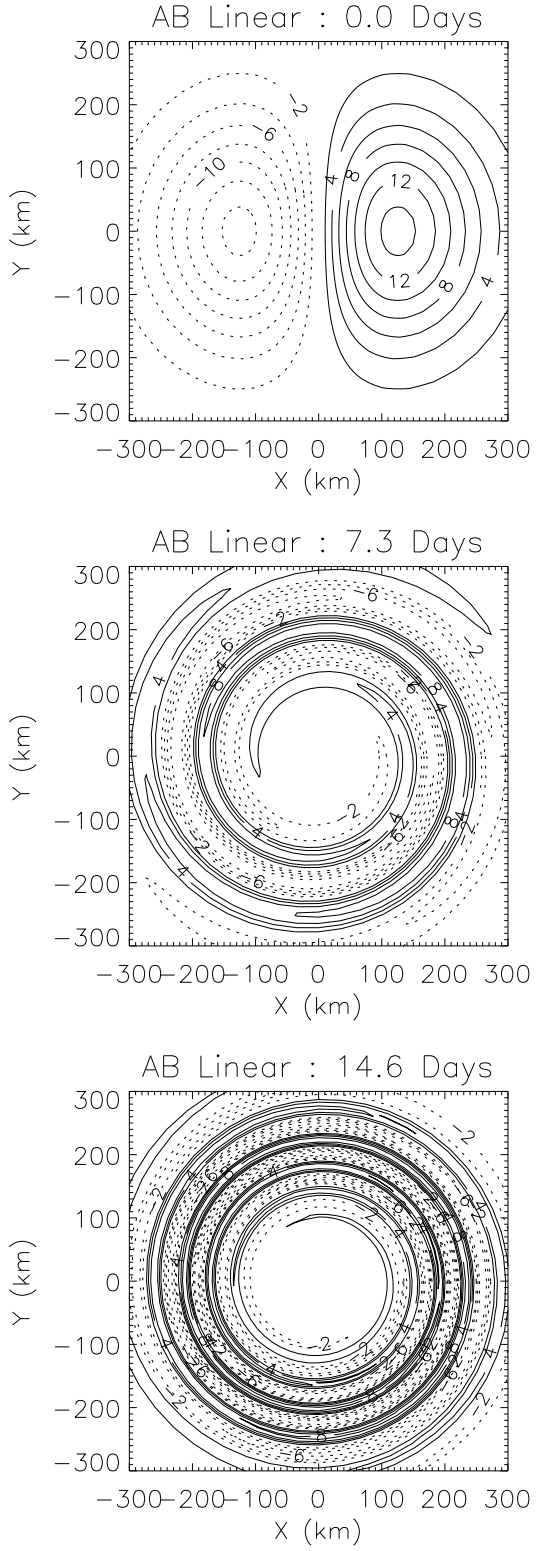

Figure 6.3: As in Fig. 6.2, but for a larger value of $f = 4.0 \times 10^{-4}$ s^{-1}. Contour interval 2×10^{-9} s^{-3}.

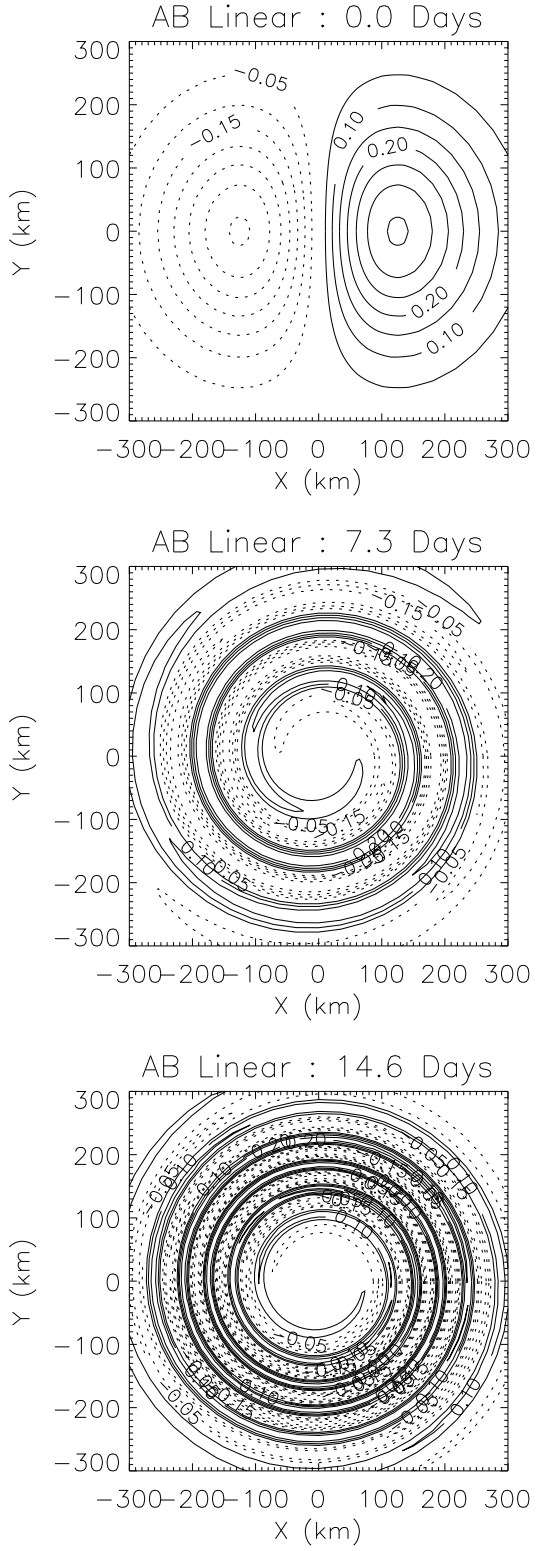

Figure 6.4: As in Fig. 6.2, but for a smaller value of $N = 2.5 \times 10^{-3}$ s^{-1}. Contour interval 0.05×10^{-9} s^{-3}.

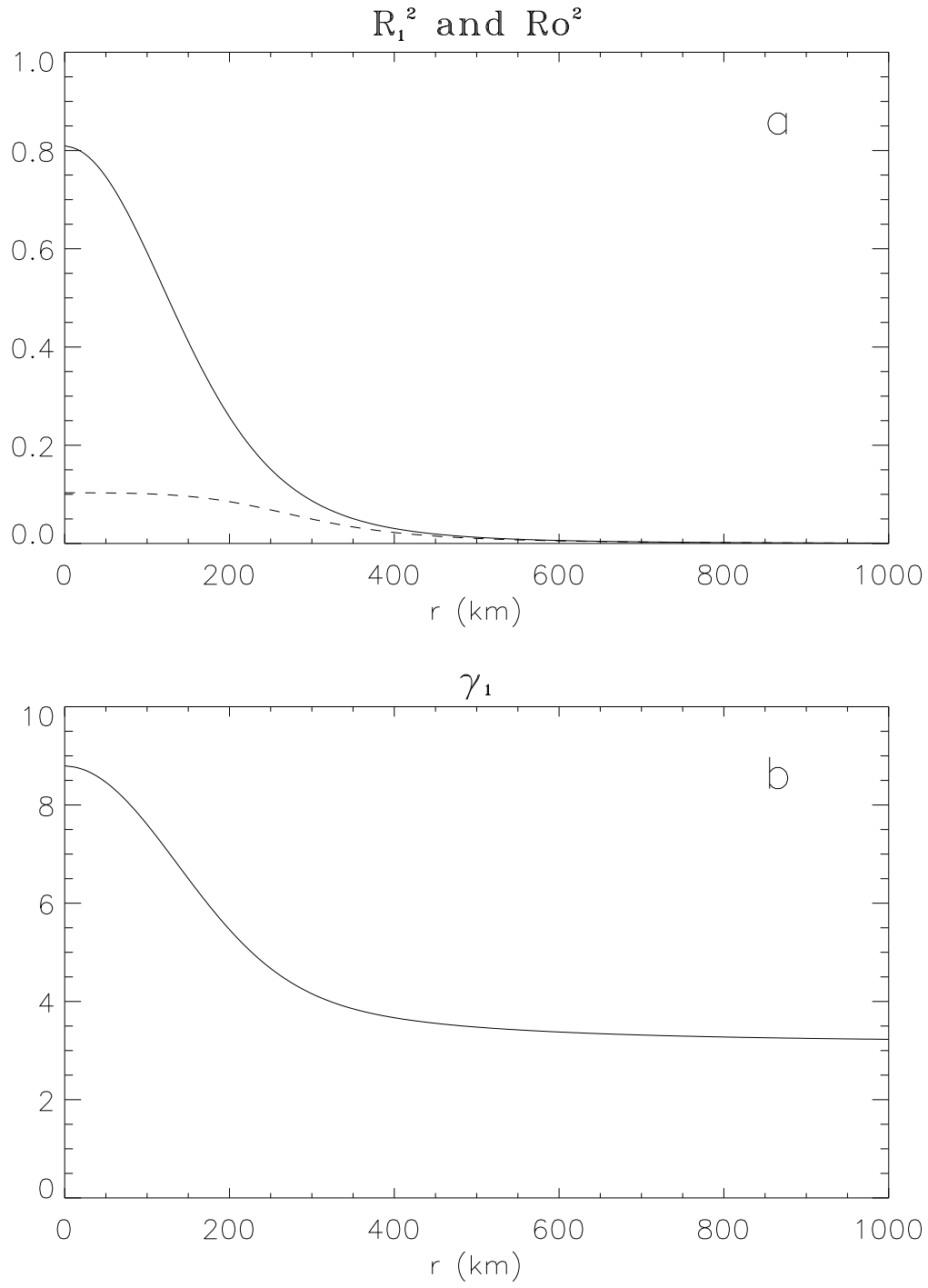

Figure 6.5: As in Fig. 6.1, but for a stronger vortex with maximum tangential wind of 10 ms^{-1}.

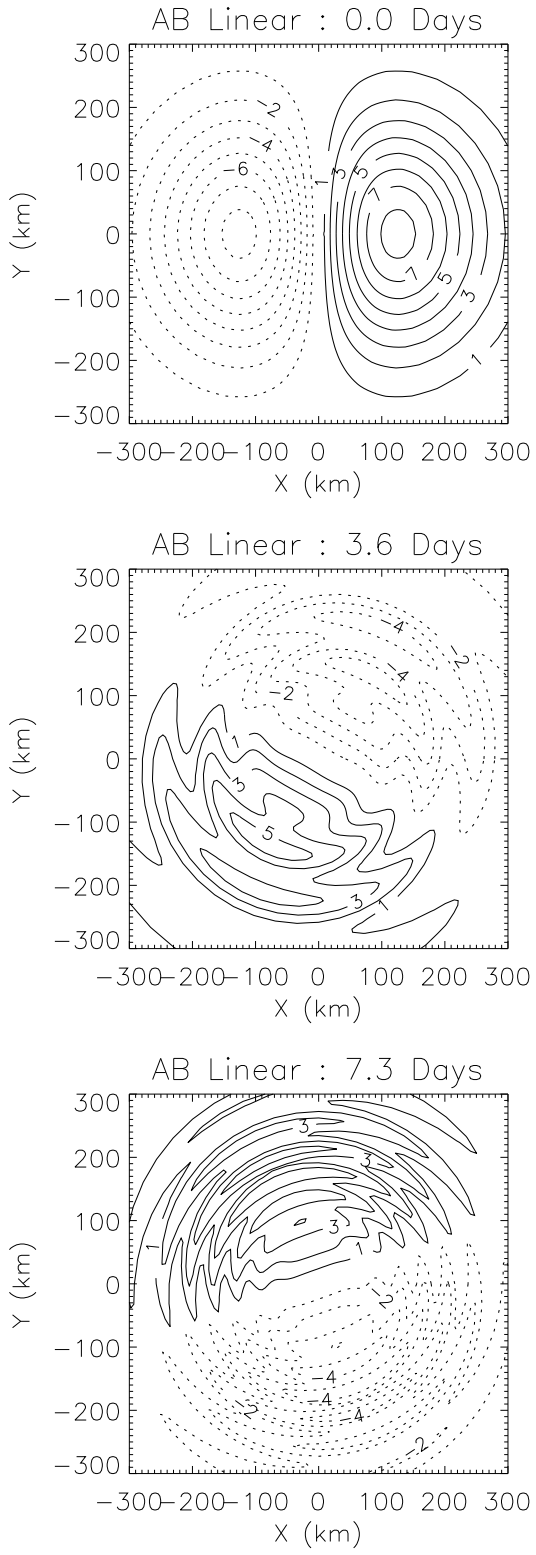

Figure 6.6: As in Fig. 6.2, but for a vortex with maximum mean tangential wind of 10 ms^{-1}. Note that the time period considered has been reduced due to the shorter circulation period. Contour interval 1×10^{-9} s^{-3}.

for weak incipient vortices. The addition of finite Rossby number effects modifies the radial structure of the quasi-mode and governing dynamical equations somewhat, but the transition from alignment to non-alignment regimes deduced from the QG simulations remains approximately true. Second, it is likely that a quasi-mode in near-gradient balance exists at higher swirls. The precise radial structure of this quasi-mode is currently unknown. The quasi-mode may be relevant to hurricane-strength vortices, although the combination of higher swirl speeds and reduced static stability would put the vortex well into the alignment regime according to the QG picture. It remains to be demonstrated at what horizontal scale and internal deformation radius the transition from alignment to non-alignment actually occurs in the higher swirling case.

6.2 The Effects of Vertical Shear

6.2.1 Forced Vortex Alignment

Vertical shear can be included in the linear model as follows. For simplicity we consider the QG problem. First, let

$$v(r,\lambda,z,t) = \overline{v}(r,z) + v'(r,\lambda,z,t) + v_s(r,\lambda,z) \tag{6.1}$$

$$u(r,\lambda,z,t) = u'(r,\lambda,z,t) + u_s(r,\lambda,z)$$

$$q(r,\lambda,z,t) = \overline{q}(r,z) + q'(r,\lambda,z,t) + q_s(r,\lambda,z)$$

where $\overline{(\,)}$ and $(\,)'$ are here defined as the vortex azimuthal mean and perturbation components, respectively, and $(\,)_s$ are the environmental shear components of the total wind and PV fields. Linearizing the QG PV equation (4.1) by first neglecting the product of vortex perturbation quantities yields

$$\left(\frac{\partial}{\partial t} + \frac{\overline{v}}{r}\frac{\partial}{\partial \lambda}\right) q' + u' \frac{\mathrm{d}\overline{\mathrm{q}}}{\mathrm{dr}} = F_s \tag{6.2}$$

where

$$F_s = -\left[(\overline{v}+v')\frac{1}{r}\frac{\partial q_s}{\partial \lambda} + u_s\frac{\partial}{\partial r}(q'+\overline{q}) + \frac{v_s}{r}\frac{\partial q'}{\partial \lambda} + u'\frac{\partial q_s}{\partial r} + \frac{v_s}{r}\frac{\partial q_s}{\partial \lambda} + u_s\frac{\partial q_s}{\partial r}\right]. \tag{6.3}$$

Let the environmental flow be purely zonal and vary with height so as to preserve the isothermal vertical boundary conditions, i.e.,

$$u_s = U\cos\lambda\cos\left(\frac{m\pi z}{H}\right) = -\frac{1}{r}\frac{\partial\psi_s}{\partial\lambda} \tag{6.4}$$

$$v_s = -U\sin\lambda\cos\left(\frac{m\pi z}{H}\right) = \frac{\partial\psi_s}{\partial r},$$

where U is the maximum zonal wind. The environmental streamfunction and PV are then given by

$$\psi_s = -Ur\sin\lambda\cos\left(\frac{m\pi z}{H}\right) \tag{6.5}$$

$$q_s = \frac{1}{r}\frac{\partial}{\partial r}\left(r\frac{\partial\psi_s}{\partial r}\right) + \frac{1}{r^2}\frac{\partial^2\psi_s}{\partial\lambda^2} + \frac{f^2}{N^2}\frac{\partial^2\psi_s}{\partial z^2} = \gamma_m^2 Ur\sin\lambda\cos\left(\frac{m\pi z}{H}\right).$$

Note that the last two terms of Eq. (6.3) cancel since

$$\frac{v_s}{r}\frac{\partial q_s}{\partial\lambda} + u_s\frac{\partial q_s}{\partial r} = \left(\frac{-U\sin\lambda}{r}\cdot\gamma_m^2 Ur\cos\lambda + U\cos\lambda\cdot\gamma_m^2 U\sin\lambda\right)\cos\left(\frac{m\pi z}{H}\right) = 0, \tag{6.6}$$

i.e., the zonal mean flow is itself an exact solution to the linearized PV equation (6.2). Therefore, F_s can be written

$$F_s = -U\left\{\left(\gamma_m^2\overline{v} + \frac{\mathrm{d}\overline{\mathrm{q}}}{\mathrm{dr}} + \gamma_m^2 v' + \frac{\partial q'}{\partial r}\right)\cos\lambda + \left(\gamma_m^2 u' - \frac{1}{r}\frac{\partial q'}{\partial\lambda}\right)\sin\lambda\right\}\cos\left(\frac{m\pi z}{H}\right). \tag{6.7}$$

The only deformation radius in the QG system is $L_R = NH/f$, so there is no way to independently change the deformation radius of the vortex and environment. Since the PV associated with the environmental flow consists entirely of thermal vorticity and is proportional to γ_1^2 times the streamfunction, the PV and its meridional gradient will increase with decreased deformation radius (assuming the mean zonal wind remains fixed). Therefore, for very large γ_1 the solution to the forced linear problem will be dominated by Rossby waves propagating on the environmental PV gradient excited by the vortex. The degree to which the initial vortex disperses as Rossby waves is characterized by the beta Rossby number. The beta Rossby number differs from the *vortex* beta Rossby number (5.6) in that the vortex is now regarded as the perturbation and the mean PV gradient is associated with the environment. The ratio of the vortex interaction terms in the linear PV

equation (6.2) to the "effective β" term in (6.7), which is proportional to $\beta_{eff}\overline{v} = \gamma_1^2 U\overline{v}$, scales as

$$R_\beta \sim \frac{v_{max}^2/L^2}{\beta_{eff} v_{max}} = \frac{v_{max}}{\beta_{eff} L^2}, \tag{6.8}$$

where v_{max} is the maximum tangential wind of the vortex and L is the horizontal vortex scale. For $v_{max} = 5$ ms^{-1}, $L = 200$ km, $U = 0.5$ ms^{-1}, and $\gamma_1 = 20.0 \times 10^{-6}$ m^{-1}, the beta Rossby number is approximately 0.6. The vortex will therefore tend to disperse in this limit. The dispersion of the vortex can be prevented by incorporating sloping boundaries to offset the effective beta of the environmental flow (Smith et al. 2000), or it can be controlled by using a balanced system which allows one to change the deformation radius of the vortex without changing the environmental PV gradient (which we want to remain small for a wide range of γ_1). The inclusion of vertical shear in the linear AB system is briefly discussed below.

In the limit of small γ_1 and weak vertical shear, F_s can be further simplified:

$$F_s \approx -U \frac{\mathrm{d}\overline{\mathrm{q}}}{\mathrm{dr}} \cos\lambda \cos\left(\frac{m\pi z}{H}\right). \tag{6.9}$$

This forcing represents the radial advection of azimuthal mean vorticity by the environmental flow. Expressing $\cos\lambda$ as $(e^{i\lambda} + e^{-i\lambda})/2$, the PV equation for $(m, n) = (1, 1)$ is

$$\left(\frac{\partial}{\partial t} + i\overline{\Omega}\right) \tilde{q}_{11}(r,t) - \frac{i}{r}\frac{\mathrm{d}\overline{\mathrm{q}}}{\mathrm{dr}} \tilde{\psi}_{11}(r,t) = -\frac{U}{2}\frac{\mathrm{d}\overline{\mathrm{q}}}{\mathrm{dr}}. \tag{6.10}$$

The $\tilde{q}_{1,-1}$ PV perturbation is given by the complex conjugate of $\tilde{q}_{1,1}$. The RHS forcing is easily incorporated into the linear EQB semi-spectral model (6.10). Using this linear model, we expect to be able to approximately reproduce the boundary between co-rotation (or alignment) and the irreversible shearing apart of the vortex determined by Smith et al. (2000), who used a two-layer nonlinear QG model. Qualitatively we know that the vortex will tend to shear apart when it is initially in the co-rotation regime, and will resist the effects of shear in the vortex alignment regime. The linear model can be used to quantify the value of γ_1 at which alignment takes place as a function of the shear magnitude, $\pi U/H$, or, equivalently, determine the shear threshold above which the vortex is unable to hold together.

Extension to the linear equivalent barotropic AB system yields a model for rapidly rotating vortices. The two-layer nonlinear analogue model of Smith et al. (2000) for rapidly rotating, distributed vortices involved an ad-hoc coupling parameter. The "coupling parameter" in our case is known, and is simply $\gamma_1^2(r) = (\pi/NH)^2(\overline{\eta}\overline{\xi})$. Consequently, our model can be applied in a more straightforward manner to a physical scenario like the alignment of a TC. It remains to be seen how well the linear AB model reproduces the boundary between co-rotation (or alignment) and irreversible separation of upper and lower vortex centers for the stronger vortices (Ro $\sim$ 5–10) described by Smith et al. (2000).

In Chapter 5 we alluded to the possibility that a tilted vortex could realign itself through the secondary circulation required to maintain thermal wind balance. The secondary circulation itself is not responsible for the alignment, for it is merely the response of the balanced vortex to changes in the geostrophic (QG system) or gradient (AB system) winds. Through enhanced low-level convergence and, as a consequence of coupling with the boundary layer, enhanced convection, the secondary circulation can excite asymmetric low-level PV generation. If the magnitude of the low-level asymmetric convergence is much larger than the low-level axisymmetric convergence, the axisymmetrization of this PV will strengthen the mean vortex. The dynamics of vortex interaction with vertical shear and supporting observations from Hurricane Olivia (1994) are presented below.

6.2.2 TC Secondary Circulation Response to Vertical Shear

Raymond and Jiang (1990) proposed a mechanism by which the PV anomaly associated with a midlatitude mesoscale convective system interacts with environmental vertical shear to produce enhanced low-level lifting and cumulus convection, thus prolonging the life of the mesoscale convective system. In their conceptual model they assumed that the distortion of the PV anomaly by the vertical shear was negligible. Upward motion then arose downshear as the ambient flow followed the distorted isentropes of the PV anomaly, and the vortex flow followed the tilted ambient isentropes. They estimated that vertical displacements in excess of 500 m could occur over a 24 h period, large enough to release conditional instability. In a subsequent study Raymond (1992) considered the additional

effect of distorting the vortex isentropes through tilting by ambient shear. In his simulations he found that the vortex flow on the distorted isentropes of the tilted vortex produced an important contribution to the vertical motion, with maximum values in the downshear-right quadrant.

The relation between vertical shear and convective asymmetry in hurricanes has been noted observationally (Willoughby et al. 1984; MHG; Franklin et al. 1993; Reasor et al. 2000; Black et al. 2000) and explored recently using idealized and operational hurricane numerical models (Jones 1995; DeMaria 1996; Bender 1997; Frank and Ritchie 1999). Jones (1995) simulated the evolution of an initially barotropic hurricane-strength vortex in unidirectional vertical shear. The early stages of the simulation produced upward motion downshear via the vortex flow on ambient isentropes and the upward motion of isentropic surfaces as the tilting vortex tried to maintain thermal wind balance. The coupling of upper- and lower-level PV anomalies lead to changes in the direction of vortex tilt with respect to the ambient vertical shear vector. As the tilt became more substantial, the pattern of vertical motion was governed increasingly by the vortex flow on distorted isentropes. The maximum upward motion then occurred to the right of the local tilt vector.

Insight into the relative contributions of vertical shear and vortex tilt to the vertical motion pattern may be obtained by first considering the dynamics in a QG framework. We begin by defining an initially circular barotropic vortex in pseudo-height coordinates tilted linearly with height in the zonal direction. In Cartesian coordinates the tilted vortex is described as follows:

$$U = \frac{-2Rv_{max}y}{R^2 + (x - \alpha z)^2 + y^2}, \qquad (6.11)$$
$$V = \frac{2Rv_{max}(x - \alpha z)}{R^2 + (x - \alpha z)^2 + y^2},$$

where U and V are the zonal and meridional components of the wind, respectively, R the RMW, v_{max} the maximum tangential wind, and α the constant change in vortex center displacement with height. A vertically-sheared zonal environmental wind, U_e, is then added to this vortex wind field, and the total wind field is transformed into a cylindrical coordinate system (r, λ, z) whose origin is the vortex center on the lowest surface, $z = 0$.

The vertical velocity field required to maintain thermal wind balance is obtained by solving the well-known Q-vector form of the omega equation written in cylindrical coordinates (Hoskins et al. 1978):

$$N^2\nabla^2 w + f^2\frac{\partial^2 w}{\partial z^2} = 2\nabla\cdot\mathbf{Q}, \tag{6.12}$$

where N is the Brunt Väisällä frequency, ∇ the horizontal gradient operator, and $\mathbf{Q}$ is the horizontal Q vector

$$\mathbf{Q} = \left(f\left[\frac{\partial u}{\partial z}\frac{\partial v}{\partial r} - \frac{\partial u}{\partial r}\frac{\partial v}{\partial z}\right], \frac{f}{r}\left[\frac{\partial u}{\partial z}\left(\frac{\partial v}{\partial \lambda} + u\right) - \frac{\partial v}{\partial z}\left(\frac{\partial u}{\partial \lambda} - v\right)\right]\right) \tag{6.13}$$

where u and v are the geostrophic radial and tangential winds, respectively. We first substitute the expression for the winds into (6.13) and then compute the horizontal divergence. A new coordinate system (r', λ', z) is defined with the origin at the center of the displaced vortex at each height (see Appendix A for details). Defining a nondimensional radius $b' = r'/R$, the expression for the Q-vector divergence becomes simply

$$\nabla\cdot\mathbf{Q} = \frac{16 b' f^3 Ro}{R(1+b'^2)^4}\left[(\alpha Ro)\left(2 - b'^2\right)\sin\lambda' - \frac{1}{f}\left(\frac{\partial U_e}{\partial z}\right)\left(1 + b'^2\right)\cos\lambda'\right] \tag{6.14}$$

where $Ro \equiv v_{max}/fR$ is the Rossby number. The first term on the right-hand side represents the forcing due to vortex flow on distorted isentropes, while the second term represents the effects of vortex flow on ambient isentropes. Note that in the transformed coordinate system the Q-vector divergence projects *only* onto wavenumber 1. Since w is proportional to $-\nabla\cdot\mathbf{Q}$, it follows that the maximum upward motion due to vortex flow on distorted isentropes occurs to the right of the tilt vector, whereas the upward motion along ambient isentropes occurs downshear, as expected. The radius of maximum Q-vector divergence and, hence, vertical motion tends to occur around 0.5R for this particular vortex profile. If solid-body rotation is used instead inside the RMW, the maximum upward motion moves closer to the RMW.

Although (6.14) is strictly valid for $Ro \ll 1$, it can be used to describe the qualitative features of the vertical motion field at near unity Rossby number. As an example of its applicability, we consider the vortex discussed by Trier et al. (1998) in their non-hydrostatic primitive equation (PE) simulation of the interaction of a mesoscale vortex

with environmental vertical shear. Since they initialized their model with a baroclinic vortex different from the barotropic vortex described by (6.11), we focus primarily on qualitative agreement. At 2.1 km height, $R = 30$ km and $Ro \sim 1.5$. The low-level westerly environmental shear is approximately 2×10^{-3} s^{-1}. If the PV anomaly at each height is simply advected by the mean flow, then $\alpha \sim 3$ after 0.5 h and $\alpha \sim 40$ after 6 h. We find that at 0.5 h the vertical motion downshear near $b' = 0.5$ is approximately three times larger than that to the right of the tilt vector. This is consistent with the simulation of Trier et al. which produced upward motion primarily downshear at this time (see Fig. 6.7a). At 6 h, when the vortex tilt is more substantial, we estimate that the upward motion to the right of the tilt vector is about four times greater than the downshear component. This is again consistent with their simulated vertical motion (see Fig. 6.7b).

Using the actual initial vortex and environmental flow parameters of Trier et al. in a standard QG omega-equation solver produces a vertical velocity pattern in good agreement with their simulated results at 0.5 and 6 h (see Fig. 6.8). The magnitude of the QG vertical velocity, however, is a factor of 2-3 less than the PE values. Employing a balance theory more appropriate for rapidly rotating vortices would reduce this discrepancy. An equation similar to (6.12) was derived by Shapiro and Montgomery (1993) for the asymmetric balance (AB) system valid for hurricane-strength swirling flows. The AB omega equation, assuming a barotropic mean vortex, is given by

$$\frac{N^2}{r}\frac{\partial}{\partial r}\left[r\frac{\partial w'}{\partial r}\right] + \overline{\eta}\overline{\xi}\frac{\partial^2 w'}{\partial z^2} + \frac{N^2}{r^2}\frac{\partial^2 w'}{\partial \lambda^2} = \nabla_{\mathbf{3D}} \cdot \mathbf{A}, \tag{6.15}$$

where

$$\mathbf{A} = \left\{ \frac{\overline{\xi}}{r}\frac{\partial}{\partial z}\left(\frac{\partial \phi'}{\partial \lambda}\right) - \frac{\partial \overline{\Omega}}{\partial r}\frac{\partial}{\partial z}\left(\frac{\partial \phi'}{\partial \lambda}\right), -\overline{\eta}\frac{\partial}{\partial z}\left(\frac{\partial \phi'}{\partial r}\right), u'\frac{\partial(\overline{\eta}\overline{\xi})}{\partial r} \right\} \tag{6.16}$$

is the three-dimensional generalization of the horizontal Q-vector from QG theory. This AB generalization of the QG omega equation may allow one to obtain an expression similar to (6.14). A more quantitative comparison with PE simulations and actual observations will be investigated in future work.

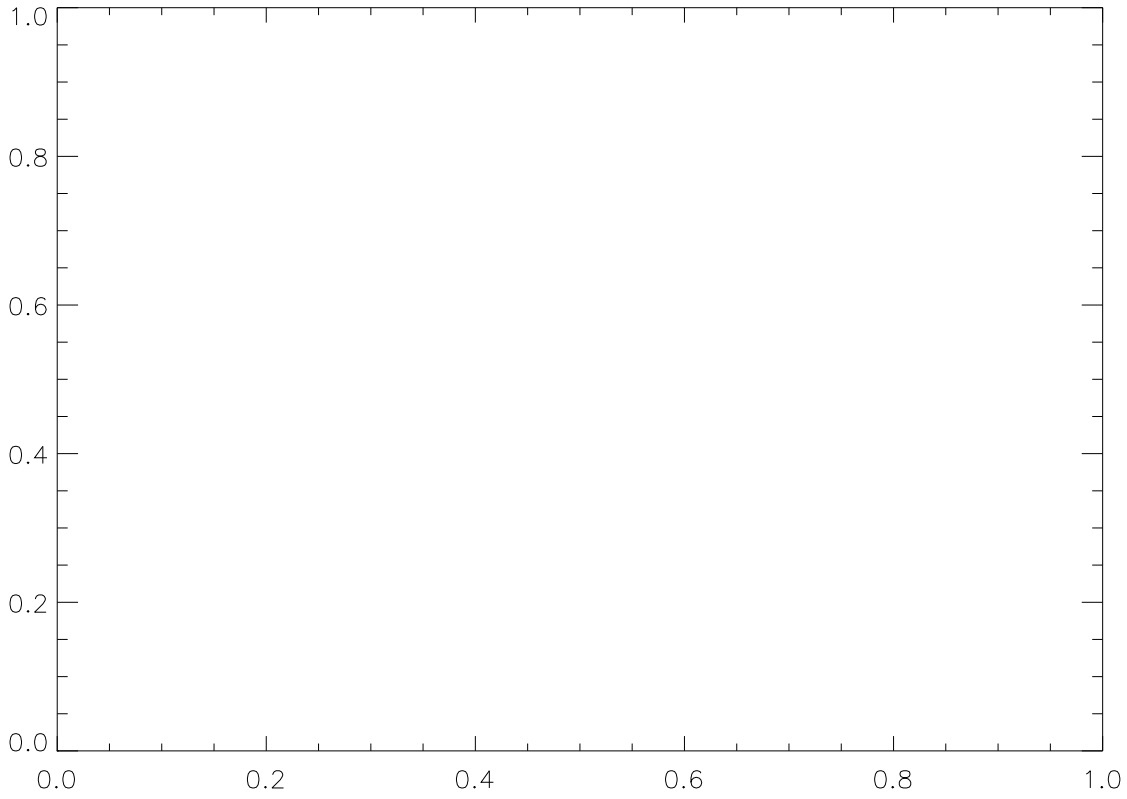

Figure 6.7: Vertical velocity at 2 km height resulting from the interaction of the vortex and vertical shear described by Trier et al. (1998). The results at (a) 0.5 hr and (b) 6 hr are shown. Dark shading denotes values from -1 to -3 cm s^{-1} and light shading values from 1 to 3 cm s^{-1}. From Trier et al. (1998), used with permission.

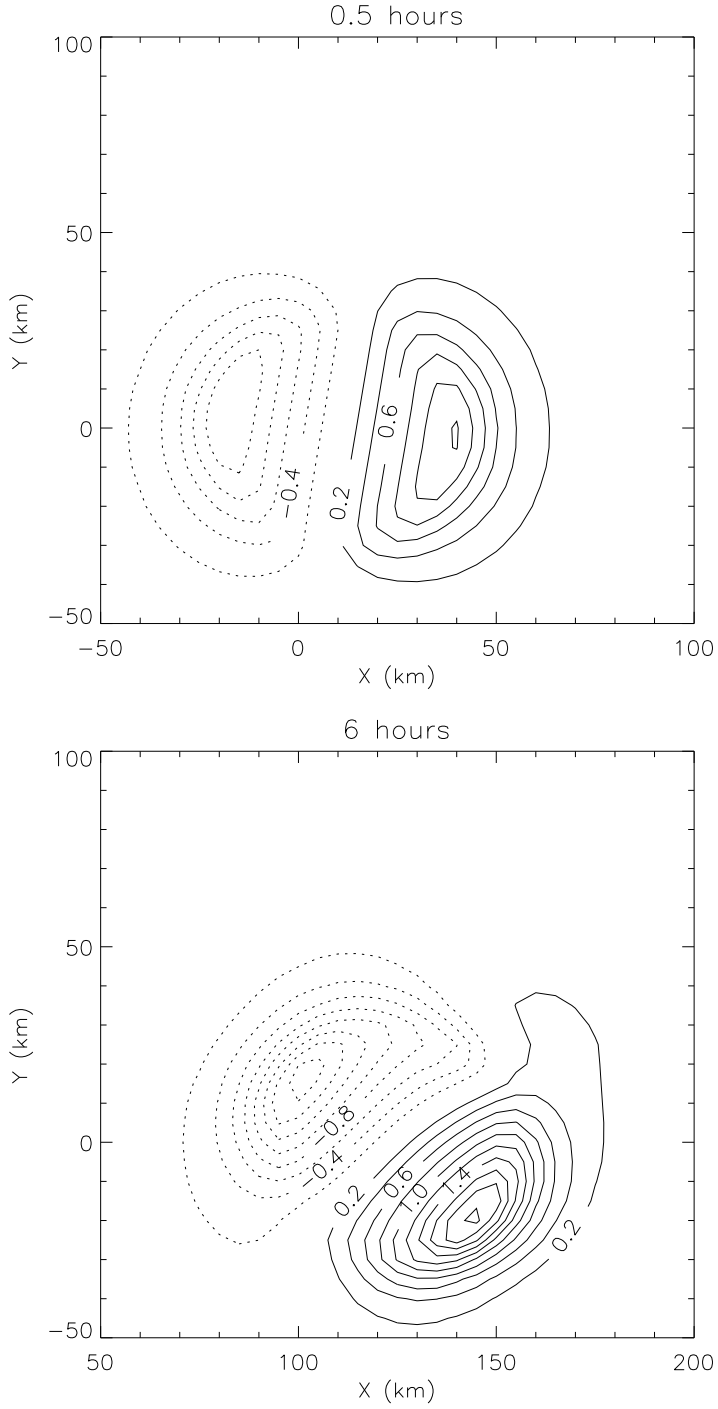

Figure 6.8: Vertical velocity derived from the omega-equation at 2 km height resulting from the interaction of the vortex and vertical shear described by Trier et al. (1998). The results at (a) 0.5 hr and (b) 6 hr agree with the PE simulations of Trier et al. The grid is shifted to the east to account for the eastward translation and increased vertical tilt of the vortex with time. Contour interval is 0.2 cm s^{-1} with dashed contours representing downward motion.

6.3 Observations of TC Vortex Alignment

The observations of Hurricane Olivia on 25 September 1994 provide a unique look at the role of vertical shear in producing structural changes to the inner-core wind field. The seven consecutive wind composites capture for the first time the asymmetric response of a hurricane to dramatic changes in vertical shear over a relatively short time period. Figure 6.9 shows hodographs of area-averaged storm-relative wind ($\mathbf{V}_e - \mathbf{V}_s$) during the observation period. Figure 6.10 shows the best estimate of inner-core vortex tilt derived from the simplex algorithm. Initially the maximum local vertical shear is weak west-northwesterly, with values on the order of 3-5 m s^{-1} over the 0.75 km to 10.5 km depth. Consistent with the weak shear, the vortex is nearly vertically aligned. Over the next 2.5 h the maximum shear increases to 15 m s^{-1} over the 0.75 km to 10.5 km depth and is westerly. A west to east tilt of the vortex with height evolves, with a maximum displacement from low to middle levels of about 3 km. Inspection of the flow field from 6 km to 10.5 km height, where the simplex algorithm for finding the vortex center is less reliable, indicates that the inner-core does not tilt more than 5 km (not shown).

According to the adiabatic mechanism for vertical velocity production, the preferred location for enhanced convection due to vertical shear effects should be downshear-right in the east to southeast quadrant of the storm. Olivia was moving to the north-northeast at about 5 m s^{-1} during this time, so enhanced asymmetric boundary layer convergence and, hence, convection might also be expected in the north-northeast quadrant (Shapiro 1983). Figure 6.11 shows an azimuth-height cross-section of vertical velocity in Olivia's inner core at 14 km radius. The upward velocity is generally maximum downshear during legs 1 and 2, and consistent with the weak vertical shear during this time the values are smaller than observed during latter legs. The front to back convective asymmetry discussed by Shapiro (1983) is not apparent during the small shear/tilt period. It may exist at low levels unresolved in the present analysis.

As the vertical shear and vortex tilt increase, the maximum upward velocity increases from 1-2 m s^{-1} to 6-10 m s^{-1} and the pattern of convection becomes more complicated. A "double maximum" in upward motion develops on the downshear side of the vortex

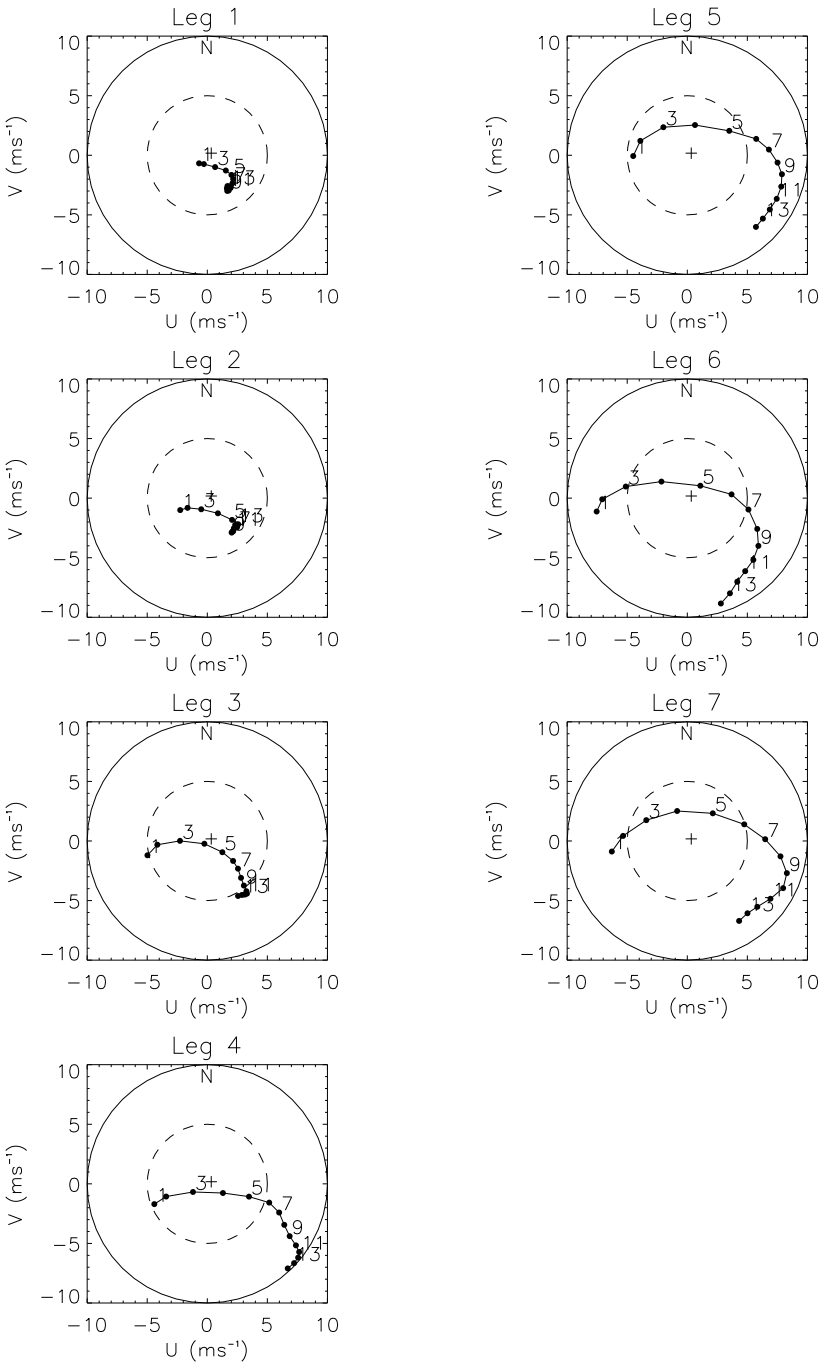

Figure 6.9: Hodographs of the area-averaged storm-relative wind ($\mathbf{V}_e - \mathbf{V}_s$) from 0.75 km to 10.5 km height for each flight leg. The vertical distance between points is 0.75 km.

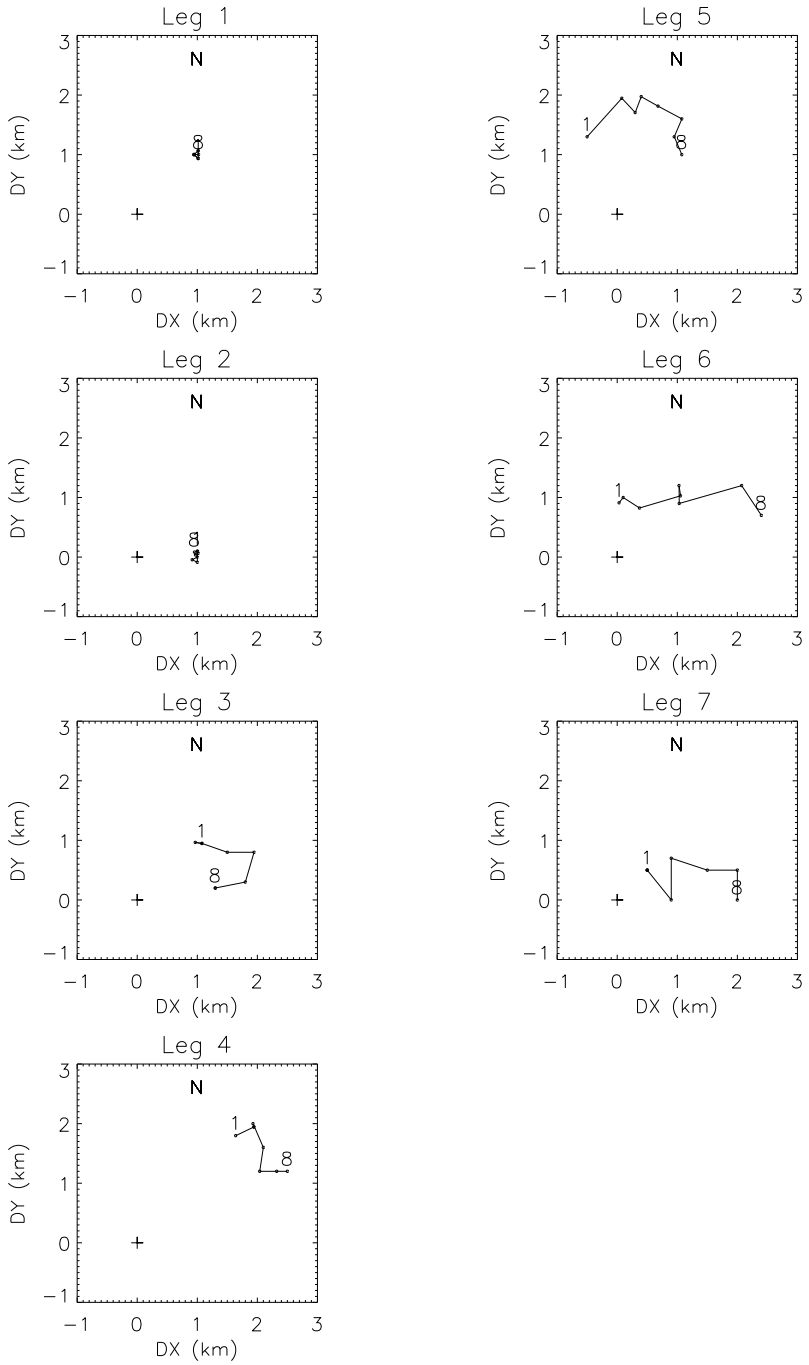

Figure 6.10: Departures of the simplex-algorithm center (•) from the flight-level center (+) as a function of height from 0.75 km to 6 km for each flight leg.

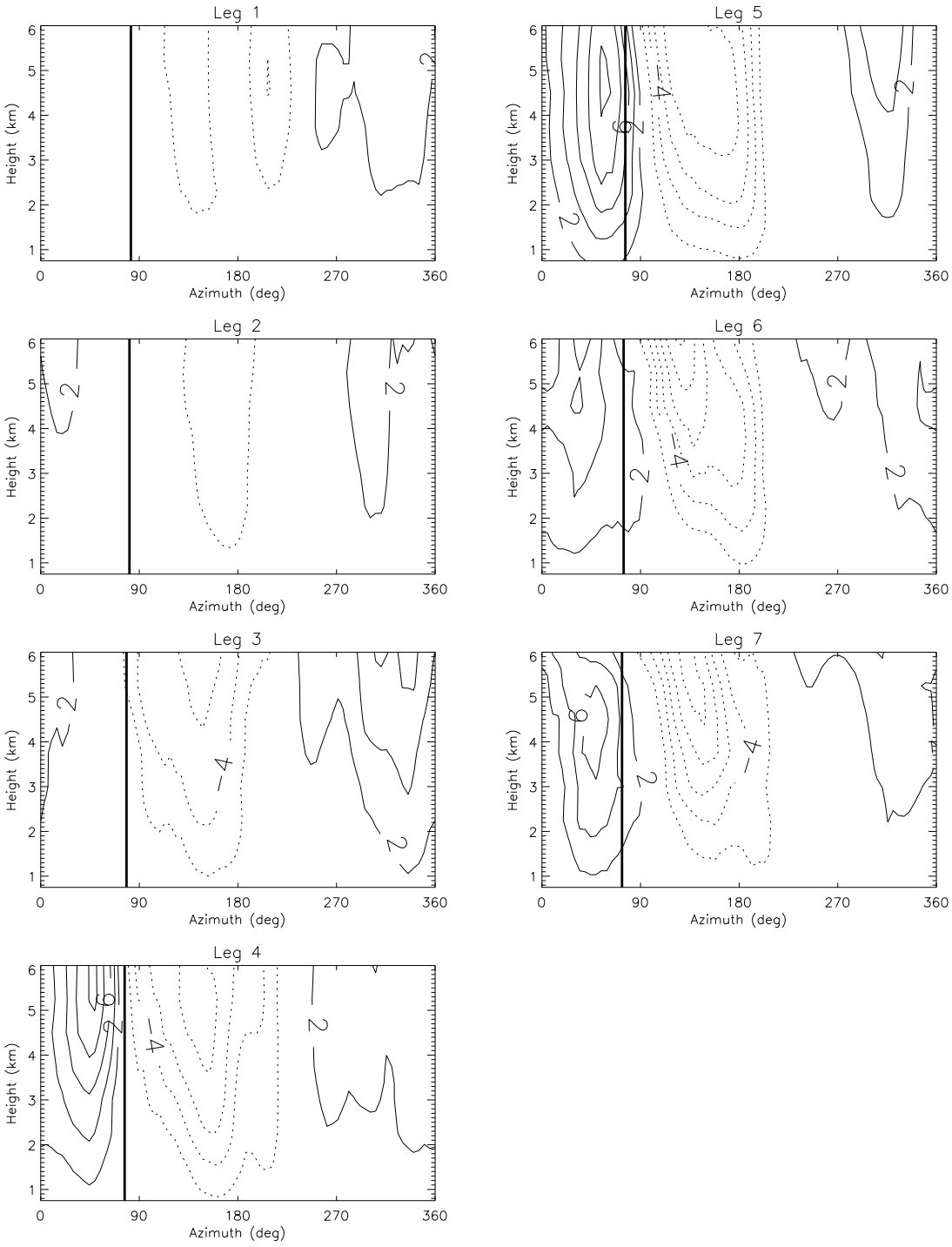

Figure 6.11: Azimuth-height cross-section of vertical velocity at 14 km radius from the storm center for each flight leg. North is located at 90° and West is located at 180°. Contour interval is 2 m s^{-1}. Negative values are depicted by the dashed curves. The heavy, solid vertical line denotes the direction of storm motion.

with one maximum downshear-left and the other downshear-right. The downshear-left maximum tends to be the stronger of the two. The storm motion during the period from leg 1 to leg 7 is relatively steady and the direction of motion changes gradually by only 10 degrees, so it is unlikely that the dramatic *changes* in vertical motion could be attributed to the asymmetric boundary layer convergence described by Shapiro (1983).

The observed trend of increased upward motion downshear and downshear-right with increased vertical shear and vortex tilt is consistent with the adiabatic mechanisms discussed in Section 6.2. Frank and Ritchie (1999) found, however, that in their numerical simulations of hurricanes in unidirectional vertical shear the downshear cold potential temperature anomaly produced via adiabatic mechanisms was eradicated in regions where layers were lifted to saturation. The contribution to upward vertical motion from vortex flow on the distorted isentropes of the tilted vortex was then eliminated. The emergence of a downshear-left convective asymmetry was hypothesized to result from low-level convergence through the downward projection of the downshear-displaced upper-level vortex PV at the surface. Olivia's tilt with height, while generally from west to east, shows an anticyclonic curvature consistent with the anticyclonic rotation of the shear vector with height. The surface projection of Olivia's tilted PV at different upper levels could force more broadly distributed mesoscale convection on the downshear side of the vortex, as observed. Although the relative roles of the mechanisms described above are unclear in this case, the involvement of vertical shear in producing the convective asymmetry is very likely.

If a tilted vortex supports a long-lasting quasi-mode, a persistent region of asymmetric convection and low-level positive PV generation is expected. In the initial stages of tropical cyclogenesis this may be especially important as it provides a means of producing pulses of PV near the vortex core over an extended period of time. The pulsing of PV followed by its axisymmetrization are an integral part of the TC genesis mechanism of ME98. That the asymmetric convection is tied to the vortex core results in a more efficient axisymmetrization and mean flow intensification mechanism (ME98).

Understanding the influence of vortex-scale dynamics on the distribution of convection in the hurricane inner core should also aid in the prediction of the gross precipitation

structure of a hurricane as it enters or is embedded in different environmental flows. A clear relationship exists between the mesoscale asymmetry in convection believed to be forced by the vertical shear of the environmental winds (Fig. 6.11) and the asymmetric pattern of reflectivity (Fig. 2.2). The largest values of reflectivity occur immediately downwind of the regions of enhanced convection, consistent with hydrometeors being carried up by the updrafts of the convective cells and simultaneously swept downwind by the much stronger primary tangential circulation.

Chapter 7

CONCLUSIONS

The axisymmetric conceptual model of the TC life-cycle (e.g., Ooyama 1969) has added tremendously to our basic understanding of TC intensity change. The axisymmetric view continues to provide new insight into TC evolution (e.g., Montgomery et al. 2000). In spite of the contributions of symmetric models to fundamental understanding, they have not demonstrated the capacity to accurately predict TC intensity change in all cases. The effects of asymmetric environmental influences like synoptic-scale troughs and vertical shear are generally not parametrized in these models and can have significant impacts on TC evolution. In cases where environmental asymmetries are not observed to play a large role in the evolution of the TC, symmetric ocean-atmosphere models have shown modest success in predicting gradual changes in TC intensity over open ocean. A notable example is the axisymmetric model of Emanuel (1995). Emanuel (1999) predicted the temporal evolution of maximum tangential wind for several observed hurricanes with this model using as input the initial observed maximum tangential wind, the ocean structure along the observed track, and the degree of saturation required to obtain the initial observed intensification rate. Asymmetric redistribution of vorticity, which is central to this dissertation, was simply parametrized as an enhanced radial momentum diffusion (Emanuel 1989). Emanuel (1989) states that some radial momentum diffusion is necessary to maintain a realistic eye and to obtain realistic vortex amplification rates at early times, but the actual magnitude of the diffusion is not crucial. Based on the examples shown, taken at face value, the model demonstrates skill in predicting the basic trends in intensity. The ocean is, after all, the primary energy source for the hurricane, so the ocean make-up should be reflected in the intensity evolution of the vortex. Therefore, for the

purpose of intensity prediction, do we really need to resolve asymmetric dynamical processes, or is it sufficient to simply parameterize their effect through enhanced momentum diffusion?

A closer look at the examples chosen by Emanuel (1999), which are likely the best possible cases (although a couple failures attributed to vertical shear and nuances of the ocean structure were presented), shows that the more rapid fluctuations in intensity (aside from the initial intensification over open ocean and spin-down over land) are generally not captured by his model. The model sometimes produces fluctuations in maximum tangential wind qualitatively consistent with the observations, but in other instances the fluctuations are temporally offset from the observed fluctuations by a day or two, creating the illusion that the changes in intensity are related. Given that the simulated vortex evolution is, according to Emanuel (1999), "quite sensitive to the initial state," the results must be approached with caution. The axisymmetric simulations do not provide convincing evidence that one need only represent the symmetric ocean-atmosphere interaction to capture *all* (non-environmental related) intensity fluctuations. Internal asymmetric dynamical mechanisms may be responsible for some of the observed fluctuations. Furthermore, to obtain the correct amplitude of the fluctuations, the asymmetric mechanisms will likely need to be represented explicitly.

From an operational standpoint, why should we care about accurately resolving these fluctuations if the basic trends are captured? The answer is quite simple: These fluctuations in tangential wind can, in some cases, mean the difference between a 45 ms^{-1} and 60 ms^{-1} hurricane at landfall, which in practical terms translates into the difference between minor structural damage and potentially extensive damage. Additionally, the maximum tangential wind can appear as a localized anomaly generated internally, as in the case of eyewall mesovortices produced through the barotropic instability of the vortex flow (S99). The peak tangential wind associated with the anomaly superposed on the background mean flow may be substantially larger than that produced through an axisymmetric simulation using the same vortex profile.

The above discussion pertains to the intensity change of already well-developed storms. Can the genesis of a TC be captured using an axisymmetric model? Rotunno and

Emanuel (1987), using an axisymmetric model, demonstrated that finite-amplitude incipient vortices whose strength lies above a threshold can develop into mature cyclones. Bister and Emanuel (1997) through a combined observational and axisymmetric model study of the genesis of Hurricane Guillermo (1991) proposed that following the formation of a mid-level MCV, lower-tropospheric evaporation of rain moistens the low levels and generates a downdraft. This downdraft advects the mid-level vorticity downward. Enhancement of surfaces fluxes due to the increased low-level winds leads to enhanced convection and, therefore, low-level vorticity. Through thermal wind balance, the strengthening of the winds then leads to a warm-core vortex. Agreement between observations and the axisymmetric simulation were demonstrated. Bracken (1999) performed a re-analysis of the Guillermo observations using the entire data set and found at low (1–3 km) and middle (5–7 km) levels a more asymmetric evolution of the vorticity associated with pre-Guillermo than described by Bister and Emanuel, with the vortex centers at low and middle levels often offset horizontally. Obviously one could not simulate the asymmetric vortex interaction suggested by these observations with an axisymmetric model.

The focus of this dissertation was on the role of asymmetric dynamical processes internal to the TC vortex in promoting structure and intensity change, specifically mechanisms that cause redistribution of vorticity. Changes in the PV field, through invertibility, yield changes in the wind structure of the vortex. The internal dynamics was considered in two stages: We first explored the horizontal redistribution of vorticity using wind fields derived from dual-Doppler measurements within Hurricane Olivia (1994). Some of the two-dimensional ideas presented were then applied to the problem of three-dimensional vorticity redistribution in the context of vortex vertical alignment and vortex merger within incipient tropical vortices.

7.1 Horizontal vorticity redistribution

For completeness, we first considered the symmetric weakening of Hurricane Olivia. We did not speculate as to the primary cause of the weakening, but it likely involved both increases in the environmental vertical shear and reductions in the SSTs as Olivia

moved northward. The magnitude of the observed near-linear decrease in tangential winds with time in the vicinity of the RMW agreed with the axisymmetric vortex spin-down predictions of Eliassen and Lystad (1977) despite the observation of inflow up to 3.5 km height and the presence of environmental vertical shear. Comparison of the observed mean tangential wind tendency and estimated tendency based on the symmetric radial and vertical advection of tangential momentum showed qualitative agreement over the 3.5 hr observation period, with a negative tendency in the vicinity of the RMW and positive tendency radially outside the RMW. It was not readily apparent that the observed spin-up of tangential winds inside the eye could be accounted for by purely axisymmetric phenomena. We therefore hypothesized that asymmetric mechanisms might be playing an important role in Olivia's symmetric evolution.

The vorticity asymmetry in Olivia's inner core was dominated by an azimuthal wavenumber 2 feature below 3 km height and a wavenumber 1 feature above 3 km, both maximum near the RMW. During leg 1 the wavenumber 2 asymmetry extended from low to middle levels of the storm and appeared to decay through leg 2. An increase in the wavenumber 1 asymmetry at middle levels around leg 3 coincided with the increase in vertical shear. Tilting of horizontal vorticity by enhanced convection on the east side of Olivia, as suggested by Gamache et al. (1997), is a possible mechanism for the production of the wavenumber 1 asymmetry, but a consistent vorticity budget could not be performed with this data and, thus, no definitive conclusions could be drawn. Following leg 3 a low-level wavenumber 2 asymmetry re-emerged and persisted through the end of the observation period.

Lower fuselage reflectivity composites at low levels during leg 5 depicted an elliptical eye rotation. The rotation period was consistent with Kelvin's predictions for a wavenumber 2 vorticity asymmetry propagating on the discontinuity of a Rankine vortex (Olivia's mean vorticity gradient outside 10 km radius was indeed sharp). The major axis of the reflectivity ellipse was found to be aligned with the axis of positive vorticity of the wavenumber 2 vorticity asymmetry observed during leg 5. Since this asymmetry likely had its structure and azimuthal phase speed modified by convection and axisymmetrization,

we did not observe general agreement between the phase evolution from leg to leg and Kelvin's simple dispersion relation, except between legs 5 and 6.

The possibility that the low-level wavenumber 2 asymmetry formed as a result of internal dynamical mechanisms was considered in light of recent theoretical and numerical work by S99 exploring the two-dimensional barotropic instability of hurricane-like vorticity profiles. Olivia's inner-core vorticity profile during leg 1 was found to take the form of a vorticity ring and was most unstable to wavenumber 2 perturbations. The profile during later legs took on a more monotonic structure with increased values at the vortex center and reduced values in the vicinity of the ring peak. This evolution of the symmetric vorticity is consistent with the numerically-simulated breakdown of a vorticity ring through barotropic instability described by S99 and our own simulations using Olivia-like profiles. The wavenumber 2 vorticity asymmetry found in Olivia's eyewall region is an expected by-product of the vorticity ring breakdown.

Part of the vorticity mixing hypothesized to occur in the hurricane near-core region is the expulsion of high vorticity from the eyewall in the form of linear and nonlinear vortex Rossby waves (MK; S99). The perturbation vorticity at 3 km height showed trailing spiral bands of vorticity with radial wavelengths of 5-10 km outside of the regions of high vorticity associated with the wavenumber 2 vorticity asymmetry. These features may be symmetrizing vortex Rossby waves. A secondary bump in symmetric vorticity outside the RMW was hypothesized to result from the interaction of outward-propagating vortex Rossby waves with the mean vortex flow. The estimated stagnation radius for vortex Rossby waves excited in the eyewall was consistent with the location of the vorticity bump. Spiral bands of enhanced reflectivity were observed in the vicinity of the vorticity bands, suggesting a coupling of the vorticity bands to the boundary layer through a forced asymmetric transverse circulation. The possible connection between these vorticity and reflectivity features is of great interest and is a topic of current study using full-physics numerical model output.

7.2 Three-dimensional vorticity redistribution

The conditions under which a vertically-tilted vortex aligns have been documented in previous studies (e.g., Polvani 1991). The cause for alignment (or non-alignment) offered in these studies is based on a nonlinear view of the dynamics: Given the basic geometry of the initial vortex (e.g., a two-layer vortex consisting of circular patches of PV horizontally offset from one another) and the Rossby deformation radius, a vortex configuration can be derived which is a stationary solution of the nonlinear equations of motion formulated in a rotating coordinate system. The nearness of the initial vortex to one of these co-rotating vortex states (i.e., V-states) determines whether or not alignment will occur. A vortex in a parameter regime (defined by the tilt and deformation radius) far removed from a V-state is said to align through nonlinear filamentation and wave breaking. In the context of the laboratory and numerical simulations that have motivated this interpretation where a random distribution of vorticity evolves into horizontally-coherent vortices, which then align from great horizontal distances to form vertically-coherent vortices, this is a natural and useful approach to the problem. The question we have addressed here is whether the geometric interpretation of three-dimensional vortex alignment is the most insightful one once the vortex cores at upper and lower levels begin to overlap. We demonstrated that in this limit a new, physically-based understanding of vortex alignment supplants the geometric interpretation. The dynamics is accurately characterized as linear, thus reducing the parameter space that one must consider in order to predict the subsequent vortex evolution.

The evolution of an initially-tilted PV column for which the nonlinear advective PV tendency is small compared to the linear radial advective tendency (i.e., $R_\beta << 1$) is captured by linear vortex Rossby wave processes. In this situation the vortex is meaningfully decomposed into azimuthal-mean and perturbation components. The conceptual picture of vortex alignment is then as follows: The perturbation PV tendency at upper(lower) levels is ascribed to the azimuthal advection of perturbation PV by the upper(lower)-level mean flow and the radial advection of mean PV by the perturbation wind. The perturbation wind at upper(lower) levels is the sum of the flow associated with the upper(lower)-level PV anomaly and, according to the vertical penetration depth, the lower(upper)-level

PV anomaly. For continuously-distributed PV this problem has not yet allowed analytical solution despite its linear nature. Numerical vortex simulations based on the linear equivalent-barotropic QG system, and validated with a nonlinear three-dimensional QG model, show a dependence on the internal Rossby deformation radius consistent with previous studies. The physical explanation for the tilted vortex evolution, however, departs from these studies.

In the non-divergent limit (i.e., infinite internal deformation radius) the stationary pseudo-mode is recovered. For large but finite internal deformation radii the upper and lower PV anomalies slowly co-rotate. As the deformation radius is decreased, the co-rotation frequency increases. An azimuthally-propagating quasi-mode with the vertical structure of the first internal baroclinic mode and wavenumber one azimuthal structure is found to be responsible for the co-rotation and inhibits vortex alignment. The quasi-mode, defined as a superposition of singular neutral modes sharply peaked in the phase speed spectrum, decays slowly in the presence of differential rotation. A transition region centered on the horizontal vortex scale separates this regime from the alignment regime at smaller internal deformation radii. The transition is accounted for by the spectral broadening of the quasi-mode. In the alignment regime the decay rate of the quasi-mode is so large that the initial perturbation is essentially projected onto the (non-quasi-modal) continuous spectrum of vortex Rossby waves whose integrated perturbation energy decays algebraically to zero in the limit of long times. Alignment is defined here as when the intercentroid separation distance between upper- and lower-level PV anomalies is zero. We believe this to be a more accurate definition than used by Polvani (1991) who defined alignment as a net decrease in the intercentroid separation distance over one circulation period. In the single-interface CD model, Rossby edge waves persist where alignment is observed for continuously-distributed vortices. Sheared linear vortex Rossby waves promote the irreversible redistribution of PV necessary for complete alignment.

We argued that linear theory captures the essence of co-rotation even as R_β approaches unity due to the robustness of the quasi-mode. In this regime nonlinear advection simply tries to counteract the sheared vortex Rossby wave dispersion. As the internal

deformation radius is decreased within the alignment regime (vortex Burger number order unity or less), R_β for the baroclinic portion of the asymmetry decreases rapidly. Thus, linear theory will capture the vortex alignment process for a wider range of initial tilts the smaller the internal deformation radius. The largest tilt considered here was when the RMW of the upper-level vortex overlapped the vortex center at lower levels. R_β was less than 0.2 for this tilted configuration for an internal deformation radius near 50 km. Thus, it is possible that alignment can still be approximately described with linear dynamics even for vortices with barely overlapping upper- and lower-level PV centers. The determination of the precise boundary in parameter space which delineates complete breakdown of the linear approximation remains for future work.

These ideas are believed to have practical application to the problem of tropical cyclogenesis. One of the basic questions in TC research is how a weak vortex with nearby convection resists the effects of external shear and strengthens. The dynamics of the asymmetric TC genesis mechanism of ME98 was further clarified by explicitly demonstrating that the merger and alignment of convectively-generated low-level positive PV within the RMW of a pre-existing vortex can be captured by linear vortex Rossby wave processes. The attendant strengthening of the low-level mean vortex was also captured by wave-mean dynamics.

In typical tropical conditions this process is frustrated by vertical shear. Smith et al. (2000) found that a tilted vortex will either break apart under the influence of vertical shear or co-rotate. Co-rotation did not occur in their two-layer model with distributed vortices when twice the product of coupling constant (ranging between 0 and 1) and maximum mean tangential wind was less than the difference between upper and lower level "environmental" zonal flow. Depending upon the value of the internal deformation radius, the linear alignment mechanism discussed here suggests that the tilting of a vertically-aligned vortex by shear will either project perturbation energy onto the wavenumber one quasi-mode or entirely onto sheared vortex Rossby waves. In the latter case axisymmetrization of the perturbation PV through the interaction of vortex Rossby waves with the mean flow will resist the tilting by shear. In this regard, vertical shear acts as a sheared vortex

Rossby wave generator. This interpretation of the interaction of a vortex with vertical shear is another way of viewing the vortex tilt evolution described by Jones (1995) for $R_\beta < 1$. Jones correctly noted that the asymmetric transverse circulation associated with a tilted vortex is not fundamentally responsible for countering the effects of vertical shear, as suggested by Wang et al. (1993). The transverse circulation is simply a requirement of a balanced vortex whose flow is evolving in time. Jones' conclusion that "the rotary behaviour of the vortex provides a mechanism which opposes the destructive action of the vertical shear" is consistent with the interpretation provided here, but does not fully elucidate the underlying dynamics. The vortex tilt evolutions shown by Jones may very well be captured by linear vortex Rossby wave theory at early times. As the upper- and lower- level PV centers become substantially removed from each other in the horizontal, the linear theory will break down.

The asymmetric transverse circulation of a tilted vortex can effect vortex tilt *indirectly* by forcing asymmetric convection and low-level asymmetric PV generation. The basic dynamics of this convective enhancement mechanism was illustrated using data from Hurricane Olivia. The increase in westerly local vertical shear of Olivia's environment from 3-5 m s^{-1} to 15 m s^{-1} over the lowest 10 km depth during the 3.5 h observation period was accompanied by an increase in the west to east tilt of the storm center with height and a dramatic increase in convection on the east side of the vortex. A double maximum in the convection was found with largest upward motion downshear-left ($\sim$ 8-12 m s^{-1}) and weaker upward motion downshear-right ($\sim$ 4-6 m s^{-1}). These observations are consistent with recent numerical simulations of hurricane-like vortices in vertical shear (Jones 1995; DeMaria 1996; Bender 1997; Frank and Ritchie 1999).

For barotropic vortices tilted by vertical shear with small Rossby numbers we derived an expression for the Q-vector convergence, illustrating the relative contributions to vertical motion from vortex motion on ambient isentropes and vortex motion on the isentropes of the tilted vortex. This formula was verified to produce qualitatively correct results for Rossby numbers near unity through a comparison with PE simulations performed by Trier et al. (1998). Future work will extend these results to mesoscale convective vortices and hurricane-strength vortices by utilizing the AB generalization of the QG omega equation.

In addition to adding vertical shear to the linear problem, the next step is to extend the QG results to more rapidly rotating flows. The vertical penetration depth will not only become a function of radius, but will also increase over the QG value. This was clearly demonstrated by Shapiro and Montgomery (1993) in the context of the AB formulation for hurricane-like flows, where the local penetration depth is proportional to the square root of the product of the modified Coriolis parameter and absolute vorticity of the associated vortex flow. Preliminary simulations in which the linearized equivalent barotropic AB model is initialized with our tilted benchmark vortex agree with the corresponding QG simulations. Further work is required, however, to understand the effect of variable penetration depth on the evolution of the tilted vortex. It is possible that an altogether new quasi-mode in quasi-gradient balance exists at higher swirl speeds. Its characteristics and relevance to hurricane-like flows (e.g., track wobbles) would be of great interest. This will be the subject of future investigation.

As an immediate application of the present study, work is under way to use output from cloud-resolving numerical model simulations (e.g., MM5 or RAMS) of TC genesis to examine the asymmetric distribution of vorticity and its evolution in time. The ideas presented here regarding linear vortex alignment will be tested in a situation where a blow-up of convection is observed inside the RMW of a pre-existing vortex. Is there positive vorticity generation at low levels and does it move closer to the vortex core in time? Is R_β less than unity? Based on the relative magnitudes of the internal deformation radius and horizontal vortex scale, is alignment or co-rotation favored? It is important to determine if the dry, idealized model predictions (and perhaps ultimately closed-form solutions) have relevance even in convective situations where large vertical momentum transports are allowed to occur and the dynamics is not so tightly constrained to the slow manifold.

Plans are to extend this work ultimately to the analysis of observational TC genesis data sets, like Guillermo (1991). Very few of these type of data sets exist, and none have been analyzed with the asymmetric mechanisms presented here and in other theoretical studies (e.g., ME98) in mind. So from an observational standpoint, how a TC initially

forms is still an open question. Asymmetric theories for TC genesis do provide a viable alternative to symmetric finite amplitude instability theories (Emanuel 1989), and we hope to demonstrate the usefulness of these ideas in the near future.

Appendix A

Q-VECTOR DIAGNOSTIC

In cylindrical coordinates (r, λ, z) the geostrophic radial and tangential winds are

$$u = \frac{-2Rv_{max}\alpha z \sin\lambda}{R^2 + (r\cos\lambda - \alpha z)^2 + (r\sin\lambda)^2} + U_e(z)\cos\lambda, \tag{A.1}$$

$$v = \frac{2Rv_{max}(r - \alpha z\cos\lambda)}{R^2 + (r\cos\lambda - \alpha z)^2 + (r\sin\lambda)^2} - U_e(z)\sin\lambda.$$

Substituting (u,v) into Eq. (6.13), we obtain the radial and azimuthal components of the Q-vector. Taking the horizontal divergence of $\mathbf{Q}$ in cylindrical coordinates and defining nondimensional parameters, $b = r/R$ and $a = \alpha z/R$, yields

$$\begin{aligned}\nabla\cdot\mathbf{Q} \;=\; & \frac{16f^3Ro}{R(1+b^2+a^2-2ab\cos\lambda)^4}[(\alpha Ro)(2b - b^3 + \\ & 2ab^2\cos\lambda - a^2b)\sin\lambda - \frac{1}{f}(\frac{\partial U_e}{\partial z})((1+b^2)b\cos\lambda - \\ & a(1+b^2+2b^2\cos^2\lambda) + 3a^2b\cos\lambda - a^3)].\end{aligned} \tag{A.2}$$

This expression for $\nabla\cdot\mathbf{Q}$ is defined in a cylindrical coordinate system whose origin is the vortex center on the lowest surface, $z = 0$. Thus, as the tilt (i.e., αz) becomes large, harmonics other than wavenumber one will attain significance in the expression for $\nabla\cdot\mathbf{Q}$ in this coordinate system. If we instead transform to a coordinate system (r', λ', z) in which the origin at each level is the vortex center at that level, i.e., let

$$r'\sin\lambda' = r\sin\lambda \tag{A.3}$$

$$-r'\cos\lambda' = \alpha z - r\cos\lambda,$$

then the simpler and more concise expression for $\nabla\cdot\mathbf{Q}$ given in Eq. (6.14) is obtained which projects only onto wavenumber one.

Appendix B

SIMULATING VORTEX ALIGNMENT: PV PATCHES VERSUS CONTINUOUS PROFILES

Closed-form EQB solutions to the linear tilted vortex problem can be obtained for mean vortices whose radial structure is that of a vortex patch, i.e.,

$$\overline{\zeta}(r) = \begin{cases} \overline{\zeta}_{max}, & 0 \geq r < a \\ 0, & a < r \leq \infty \end{cases} \tag{B.1}$$

Solutions to Eqs. (4.13)–(4.15) are sought of the form:

$$\tilde{\psi}_{mn}(r,t) = \tilde{\psi}_{cs}(r,t) + \tilde{\psi}_{ew}(r,t), \tag{B.2}$$

$$\tilde{q}_{mn}(r,t) = \tilde{q}_{cs}(r,t) + \tilde{q}_{ew}(r,t),$$

where 'cs' denotes the continuous spectrum and 'ew' the edge wave component. The solution method follows Smith and Montgomery (1995) and its generalization to the shallow water system (courtesy Prof. M. Montgomery, personal communication).

The continuous spectrum solution is given by

$$\tilde{\psi}_{cs}(r,t) = \int_0^\infty G(r,\rho)\tilde{q}_0(\rho)e^{-in\overline{\Omega}t}\rho d\rho, \tag{B.3}$$

where

$$G(r,\rho) = -\begin{cases} I_n(\gamma_m\rho)K_n(\gamma_m r), & \rho \geq r \\ I_n(\gamma_m r)K_n(\gamma_m\rho), & \rho \leq r \end{cases} \tag{B.4}$$

is the Green's function and $\tilde{q}_0$ is the initial PV perturbation. I_n and K_n are the modified Bessel functions.

The edge wave solution is found by solving the modified Bessel equation on both sides of the basic state discontinuity. In both regions the mean vorticity gradient is identically zero. It follows that

$$\tilde{\psi}_{ew}(r,t) = C_n(t)\tilde{\phi}_{ew}(r), \tag{B.5}$$

where

$$\tilde{\phi}_{ew}(r) = -a \begin{cases} I_n(\gamma_m r)K_n(\gamma_m a), & r \leq a \\ I_n(\gamma_m a)K_n(\gamma_m r), & r \geq a \end{cases} \tag{B.6}$$

The dynamic condition requires pressure continuity at $r = a$. From this condition $C_n(t)$ can be determined, completing the solution:

$$C_n(t) = -\frac{n\overline{\zeta}_{max}}{a} \int_0^\infty \frac{d\rho\rho G(a,\rho)\tilde{q}_0(\rho)}{\sigma_n - n\overline{\Omega}} e^{-in\overline{\Omega}t} + \tag{B.7}$$

$$\left\{ C_0 + \frac{n\overline{\zeta}_{max}}{a} \int_0^\infty \frac{d\rho\rho G(a,\rho)\tilde{q}_0(\rho)}{\sigma_n - n\overline{\Omega}} \right\} e^{-i\sigma_n t}, \tag{B.8}$$

where C_0 is a constant of integration and

$$\sigma_n = n\overline{\zeta}_{max}[1/2 - I_n(\gamma_m a)K_n(\gamma_m a)] \tag{B.9}$$

is the edge wave rotation frequency.

This solution is intended to mimic the single-interface CD solution in the limit of infinitesimal vertical tilt. There are two points worth making regarding the linear solution. First, note that σ_n is nonzero for all $n > 0$ and $\gamma_1 > 0$. Therefore, as $t \to \infty$, oscillatory edge wave solutions exist for all wavenumbers. For continuous vortex monopoles, wavenumbers greater than one symmetrize within a couple τ_e (see Fig. 5.7). Second, note that as $\gamma_1 a \to \infty$, (Abramowitz and Stegun 1972)

$$K_1 \sim \sqrt{\frac{\pi}{2a\gamma_1}} e^{-a\gamma_1} \tag{B.10}$$

and

$$I_1 \sim \frac{1}{\sqrt{2\pi a\gamma_1}} e^{a\gamma_1}, \tag{B.11}$$

so σ_1 approaches $\overline{\zeta}_{max}/2$ and wavenumber one propagates around the vortex indefinitely. This is consistent with the CD simulations of Polvani (1991) where co-rotation was found in this parameter regime. Continuous vortex monopoles, however, do not exhibit this behavior.

As γ_1 increases, the Green's function involved in the inversion of perturbation PV for streamfunction decays rapidly away from its source point. The convolution of perturbation PV and Green's function, which defines the streamfunction, will yield smaller values the

larger γ_1 is (see Fig. 5.17). The radial advection of mean vorticity by the perturbation radial wind can then be neglected compared to the azimuthal advection of perturbation PV by the mean tangential wind (which does not depend on γ_1) in the limit $\gamma_1 \to \infty$. The resulting linear PV tendency equation is

$$\left(\frac{\partial}{\partial t} + in\overline{\Omega}\right)\tilde{q}_{mn}(r,t) = 0. \tag{B.12}$$

Thus, the perturbation PV is materially conserved following the mean tangential winds and will take on a spiral pattern around the vortex in time since

$$\tilde{q}_{mn}(r,t) = \tilde{q}_{mn}(r,0)e^{-in\overline{\Omega}t}. \tag{B.13}$$

The streamfunction is given by $\tilde{\psi}_{cs}$ above, and decays algebraically in the limit of long times (Carr and Williams 1989; Smith and Montgomery 1995). Therefore, continuous vortices always align in the small tilt, large γ_1 limit.

Appendix C

NONDIVERGENT BAROTROPIC EIGENSOLVER

We begin with the linearized vertical vorticity equation for two-dimensional barotropic nondivergent flow

$$(\frac{\partial}{\partial t} + \overline{\Omega}\frac{\partial}{\partial \lambda})\left[\frac{1}{r}\frac{\partial}{\partial r}(r\frac{\partial \psi'}{\partial r}) + \frac{1}{r^2}\frac{\partial^2 \psi'}{\partial \lambda^2}\right] - \frac{1}{r}\frac{\partial \psi'}{\partial \lambda}\frac{d\overline{\zeta}}{dr} = 0, \tag{C.1}$$

where ψ' is the perturbation streamfunction. Given the azimuthal-mean tangential wind and vorticity profiles, solutions to (C.1) of the form

$$\psi'(r, \lambda, t) = \hat{\psi}(r)e^{i(n\lambda + \nu t)} \tag{C.2}$$

are sought, where n is the azimuthal wavenumber, $\hat{\psi}$ the eigen-streamfunction, and ν the eigen-frequency. We require $\hat{\psi}(r)$ vanish as $r \to 0$ and $r \to \infty$. A standard eigenvalue solver is used to perform the numerical calculations following Gent and McWilliams (1986). Independence of the solutions under changes to domain size and radial grid-spacing have been verified.

REFERENCES

Abramowitz, M. and I. A. Stegun, 1972: *Handbook of mathematical functions.* Dover Publications, 1046 pp.

Bargen, D. W., and R. C. Brown, 1980: Interactive radar velocity unfolding. Preprints, *19th Conf. on Radar Meteorology*, Miami Beach, FL, Amer. Meteor. Soc., 278–285.

Battan, L., 1973: *Radar Observations of the Atmosphere.* The University of Chicago Press, 324 pp.

Bender, M. A., 1997: The effect of relative flow on the asymmetric structure in the interior of hurricanes. *J. Atmos. Sci.*, **49**, 703–724.

Bister, M., and K. A. Emanuel, 1997: The genesis of Hurricane Guillermo. TEXMEX analyses and a modeling study. *Mon. Wea. Rev.*, **125**, 2662–2682.

Black, M. L., and H. E. Willoughby, 1992: The concentric eyewall cycle of Hurricane Gilbert. *Mon. Wea. Rev.*, **120**, 947–957.

_____, J. F. Gamache, F. D. Marks, C. S. Samsury, and H. E. Willoughby, 2000: Eastern-Pacific Hurricanes Jimena of 1991 and Olivia of 1994: The effects of vertical shear and ocean temperature on structure and intensity.

Black, P. G., and F. D. Marks, 1991: The structure of an eyewall meso-vortex in Hurricane Hugo (1989). Preprints, *19th Conf. on Hurricanes and Tropical Meteorology*, Miami, FL, Amer. Meteor. Soc., 579–582.

Bosart, L. F., C. S. Velden, W. E. Bracken, J. Molinari, and P. G. Black, 2000: Environmental influences on the rapid intensification of Hurricane Opal (1995) over the Gulf of Mexico. *Mon. Wea. Rev.*, **128**, 322–352.

Bousquet, O., and M. Chong, 1998: A multiple-Doppler synthesis and continuity adjustment technique (MUSCAT) to recover wind components from Doppler radar measurements. *J. Atmos. Oceanic Technol.*, **15**, 343–359.

Bracken, W. E., 1999: A multiscale examination of tropical cyclogenesis. Ph.D. Dissertation, University at Albany, State University New York, 340 pp. [Available from University at Albany, State University New York, Dept. of Earth and Atmospheric Sciences, Albany, NY, 12222.]

Carr, L. E. III, and R. T. Williams, 1989: Barotropic vortex stability to perturbations from axisymmetry. *J. Atmos. Sci.*, **46**, 3177–3191.

Case, K. M., 1960: Stability of inviscid plane Couette flow. *Phys. Fluids*, **3**, 143–148.

Cunning, J. B., and R. I. Sax, 1977: A Z-R relationship for the GATE B-scale array. *Mon. Wea. Rev.*, **105**, 1330–1336.

DeMaria, M., 1996: The effect of vertical shear on tropical cyclone intensity change. *J. Atmos. Sci.*, **53**, 2076–2087.

_____, and J. Kaplan, 1997: An operational evaluation of a statistical hurricane intensity prediction scheme (SHIPS). Preprints, *22nd Conf. on Hurricanes and Tropical Meteorology*, Ft. Collins, CO, Amer. Meteor. Soc., 280–281.

Dritschel, D. G., and M. de la Torre Juarez, 1996: The instability and breakdown of tall columnar vortices in a quasi-geostrophic fluid. *J. Fluid Mech.*, **328**, 129–160.

Dritschel, D. G., M. de la Torre Juarez, and M. Ambaum, 1999: The three-dimensional vortical nature of atmospheric and oceanic turbulent flows. *Phys. Fluids*, **11**, 1512–1520.

Eliassen, A., 1951: Slow thermally or frictionally controlled meridional circulation in a circular vortex. *Astrophys. Norvegica*, **5**, 19–60.

_____, and M. Lystad, 1977: The Ekman layer of a circular vortex: A numerical and theoretical study. *Geophysica Norvegica*, **31**, 1–16.

Emanuel, K. A., 1986: An air-sea interaction theory for tropical cyclones. Part I: Steady-state maintenance. *J. Atmos. Sci.*, **43**, 585-604.

_____, M. Fantini, and A. J. Thorpe, 1987: Baroclinic instability in an environment of small stability to slantwise moist convection, Pt. 1, Two-dimensional models. *J. Atmos. Sci.*, **44**, 1559–1573.

———, 1989: The finite-amplitude nature of tropical cyclogenesis. *J. Atmos. Sci.*, **46**, 3431–3456.

———, 1995: The behavior of a simple hurricane model using a convective scheme based on subcloud-layer entropy equilibrium. *J. Atmos. Sci.*, **52**, 3960–3968.

———, 1999: Thermodynamic control of hurricane intensity. *Nature*, **401**, 665–669.

Enagonio, J., and M. T. Montgomery, 2000: Tropical cyclogenesis via convectively forced vortex Rossby waves. Part II. Validation of quasigeostrophic results with a shallow water primitive equation model. In review.

Farge, M., and R. Sadourny, 1989: Wave-vortex dynamics in rotating shallow water. *J. Fluid Mech.*, **206**, 433–462.

Flierl, G. R., 1988: On the instability of geostrophic vortices. *J. Fluid Mech.*, **197**, 349–388.

Fowles, G. R., 1989: *Introduction to Modern Optics*. 2nd ed. Dover, 328 pp.

Frank, N. L., 1975: Atlantic tropical systems of 1974. *Mon. Wea. Rev.*, **103**, 294–300.

Frank, W. M., and E. A. Ritchie, 1999: Effects of environmental flow upon tropical cyclone structure. *Mon. Wea. Rev.*, **127**, 2044–2061.

Franklin, J. L., S. J. Lord, S. E. Feuer, and F. D. Marks, 1993: The kinematic structure of Hurricane Gloria (1985) determined from nested analyses of dropwindsonde and Doppler wind data. *Mon. Wea. Rev.*, **121**, 2433–2451.

Fung, I. Y.-S., 1977: The organization of spiral rainbands in a hurricane. Ph.D. dissertation, Massachusetts Institute of Technology, 139 pp. [Available from Massachusetts Institute of Technology, Dept. of Meteorology, Cambridge, MA 02139.]

Gall, R., J. Tuttle, P. Hildebrand, 1998: Small-scale spiral bands observed in Hurricanes Andrew, Hugo, and Erin. *Mon. Wea. Rev.*, **126**, 1749–1766.

Gamache, J. F., F. D. Marks, and F. Roux, 1995: Comparison of three airborne Doppler sampling techniques with airborne in situ wind observations. *J. Atmos. Oceanic Technol.*, **12**, 171–181.

Gamache, J. F., H. Willoughby, M. Black, and C. Samsury, 1997: Wind shear, sea surface temperature, and convection in hurricanes observed by airborne Doppler radar. Preprints, *22nd Conf. on Hurricanes and Tropical Meteorology*, Ft. Collins, CO, Amer. Meteor. Soc., 121–123.

———, 1998: Evaluation of a fully three-dimensional variational Doppler analysis technique. Preprints, *28th Conf. on Radar Meteorology*, Austin, TX, Amer. Meteor. Soc., 422–423.

Gent, P. R., and J. C. McWilliams, 1986: The instability of barotropic circular vortices. *Geophys. Astrophys. Fluid Dynamics*, **35**, 209–233.

Glatz, A., and R. K. Smith, 1996: Vorticity asymmetries in Hurricane Josephine (1984). *Quart. J. Roy. Meteor. Soc.*, **122**, 391–413.

Gray, W. M., 1968: Global view of the origin of tropical disturbances and storms. *Mon. Wea. Rev.*, **96**, 669–700.

Guinn, T. A., and W. H. Schubert, 1993: Hurricane spiral bands. *J. Atmos. Sci.*, **50**, 3380–3403.

Hasler, A. F., P. G. Black, V. M. Karyampudi, M. Jentoft-Nilsen, K. Palaniappan, and D. Chesters, 1997: Synthesis of eyewall mesovortex and supercell convective structures in Hurricane Luis with GOES-8/9 stereo, concurrent 1-min GOES-9 and NOAA airborne radar observations. Preprints, *22nd Conf. on Hurricanes and Tropical Meteorology*, Ft. Collins, CO, Amer. Meteor. Soc., 201–202.

Hawkins, H. F., and D. T. Rubsam, 1968: Hurricane Hilda, 1964: II, The structure and budgets of the hurricane on October 1, 1964. *Mon. Wea. Rev.*, **96**, 617–636.

Haynes, P. H., and M. E. McIntyre, 1987: On the evolution of vorticity and potential vorticity in the presence of diabatic heating and frictional or other forces. *J. Atmos. Sci.*, **44**, 828–841.

Held, I. M., and P. J. Phillips, 1987: Linear and nonlinear barotropic decay on the sphere. *J. Atmos. Sci.*, **44**, 200–207.

Holton, J. R., 1992: *An introduction to Dynamic Meteorology.* 3rd ed. Academic Press, 511 pp.

Hoskins, B. J., I. Draghici, and H. C. Davies, 1978: A new look at the ω-equation. *Quart. J. Roy. Meteor. Soc.*, **104**, 31–38.

Jones, S. C., 1995: The evolution of vortices in vertical shear: Initially barotropic vortices. *Quart. J. Roy. Meteor. Soc.*, **121**, 821–851.

Jorgensen, D. P., and P. T. Willis, 1982: A Z-R relationship for hurricanes. *J. Appl. Meteor.*, **21**, 839–856.

_____, P. H. Hildebrand, and C. L. Frush, 1983: Feasibility test of an airborne pulse-Doppler meteorological radar. *J. Climate Appl. Meteor.*, **22**, 744–757.

_____, 1984: Mesoscale and convective-scale characteristics of mature hurricanes. Part I: General observations by research aircraft. *J. Atmos. Sci.*, **41**, 1268–1285.

Kloosterzeil, R. C., and G. J. van Heijst, 1991: An experimental study of unstable barotropic vortices in a rotating fluid. *J. Fluid Mech.*, **223**, 1–24.

Kossin, J. P., and M. D. Eastin, 2000: Observational evidence for turbulent exchange between the hurricane eye and eyewall. *J. Atmos. Sci.*, accepted.

_____, W. H. Schubert, and M. T. Montgomery, 2000: Unstable interactions between a hurricane's primary eyewall and a secondary ring of enhanced vorticity. *J. Atmos. Sci.*, accepted.

Kuo, H.-C., R. T. Williams, and J.-H. Chen, 1999: A possible mechanism for the eye rotation of Typhoon Herb. *J. Atmos. Sci.*, **56**, 1659–1673.

Lamb, H., 1932: Hydrodynamics, sixth ed., Dover, 732 pp.

Lee, W.-C., F. D. Marks, P. Dodge, and P. H. Hildebrand, 1994: Mapping of the airborne Doppler radar data. *J. Atmos. Oceanic Technol.*, **11**, 572–578.

Legras, B., P. Santangelo, and R. Benzi, 1988: High resolution numerical experiments for forced forced two-dimensional turbulence. *Europhys. Lett.*, **5**, 37–42.

Lhermitte, R. M., 1971: Probing of atmospheric motion by airborne pulse-Doppler radar techniques. *J. Appl. Meteor.*, **10**, 234–246.

Marks, F. D., and R. A. Houze, 1984: Airborne Doppler radar observations in Hurricane Debby. *Bull. Amer. Meteor. Soc.*, **65**, 569–582.

———, 1985: Evolution of the structure of precipitation in Hurricane Allen (1980). *Mon. Wea. Rev.*, **113**, 909–930.

———, and ———, 1987: Inner core structure of Hurricane Alicia from airborne Doppler radar observations. *J. Atmos. Sci.*, **44**, 1296–1317.

———, ———, and J. Gamache, 1992: Dual-aircraft investigation of the inner core of Hurricane Norbert: Part I: Kinematic structure. *J. Atmos. Sci.*, **49**, 919–942.

McWilliams, J. C., and G. R. Flierl, 1979: On the evolution of isolated, nonlinear vortices. *J. Phys. Oceanogr.*, **9**, 1155–1182.

———, 1984: The emergence of isolated coherent vortices in turbulent flow. *J. Fluid Mech.*, **146**, 21–43.

———, 1989: Statistical properties of decaying geostrophic turbulence. *J. Fluid Mech.*, **198**, 199–230.

———, J. B. Weiss, and I. Yavneh, 1999: The vortices of homogeneous geostrophic turbulence. *J. Fluid Mech.*, **401**, 1–26.

Melander, M. V., J. C. McWilliams, and N. J. Zabusky, 1987: Axisymmetrization and vorticity-gradient intensification of an isolated two-dimensional vortex through filamentation. *J. Fluid Mech.*, **178**, 137–159.

———, N. J. Zabusky, and J. C. McWilliams, 1988: Symmetric vortex merger in two dimensions. *J. Fluid Mech.*, **195**, 303–340.

Michalke, A. and A. Timme, 1967: On the inviscid instability of certain two-dimensional vortex-type flows. *J. Fluid Mech.*, **29**, 647–666.

Möller, J. D., and R. K. Smith, 1994: The development of potential vorticity in a hurricane-like vortex. *Quart. J. Roy. Meteor. Soc.*, **120**, 1255–1265.

———, and S. C. Jones, 1998: Potential vorticity inversion for tropical cyclones using the asymmetric balance theory. *J. Atmos. Sci.*, **55**, 259–282.

_____, and M. T. Montgomery, 1999: Vortex Rossby waves and hurricane intensification in a barotropic model. *J. Atmos. Sci.*, **56**, 1674–1687.

_____, and _____, 2000: Tropical cyclone evolution via potential vorticity anomalies in a three-dimensional balance model. *J. Atmos. Sci.*, in press.

Molinari, J., S. Skubis, and D. Vollaro, 1995: External influences on hurricane intensity. Part III: Potential vorticity structure. *J. Atmos. Sci.*, **52**, 3593–3606.

Montgomery, M. T., and B. F. Farrell, 1992: Polar low dynamics. *J. Atmos. Sci.*, **49**, 2484–2505.

_____, and _____, 1993: Tropical cyclone formation. *J. Atmos. Sci.*, **50**, 285–310.

_____, and R. Kallenbach, 1997: A Theory for vortex Rossby-waves and its application to spiral bands and intensity changes in hurricanes. *Quart. J. Roy. Meteor. Soc.*, **123**, 435–465.

_____, and J. Enagonio, 1998: Tropical cyclogenesis via convectively forced vortex Rossby waves in a three-dimensional quasigeostrophic model. *J. Atmos. Sci.*, **55**, 3176–3207.

_____, J. D. Möller, and C. T. Nicklas, 1999: Linear and nonlinear vortex motion in an asymmetric balance shallow water model. *J. Atmos. Sci.*, **56**, 749–768.

_____, J. M. Hidalgo, P. D. Reasor, 2000: A semi-spectral numerical method for modeling the vorticity dynamics of the near-core region of hurricane-like vortices. *Colorado State University*, Atmospheric Science Paper.

_____, H. D. Snell, and Z. Yang, 2000: Axisymmetric spin-down dynamics of hurricane-like vortices. *J. Atmos. Sci.*, accepted.

Neldar, J. A., and R. Mead, 1965: A simplex method for function minimization. *Comp. J.*, **7**, 308–313.

Nolan, D. S., and M. T. Montgomery, 2000: The algebraic growth of wavenumber one disturbances in hurricane-like vortices. *J. Atmos. Sci.*, **57**, in press.

Ooyama, K. V., 1969: Numerical simulation of the life cycle of tropical cyclones. *J. Atmos. Sci.*, **26**, 3–40.

Pasch, R. J., and M. Mayfield, 1996: Eastern North Pacific hurricane season of 1994. *Mon. Wea. Rev.*, **124**, 1579–1590.

Polvani, L. M., and X. J. Carton, 1990: The tripole: A new coherent vortex structure of incompressible two-dimensional flows. *Geophys. Astrophys. Fluid Dynamics*, **51**, 87–102.

_____, 1991: Two-layer geostrophic vortex dynamics. Part 2. Alignment and two-layer V-states. *J. Fluid Mech.*, **225**, 241–270.

Raymond, D. J., and H. Jiang, 1990: A theory for long-lived mesoscale convective systems. *J. Atmos. Sci.*, **47**, 3067–3077.

_____, 1992: Nonlinear balance and potential-vorticity thinking at large Rossby number. *Quart. J. Roy. Meteor. Soc.*, **118**, 987–1015.

Reasor, P. D., M. T. Montgomery, F. D. Marks, Jr., and J. F. Gamache, 2000: Low-wavenumber structure and evolution of the hurricane inner core observed by airborne dual-Doppler radar. *Mon. Wea. Rev.*, **128**, 1653–1680.

Ritchie, E. A., and G. J. Holland, 1993: On the interaction of tropical-cyclone-scale vortices. II: Discrete vortex patches. *Quart. J. Roy. Meteor. Soc.*, **119**, 1363–1379.

Rivest, C., and B. F. Farrell, 1992: Upper-tropospheric synoptic-scale waves. Part II: Maintenance and excitation of quasi modes. *J. Atmos. Sci.*, **49**, 2120–2138.

Roll, H. V., 1965: Physics of the marine atmosphere. Academic Press, 426 pp.

Rotunno, R., and K. A. Emanuel, 1987: An air-sea interaction theory for tropical cyclones. Part II: Evolutionary study using a nonhydrostatic axisymmetric numerical model. *J. Atmos. Sci.*, **44**, 542–561.

Roux, F., and N. Viltard, 1995: Structure and evolution of Hurricane Claudette on 7 September 1991 from airborne Doppler radar observations. Part I: Kinematics. *Mon. Wea. Rev.*, **123**, 2611–2639.

_____, and F. D. Marks, 1996: Extended velocity track display (EVTD): An improved processing method for Doppler radar observations of tropical cyclones. *J. Atmos. Oceanic Technol.*, **13**, 875–899.

Schecter, D. A., D. H. E. Dubin, A. C. Cass, C. F. Driscoll, I. M. Lansky, and T. M. O'Neil, 1999: Inviscid damping and growth of asymmetries on a 2D vortex. *Phys. Fluids*, in press.

Schubert, W. H., M. T. Montgomery, R. K. Taft, T. A. Guinn, S. R. Fulton, J. P. Kossin, and J. P. Edwards, 1999: Polygonal eyewalls, asymmetric eye contraction and potential vorticity mixing in hurricanes. *J. Atmos. Sci.*, **56**, 1197-1223.

Shapiro, L. J., and H. E. Willoughby, 1982: The response of balanced hurricanes to local sources of heat and momentum. *J. Atmos. Sci.*, **39**, 378–394.

———, 1983: The asymmetric boundary layer flow under a translating hurricane. *J. Atmos. Sci.*, **40**, 1984–1998.

———, and M. T. Montgomery, 1993: A three-dimensional balance theory for rapidly rotating vortices. *J. Atmos. Sci.*, **50**, 3322–3335.

Shay, L. K., G. J. Goni, and P. G. Black, 2000: Effects of a warm core oceanic feature on Hurricane Opal. *Mon. Wea. Rev.*, in press.

Simpson, R. H., and R. H. Riehl, 1958: Mid-tropospheric ventilation as a constraint on hurricane development and maintenance. *Proc. Tech. Conf. on Hurr.*, Miami Beach, FL, Amer. Meteor. Soc., D4.1–D4.10.

Smith, G. B., and M. T. Montgomery, 1995: Vortex axisymmetrization: Dependence on azimuthal wavenumber or asymmetric radial structure changes. *Quart. J. Roy. Meteor. Soc.*, **121**, 1615–1650.

Smith, R. A., and M. N. Rosenbluth, 1990: Algebraic instability of hollow electron columns and cylindrical vortices. *Physical Review Letters*, **64**, 649–652.

Smith, R. K., W. Ulrich, and G. Sneddon, 2000: On the dynamics of hurricane-like vortices in vertical shear flows. In review.

Snell, H. D., and M. T. Montgomery, 1999: Spin-down dynamics of axisymmetric hurricanes. *23rd Conf. on Hurricanes and Tropical Meteorology*, Dallas, TX, Amer. Meteor. Soc., 1031.

Sutyrin, G. G., 1989: Azimuthal waves and symmetrization of an intense vortex. *Sov. Phys. Dokl.*, **34**, 104–106.

_____, J. C. McWilliams, and R. Saravanan, 1998: Co-rotating stationary states and vertical alignment of geostrophic vortices with thin cores. *J. Fluid Mech.*, **357**, 321–349.

Trier, S. B., C. A. Davis, and W. C. Skamarock, 1998: Influence of mesoconvective vortices on the environment of deep convection. Preprints, *19th Conf. on Severe Local Storms*, Minneapolis, MN, Amer. Meteor. Soc., 36–39.

Velden, C. S., and K. F. Brueske, 1999: Tropical cyclone warm cores as observed from the NOAA polar orbiting satellite's new advanced microwave sounding unit. *23rd Conf. on Hurricanes and Tropical Meteorology*, Dallas, TX, Amer. Meteor. Soc., 182–185.

Viera, F., 1995: On the alignment and axisymmetrization of a vertically-tilted geostrophic vortex. *J. Fluid Mech.*, **289**, 29–50.

Weber, H. C., and R. K. Smith, 1993: The stability of barotropic vortices: Implications for tropical cyclone motion. *Geophys. Astrophys. Fluid Dynamics*, **70**, 1–30.

Willoughby, H. E., 1979: Forced secondary circulations in hurricanes. *J. Geophys. Res.*, **84**, 3173–3183.

_____, and M. B. Chelmow, 1982: Objective determination of hurricane tracks from aircraft observations. *Mon. Wea. Rev.*, **110**, 1298–1305.

_____, F. D. Marks, and R. J. Feinberg, 1984: Stationary and propagating convective bands in asymmetric hurricanes. *J. Atmos. Sci.*, **41**, 3189–3211.

Zehr, R., 1992: Tropical cyclogenesis in the Western North Pacific. NOAA Tech. Rep. NESDIS 61, 181 pp.